FORSCHUNGSZENTRUM ROSSENDORF FZR

Archiv-Ex.:

Timo Hauschild

Investigating
interatomic solid state potentials
using Crystal-GRID:
a study of applicability

Timo Hauschild

Investigating
interatomic solid state potentials
using Crystal-GRID:
a study of applicability

Dissertation

Investigating
interatomic solid state potentials
using Crystal-GRID:
a study of applicability
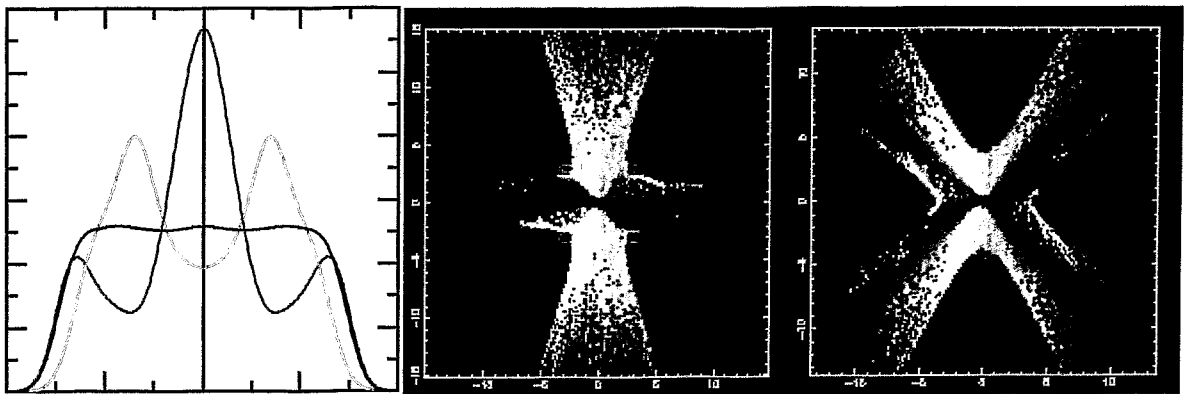
von der
Fakultät Mathematik und Naturwissenschaften
Der Technischen Universität Dresden
genehmigte

Dissertation
zur Erlangung des akademischen Grads
Dr. rer. nat.

vorgelegt von
Dipl.-Phys. Timo Hauschild geb. Koch
geboren am 6. Januar 1971 in Köln

Contents

Symbols

$\dot{I}\left(\Delta E_{\gamma_2}\right)$	Crystal-GRID count rate	(C.1), (C.8)
I_{bg}, I_{bg}^k	background level (in scan k)	(6.2), (6.4)
I_c, I_c^k	centre height (in scan k)	(6.3)
$I_{\text{pr}}\left(\Delta E_{\gamma_2}\right)$	theoretical Crystal-GRID line, normalized to I_{tot}	(5.7)
I_{tot}	total intensity of diffracted photons belonging to E_{γ_2} transition as measured in non-dispersive scan	(6.2)
J	number of parameters a_j	(6.2)
K	number of scans in series of scans	
L	spectrometer crystal thickness	(C.10)
L_P	Poisson likelihood	(6.9)
m	diffraction order of 2nd spectrometer crystal	(3.1)
m	mass of recoiling atom	
m_{a}	model function to be fitted to data, depending on parameters $\mathbf{a}$	(6.2), (6.4)
$m_{\text{a}}\left(\theta_i^k\right)$	predicted model value at position θ_i^k	(6.5)
m_i	mass of atom i	
m_s	sample mass	(C.3)
$\bar{\mathbf{M}}_s$	symmetry operator (matrix)	(5.2)
n	diffraction order of 1st spectrometer crystal	(3.1)
$\mathbf{n}$	direction of observation (unit vector)	(2.4)
$\mathbf{n}_{\gamma_1}$, $\mathbf{n}_{\gamma_2}$	direction of emission of γ_1, γ_2 (unit vector)	(2.8), (2.9)
N	number of atoms in simulation cell	(4.1)
N_{n}	number of neutrons captured by the sample	(C.2)
N_{X}	number of atoms of atom species X in sample	(C.2)
N_S	number of symmetry operators	(5.2)
N_T	number of simulated trajectories	(5.2)
$P\left(t\right)$	radioactive decay probability	(2.1)
$P\left(v_{\parallel}, t\right)$	probability of velocity projection	(5.2), (5.3)
$P_P\left(c_i; m_{\text{a}}\left(\theta_i\right)\right)$	Poisson probability	(6.9)
$P_{\tau}(v_{\parallel})$	probability of velocity projection at γ_2 emission	(5.4)
$P_{\tau}(\Delta E_{\gamma_2})$	ideal Crystal-GRID line	(5.6)
$P_{\gamma_2|\text{n}}$	probability that a photon of energy E_{γ_2} is emitted if a thermal neutron is captured	(C.8)
Q	goodness-of-fit	(6.21)

$\mathbf{r}(t)$	position vector of recoiling atom	
r_0	switch parameter in s_1, s_2	(1.15), (1.16)
$\mathbf{r}_i(t)$	position vector of atom i	(1.2), (4.1)
$\mathbf{r}_{ij}$, r_{ij}	interatomic distance $\mathbf{r}_i - \mathbf{r}_j$	(1.3)
$r_{c,n}$	neighbour cutoff radius	(4.7)
$r_{c,p}$	potential cutoff radius	(4.7)
δr	switch parameter in s_1	(1.15)
Δr_c	difference of cutoff radii $r_{c,n} - r_{c,p}$	(4.7)
$R^0_{E_\gamma,n,m}(\Delta\theta)$	ideal instrumental response function	(3.3)
$R^{\sigma_{ew}}_{E_\gamma,n,m}(\Delta\theta)$	instrumental response function	(3.3)
$\hat{R}^{\sigma_{ew}}_{E_\gamma,n,m}(\Delta E_\gamma)$	normalized instrumental response function (maximum $= 1$)	(3.8)
R_{MFP}	mean free path	(8.3)
$s_1(r_{ij})$	Fermi switch function	(1.15)
$s_2(r_{ij})$	power switch function	(1.16)
t	time	
Δt	variable time step in simulation	(4.3), (4.6)
Δt_0	fixed time step for recording trajectory	(4.6)
Δt_{nn}	time before recalculation of neighbour list	(4.8)
t_{end}	maximum time in simulation	(5.5)
t'	time of γ_2 emission (after γ_1)	
T	sample temperature	
u	unit mass	
v^0, $\mathbf{v}^0$	initial recoil velocity	(2.2)
$\mathbf{v}(t)$	velocity vector of recoiling atom	(2.4)
$\mathbf{v}_i(t)$	velocity vector of atom i	(4.1)
v_{max}	highest possible velocity of any atom in cell	(4.4)
$v_\parallel$	velocity projection	(5.1)
V	interatomic potential	(1.2)
V^{BM}	Born-Mayer potential	(1.7)
V^{EAM}	embedded-atom potential	(1.14)
V^{EQ}	equilibrium potential (V^{SW}, V^{EAM})	(1.19)
V^{GH}	Gärtner-Hehl potential	
V^{HE}	high-energy potential (V^{SC}, V^{GH}, V^{BM})	(1.19)
V^{K}	Keating potential	(B.1)
V^{SC}	screened Coulomb potential	(1.4)
V^{SW}	Stillinger-Weber potential	(1.8)–(1.10)
V_n	n-body term in potential V	(1.2)
$W(\phi)$, $W'(\cos\phi)$	angular correlation function	(2.6)
Z	atomic charge number	

α	absorption coefficient	(C.10)
α, β	Keating potential parameters	(B.1)
γ_1, γ_2	primary photon, secondary photon	
ε	binding energy per atomic bond	(1.8)
ε_0	vacuum permittivity	
$\theta, \theta_i, \theta_i^k$	diffraction angle (at measuring point i, in scan k)	(3.1), (6.1)
$\theta_{\mathrm{c}}, \theta_{\mathrm{c}}^k$	centre position (in scan k)	(6.1)
θ_{jik}	angle between $\mathbf{r}_{ij}$ and $\mathbf{r}_{ik}$	(1.2)
θ_n	diffraction angle with max. intensity in diffraction order n	(3.2)
λ, λ^*	photon wavelength	(3.1)
λ, λ^*	likelihood ratio	(6.11)
ξ	switch parameter in s_2	(1.16)
σ_{ew}	excess width	(3.4)
σ_i	standard deviation (error) of measurement i	(6.6)
$\sigma_{\mathrm{X}*}$	(n, γ) capture cross section of isotope X*	(C.2)
σ_τ	standard deviation (error) of lifetime τ	
τ	nuclear level lifetime	(2.1)
ϕ	angle between $\mathbf{n}_{\gamma_1}$ and $\mathbf{n}_{\gamma_2}$	(2.9)
$\Phi\left(\frac{r_{ij}}{a_s}\right)$	screening function	(1.5)
χ_N^2	Neyman's χ^2	(6.8)
χ_P^2	Pearson's χ^2	(6.7)
$\chi_{\lambda,P}^2$	Poisson maximum likelihood χ^2	(6.16)
χ_ν^2	reduced χ^2	(6.20)
Ω	solid angle	

Glossary

BCA	Binary Collision Approximation
BID	Beta Induced Doppler broadening
BM	Born-Mayer potential
Cr	chromium
DFT	Density Functional Theory
DSA	Doppler Shift Attenuation
EAM	Embedded-Atom Method
EQ	EQuilibrium potentials
Er	erbium
Fe	iron
FZR	Forschungszentrum Rossendorf
GAMS	GAMma Spectrometer
GaP	gallium phosphite
Gd	gadolinium
Ge	germanium
GH	Gärtner-Hehl potential
GRID	Gamma-Ray Induced Doppler broadening
GRIDSA	Gamma-Ray Induced DSA
HE	High-Energy potential
ILL	Institut Laue-Langevin
InP	indium phosphite
KrC	Krypton-Carbon potential [Wil 77]
MD	Molecular Dynamics
MFPA	Mean Free Path Approach
MLE	Maximum Likelihood Estimation
Ni	nickel
NID	Neutrino Induced Doppler broadening
NIST	National Institute of Standards and Technology
RMD	Restricted Molecular Dynamics
SC	Screened Coulomb potential
Si	silicon
SW	Stillinger-Weber potential [StiWeb 85]
TiO_2	titanium dioxide
ZBL	universal potential of Ziegler, Biersack, and Littmark [Zie 85]
ZnS	zinc sulphide

Introduction

Ion-beam techniques play an important role for the modification of materials. Ion implantation is commonly applied in microelectronics and for the hardening of steel, e.g., ion sputtering and ion etching to modify surfaces or to deposit thin layers. The application of these techniques is not always straightforward. Many experimental parameters, i.e. ion energy and dose, annealing time and temperature, have to be well chosen. In ion implantation, e.g., the depth distribution of the implanted ions is strongly influenced by the kinetic energy of the ions.

As the relevant processes are very complex, no adequate theory exists to predict material properties. In order to experimentally optimize the process parameters, large series of experiments are needed. Alternatively, computer simulations can be used, as for example with the well-known computer code TRIM [Zie 92] which sufficiently predicts depth distributions for ion energies above several keV. They are often less expensive and less time-consuming than true experiments which is much appreciated by researchers and industry alike.

Simulating atomic interaction presents a second appealing advantage. Within the simulation, the behaviour of the single atoms is calculated and can be observed in any desired detail. Thereby, simulations can be used as a time-resolved microscope on the nanometer scale, giving a deeper insight into the physical processes, which, in real experiments, is often very difficult to obtain.

In order to have reliable results with computer simulations a well-suited model is needed. Besides the description of the solid via its constituents and its crystal structure, the main assumptions of the model are related to the interactions within the system under study. Starting from the initial conditions and using the defined model, physical problems can be solved iteratively or statistically, thus allowing to predict properties in a deterministic way. If the model is well known and experimentally tested, experiments can be avoided or optimized in the tested range of the model.

The interaction of atoms within a solid is usually approximated by so-called *interatomic solid state potentials*. Experimentally, potentials have mainly been investigated in two limiting cases, very low and very high energies. In the high-energy regime, above several keV, experiments have been performed using ion scattering at gas targets or ion transmission through thin foils. Furthermore, depth distributions after ion implantation have been analysed. At the other extreme, potential functions can be fitted to equilibrium properties as elastic constants, the cohesive energy, or crystal structure. Neutron scattering at phonons can also be used to experimentally access this region. The most important high-energy and equilibrium potentials, applied within this work, are presented in Chapter 1.

Due to the continuous miniaturization, especially in microelectronics, ion energies are continuously reduced. Interest that focused on MeV or high keV energies for a long time, is more and more extending to the low keV regime, as for the creation of shallow p-n junctions. In the relevant energy range, between the vacuum level (0 eV) and about 1000 eV, the knowledge of interatomic potentials is very limited. The only experimental method, low-energy ion (surface) scattering, mainly tests the interatomic potentials at the surface of the sample and not within the bulk crystal.

An alternative approach is given by the Gamma-Ray Induced Doppler broadening (GRID) technique which was developed in the mid-1980s at the Institut Laue-Langevin (ILL) for the measurement of nuclear level lifetimes [Bör 88, BörJol 93]. The use of single-crystalline samples was proposed in 1992 [HeiJan 92]. This so-called *Crystal-GRID* method was predicted to yield *Doppler broadened energy spectra* with a fine structure, depending on the crystal orientation.

In GRID experiments, sample nuclei are excited by thermal neutrons that penetrate the bulk. The capture reaction leads to excited nuclei that de-excite via successive photon emissions. The primary photon entails a recoil of the capture nucleus that starts moving through the crystal with an initial kinetic energy of several hundred eV. The secondary photon allows to read out information about the velocity of the recoiling atom via the Doppler shifted energy. As this velocity is related to the interatomic forces experienced, the recoiling atoms probe the interatomic potentials. In a measurement, many photons are observed, a Doppler broadened energy spectrum is obtained. Its fine structure should allow the study of interatomic potentials at intermediate energies going from several eV up to 200 eV to 300 eV, typically.

As the neutron capture reaction takes place within the bulk and the kinetic energy of the captured neutron can be neglected, Crystal-GRID is not influenced by the interaction of a probing particle with the surface of the material under study. A detailed description of the experimental method is given in Chapter 2.

The first Crystal-GRID experiments were performed in 1995 [Jen 96b, Jen 97a], proving the existence of the predicted orientation-dependent fine structure. It was further shown that it might be possible to study interatomic potentials. However, statistics were insufficient for definite proof.

This work focuses on the applicability of the Crystal-GRID method. Its major aim is to show if and to what extent Crystal-GRID can be applied to the study of interatomic solid state potentials at intermediate energies. For that purpose, three important sub-topics can be defined. First, it must be checked which solids are suited due to their nuclear properties. Second, as the Crystal-GRID method is very young, studies with respect to the theoretical description and data evaluation are needed. And third, an experimental proof of the applicability needs to be obtained on the basis of a correct data evaluation.

In order to obtain the high energy resolution, needed to resolve the energy spectra, double crystal spectrometers have to be applied. Due to the low efficiency of these devices, measurements can only be performed at the world's most intense source of thermal neutrons, the *high-flux reactor* of the Institut Laue-Langevin (ILL) in Grenoble. It quickly turned out that the efficiency of the *ultra-high resolution spectrometers* GAMS 4/5 presents one of the major limitations of the method.
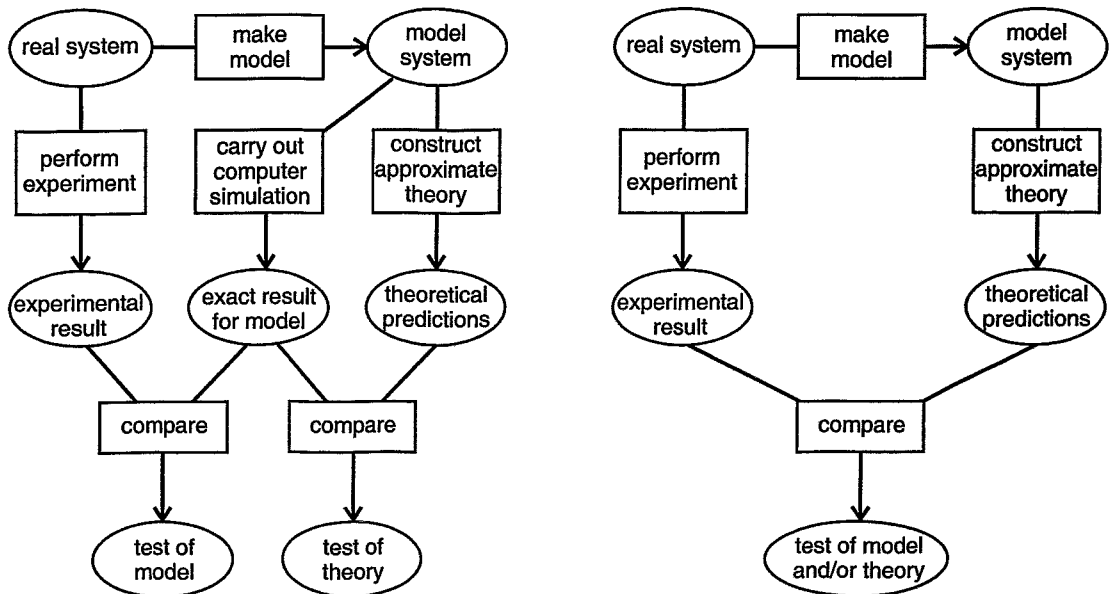
FIGURE 1: *The real system is modelled by the crystal structure and the interactions among the particles. Using an appropriate theory, results of experiments can be predicted. Comparing these results to experimental findings, the model and the approximations of the theory are tested simultaneously (right side). Computer simulations allow to distinguish the influence of the model and of the approximate theory. When comparing the predictions from computer simulations to the theoretical results, only the approximations of the theory are tested. Comparing the predictions to experimental findings, the model can be improved. As the interatomic potential is part of the model, its parameters can be optimized by fitting the predicted lines to the experimental scans (Figure adapted from [AllTil 87, p.5] [Hab 95, p.2]).*

Neutron capture cross sections of different nuclei vary by several orders of magnitude. Unfortunately, most solids of interest only consist of atoms with low cross sections. A systematic study within this work shows that expected count rates in Crystal-GRID measurements are much lower than those previously obtained in many nuclear physics GRID measurements. The experimental setup and the results of the study of applicability due to the nuclear properties are discussed in Chapter 3.

In the case of Crystal-GRID, *Molecular Dynamics (MD)* or *Restricted Molecular Dynamics (RMD) simulations* are used to calculate the slowing down of the recoiling atoms and thus to predict the Doppler broadened energy spectra on the basis of the model. Details on how to perform computer simulations of the slowing down and how to derive Doppler broadened energy spectra from these simulations are given in Chapters 4 and 5. For the first time, a microscopic study is used to explain the observed fine structure of the spectra, which attributes the fine structure to single collisions with neighbouring atoms.

The aim of improving interatomic potentials can be achieved by comparing experimental and simulated spectra (see left side of Fig. 1). If both spectra agree, the model sufficiently describes the physics being studied, it is correct in the tested domain and to the precision of the experiment. Otherwise, the model must be improved until the best fit

is achieved.

In order to judge the consistency of model lines and experimental data, a statistic is needed. Due to the low yield in the measurements, the applicability of different statistics to Crystal-GRID measurements is tested. It turns out that the statistic used for the data evaluation until this work, may *not* be applied to Crystal-GRID measurements. The different statistics and their application to Crystal-GRID data is discussed in Chapter 6.

GRID lines for poly-crystalline samples are commonly predicted by a mean free path approach (MFPA) of the slowing down. This theory is based on the same model as the simulations. It avoids time-consuming calculations, but using further approximations instead. As can be seen in the right part of Fig. 1, the influence of the model and of the approximations of the theory are not separated, if comparing these theoretical predictions to experimental results. When comparing the derived theoretical Doppler broadened energy spectra to the results from the computer simulations, however, it can be checked whether the approximations of the theory are justified (see left side of Fig. 1). Only if the correctness of the approximations has been verified, can this comparison be used to test the model. Therefore, the different approaches are compared in Section 8.3.

For over ten years, scientists have tried to apply GRID measurements to the investigation of interatomic potentials. A first try has been published by Jolie *et al.* in 1989 [Jol 89] using different poly-crystalline samples containing Ti. In 1991 and 1992, a series of papers was published by Kuronen and Keinonen. Therein, several GRID measurements were re-evaluated, comparing different interatomic potentials [Kur 91, Kei 91, Kur 92]. The first application of *Crystal*-GRID to the investigation of interatomic potentials was performed by Jentschel *et al.* [Jen 97a]. In parallel to the present work, Stritt *et al.* investigated interatomic potentials in single-crystalline metals [Str 99b, Str 99c, Str 99a].

However, due to several problems, the definite proof of applicability is not obtained until this work. A complete survey of the attempts and a discussion of different criteria to judge which potential is best is found in Chapter 7.

Due to the low experimental yield, measured data are not suited for methodical studies of the sensitivity of Crystal-GRID measurements to nuclear level lifetimes and to potential parameters, e.g. For that reason, artificial GRID data are applied within this work, allowing for the first time to check several predictions concerning the application of Crystal-GRID. As the Crystal-GRID method is very young, similar studies have not yet been performed. The results are discussed in Chapter 8.

Within this work, Crystal-GRID measurements have been performed using ZnS, Si, and TiO_2 single crystals. The data have been evaluated in order to determine best potential parameters, nuclear level lifetime, or to determine angular correlation parameters. The results are reported in Chapter 9. As the commonly applied data evaluation had to be essentially revised, measurements using Cr, Fe, and Ni single crystals were re-evaluated. This re-evaluation allows to show that a correct statistical data treatment is essential to avoid false conclusions from measurements.

Finally, after the summation, a brief look at the future of Crystal-GRID is discussed.

Chapter 1

Classical interatomic solid state potentials

Interactions between particles are described by the forces acting between them. If these forces **F** are conservative, they can be related to an *interatomic potential* V, also called *potential-energy function*

$$\mathbf{F} = -\boldsymbol{\nabla} V \tag{1.1}$$

where V only depends on the position vectors of the interacting particles.

Any potential-energy function V describing interactions among N particles can be resolved into one-body, two-body, three-body, etc. contributions

$$V\left(\mathbf{r}_1, \mathbf{r}_2, ..., \mathbf{r}_N\right) = \sum_{i=1}^{N} V_1\left(\mathbf{r}_i\right) + \sum_{i<j} V_2\left(\mathbf{r}_i, \mathbf{r}_j\right) + \sum_{i<j<k} V_3\left(\mathbf{r}_i, \mathbf{r}_j, \mathbf{r}_k\right) + ... \tag{1.2}$$

In order that this representation be useful, it is necessary that the component functions V_n converge quickly to zero with increasing n. For closely packed systems with ionic bonding, only two-body terms are needed to describe the system. In semiconductors of the diamond or zinc-blende structure, however, three-body terms are essential to stabilize the crystal structure. Higher terms are generally neglected.

The first term is a constant value as long as no external forces are regarded. It has no influence on the calculation of forces and can therefore be freely chosen. The two-body term V_2 only depends on the distance $r_{ij} = |\mathbf{r}_{ij}| = |\mathbf{r}_i - \mathbf{r}_j|$ of the two particles, and not on the absolute positions in space. Also, the three-body term V_3 must possess full translational and rotational symmetry; it only depends on the interatomic distances r_{ji} and r_{ik} as well as on the angle θ_{jik} in between $\mathbf{r}_{ij}$ and $\mathbf{r}_{ik}$, leading to

$$V\left(\mathbf{r}_1, \mathbf{r}_2, ..., \mathbf{r}_N\right) = \sum_{i<j} V_2\left(r_{ij}\right) + \sum_{i<j<k} V_3\left(r_{ji}, r_{ik}, \theta_{jik}\right) + \text{const.} \tag{1.3}$$

As discussed in the introduction, experimental methods allow to access interatomic potentials in the two limiting regions of very high and very low energies, respectively. Typical high-energy (HE) and equilibrium (EQ), i.e. low-energy potentials will be presented in the following two sections. Section 1.3 will be dedicated to the interpolation between the two regions allowing to get a complete interatomic potential function for the full energy range.

1.1   High-energy potentials

In ion beam physics, samples are mostly bombarded by high-energy ions (typically 10 keV
to 2 MeV). These ions penetrate the bulk and approach the bulk nuclei to very small
distances. They lose energy to the target via electronic and nuclear interactions. For
the energies, relevant in this work, electronic stopping is negligible compared to nuclear
stopping. The nuclear stopping in high-energetic collisions can be well approximated by
a sequence of two-body collisions. Consequently, so-called *pair potentials*, only containing
two-body terms, are sufficient to describe the high-energy regime.

1.1.1   Screened Coulomb potentials

Free nuclei (fully stripped ions) interact via the Coulomb force. If looking at two colliding
atoms, the Coulomb interaction is partially screened by the surrounding electrons. This
behaviour is reflected by the so-called *screened Coulomb potential* V_2^{SC}, defined for a pair
of interacting atoms as

$$V_2^{SC}\left(r_{ij}\right) = \underbrace{\frac{1}{4\pi\varepsilon_0}\frac{Z_iZ_je^2}{r_{ij}}}_{\text{Coulomb potential}} \cdot \underbrace{\Phi\left(\frac{r_{ij}}{a_s}\right)}_{\text{screening function}} \tag{1.4}$$

where r_{ij} is the distance between the two particles, Z_i and Z_j are the atomic charge
numbers, e is the electron charge (1.602×10^{-19} C), and ε_0 the vacuum permittivity (8.854×10^{-12} Fm^{-1}).

The screening function Φ depends on the interatomic distance r_{ij} which is scaled to the
so-called *screening length* a_s. Several expressions have been proposed, e.g. in the famous
potentials of Thomas-Fermi, Moliere, Lenz-Jensen, or Bohr (see [Zie 85]).

In this work, mostly the so-called *universal (ZBL) potential* will be used where the
screening function Φ is defined as

$$\Phi\left(\frac{r_{ij}}{a_s}\right) = \sum_{l=1}^{4} c_l \exp\left(\frac{-d_l\, r_{ij}}{a_s}\right) \tag{1.5}$$

$$\text{with} \qquad a_s = 0.88534\, a_B \left(Z_i^x + Z_j^x\right)^y \tag{1.6}$$

Here, a_B is the Bohr radius (0.529 Å), and c_l, d_l, x, and y are constants, listed in Table 1.1.

This potential has been developed by Ziegler, Biersack, and Littmark. They calculated
the screening functions for 522 randomly chosen atom pairs using a simplified quantum-
mechanical approach starting with the two atomic charge distributions of the colliding
atoms (for any details see [Zie 85, p.24ff]). After scaling the distance r_{ij} to the Z-dependent
screening length a_s, the screening functions of all the combinations of atom sorts became
very similar. By optimizing the parameters x and y in the definition of a_s (Equation 1.6),
the scatter of screening lengths could be reduced to $\sigma \approx 18\%$ for $V_2^{SC} > 2$ eV. The
parameters c_l and d_l were then fitted to the average screening function. The universal
(ZBL) potential is assumed to be the best mean potential available for high energies
[Eck 91, p. 62].

A different set of parameters had been derived, some years before, by Wilson, Hag-
gmark, and Biersack [Wil 77]. The so-called *Krypton-Carbon (KrC) potential* has the

	universal (ZBL) potential [Zie 85]	KrC potential [Wil 77]
c_1	0.028171	0.190945
c_2	0.28022	0.473674
c_3	0.50986	0.335381
c_4	0.18175	0
d_1	0.20162	0.278544
d_2	0.40290	0.637174
d_3	0.94229	1.919249
d_4	3.1998	0
x	0.23	0.5
y	-1	-0.666667

TABLE 1.1: *Parameters of the two screened Coulomb potentials applied in this work.*

same functional form as the universal (ZBL) potential, its parameters are also listed in the table. The KrC potential will be occasionally used in this work. Both of these potentials are mean potentials and are therefore universally applicable, but not optimally suited for a specific pair of atoms.

Gärtner and Hehl applied a similar method to derive interatomic potentials [GärHeh 79]. Their screening functions are calculated for a special pair of interacting atoms, the representation is numerical. In this work, these so-called *Gärtner-Hehl (GH) potentials* will be applied in the case of ZnS and TiO$_2$. The screening functions have been calculated by Gärtner [Gär 98, Gär 00]. The disadvantage of a numerical representation is that there is no parameter that can be easily varied in order to further optimize the potential function.

The applied screened Coulomb potentials are good approximations in the high energy region, certainly down to 1000 eV. Below this energy, it is difficult to experimentally check their validity.

Optimizing a screened Coulomb potential is most effectively done by varying the screening length. As for a given atomic interaction, the charge numbers are fixed, the parameters x and y are correlated. In order to optimize the screening length, only one parameter is needed. In this work, the number 0.88534 in Equation (1.6) will be multiplied with a factor between 50% and 200%.

1.1.2 Born-Mayer potential

A different, very simple formulation of a pair potential is given by the so-called *Born-Mayer (BM) potential* V_2^{BM} which can be written in the form[1]

$$V_2^{BM} = A_{BM} \exp\left(-\frac{r_{ij}}{B_{BM}}\right) \qquad (1.7)$$

with the adjustable parameters A_{BM} and B_{BM}. Parameters for 104 homo-nuclear pairs of neutral ground-state atoms as well as a combining rule for hetero-nuclear pairs are

---

[1]The BM potential is sometimes defined as $A_{BM} \exp\left(-b_{BM} r_{ij}\right)$ with $b_{BM} = 1/B_{BM}$. This is the case in the original publication [Abr 69].
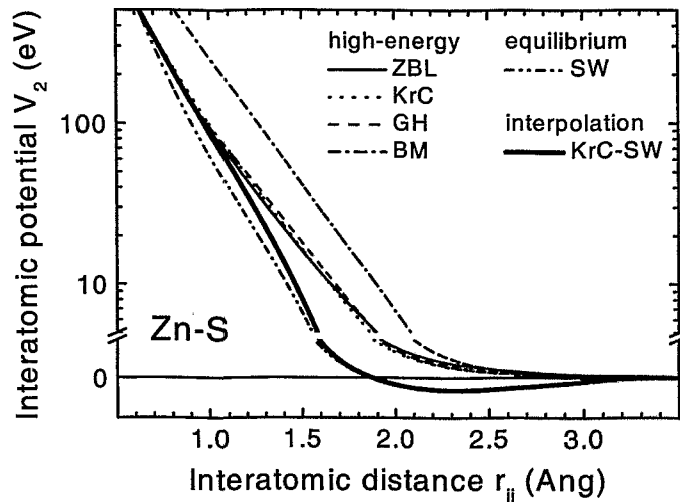
FIGURE 1.1: *Interatomic potentials for the Zn–S interaction. The high-energy potentials ZBL, KrC, and GH show a very similar run. The BM potential, however, is completely different. A typical interpolation between the high-energy and the equilibrium potential is also shown. The V_2-axis is plotted in a linear scale below 4 eV, and in a logarithmic scale above 5 eV.*

given in [Abr 69]. The parameters have been derived basing on the Thomas-Fermi-Dirac approximation. They are supposed to be correct to about 4% for interatomic distances $0.8\,\text{Å} < r_{ij} < 1.8\,\text{Å}$ [Abr 69]. As can be seen from Fig. 1.1, the BM potential using the parameters of [Abr 69] looks very different compared to the screened Coulomb potentials. It is more repulsive for low energies. The stated accuracy is not correct. However, by changing the parameters A_{BM} and B_{BM}, a good potential in the medium energy range can be obtained.

The BM potential is often used as it can be easily implemented. Many authors who developed potentials for metals, e.g., used the BM form with individually adapted parameters for the high-energy part (compare Sections 1.2.2 and 9.4). Furthermore, the BM potential is of special importance to GRID, as the MFPA theory, still commonly applied to calculate powder GRID lines, bases on this potential (compare Section 8.3.2).

1.2   Equilibrium potentials

Equilibrium potentials are developed in order to describe the solid (or liquid) phase of a material. These potentials must reproduce the correct crystal structure. Among different possible atomic arrangements, the stable structure must yield a minimum of the potential energy. It is evident that equilibrium potentials depend strongly on the material studied, i.e. on the crystal structure and on the type of binding.

Whilst the screened Coulomb potentials are purely repulsive, equilibrium potentials are repulsive for distances smaller than the nearest neighbour distance and attractive for larger distances. Quite generally, the additional constant in V is chosen in such a way that the vacuum level is at 0 eV and thus the potential minimum at $-\varepsilon$ where ε is the binding energy per atomic bond.

parameter		Si [StiWeb 85]	GaP [Ich 96]	ZnS (this work)
ε	eV/bond	2.1675	1.78	1.58
A		7.049556277	7.62333	7.71484
B		0.6022245584	0.681	0.693
σ	Å	2.0951	2.0642	2.0439
λ		21.0	29.57	15.266
a		1.80	1.80	1.80
γ		1.20	1.20	1.20

TABLE 1.2: *Stillinger-Weber potential parameters for Si, GaP, and ZnS.*

1.2.1 Stillinger-Weber potential

The so-called *Stillinger-Weber (SW) potential* [StiWeb 85] was first proposed in 1985 in order to describe interactions in solid and liquid forms of Si. Its functional form and parameters are chosen so that the diamond structure is the most stable structure and typical crystal properties are reproduced. As "no reasonable pair potential will stabilize the diamond structure", the Stillinger-Weber potential consists of two-body and three-body terms. It is defined as

$$V_2^{SW}(r_{ij}) = \varepsilon A \left[B \left(\frac{\sigma}{r_{ij}} \right)^4 - 1 \right] \exp \left[\left(\frac{r_{ij}}{\sigma} - a \right)^{-1} \right] \quad \text{for} \quad r_{ij} < a\sigma \qquad (1.8)$$

$$V_3^{SW}(\mathbf{r}_i, \mathbf{r}_j, \mathbf{r}_k) = h(r_{ji}, r_{ik}, \theta_{jik}) + h(r_{kj}, r_{ji}, \theta_{kji}) + h(r_{ik}, r_{kj}, \theta_{ikj}) \qquad (1.9)$$

$$h(r_{ji}, r_{ik}, \theta_{jik}) = \varepsilon\lambda \exp \left[\gamma \left(\frac{r_{ji}}{\sigma} - a \right)^{-1} + \gamma \left(\frac{r_{ik}}{\sigma} - a \right)^{-1} \right]$$
$$\cdot \left(\cos\theta_{jik} + \frac{1}{3} \right)^2 \quad \text{for} \quad r_{ji} < a\sigma \ \wedge \ r_{ik} < a\sigma \qquad (1.10)$$

The three-body term equals 0 for the ideal tetrahedral angle θ_t ($\cos\theta_t = -1/3$) and becomes positive as soon as this angle is changed. The resulting force acts on the atoms so that they regain the optimal tetrahedral configuration. The potential is smoothly cut off at the interatomic distance $a\sigma$; the second neighbour shell lies outside this cutoff.

Parameters for some III-V compound semiconductors were derived by Ichimura [Ich 96]. Following Ichimura, potential parameters for ZnS are calculated within this work (see Appendix B), the values are listed in Table 1.2 for Si, GaP, and ZnS.

1.2.2 Embedded-atom potentials

Metals are intensively studied in literature, where a large number of interatomic potentials is published (see Table 9.11). The so-called *embedded-atom method (EAM)* is a technique for constructing potentials especially for metals, originally developed by Daw and Baskes [DawBas 83, DawBas 84]. Therein, the potential energy V is divided into two contributions: the energy Ψ^{EAM} to embed an atom into the local-electron density ρ_i at the position

of the atom i provided by the other atoms of the metal and the energy due to a short-range screened repulsive pair interaction Φ^{EAM}.

$$V^{EAM} = \sum_i \Psi^{EAM}(\rho_i) + \sum_{i<j} \Phi^{EAM}(r_{ij}) \qquad (1.11)$$

The electron density ρ_i is approximated by the superposition of the atomic electron densities ρ_j^a of all the atoms.

$$\rho_i = \sum_j \rho_j^a(r_{ij}) \qquad (1.12)$$

The embedded-atom potentials are designed to describe the bound state. The repulsive pair term Φ^{EAM} is of the same form as the term V_2 in the general definition of the interatomic potential, Equation 1.2. Indeed, it is often set to be equal to a known repulsive pair potential, as the BM potential, and thereby allows to extrapolate to closer approaches, i.e. to higher energies. However, less care is usually given to the short-range interaction and thus it is not clear whether this extrapolation is useful.

In this work, EAM potentials are used in the re-evaluation of experiments originally performed by Stritt *et al.* (compare Section 9.4). To simplify the application of the EAM potentials, he used an effective pair potential [Str 99b]. In this approach, $\Psi^{EAM}(\rho_i)$ is developed around the electron density ρ_0 in a perfect lattice. This allows to transfer the first term of the expansion to the pair potential. The so-called *effective pair potential* Φ_{eff}^{EAM} is obtained [Rud 96]

$$\Phi_{eff}^{EAM}(r_{ij}) = \Phi^{EAM}(r_{ij}) + 2\rho(r_{ij}) \left.\frac{d\Psi^{EAM}}{d\rho}\right|_{\rho=\rho_0} \qquad (1.13)$$

Due to this transformation, the new embedding function has null first derivative, it becomes less important. Stritt neglected the embedding function completely and used only the effective pair potential in his simulations, i.e.

$$V_2^{EAM}(r_{ij}) = \Phi_{eff}^{EAM}(r_{ij}) \qquad (1.14)$$

It is not checked whether this additional approximation is justified.

1.3   Interpolating potentials

The high-energy (HE) potentials are valid above 1000 eV, the equilibrium (EQ) potentials well describe the bound state, they may be a good approximation up to several eV. In order to close the gap, some interpolation method must be applied.

In this work, a function is used to smoothly switch from one potential function to the other. Two different functional forms are applied: the Fermi function $s_1(r_{ij})$ with the adjustable parameters r_0 and δr

$$s_1(r_{ij}) = \frac{1}{1 + \exp\left(\frac{r_{ij}-r_0}{\delta r}\right)} \qquad (1.15)$$

and a function — called *power-switch function* in the following — depending on the parameters r_0 and ξ ($\xi > 0$)

$$s_2\left(r_{ij}\right) = \frac{1}{1 + \left(\frac{r_{ij}}{r_0}\right)^{\xi}} \qquad (1.16)$$

The parameter r_0 defines the switch centre, the parameters δr and ξ the relevant range over which the switching is performed. The power-switch function is more adapted to the interpolation of interatomic potentials, as its value tends to 1 as r_{ij} tends to 0, and thus for very near approaches, the combined potential equals the high-energy potential.

The switching is only applied to the two-body part, as the high-energy potentials do not include any three-body term. For near approaches, the three-body force becomes negligible compared to the two-body forces, anyway.

Potentials are only defined to an arbitrary constant which cancels out when deriving the interatomic force from the potential function. However, if two potentials are connected as in

$$
\begin{aligned}
V_2 &= \left(V_2^{\mathrm{HE}} + C_1\right) \cdot s_i\left(r_{ij}\right) + \left(V_2^{\mathrm{EQ}} + C_2\right) \cdot (1 - s_i\left(r_{ij}\right)) \qquad (1.17) \\
&= \left[V_2^{\mathrm{HE}} \cdot s_i\left(r_{ij}\right) + V_2^{\mathrm{EQ}} \cdot (1 - s_i\left(r_{ij}\right))\right] + (C_1 - C_2) \cdot s_i\left(r_{ij}\right) + C_2 \qquad (1.18)
\end{aligned}
$$

the difference of the constants, $C_1 - C_2$, does not cancel out when calculating the force. This additional parameter, not having any physical meaning, is avoided by directly connecting the two-body forces F_2

$$F_2 = -\frac{dV_2}{dr_{ij}} \equiv \left(-\frac{dV_2^{\mathrm{HE}}}{dr_{ij}}\right) \cdot s(r_{ij}) + \left(-\frac{dV_2^{\mathrm{EQ}}}{dr_{ij}}\right) \cdot (1 - s(r_{ij})) \qquad (1.19)$$

and deriving the combined interatomic potential by an integration.

$$V_2 = -\int F_2 \, dr \qquad (1.20)$$

This additionally ensures that the combined force function does not have an unphysical local maximum which could occur when interpolating the potentials and badly choosing the constants C_1 and C_2.

Chapter 2

Experimental Method – Crystal-GRID

The investigation of interatomic solid state potentials at energies below 500 eV is often perturbed by the interaction of the probing particles with the surface of the solid under study. The GRID (*Gamma-Ray Induced Doppler broadening*) method avoids this problem by using thermal neutrons that penetrate the bulk. A capture reaction leads to excited sample nuclei without any significant transfer of kinetic energy. The first de-excitation entails a recoil motion of still excited nuclei. Information on this motion can be read out via Doppler shifted photons from secondary photons, the recoiling nuclei form *nuclear probes.*

The GRID method has been developed by Börner *et al.* for the measurement of nuclear level lifetimes [Bör 88]. A reviewing description can be found in [BörJol 93]. While originally only poly-crystalline samples were used, Heinig and Janssen proposed in 1992 to apply GRID to single crystals [HeiJan 92]. The first so-called *Crystal-GRID* experiments were performed in 1995 by Jentschel *et al.* [Jen 96b], proving the existence of a predicted *orientation-dependent* fine structure in the measured energy spectra. In the present work, GRID using powder or other poly-crystalline samples is called *powder GRID*; the general term GRID refers to measurements with both, powder and single-crystalline samples.

The physical effects underlying GRID measurements will be discussed in the following. A summarizing sketch is displayed in Figure 2.1.

2.1   Neutron capture and de-excitation

In GRID experiments, the material to be studied is exposed to an intense flux of thermal neutrons. Neutron capture reactions generate excited nuclei of mass number $A + 1$ and charge number Z, where A and Z are the mass and charge numbers of the capturing nuclei. The excitation energy is given by the binding energy of the thermal neutrons (≈ 10 MeV), as the kinetic energy of the neutrons can be neglected (≈ 25 meV).

GRID can be observed if the de-excitation takes place via at least one intermediate excited state (γ cascade). A typical cascade is displayed in Fig. 2.2. The capture level, $E_{\text{level}} = 8.642$ MeV, in this case, is depopulated by a first, primary photon γ_1, emitted in an arbitrary direction. Due to momentum conservation, the emitting nucleus recoils in the opposite direction.
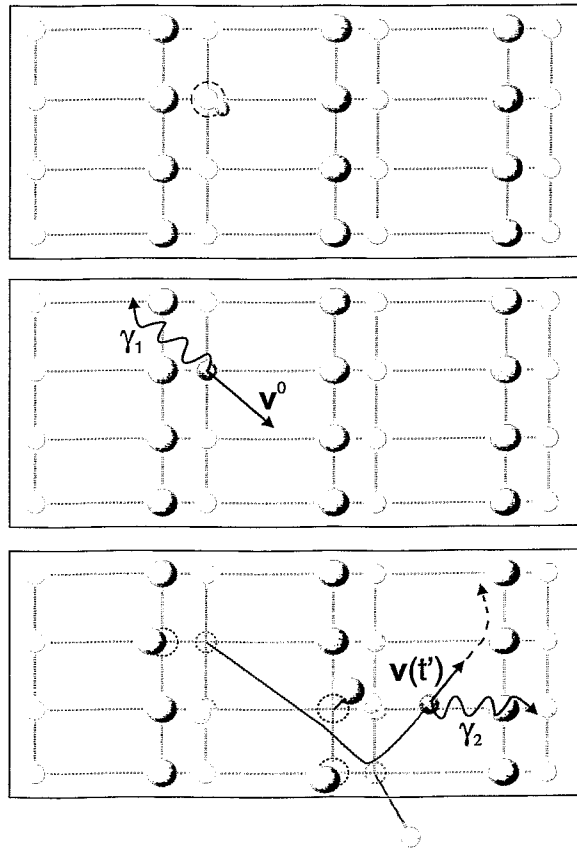
FIGURE 2.1: *Scheme of the GRID method. A thermal neutron is captured by a nucleus of the solid leading to an excited nuclear state. The de-excitation takes place via a γ cascade. The emission of a primary photon γ_1 entails a recoil of the still excited nucleus. The trajectory of the recoiling atom (initial velocity $\mathbf{v}^0$) is defined by the collisions with neighbouring atoms, thus by the crystal structure and the interatomic solid state potential. At the time t', a secondary photon is emitted and observed by the spectrometer. As the emitting nucleus is moving, the photon's energy is Doppler shifted.*

If the intermediate excited state, $E_{\text{level}} = 3.221\,\text{MeV}$, has a short lifetime and decays under emission of a secondary photon γ_2, this secondary photon allows to read out information on the recoiling atom's velocity. It forms a nuclear probe. The decay probability $P(t')\,dt'$ is given by the radioactive decay law

$$P(t')\,dt' = \frac{1}{\tau}\exp\left(\frac{-t'}{\tau}\right)\,dt' \qquad (2.1)$$

where τ is the nuclear level lifetime[1].

Ideally, the intermediate level is only fed by one transition depopulating the capture

---

[1]Often, the half life $T_{1/2} = \tau \cdot \ln 2 \approx 0.69 \cdot \tau$ is given instead of the lifetime τ. In the context of GRID measurements, the lifetime τ is used by convention.
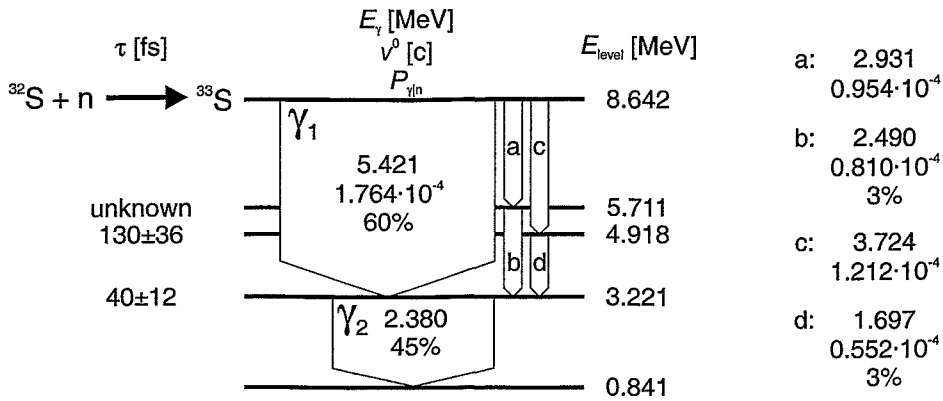
FIGURE 2.2: *De-excitation cascade of the nuclear reaction $^{32}_{16}S(n,\gamma)^{33}_{16}S$. The 2.380 MeV transition has been used for Crystal-GRID measurements. It depopulates the 3.221 MeV level which is mainly primarily fed. Two two-step cascades contribute less than 10%. The numbers given are the nuclear level lifetimes τ, the photon energies E_γ, the initial velocities v^0 of the recoiling atom (calculated from E_γ) for the feeding transitions, the absolute probabilities $P_{\gamma|n}$ for the transition to occur (% refers to the total number of neutron captures), where relevant, and the nuclear level energies E_{level}.*

state. In this case, all nuclei under study are at rest at their original lattice sites[2] and start moving with one fixed recoil velocity v^0. In most nuclei, however, additional so-called *side feeding* exists. In Fig. 2.2, e.g., two further two-photon transitions populate the studied intermediate level. Due to the first recoil of the two-step cascade (transition a and c in the figure), the nuclei are moving when the second transition (b and d) occurs. Instead of a mono-energetic initial recoil velocity, a distribution of velocities exists [Jen 97a, Appendix A.1]. For that reason, it becomes more difficult to extract information on the interatomic potential from the Doppler shifted photons.

How can one be sure that the observed secondary photon belongs to the cascade under study? Even though the sample contains different isotopes of the same species and a multitude of decay channels exists, the energy of the secondary photon can generally be clearly resolved by the spectrometer. The level schemes of the studied isotopes are sufficiently well known, so that a measurement of the primary photon is not necessary. A coincidence measurement of both photons would avoid including the side feeding; however, the measured yield would be orders of magnitude lower.

Besides the γ cascades, decay channels including β or neutrino emission also exist. Corresponding measurements are called BID (*Beta decay Induced Doppler broadening*) or NID (*Neutrino Induced Doppler broadening*). A short comparison of the three methods is given in [Jen 97a, Chapter 1]. First experimental results are reported by Jentschel *et al.* for BID [Jen 96a], as well as by Stritt *et al.* for NID [Str 97, Str 98, JolStr 00]. In this work, only GRID measurements will be discussed.

---

[2]if neglecting the thermal motion

2.2 Recoil and slowing down

The emission of a primary photon γ_1 entails a recoil to the emitting nucleus because of the conservation of momentum

$$mv^0 = E_{\gamma_1}/c \qquad (2.2)$$

where m is the mass and v^0 the initial velocity of the recoiling nucleus, E_{γ_1} the energy of the primary photon, and c the velocity of light. The direction of the initial recoil is opposite to the random direction of the photon emission.

Typically, the energy E_{γ_1} of the primary photon is of the order of several MeV. Consequently, the initial velocity v^0 of the recoiling nucleus lies in between 0.1 Å/fs and 2 Å/fs, i.e. between $10^{-5} c$ and $2 \cdot 10^{-4} c$, corresponding to an initial kinetic energy

$$E_{\text{kin}}^0 = \frac{1}{2} m \left(v^0 \right)^2 = \frac{1}{2} \frac{\left(E_{\gamma_1} \right)^2}{mc^2} \qquad (2.3)$$

of approximately 100 eV to 1000 eV (Numerical relations are given in Appendix A).

This initial kinetic energy E_{kin}^0 is well above typical atomic binding energies. The recoiling nucleus can leave its lattice site and travel several neighbour distances. The velocity is slow, however, compared to typical electron velocities. The electrons can adiabatically adjust to the nucleus; the nuclear probe consists of a recoiling atom.

The motion of this recoiling atom is governed by the collisions with the neighbouring lattice atoms leading to a slowing down. Its trajectory through the phase space (position $\mathbf{r}(t)$ and velocity $\mathbf{v}(t)$) is defined by the crystal structure and the interatomic forces, i.e. by the interatomic solid state potentials. As the collision partners can be found on neighbour shells that have well-defined distances to the starting position of the recoiling atom, the slowing down will be enhanced near a neighbour shell and reduced elsewhere. After about 100 fs the atom has lost most of its initial recoil energy and moves slowly, again. On the time scale of several 100 fs, the situation can be described as an equilibrium at enhanced temperatures, due to the deposited energy. This regime will be called *"quasi-thermal"* within this work.

In a single crystal, the motion of the recoiling atoms is highly anisotropic. For example, the slowing down in the direction of the nearest neighbour (*"blocking"*) is more efficient than in the direction between two nearest neighbours (*"channelling"*). The isotropic distribution of velocities just after the recoil becomes anisotropic as soon as the interaction with nearest neighbours becomes non-negligible. In a powder target, this anisotropy is averaged out by the arbitrary alignment of the micro-crystals. However, in the case of a single crystal, the anisotropy exists macroscopically.

2.3 Doppler shifted photons and GRID line

The intermediate excited nuclear level of the recoiling atom will decay further. If a secondary photon γ_2 of energy $E_{\gamma_2}^0$ is emitted at time t' (see Eq. 2.1) along the direction of observation $\mathbf{n}$, it is detected by the spectrometer. Due to the first recoil, the emitting atom is moving. Measured in the laboratory system, the energy of the secondary photon
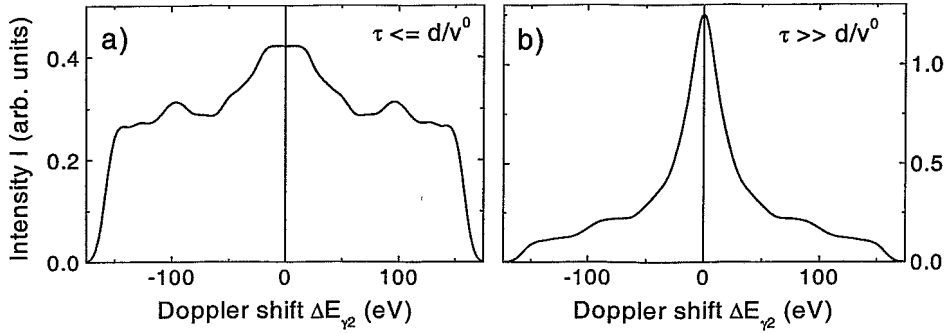
FIGURE 2.3: *Theoretical Crystal-GRID lines. The shape of the Doppler broadened energy spectrum depends strongly on the lifetime. a) For short lifetimes with $\tau \lesssim d/v^0 \approx 10\,\text{fs}$ where d is the nearest neighbour distance, the line is well structured. b) For long lifetimes with $\tau \gg d/v^0$, a central peak becomes dominant and the fine structure in the wings less visible.*

is Doppler shifted by

$$\Delta E_{\gamma_2} = E_{\gamma_2} - E_{\gamma_2}^0 = E_{\gamma_2}^0 \frac{\mathbf{v}(t') \cdot \mathbf{n}}{c} \qquad (2.4)$$

The natural line width of the transition is small. Compared to the resolution obtained in the measurements, its influence on the GRID line can be neglected for lifetimes $\tau > 1\,\text{fs}$ [Jen 97a, Figure 1.4].

In a GRID measurement, a large number of neutrons are captured, leading to many recoiling atoms. However, the number of capture events ($\approx 10^{17}/\text{d}$ for the samples studied in this work) is small, compared to the number of atoms in the crystal ($\approx 10^{23}$), so that almost every recoiling atom moves in a perfect crystal.

The recoiling atoms travel on different trajectories, as the primary photons are emitted in arbitrary directions. The emission of the secondary photons occur at different times. Therefore, observing many of them, a Doppler broadened photon energy spectrum $I(\Delta E_{\gamma_2})$ is obtained, the so-called *Crystal-GRID line*. The maximum Doppler shift $\Delta E_{\gamma_2}|_\text{max}$ corresponds to the maximum possible velocity projection $(\mathbf{v}(t') \cdot \mathbf{n})|_\text{max} = v^0$. It is typically a few hundreds of eV and can be calculated by combining Eq. (2.2) and (2.4):

$$\Delta E_{\gamma_2}|_\text{max} = E_{\gamma_2}^0 \frac{v^0}{c} = E_{\gamma_2}^0 \frac{E_{\gamma_1}}{mc^2} \qquad (2.5)$$

What does a typical Crystal-GRID line look like? If the intermediate nuclear level is short-lived, i.e. $\tau \lesssim d/v^0 \approx 10\,\text{fs}$ where d is the nearest neighbour distance, most of the secondary photons are emitted by fast moving atoms. The Doppler broadened line will be broad and fine structured due to the anisotropic and time-dependent slowing down (compare Fig. 2.3a). For long-lived levels, most photons are emitted from slowly moving atoms, leading to a small shift. In this case, the Doppler broadened line $I(\Delta E_{\gamma_2})$ will have a significant peak around $\Delta E_{\gamma_2} = 0$ and only small contributions in the wings. The fine structure is less visible (see Fig. 2.3b). A more detailed look at Crystal-GRID lines will be given in Chapter 5.
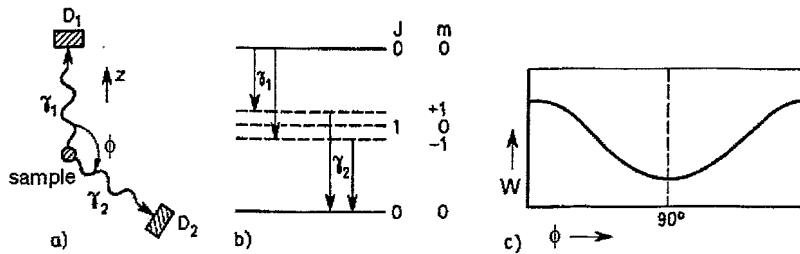
FIGURE 2.4: *Principle of angular correlation measurements. a) Two detectors are placed under an angle ϕ relative to each other. The simultaneous counts of both are recorded as a function of the angle. b) Example of a 0-1-0 cascade with the quantisation axis chosen parallel to z. c) Result from angular correlation measurement. (Figure taken from [MK 94].)*

2.4   Angular Correlation

Angular correlation is observed if nuclei decay through successive emission of two photons, just as in the case of Crystal-GRID. The probability of emission of a single photon by an excited nucleus depends on the angle between the nuclear spin axis and the direction of emission. However, as the spins of the nuclei are randomly oriented in the crystal, the existence of a preferred orientation is averaged out when observing many emission events.

When looking at two successive photons emitted in directions making an angle ϕ between each other, the observed intensity depends on this angle. In order to understand the influence of angular correlation on Crystal-GRID, a short look at angular correlation measurements will be given. For more details as well as a general theory and a large number of references on angular correlation, refer to [Fra 55, FraSte 65].

Angular correlation measurements

Most angular correlation measurements are coincidence measurements, the principle is displayed in Figure 2.4. A primary photon is observed by a detector placed in a fixed direction. Secondary photons are only considered in coincidence, i.e. after a primary photon has been registered in the detector. Therefore, only a selected subset of the nuclei is seen. The spin distribution before the second photon emission is not isotropic in this subset, the nuclei are selected or "prepared" with a preferred spin orientation.

In this case, the angular dependence of the succeeding, secondary photon emission is no longer averaged out and can be observed. The measured coincident yield depends on the angle ϕ between the directions of emission of the two photons, it is proportional to the correlation function $W(\phi)$.

If the nuclear spin states of the initial, intermediate, and final nuclear states are known, e.g. from prior angular correlation measurements, the correlation function $W(\phi)$ can be calculated from the transition probabilities and the directional distribution functions which are specific for a certain kind of radiation. Its general form is

$$W'(\cos\phi) = W(\phi) \sim 1 + A_2 P_2(\cos\phi) + A_4 P_4(\cos\phi) + \ldots \qquad (2.6)$$

with the Legendre polynomials P_n and the parameters A_n. Normalization as a weighting
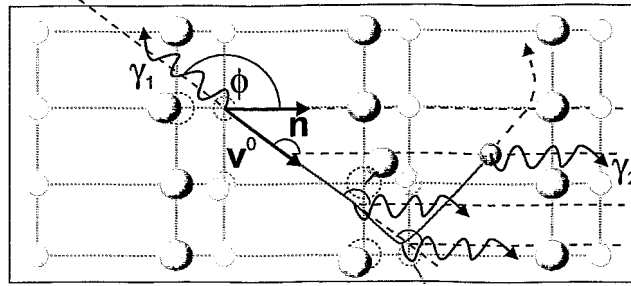
FIGURE 2.5: *After the neutron capture, a primary photon γ_1 is emitted. The excited nucleus recoils with initial velocity v^0 and is scattered along its trajectory. Secondary photons γ_2 can only be observed, if they are emitted in the direction n pointing to the spectrometer. Consequently, the angle between the directions of emission of the two photons equals ϕ for all observed photons from this trajectory.*

factor is obtained by the condition

$$\int_0^{2\pi} W(\phi)\, d\phi = 2\pi \tag{2.7}$$

Only even polynomials are needed as the parity is conserved under emission of a photon; the angular correlation function $W(\phi)$ is symmetric with respect to $\phi = 90°$, $W'(\cos\phi)$ is symmetric with respect to 0.

Angular correlation in Crystal-GRID

In Crystal-GRID measurements, the initial velocity v^0 of the recoiling atom is opposite to the arbitrary direction n_{γ_1} of the primary photon emission after neutron capture.

$$v^0 = -v^0 \cdot n_{\gamma_1} \tag{2.8}$$

A secondary photon can only be observed if it is emitted along the direction $n_{\gamma_2} = n$ pointing to the spectrometer. Looking at a single trajectory with a fixed direction n_{γ_1}, the angle ϕ is fixed for all secondary photons from this trajectory (see Figure 2.5).

$$\cos\phi = n_{\gamma_1} \cdot n_{\gamma_2} = n_{\gamma_1} \cdot n = \frac{-v(0)}{|v(0)|} \cdot n \tag{2.9}$$

Every trajectory makes a different angle ϕ with the direction of observation n, fixed in a measurement. Consequently, the probability of observing a Crystal-GRID photon originating from a trajectory is enhanced or reduced by the angular correlation factor $W'(\cos\phi)$.

2.5   What is Crystal-GRID used for?

Crystal-GRID belongs to the area of nuclear solid state physics. Measurements are performed in order to determine interatomic solid state potentials in the energy range of

approximately 5 eV to 500 eV. The measured signal, the Doppler broadened energy spectrum, however, also depends on the nuclear level lifetime of the intermediate level. As reported values have large errors, a precise value needs to be determined by the Crystal-GRID measurement, as well.

In powder GRID measurements, the influence of interatomic potential and nuclear level lifetime largely compensates, so that only one of the two quantities can be determined at once. As nuclear level lifetimes span more than 20 orders of magnitude, errors of around 50% are acceptable. By fixing an interatomic potential, which is expected to be correct within perhaps 30%, it is possible to determine nuclear level lifetimes which are sufficiently accurate for nuclear physics.

The use of single crystals is supposed to separate the two variables; the interatomic potential and the nuclear level lifetime should become measurable at the same time. It is one of the major aims of this work to examine to what extent this prediction holds true in real experiments.

Up to now, Crystal-GRID has been used by three different groups. Starting from 1995, Jentschel and Heinig (Forschungszentrum Rossendorf[3], Germany) performed the first Crystal-GRID experiments, confirming the orientation-dependence of Crystal-GRID lines and showing that the technique should be applicable to the investigation of interatomic solid state potentials [Jen 96b, Jen 96a, Jen 97a, Jen 97b]. After these encouraging results, Karmann and Wesch (Friedrich-Schiller-University Jena[4], Germany) started investigating foreign atom sites with Crystal-GRID [Wes 98, Kar 00]. The investigation of interatomic potentials was the subject of two almost simultaneous research projects: the work presented here, as well as an investigation by Stritt and Jolie (University of Fribourg[5], Switzerland) [Str 99b, Str 99c, Str 99a, Str 00], revised in this work (see Section 9.4). The measurements of all three groups were done in close collaboration with the ILL[6] (Grenoble, France), mainly with Börner and Jentschel.

A historical overview of the investigation of interatomic potentials using both, powder and Crystal-GRID will be given in Section 7.1, after all concepts have been presented in the following chapters.

---

[3]http://www.fz-rossendorf.de/FWI/
[4]http://www.physik.uni-jena.de/
[5]http://www.unifr.ch/physics/
[6]http://www.ill.fr/nfp/

Chapter 3

Experimental Setup and its Application

Crystal-GRID experiments can be performed at the ultra-high resolution γ spectrometers GAMS 4 and GAMS 5 (*GAMma Spectrometer*) at the Institut Laue-Langevin (ILL) in Grenoble, France (see Fig. 3.1). The main reason of using the GAMS spectrometers is that they attain a very high energy resolution, $\Delta E_\gamma / E_\gamma$ is typically $5 \cdot 10^{-6}$, i.e. $\Delta E_\gamma = 10 \, \text{eV}$ for a typical Crystal-GRID transition of about $E_\gamma = 2 \, \text{MeV}$. As the maximum Doppler shift usually amounts to a few hundred eV, this allows to measure the fine structure of Doppler broadened lines. Unfortunately, the efficiency of the spectrometers is extremely low. Even though they are installed at the ILL's high-flux reactor generating the highest permanent flux of thermal neutrons in the world ($\approx 5 \cdot 10^{14} \, \text{cm}^{-2} \, \text{s}^{-1}$ at the sample), the experimental yield presents the main problem for Crystal-GRID studies. The new spectrometer GAMS 5 is being developed in order to cope with this problem. Its anticipated improvements will be described in Section 3.2.

FIGURE 3.1: *Polygone Scientifique in Grenoble, France. The marked cylinder-like building is the high-flux reactor of the Institut Laue-Langevin (ILL). Just next to the ILL, the synchrotron facility ESRF can be found.*
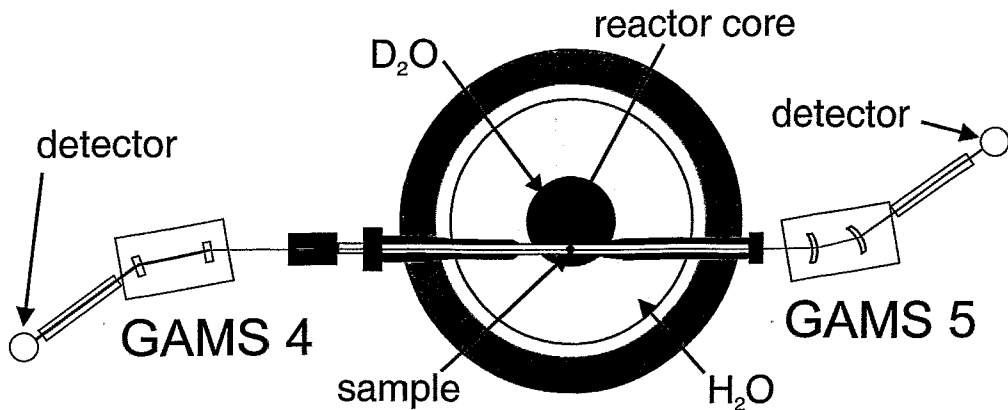
FIGURE 3.2: *ILL, Grenoble. Sketch of the high-flux reactor with the γ spectrometers GAMS 4 and GAMS 5 (figure adapted from [Jen 97a]).*

The two spectrometers are placed on either side of a through-going tangential beam tube (H6/H7) containing the sample crystals placed at a distance of 55 cm from the reactor core. The distance between the sample and the spectrometers is 15 m and 17 m for GAMS 4 and GAMS 5, respectively. Each spectrometer is located in an experimental casemate together with a γ detector. The setup can be seen in Fig. 3.2.

The spectrometers are built upon vibration isolation platforms. The temperature in the environmental chambers is stabilized, further humidity and air pressure are recorded. A short description of the spectrometers will be given in the next section. For any further details refer to a recent article of Kessler *et al.* [Kes 01].

3.1 Double flat crystal spectrometer

GAMS 4 is a double flat crystal spectrometer which has been installed as a collaboration of the National Institute of Standards and Technology (NIST[1], Gaithersburg, USA) and the ILL. For all measurements described in this work, GAMS 5 has also been used in double flat crystal mode. Fig. 3.3 shows the two common crystal arrangements, called non-dispersive (left) and dispersive geometry (right), respectively.

Radiation from the sample strikes the first spectrometer crystal. The diffraction at a set of lattice planes (*hkl*) can be described by the Bragg condition

$$n\lambda = 2d\sin\theta \tag{3.1}$$

where n is the diffraction order, $\lambda = hc/E_\gamma$ the photon wavelength, d the lattice plane spacing of the spectrometer crystal, and θ the angle between the incident radiation and the lattice planes.

The Bragg condition allows to determine the angular positions θ_n of the maxima in the diffraction pattern of a given wavelength λ

$$\theta_n(\lambda) = \arcsin\left(\frac{n\lambda}{2d}\right) \tag{3.2}$$

---

[1]http://www.nist.gov/
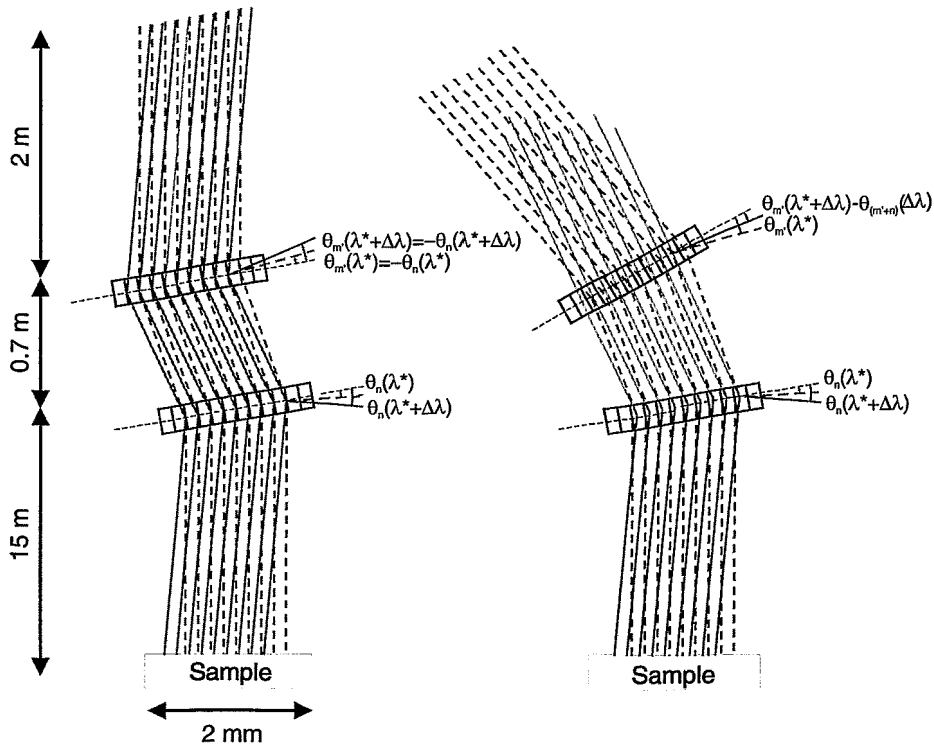
FIGURE 3.3: *Measuring geometries of a double flat crystal spectrometer. The non-dispersive geometry, shown on the left side, is used to experimentally determine the instrumental response function. The dispersive geometry (right) is selective in energy and allows to record the Doppler broadened energy spectra. For further details, refer to the text.*

When studying a certain transition of wavelength λ^*, the first crystal is positioned to fulfil the Bragg condition for this wavelength in a chosen diffraction order n. The diffracted radiation leaves the crystal under the angle $-\theta_n(\lambda^*)$.

Due to the finite thickness of the sample, an angular spread of the incoming beam exists. For the GAMS 4 facility this spread is given by $2\delta\theta = 2\,\mathrm{mm}\,/15\,\mathrm{m} \approx 0.13\,\mathrm{mrad} \approx 27\,\mathrm{arcs}$. For each incident angle within the spread, a different wavelength λ within the wavelength region $[\lambda^* - \delta\lambda, \lambda^* + \delta\lambda]$ with $\delta\lambda \approx 2d \cdot \delta\theta/n$ satisfies the Bragg condition of the first crystal. Every wavelength λ leaves the spectrometer only under its specific angle $-\theta_n(\lambda)$.

Non-dispersive geometry / Instrumental response function

In the non-dispersive geometry, shown on the left side of Fig. 3.3, the lattice planes of the two crystals are parallel. In this case, the incident angle at the second crystal is $-\theta_n(\lambda)$ for all wavelengths λ within the diffracted interval. All wavelengths λ that are diffracted by the first crystal, simultaneously satisfy the Bragg condition at the second crystal; the second diffraction does not additionally select in energy.

In Crystal-GRID measurements, the maximum Doppler shift in wavelength is always much smaller than the spread $2\delta\lambda$ of diffracted wavelengths. Consequently, in a non-dispersive measurement all photons belonging to one transition, Doppler shifted or not,
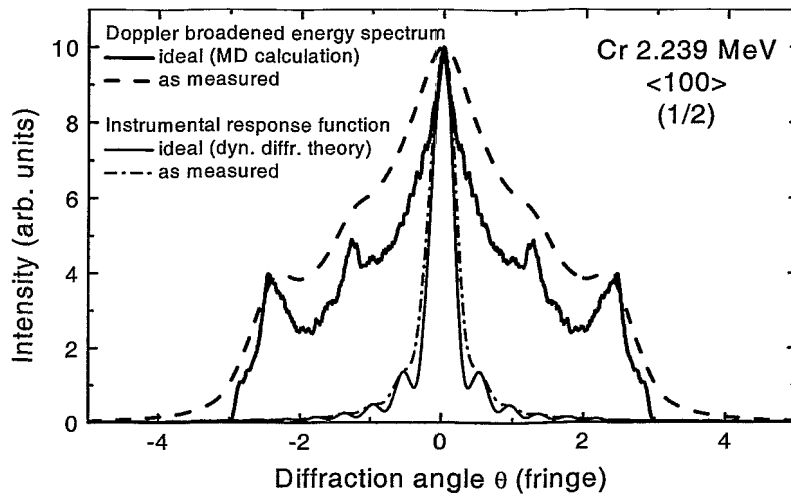
FIGURE 3.4: *Example of instrumental response and Doppler broadened energy spectrum. The instrumental response function as calculated by dynamical diffraction theory (narrowest curve) is broadened by crystal imperfections and small vibrations (dash-dotted line). The theoretical Doppler broadened energy spectrum, as calculated from MD simulations, is convoluted with this experimental instrumental response function before comparing theory and experiment. The spectrum is calculated for the 2.239 MeV transition in Cr, observed in <100> orientation and in diffraction order (1/2).*

are diffracted simultaneously if the second crystal is parallel to the first one.

The Bragg condition only allows to calculate the positions of the diffraction maxima. A more elaborate description is given by the dynamical diffraction theory. Its application to a double flat crystal spectrometer like GAMS 4, diffracting photons of energy E_γ in diffraction order $(\pm n, \pm m)$, is implemented in the code Xfneval. For perfect spectrometer crystals, a Lorentzian-like rocking curve $R^0_{E_\gamma,n,m}(\Delta\theta)$ with Pendellösung oscillations is obtained (see [Kes 88, Kes 01] and references therein), where $\Delta\theta = 0$ refers to the optimal position of the second spectrometer crystal in $\pm m^{\text{th}}$ order diffraction.

By rocking the second spectrometer crystal around the Bragg angle while keeping the first one fixed, the instrumental response function can be measured. Due to remaining imperfections of the spectrometer crystals, the measured instrumental response slightly deviates from the perfect theory. It can be approximated by convoluting the ideal response function $R^0_{E_\gamma,n,m}(\Delta\theta)$ from dynamical diffraction theory with a Gaussian $G(\Delta\theta, \sigma_{\text{ew}})$ of width σ_{ew}, the so-called *excess width* (see Fig. 3.4).

$$R^{\sigma_{\text{ew}}}_{E_\gamma,n,m}(\Delta\theta) = R^0_{E_\gamma,n,m}(\Delta\theta) * G(\Delta\theta, \sigma_{\text{ew}}) \tag{3.3}$$

$$\text{with} \quad G(\Delta\theta, \sigma_{\text{ew}}) = \frac{1}{\sqrt{2\pi}\sigma_{\text{ew}}} \exp\left(-\frac{(\Delta\theta)^2}{2\sigma_{\text{ew}}}\right) \tag{3.4}$$

Dispersive geometry / Energy-resolved measurement

The spectrometer is transformed to the dispersive geometry, shown on the right of Fig. 3.3, by rotating the second crystal through $\theta_n(\lambda^*) + \theta_m(\lambda^*)$ compared to the non-dispersive geometry while keeping the first crystal fixed. Here, n is the diffraction order of the first, m of the second spectrometer crystal, and λ^* the wavelength of the studied transition. As in the non-dispersive case, a large number of wavelengths λ are diffracted by the first crystal. In the dispersive geometry, however, the incident angle at the second crystal is $-\theta_n(\lambda) + \theta_n(\lambda^*) + \theta_m(\lambda^*)$. For m^{th} order diffraction this angle has to be equal to $\theta_m(\lambda)$. The diffracted wavelengths λ can be calculated by solving this equation

$$-\theta_n(\lambda) + \theta_n(\lambda^*) + \theta_m(\lambda^*) \stackrel{!}{=} \theta_m(\lambda)$$
$$\theta_n(\lambda^*) + \theta_m(\lambda^*) \stackrel{!}{=} \theta_n(\lambda) + \theta_m(\lambda)$$
$$\arcsin\left(\frac{n\lambda^*}{2d}\right) + \arcsin\left(\frac{m\lambda^*}{2d}\right) \stackrel{!}{=} \arcsin\left(\frac{n\lambda}{2d}\right) + \arcsin\left(\frac{m\lambda}{2d}\right) \tag{3.5}$$

As arcsin is a monotonous function, and $\arcsin(x) = -\arcsin(-x)$, the previous equation can only be fulfilled if

$$\lambda = \lambda^* \quad \vee \quad \underbrace{n = -m}_{\text{non-dispersive geometry}} \tag{3.6}$$

The second solution, namely $n = -m$, corresponds to parallel crystals, i.e. to the non-dispersive geometry where all wavelengths are diffracted. In the dispersive geometry, only one wavelength is diffracted, namely $\lambda = \lambda^*$. By rocking the second crystal about the Bragg angle, i.e. by slightly changing λ^*, the Bragg condition is sequentially satisfied for different wavelengths λ diffracted by the first crystal.

Thus, in the dispersive geometry, the recorded profile reproduces the wavelength spread of the incoming gamma ray, convoluted by the instrumental response. In this geometry, the Crystal-GRID line can be measured. Due to the selectivity in energy, the peak height is generally lower than in a non-dispersive scan.

Spectrometer Crystals / Interferometer

The spectrometer crystals are made out of nearly perfect Si or Ge crystals. The diffraction efficiency depends on the thickness and material of the crystals, as well as on the energy of the radiation to be diffracted. Different crystal thicknesses are available. Depending on the studied energy, it might be useful to change the spectrometer crystals (for more details see Appendix C.2). However, crystal changing is a time-consuming work and is only done if a high gain in efficiency can be obtained. Most measurements in this work have been performed with 2.47 mm and 2.72 mm thick Si crystals on GAMS 4 and GAMS 5, respectively. Diffraction takes place at the (220) lattice planes.

The high resolution of the gamma spectrometers necessitates a very precise positioning of the crystals. The rotation of each crystal is controlled by a polarization sensitive Michelson interferometer with an angular sensitivity of a few times 10^{-4} arcs (for details see [Kes 01]). The angles are measured in interferometer fringes, one fringe corresponding

to 0.0402 arcs (GAMS 4) or 0.0322 arcs (GAMS 5). In a dispersive scan, conversion from this unit to energy, can be done by an equation derived on the basis of Bragg's Equation (3.1) [RobJol 90].

$$\frac{\Delta E_{\gamma_2}}{\Delta \theta} \left[\frac{eV}{GAMS\,4\text{-fringe}} \right] = \frac{\left(E_{\gamma_2}^0 \,[\text{MeV}] \right)^2}{0.01657308473} \cdot \left| \frac{1}{n-m} \right| \qquad (3.7)$$

The conversion is applied to angle differences, in order to avoid errors of the absolute energy calibration. Precise absolute energies are not needed for Crystal-GRID measurements. Conversion from GAMS 4-fringes to GAMS 5-fringes is done by the factor 1.249438271, determined by Jentschel from measurements using TiO_2 on July, 2nd, and July, 5th, 1999.

For dispersive measurements, it is convenient to rewrite the instrumental response function $R_{E_\gamma,n,m}^{\sigma_{ew}} (\Delta \theta)$ of Eq. (3.3) as $\hat{R}_{E_\gamma,n,m}^{\sigma_{ew}} (\Delta E_{\gamma_2})$, a function of the Doppler shift energy ΔE_{γ_2}, normalized so that its maximum is 1. Using the transformation of Eq. (3.7), one obtains

$$\hat{R}_{E_\gamma,n,m}^{\sigma_{ew}} \left(\Delta E_{\gamma_2} \right) = \frac{R_{E_\gamma,n,m}^{\sigma_{ew}} (\Delta \theta)}{R_{E_\gamma,n,m}^{\sigma_{ew}} (0)} \qquad (3.8)$$

In some cases, the maximum of the response function is not located at $\Delta \theta = 0$, and the normalization would have to be done differently. However, non-centrally peaked response functions are not well suited for Crystal-GRID measurements and are therefore disregarded here.

Detector / Background suppression

The Doppler shifted photons are counted by a high-purity Ge detector. The analog signals of the detector are amplified and analysed by a multichannel analyser with 8192 channels. Under typical operation conditions, the relative energy resolution of the detector is $\Delta E_\gamma / E_\gamma = 10^{-3}$. The Doppler shifted photons belonging to the transition under study are typically spread over 5 to 10 channels of the analyser. The remaining channels only register background intensity. The additional energy resolution of the analyser allows to significantly suppress the background intensity by selecting only those channels that contain the Doppler shifted photons.

For the measurement of a GRID spectrum, the second crystal is stepped through a small angular range around the Bragg angle $\theta_m (\lambda^*)$. For each angular position θ_i of the crystal, the complete γ-ray spectrum is recorded; finally yielding a matrix $\bar{A}_i^j$ containing for each selected angular position θ_i and each channel j of the multichannel analyser a number of counts. Using the graphical user interface Xtrysf, the relevant channels $[j_-, j_+]$ are selected. Background suppression in the experimental GRID spectrum $c(\theta_i)$ is obtained by disregarding all counts recorded in channels outside the chosen window.

$$c_i = c(\theta_i) = \sum_{j_-}^{j_+} \bar{A}_i^j \qquad (3.9)$$

The choice of the window $[j_-, j_+]$ is arbitrary to some extent. However, an influence on the obtained results could never be observed.
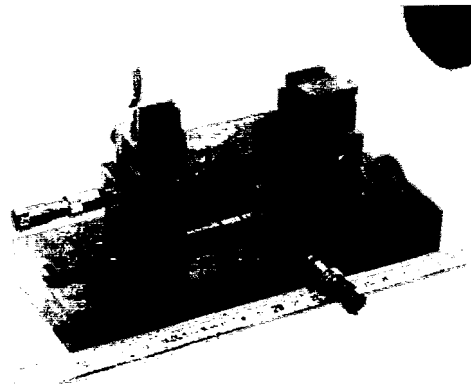
FIGURE 3.5: *Crystal bender [Dol 00]. Bent spectrometer crystals are expected to gain efficiency and accept thin films instead of thick single crystals. Unfortunately, the bending has turned out to be much more difficult than foreseen. The bent-crystal mode was not available during the present work.*

Not all photons deposit their total energy within the detector. If a photon undergoes a Compton scattering reaction, a variable part of the energy is transferred to the scattered electron. If this electron leaves the volume of the detector, the initial photon energy is only partially detected and the photon is counted in a lower channel. Compton scattering leads to an intensity distribution.

Above 1.022 MeV, photons may entail (multiple) pair production(s). If one of the created particles leaves the detector, the energy equivalent of the escaped particle is missing in the detected energy. The photon is counted in a channel corresponding to the energy $E_{\gamma_2} - 0.511$ MeV; a second peak is created, the so-called *single escape peak*. If two particles leave the detector, the photon is counted in the *double escape peak*.

Generally, the best signal-to-noise ratio is obtained by choosing only the full energy peak of the detector. However, as with increasing energies the pair production effect is enhanced, it is sometimes better to include the single and double escape peaks or even the whole region of Compton scattering for high energies.

3.2 Prospects for GAMS 5

The second spectrometer, GAMS 5, is supposed to operate in double bent crystal mode [Dol 00]. However, bending crystals at a precision needed for the GAMS facility turned out to be very difficult, and work is still in progress. A crystal bender is displayed in Fig. 3.5. All measurements in this work, including those using GAMS 5, have been performed in double flat crystal geometry as described in the preceding section.

Using a spectrometer in bent-crystal mode is supposed to significantly increase the efficiency of the spectrometer. A bent crystal can accept all incoming photons within the solid angle spanned by the crystal. Assuming a spectrometer crystal size of approximately $20 * 20$ mm^2, a solid angle of the order of 10^{-7} is covered. In the case of a flat spectrometer crystal, diffraction is only obtained for parallel radiation. Taking the distance of two neighbouring atoms within the solid as maximum allowed divergence, an effective solid angle of 10^{-11} can be estimated (≈ 2 Å$/15$ m). On the other hand, a flat crystal captures
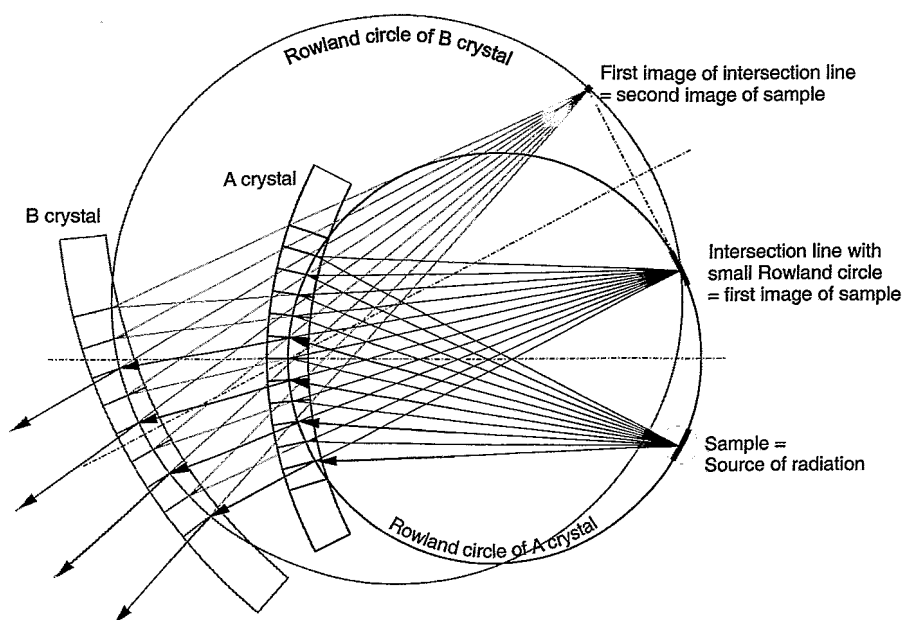
FIGURE 3.6: *Dispersive geometry of a double bent crystal spectrometer. For each uniformly bent crystal a Rowland circle visualizes the set of points allowing diffraction at the crystal. The virtual image can be found on the same circle. For further details see text.*

intensity of the whole, 2 mm thick, sample. The curved crystal focuses on a thin layer. This partly compensates the expected gain in efficiency.

The principle of a double bent crystal spectrometer is shown in Fig. 3.6. Bragg diffraction by a bent crystal of γ rays under the angle θ_i is possible for all points on the so-called "*Rowland circle*". The source intersects the small Rowland circle of the first crystal (A) in a line; different angles of incidence corresponding to different wavelengths or energies are diffracted. The diffracted radiation of the first crystal can be seen as if it was coming from the first image shown in the figure. If the second crystal (B) is positioned in such a way that its Rowland circle intersects the first Rowland circle within the first image, diffraction becomes also possible from the second crystal. As the image is a line, it intersects the big Rowland circle only at one point. Consequently, only one wavelength leads to diffraction; by this means, energy selection is obtained.

This shows that a double bent crystal spectrometer should work like a double flat crystal spectrometer while yielding higher intensities. Furthermore the focusing allows to use thin films instead of thick single crystals. A minimum thickness of approximately 0.1 mm is needed, however, in order to simultaneously diffract all Doppler shifted photons of the transition under study by the first crystal. This requirement is essential in order to measure GRID lines by rocking the second crystal while keeping the first one fixed. Both of these improvements should allow to investigate more solids with Crystal-GRID than presently possible (see Section 3.5).
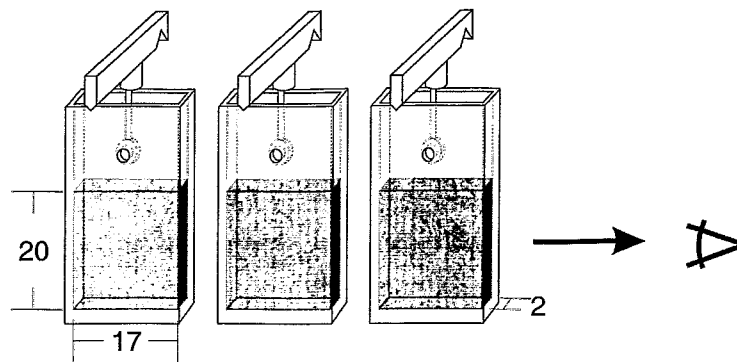
FIGURE 3.7: *Graphite containers for GAMS sources and direction of observation. The single crystals are put in three thin-walled graphite containers suspended by a zircaloy rod from a graphite hanger (distances are in* mm*). During the experiment, the sources are only* 55 cm *away from the reactor core.*

3.3 Sample Preparation

Single crystals for Crystal-GRID experiments are usually bought in the correct size, needed for the studies, so that the further sample preparation is very easy. Each single crystal is put into a separate thin-walled graphite container which is suspended by a zircaloy rod from a graphite hanger (see Fig. 3.7). The samples and graphite containers are covered by a thin carbon deposit in order to enhance heat radiation in the reactor.

In general, three oriented crystals of size $17 \times 20 \times 2 \, mm^3$ are used for the measurements, 4 mm thick graphite containers are also on-hand. If sufficiently big single crystals are unavailable or too expensive, smaller ones can be assembled in the graphite container. The assembled sample crystals should be as large as the graphite container, as otherwise the crystals might not be parallel to the optical axis during the measurement.

The graphite hanger is supported by the sample tube mechanism on "V"s which provide precise alignment. The three containers are semi-automatically introduced in the tangential beam tube and positioned next to the reactor core. They are placed one behind each other, so that the spectrometers see a source width of 2 mm, and a height of around 20 mm.

Before the experiment, the orientation of the single crystals should be verified, e.g. using standard X-ray diffraction. This is especially important, as the samples are highly activated in the reactor and can not be recovered for analysis after the experiment.

3.4 Crystal-GRID measurements —
the general practice

Crystal-GRID measurements are performed by positioning the first spectrometer crystal so that the photons of energy E_{γ_2} are diffracted in n^{th} order. The second crystal is then rocked about the position corresponding to m^{th} order diffraction. At each angular position, a photon spectrum is taken by the detector for an identical period of time. A set of about 80 to 100 measuring points corresponding to different angular positions of the second

spectrometer crystal is called a *scan*.

Several scans belonging to one transition measured in one diffraction order (n, m) using sample crystals oriented in direction $<hkl>$ is called a *series of scans*. A set of different series belonging to one transition is called a *measurement of a transition*.

Excess width

A GRID measurement consists of three different steps. First, the extra-broadening of the instrumental response, described by the excess width σ_{ew}, needs to be determined. As discussed in section 3.1 the ideal response function can be calculated using dynamical diffraction theory. The extra-broadening due to imperfections of the spectrometer crystals and other perturbations has to be determined experimentally.

Non-dispersive scans of an intense transition allow to measure the true experimental response. The excess width σ_{ew} can than be obtained by fitting the calculated instrumental response to the measured scans[2].

The excess width is related to intrinsic properties of the spectrometer. Its value can be used for all the measurements. A dependence on the energy measured or on the diffraction order used has never been observed. Nonetheless, a γ transition with an energy similar to the one measured for the Doppler shift is usually chosen. When looking at different transitions, the corresponding instrumental response is obtained by convoluting the newly calculated ideal instrumental response with a Gaussian of width σ_{ew}.

Temperature of sample crystal (thermal velocity)

In a second step, a long-lived state is measured in dispersive geometry. For a long-lived state, the Doppler broadening is mainly due to the thermal motion of the atoms within the sample crystal. Therefore, the lines are suited to determine the sample temperature which needs to be known for the evaluation of the Doppler broadened spectra. The thermal motion of the crystal atoms yields an additional broadening.

Doppler broadened energy spectra and drift correction

Once these two measurements have been performed, the true Crystal-GRID scans can be recorded. For a given transition, the diffraction order is chosen as a compromise between better resolution obtained in higher order and higher efficiency obtained in lower order. As can be seen from Fig. 3.4, good resolution is important if the fine structure of the Doppler broadened line is to be resolved.

Due to the low efficiency of the spectrometers, a Crystal-GRID measurement using one crystal orientation takes at least two weeks. Even though the temperature is stabilized within the experimental casemates, a change of the atmospheric pressure or humidity leads to a slight drift of the measured angles. Over a time as long as several weeks, a complete stability of the instrument is impossible. For that reason, a series of scans is measured instead of one very long scan, each of them not exceeding several hours.

---

[2]The extra-broadening is usually described by the full-width half-maximum (FWHM) σ_{ew}^{FWHM} of the Gaussian. This quantity is used as input value in the fitting codes gravel and griddle. The quantity σ_{ew} in the Gaussian, however, is the standard deviation, $\sigma_{ew}^{FWHM} = \sqrt{8 \ln 2}\, \sigma_{ew} \approx 2.35 \sigma_{ew}$.

Of course, the drift also influences the scans themselves. During this work, it has first been tried to correct for this drift. Fast reference scans of an intense transition have been measured between the long scans. By monitoring the peak positions of the reference scans, it becomes possible to approximate the drift function. In slowly drifting regions, the angular positions within a scan can be corrected. If a sudden strong drift occurs during a long scan, however, this scan is disregarded in the evaluation. The topic of drift correction will be addressed in a publication by Jentschel *et al.* to be submitted.

3.5 Applicability

Information on interatomic potentials can be obtained mainly from the fine structure of the Doppler broadened energy spectra. In order to contain pronounced fine structure, solids to be studied with the Crystal-GRID method must contain an isotope, which – after neutron capture – de-excites via a simple γ cascade with a mostly primarily fed, short-lived $(5 \ldots 40\,\mathrm{fs})$ intermediate nuclear level. The primary feeding guarantees a mono-energetic recoil. If the amount of side feeding was high, an unstructured line would be obtained.

Furthermore, the value of the level lifetime is essential. If, on the one hand, it is too short, the recoiling atom does not collide with its neighbours before emitting the secondary photon. The GRID line will be box-like (see Section 5.2.1) and the measurement not sensitive to the interatomic potential. If, on the other hand, the lifetime is too long, most recoiling atoms will have slowed down to thermal velocities before emitting the secondary photon. The fine-structured wings will become insignificant compared to the central peak.

If the Doppler broadened line is well structured, it further depends on the crystal structure, on the mass ratio of the different atoms in the solid, and on the initial recoil velocity, i.e. on the energy of the primary photon. However, these influences can compensate each other. It is not easy to predict whether a transition is suited without calculating the corresponding theoretical GRID line (see Chapter 5).

In an experiment, a number of additional requirements have to be met. In the reactor, the crystal temperature can become very high. The crystal structure needs to be stable up to approximately $1200\,\mathrm{K}$, in order to avoid any change in its structure. In any case, it must be excluded that material melts or evaporates under the conditions in the high-flux reactor. Further reactor safety requirements must also be considered, e.g. the total activation has to be sufficiently low to allow a save extraction of the sample at any time.

If a short-lived, mostly primarily populated level exists, the intensity requirement is the most limiting. The expected intensity mainly depends on the neutron capture cross section and the probability for the chosen γ transition to occur, including the isotopic abundance of the considered isotope. A detailed discussion of expected count rates is given in Appendix C.

Due to the intensity requirement, sufficiently big single crystals must be available. The typical size is three pieces of $17 \times 20 \times 2\,\mathrm{mm}^3$. As soon as GAMS 5 will be operational in bent-crystal mode, thin single-crystalline films should also be usable (see Section 3.2).

According to the requirement of a simple γ-cascade with short-lived levels, light nuclei would be preferential. However, these isotopes often have very small neutron capture cross sections. This currently limits the number of good candidates for Crystal-GRID experiments to nuclei such as Cl, Ti, Fe, Cr, and S.

An overview of measurable nuclei and solids is given in Fig. 3.8. Many of them,

	counts/min/mol		counts/min	
	300		30	
Cl				
Ti	100			NaCl*
			10	TiN, TiC
Fe, Cr, S	30			Fe*, TiO$_2$*, Cr*, TiP, TiS
Se				TiSi$_2$
Ca				TiS$_2$, CaTiO$_3$
Ni, Si	10		3	TiS$_2$, Ni*
P, K				TiS , K$_2$TiO$_3$
N				ZnS*
Mg	3			CaO, Ca$_3$N$_2$, Si*, TiSi$_2$
Al	1		1	CaF$_2$, CaSi, CaC$_2$
				CaTiO$_3$, CaTe
	0.3			CaSi
			0.3	K$_2$TiO$_3$, KNbO$_3$
C	0.1			(BN), TiN, AlN,
				AlN, TiP
F	0.03			InN, AlP
			0.1	InP, AlP, Ca$_3$N$_2$, AlAs
	0.01			
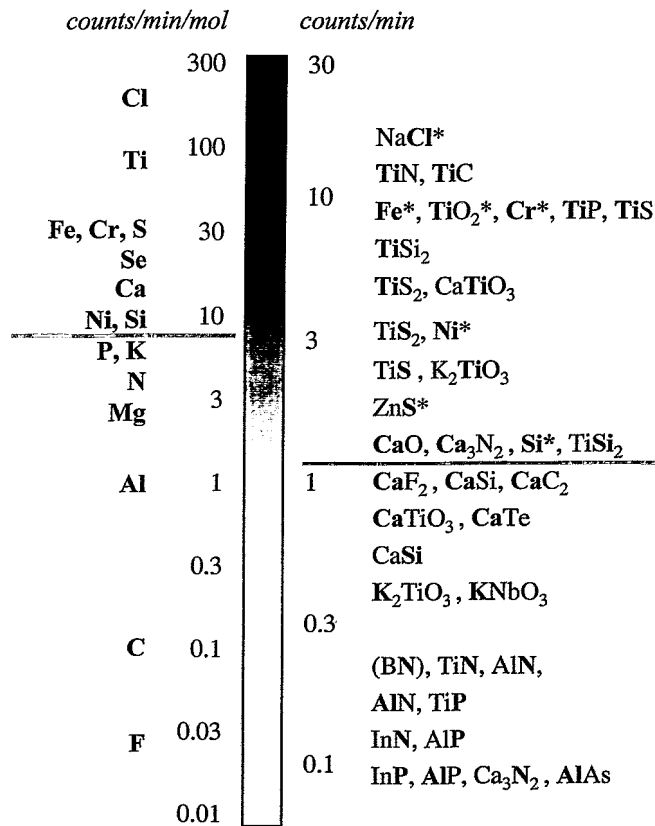
FIGURE 3.8: *Average count rates expected when measuring Crystal-GRID lines for different materials. The measurement is supposed to base on a transition in the bold-face printed nuclei. The lines indicate approximately, the current limit for the Crystal-GRID method. The scale on the left compares different nuclei. The expected count rate is given per mole. The scale on the right compares different solids containing the nuclei to be used.*

however, are unavailable as single crystals on the cm scale. This is the case for TiN, TiC, TiP, TiS, TiS$_2$, TiSi$_2$, AlN, BN, and InN, e.g. These solids will only become accessible to Crystal-GRID when thin films can be used.

Furthermore, improvements of the spectrometer efficiency are urgently needed. An efficiency improved by at least a factor of 100 would be needed, in order to investigate a lot of solids that are of great interest in solid state physics such as a number of important semiconductors.

Chapter 4

Computer simulation of the slowing down of recoiling atoms in crystals

The slowing down of the recoiling atom needs to be calculated in order to predict Doppler broadened energy spectra (GRID lines). Usually, for powder GRID experiments, it is approximated by a so-called *Mean Free Path Approach (MFPA)* developed by Jolie *et al.* around 1990 (see [BörJol 93, Appendix 1] and references therein) and implemented in the computer code `griddle` [RobJol 90]. The MFPA theory contains a large number of approximations. Nowadays, modern computers are fast enough to perform less approximate computer simulations.

As the velocity of the recoiling atom ($\leq 2\,\text{Å}/\text{fs} \approx 2 \cdot 10^{-4}\,c$) is much below typical electron velocities ($\approx 20\ \text{Å}/\text{fs}$), electronic excitation can be neglected. Kuronen showed that their effect on GRID lines is negligible [Kur 91]. Consequently, the recoil motion can be considered within non-relativistic, classical mechanics; the best numerical realisation of which being Molecular Dynamics (MD). MD is exact within classical mechanics, and, hence, the results are as good as is the description of the atomic interaction.

MD simulations were first applied to GRID experiments by Kuronen and Keinonen *et al.* in 1990 [Kur 91, Kei 91, Kur 92] when they re-evaluated a number of powder GRID experiments. MD becomes essential for the evaluation of Crystal-GRID experiments, as the MFPA does not consider any discrete crystal structure and thus can not predict any orientation-dependent differences.

In this work, an RMD (Restricted Molecular Dynamics, see Section 4.2) code by Jentschel has been improved and extended to full MD calculations. The major concepts of Molecular Dynamics as well as the performed improvements will be briefly described in the following section. For any further details refer to the standard literature [Hab 95, Hee 90, Hai 92, AllTil 87].

4.1   Molecular Dynamics (MD)

What is the main idea of molecular dynamics? The trajectories of N atoms are evaluated by simultaneously integrating Newton's equations of motion for all N particles.

$$\dot{\mathbf{r}}_i = \mathbf{v}_i \quad \text{and} \quad m_i\dot{\mathbf{v}}_i = \mathbf{F}_i = -\nabla_i V \qquad i = 1, ..., N \qquad (4.1)$$

where $\mathbf{r}_i$ and $\mathbf{v}_i$ are the position and velocity vectors of the particle i, $\mathbf{F}_i$ is the acting force, and V the interatomic potential.

MD simulations can be performed if the initial and boundary conditions are fixed and expressions for the interatomic forces between all N atoms are given. In the case of recoil simulations at $0\,\mathrm{K}$, the initial positions are given by the crystal structure, whilst the initial velocities vanish. The recoil due to the emission of the primary photon is realized by setting the initial velocity of the emitting atom to v^0 in a randomly chosen direction.

A large number of trajectories are simulated by choosing different random directions for the initial recoil. If the atomic species under investigation occupies multiple lattice sites of the unit cell, trajectories must be calculated for atoms initially starting from all of these sites, unless the sites can be transferred to each other by applying the symmetry operators of the appropriate point group.

MD at finite temperature

In order to consider the enhanced temperature near the reactor core, the initial conditions are slightly changed. As it is impossible to correctly define all initial positions and velocities, an equilibration needs to be performed. All atoms are placed on their ideal lattice sites and given randomly oriented velocities corresponding to twice the thermal energy. The recoil directions are chosen so that the total momentum of the simulation cell is zero.

Thereby, at the beginning of the equilibration, the simulation cell has twice the kinetic energy needed for the experimentally determined temperature of the crystal. An MD simulation is performed for 5 ps, a time sufficient for equilibration. Following the virial theorem, approximately half of the assigned kinetic energy will be transformed to potential energy, the other half remains as kinetic energy, once the equilibrium is reached. Consequently, the correct temperature is obtained without using a heat bath.

To avoid arbitrary effects, the phase space at the end of the equilibration is not used as an initial condition for all trajectories. Instead, the simulation at equilibrium is continued, and snapshots of the phase space are recorded every 20 fs, each of them representing the initial conditions for a new recoil event.

Simulation cell / Periodic boundary conditions

The simulation in this work is performed in a rectangular cell of finite volume. As MD simulations are time-consuming and a large number of trajectories need to be calculated, the simulation cell typically contains no more than 6^3 unit cells. By performing test simulations with smaller and larger cells, it is checked that convergence is reached, i.e. whether the cell size is sufficient. A similar test is also applied to the number of trajectories.

To avoid any influence of the cell surfaces, periodic boundary conditions are implemented, i.e. the simulation cell is thought to be repeated identically an infinite number of times in all three dimensions. All the particle properties, e.g. its velocity, are the same for all the periodic images of an atom. If an atom crosses the surface of the simulation box, one of its images enters on the opposite side of the cell with identical velocity. This approach is correct as long as the cell size is sufficiently large and the forces do not act on distances longer than the simulation box lengths.

The cell size is chosen so that the recoiling atom does not re-enter a heavily damaged region during the simulation time of approximately five times the nuclear level lifetime

τ. Damage in the simulation cell is, on the one hand, caused by the direct collisions of the recoiling atom with its neighbours and, on the other hand, by the deposited energy which leads to a drastically enhanced temperature near the recoiling atom's track. As heat dissipation is rather slow compared to the considered simulation time, the local heating does not additionally influence the trajectory of the recoiling atom. Therefore, cooling via a heat bath, by scaling all atoms' velocities, e.g., is not used.

Verlet algorithm

Recoil trajectories can be calculated, starting with the simulation cell, the initial conditions, and an interatomic potential. The motion of all N atoms in the cell is calculated by integrating Newton's Equations (4.1) numerically.

$$
\begin{aligned}
\mathbf{r}_i(t) &= \mathbf{r}_i^0 + \int_0^t \mathbf{v}_i(t')\, dt' \\
\mathbf{v}_i(t) &= \mathbf{v}_i^0 + \frac{1}{m_i} \int_0^t \mathbf{F}_i(\mathbf{r}_1(t'), \ldots, \mathbf{r}_N(t'))\, dt'
\end{aligned}
\tag{4.2}
$$

A number of algorithms have been developed. In this work, the Verlet algorithm [Ver 67] in velocity form [Swo 82] is used. It is based on the equations

$$
\begin{aligned}
\mathbf{r}_i(t+\Delta t) &= \mathbf{r}_i(t) + \Delta t \cdot \mathbf{v}_i(t) + \frac{(\Delta t)^2}{2 m_i} \mathbf{F}_i(t) \\
\mathbf{v}_i(t+\Delta t) &= \mathbf{v}_i(t) + \frac{\Delta t}{2 m_i} [\mathbf{F}_i(t) + \mathbf{F}_i(t+\Delta t)]
\end{aligned}
\tag{4.3}
$$

where Δt is the size of the time step [Hab 95, p. 66].

The implementation is as follows. Using the initial quantities $\mathbf{r}_i(t=0)$ and $\mathbf{v}_i(t=0)$, the initial forces $\mathbf{F}_i(t=0)$ are determined. Further time steps can be calculated iteratively; each iteration consists of four steps. First, preliminary values of the velocities are calculated and used to determine the new position vectors. Then, the new forces are calculated, and the velocities advanced to their new values.

1. $\mathbf{v}_i(t+\frac{1}{2}\Delta t) = \mathbf{v}_i(t) + \frac{\Delta t}{2 m_i} \mathbf{F}_i(t)$

2. $\mathbf{r}_i(t+\Delta t) = \mathbf{r}_i(t) + \Delta t \cdot \mathbf{v}_i(t+\frac{1}{2}\Delta t)$

3. $\mathbf{F}_i(t+\Delta t) = \mathbf{F}_i(\mathbf{r}_j(t+\Delta t), j = 1 \ldots N)$

4. $\mathbf{v}_i(t+\Delta t) = \mathbf{v}_i(t+\frac{1}{2}\Delta t) + \frac{\Delta t}{2 m_i} \mathbf{F}_i(t+\Delta t)$

After every time step, the velocity of the recoiling atom is recorded for the calculation of the Crystal-GRID lines.

Variable time step

In Crystal-GRID simulations, only a very few atoms are fast moving. Furthermore, speed is rapidly lost by collisions with neighbouring atoms. The MD code has been improved in order to use a minimum of computing time while keeping good precision by implementing

a variable integration time step. This is achieved by surveying that in any one step the fastest atom never moves more than $(\Delta r)_{\mathrm{max}} = 0.0234$ Å, which is 1% of the nearest neighbour distance in ZnS. As energy can be transferred from potential to kinetic energy, the highest *possible* velocity v_{max} is approximated by

$$v_{\mathrm{max}} = \max_i \left(\sqrt{\frac{2\left(E_{i,\mathrm{kin}} + E_{i,\mathrm{pot}}\right)}{m_i}} \right) \qquad (4.4)$$

maximised over all N atoms of the cell. The maximum allowed time step $(\Delta t)_{\mathrm{max}}$ can be calculated by

$$(\Delta t)_{\mathrm{max}} = (\Delta r)_{\mathrm{max}} / v_{\mathrm{max}} \qquad (4.5)$$

For historical reasons, the velocity of the recoiling atom has to be recorded with a fixed time step Δt_0 for the calculation of GRID lines. To combine both concepts, Δt_0 is divided into q equal periods Δt, the time step used in the integration.

$$\Delta t = \Delta t_0 / q \quad \text{with} \quad q = \mathrm{INT} \left(\frac{\Delta t_0}{(\Delta t)_{\mathrm{max}}} \right) + 1 \qquad (4.6)$$

Typically, Δt_0 is set to a value in between 0.25 fs and 1 fs, depending on the lifetime τ of the nuclear state. Due to the small value of $(\Delta r)_{\mathrm{max}}$, the realized time step Δt is sufficiently small for a precise simulation of the trajectory. Right after the initial recoil, q can reach values of 20.

Potential cutoff radius / Force tables

The calculation of the interatomic forces mainly determines the total duration of the simulation. Most of the potentials lead to non-negligible forces only for relatively short distances. In order to speed up the calculation, a potential cutoff radius $r_{c,p}$ is used beyond which the forces are neglected. This cutoff is inherent in some potentials, like the Stillinger-Weber potential. For the purely repulsive potentials, as ZBL or Born-Mayer, a cutoff of typically 3.7 Å is used.

For two-body interactions — only depending on the absolute distance of the two particles — force tables are calculated and used to look up the forces during the time loop of the simulation. The values in between the tabulated ones are approximated by the Newton-Gregory forward difference interpolation [AllTil 87, p.144]. Its calculation is much faster than the direct force evaluation and independent of the functional form of the force.

Neighbour lists (improved algorithm)

Even though forces are only needed for neighbours nearer than the potential cutoff radius $r_{c,p}$, it would be necessary to determine the distances for all atom pairs. As the duration of this calculation scales with N^2, a book keeping algorithm is used, the so-called *Verlet neighbour list* [Ver 67]. The number of distance calculations is reduced by listing all neighbouring atoms within the neighbour cutoff $r_{c,n} \approx 4$ Å and not renewing the list before the calculation of a few time steps.
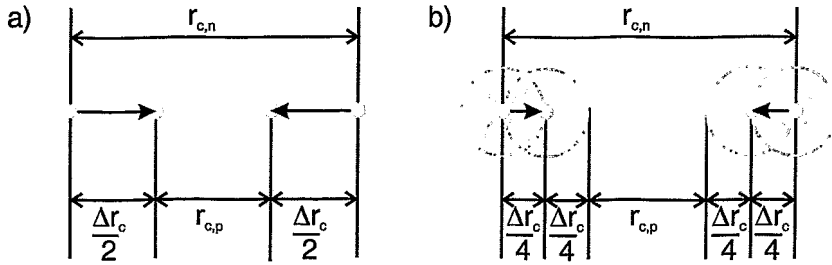
FIGURE 4.1: *Neighbour and potential cutoff radii $r_{c,n}$ and $r_{c,p}$. a) Two atoms apart by a distance $r_{c,n}$ need to be considered for the force calculation as soon as their distance is reduced by Δr_c. b) If oscillations by $\Delta r_c/4$ of the atoms around their equilibrium positions are considered without influence on the neighbour list, the allowed travelling distance is reduced to $\Delta r_c/4$.*

An update of the neighbour list has to be performed as soon as any distance between two non-listed atoms becomes smaller or equal to the potential cutoff distance $r_{c,p}$. This cannot occur before the time $2\Delta t_{nn}$ that the fastest atom needs to travel half the distance Δr_c between neighbour and potential cutoff (see Fig. 4.1a)

$$2\Delta t_{nn} = \left(\Delta r_c/2\right)/v_{max} = \left(\left[r_{c,n} - r_{c,p}\right]/2\right)/v_{max} \qquad (4.7)$$

In this work, the neighbour list algorithm has been significantly improved for Crystal-GRID simulations by taking into account the premises that most atoms in the simulation cell are moving at thermal velocities, i.e. very slowly, around their equilibrium position. Only the recoiling atom and the few atoms that had high-energetic collisions are moving fast and change neighbours rapidly.

Instead of re-calculating the whole list, new neighbours are only determined for those few atoms that have moved more than $\Delta r_c/4$ since their last neighbour calculation. As can be seen from Fig. 4.1b), the neighbour list must be renewed after the time Δt_{nn} that the fastest atom needs to travel the distance $\Delta r_c/4$, in this case.

$$\Delta t_{nn} = \left(\Delta r_c/4\right)/v_{max} \qquad (4.8)$$

Due to this improvement, the calculation time of the Verlet algorithm is reduced by a factor of approximately three and its dependency on the size of the simulation cell is reduced without losing any accuracy.

Energy stability

Usually, in an MD simulation, the total energy is conserved to high precision. However, due to the potential cutoff, atoms crossing the cutoff distance, suddenly lose or gain energy. Energy conservation can be re-established by shifting the forces and potential for all $r < r_{c,p}$.

$$
\begin{aligned}
F'(r) &= F(r) - F(r_{c,p}) \\
V'(r) &= V(r) - V(r_{c,p}) + (r - r_{c,p})\,F(r_{c,p})
\end{aligned}
\qquad (4.9)
$$

This *"shifted-force potential"* is used in the present code when checking the energy stability of a newly implemented potential. However, the shifted forces change properties of the

system, and corrections would be needed in order to extract material properties. As a perfect energy conservation is not important for GRID simulations, the forces are left unshifted in the true simulations, following a recommendation of Haile [Hai 92, p. 193].

Simulating side feeding

Besides the main feeding of the nuclear level under study leading to one initial velocity of the recoiling atom, side-feeding branches may exist in the decay cascade. These additional decay channels are considered during the simulation.

Let's assume a 5% side feeding via a two-step decay; 5% of the trajectories are calculated with the two-step feeding. One atom is first given a recoil. Its motion is simulated for a time randomly chosen from the radioactive decay distribution of the intermediate state lifetime. Thereafter, the second recoil is exerted in a randomly chosen direction. The recoiling atom has now reached the nuclear level under investigation, and the atom's trajectory is recorded for the later evaluation.

Statistics are quite bad if one calculates only 5% of the trajectories via the side feeding. If more time can be spent for the simulation, it is preferable to average over a larger number of trajectories.

Often a part of the side feeding is not even known. This is obviously the case, when the reported depopulating probability of a level is higher than its probability to be populated. In principle, it is possible to use a distribution of initial velocities that can be approximately calculated from nuclear properties. However, the transitions investigated in this work were chosen such that the entire side feeding only contributes a little to the total GRID line. Therefore, the unknown part of the side feeding was neglected.

4.2   Restricted Molecular Dynamics (RMD)

Even using the described concepts, MD simulations are very time consuming, total running times of several days are common. This is problematic when trying to optimize potential parameters, as for every set of parameters a complete calculation with a few thousand trajectories needs to be performed.

A significant gain in speed can be obtained when only calculating the interaction between the recoiling atom and its neighbours, while ignoring the interactions of the other sample atoms. This concept is not exact, as opposed to full MD calculations, but it is a better approximation than the widely-used Binary Collision Approximation (BCA), where only successive binary collisions between the impinging ion and the nearest neighbours are considered.

Two studies of range distributions after ion bombardment have compared the three methods some years ago [Gär 95, PosHei 95]. While the round robin test by Gärtner *et al.* finds that the binding of the target atoms in 200 eV B into Si implantation has only very little influence, Posselt and Heinig come to the opposite result for 250 eV Si into Si. Gärtner explains this difference by the different masses of the impinging ions. A complementary explanation, based on the results obtained in this work, will be given in Section 8.3.1.

For Crystal-GRID, only the trajectory of the recoiling atom needs to be known. The interaction between the other sample atoms has little influence on the future behaviour
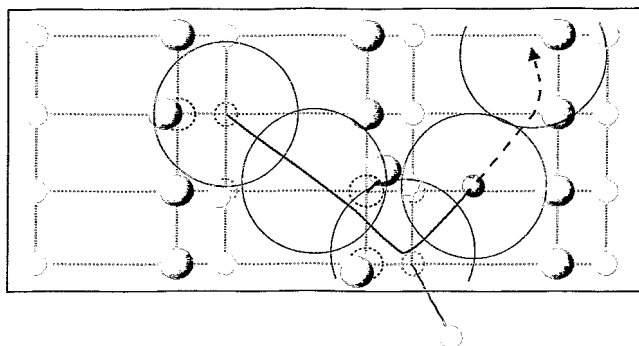
FIGURE 4.2: *Interaction sphere of Restricted Molecular Dynamics simulations. In RMD, only the interaction of the recoiling atom with its neighbours is considered. The interaction sphere follows the motion of the recoiling atom.*

of the recoiling atom. Therefore, Jentschel adopted the idea of neglecting the interaction among the sample atoms for Crystal-GRID. In his so-called *Restricted Molecular Dynamics* (RMD) simulations, only the interaction of the recoiling atom with its neighbours is calculated [Jen 97a] (see Fig. 4.2).

If finite temperatures are to be considered in RMD, all atoms are assigned displacements corresponding to the temperature of the sample. As the total simulation time is very short, these displacements reflect the temperature influence quite well, the actual movement of the sample atoms is neglected.

In the present work, RMD and MD calculations will be compared for semiconductors using artificial data (see Section 8.3.1).

Chapter 5

Theoretical view on Crystal-GRID lines (Doppler broadened energy spectra)

GRID lines for an observation along the crystal direction $\mathbf{n}$ can be calculated from the decay law of the recoiling excited nuclei and the phase space trajectories $\{\mathbf{r}_i(t), \mathbf{v}_i(t)\}$ of recoiling atoms as calculated in an MD simulation of the slowing down. The formalism of how to calculate GRID lines is presented in Section 5.1.

Information on the atomic interaction is contained in the fine structure of the lines, as the recoiling atoms' velocities $\{\mathbf{v}_i(t)\}$ are influenced by the interatomic potentials. The shape of the lines further depends on the nuclear level lifetime τ, the crystal structure, and the direction of observation $\mathbf{n}$. In order to study interatomic potentials with Crystal-GRID, a basic understanding of the Doppler broadened energy spectra is needed. Consequently, the remaining sections make different approaches to explain the fine structure.

5.1   Calculation of Crystal-GRID lines

In a measurement, the direction of observation is fixed. The Doppler shift ΔE_{γ_2} of one photon only depends on the projection

$$v_\parallel = \mathbf{v} \cdot \mathbf{n} \tag{5.1}$$

of the recoiling atom's velocity $\mathbf{v}$ on the direction of observation $\mathbf{n}$ (compare Eq. (2.4)).

For a given $\mathbf{n}$, the time-dependent probability $P\left(v_\parallel, t\right) dv_\parallel dt$ that a recoiling atom has the velocity projection $\mathbf{v}_i(t) \cdot \mathbf{n}$ in the range $v_\parallel \dots v_\parallel + dv_\parallel$ during the time interval $t \dots t + dt$ can be deduced by

$$P(v_\parallel, t) \, dv_\parallel \, dt = \frac{1}{N_T \cdot N_S} \sum_{i=1}^{N_T} \sum_{s=1}^{N_S} \delta\big(v_\parallel - \big[\mathbf{v}_i(t) \cdot \bar{\mathbf{M}}_s \cdot \mathbf{n}\big]\big) \, dv_\parallel \, dt \tag{5.2}$$

with the first sum extending over the N_T simulated trajectories. For better statistics, the N_S symmetry operators $\bar{\mathbf{M}}_s$ of the appropriate point group are applied to the trajectories. If the GRID line is calculated for a powder or for a poly-crystalline sample, the direction

of observation **n** is chosen randomly for each trajectory. Instead of applying the symmetry operators, multiple random directions are used, in order to enhance the number of trajectories.

Eq. (5.2) bases on the assumption that the emission of a secondary photon is equally probable for all of the trajectories. As discussed in Section 2.4, however, this is not the case, if angular correlation is taken into account. The emission probability must be multiplied by the angular correlation factor $W'(\cos\phi)$, where ϕ is the angle between the emission directions of the two photons, as defined in Eq. (2.9).

$$P(v_{\parallel}, t)\, dv_{\parallel}\, dt = \frac{1}{N_T \cdot N_S} \sum_{i=1}^{N_T} \sum_{s=1}^{N_S} \quad \delta\big(v_{\parallel} - \big[\mathbf{v}_i(t) \cdot \bar{\mathbf{M}}_s \cdot \mathbf{n}\big]\big)$$
$$\cdot W'\left(\frac{-\mathbf{v}_i(0) \cdot \bar{\mathbf{M}}_s \cdot \mathbf{n}}{|\mathbf{v}_i(0)|}\right) dv_{\parallel}\, dt \qquad (5.3)$$

As the percentage of side feeding is very small, no angular correlation is taken into account for these branches of the decay cascade, where multiple correlations exist.

The Crystal-GRID line is the distribution of Doppler shifted secondary photons emitted by the recoiling atoms. It is proportional to the probability density $P_\tau(v_{\parallel})$ that the recoiling atom has the velocity projection $v_{\parallel}$ at the time t' of the second γ decay. For a given nuclear level lifetime τ, $P_\tau(v_{\parallel})$ can be calculated by multiplying $P(v_{\parallel}, t)$ with the radioactive decay law, Eq. (2.1), and integrating over time:

$$P_\tau(v_{\parallel})\, dv_{\parallel} = \frac{1}{\tau} \left[\int_0^\infty \exp\left(-t'/\tau\right) P(v_{\parallel}, t')\, dt'\right] dv_{\parallel} \qquad (5.4)$$

In general, MD simulations for GRID are performed up to $t_{\text{end}} \approx 5\tau$ where 99.3% of the secondary photons have been emitted. Consequently, $P(v_{\parallel}, t')$ is only known up to t_{end} as well. The remaining part of the integral in Eq. (5.4) is approximated by

$$P(v_{\parallel}, t') = P(v_{\parallel}, t_{\text{end}}) \qquad \text{for} \qquad t' > t_{\text{end}} \qquad (5.5)$$

On the considered time scale, this approximation is exact if the simulation is performed up to thermal velocities[1]. In this case, the velocity of a single recoiling atom may further change, but the distribution of velocities remains a Maxwell distribution of the sample temperature, as it is at time t_{end}.

Using Eq. (2.4), $P_\tau(v_{\parallel})\, dv_{\parallel}$ can be transformed to the probability density $P_\tau(\Delta E_{\gamma_2})\, dE_{\gamma_2}$ of the Doppler shift energy. The transformation only uses a constant scaling factor, the shape of the line is identical.

$$\begin{aligned} P_\tau\left(\Delta E_{\gamma_2}\right) dE_{\gamma_2} &= P_\tau\left(v_{\parallel} = \frac{c\Delta E_{\gamma_2}}{E_{\gamma_2}^0}\right) \cdot \frac{dE_{\gamma_2}}{dv_{\parallel}}\, dv_{\parallel} \\ &= P_\tau\left(v_{\parallel}\right) \cdot \frac{E_{\gamma_2}^0}{c}\, dv_{\parallel} \end{aligned} \qquad (5.6)$$

---

[1] The implementation in the program `line4` necessitates that all trajectories are recorded with an identical number of time steps, i.e. that t_{end} is identical for all of them.

This distribution is called the *ideal Crystal-GRID line* and would be measured with a spectrometer yielding a δ-like response function. As discussed in Section 3.1, the normalized instrumental response function is given by $\hat{R}_{E_\gamma,n,m}^{\sigma_{ew}}(\Delta E_\gamma)$ (Eq. 3.8). Convoluting the probability density $P_\tau(\Delta E_{\gamma_2})$ with $\hat{R}_{E_\gamma,n,m}^{\sigma_{ew}}(\Delta E_\gamma)$, the *theoretical Crystal-GRID line* $I_{pr}(\Delta E_\gamma)$ can be calculated.

$$I_{pr}\left(\Delta E_{\gamma_2}\right) \equiv I_{E_\gamma,n,m}^{\sigma_{ew},\tau}\left(\Delta E_{\gamma_2}\right) = P_\tau\left(\Delta E_{\gamma_2}\right) * \hat{R}_{E_\gamma,n,m}^{\sigma_{ew}}\left(\Delta E_\gamma\right) \qquad (5.7)$$

It gives the proportion of photons, observed at the angular position of the spectrometer corresponding to the Doppler shift ΔE_{γ_2}, related to the total yield I_{tot} of diffracted photons belonging to the transition under study, as observed in a non-dispersive scan with parallel spectrometer crystals.

5.2 Understanding Crystal-GRID lines

In a well-suited material, Crystal-GRID lines contain a very pronounced structure. The fine structure is related to the scattering within the sample crystal and thereby to the interatomic potential. Jentschel explained the peaks by the scattering of the recoiling atom at the neighbour shells and consequential channelling [Jen 97a, Figure 2.5]. He showed nicely that the recoiling atoms cumulate in the velocity space. In this work, the scattering with every single neighbour is analysed in order to further explain how the structure is created.

5.2.1 Microscopic look at Crystal-GRID lines

Simulations have been performed for seven different atomic configurations. The simulation cells contain the initially recoiling atom and zero to eight neighbours. The nearest neighbour distance is 3 Å. The simulation cell is chosen to be 100 Å in each dimension, so that the recoiling atom only interacts with one image of the neighbours during its flight. For every set-up, 10,000 trajectories have been calculated. The resulting Crystal-GRID lines for three different orientations of the atomic configurations are plotted in the first column of Fig. 5.1.

The lines are derived from simulations in two dimensions (2D). As in true 2D calculations, i.e. with the initial velocity $\mathbf{v}^0$ in the x-y plane, the obtained Doppler broadened spectra would be unrealistic, the direction of $\mathbf{v}^0$ is arbitrarily chosen in three dimensions (3D) and projected into the x-y plane. This approach is identical to a 3D calculation with neighbouring slabs along the z direction instead of neighbouring atoms. Similar results could be obtained by normal 3D calculations. However, more recoiling atoms would not interact with any neighbour, and consequently, the structure would be less pronounced.

The remaining columns of Fig. 5.1 show emission points of the secondary photons. To obtain nice and comprehensible pictures, the emission points have been chosen from 720 trajectories calculated by true 2D simulations, with the initial recoil angle regularly increased in steps of $0.5°$. The observer is located to the right of the figures.

The colour of the emission points represents the Doppler shifted photon energy. Dark blue is the maximum blue-shift, i.e. the maximum positive Doppler shift ΔE_{γ_2} (maximum energy E_{γ_2}, minimum wave length λ), green indicates no shift (energy $E_{\gamma_2}^0$), and red is the

maximum negative Doppler shift (minimum energy, maximum wave length). The blue-shifted photons are emitted by atoms moving towards the spectrometer, the red-shifted by atoms moving away from it, and the unshifted by atoms moving perpendicular to the direction of observation.

The density of the plotted points indicates the probability of decay; decreasing with time and thus with distance from the starting point. The trajectories are plotted for one value of the lifetime and followed up to 2τ.

No neighbours

Fig. 5.1a) shows the GRID line of a non-interacting particle and the instrumental response function used in the calculation of all the lines. The GRID line has a box-like shape with smoothed wings due to the convolution with the instrumental response function.

The box form can be easily understood. In the case of no interactions, the velocity $\mathbf{v}_i(t)$ of the recoiling atom is unchanged for all times

$$\mathbf{v}_i(t) \quad = \quad \mathbf{v}_i(0) \tag{5.8}$$

$$\Rightarrow \quad P(v_\parallel, t) = P(v_\parallel, 0) \tag{5.9}$$

$$\Rightarrow \quad P_\tau(\Delta E_\gamma) \sim P_\tau(v_\parallel) = P(v_\parallel, 0) \tag{5.10}$$

In this case, the ideal Crystal-GRID line $P_\tau(\Delta E_\gamma)$ is directly proportional to the distribution $P(v_\parallel, 0)$ of initial velocity projections, as can be seen from Eq. (5.4).

The initial recoil directions are chosen randomly; the probability of initial recoil directions is constant as a function of the solid angle Ω. Using spherical coordinates, i.e. $d\Omega = 2\pi \sin\theta d\theta$ and $v_\parallel(0) = \mathbf{v}(0)\cdot\mathbf{n} = v^0\cdot\cos\theta$, the distribution $P(v_\parallel, 0)$ of initial velocity projections can be calculated.

$$
\begin{aligned}
P(v_\parallel, 0)\, dv_\parallel \quad &= \quad \frac{1}{4\pi} \cdot \frac{d\Omega}{dv_\parallel} dv_\parallel && \text{for } |v_\parallel| \leq v^0 \\[2mm]
&= \quad \frac{1}{4\pi} \cdot \frac{d\Omega}{d\theta} \cdot \frac{d\theta}{d(\cos\theta)} \cdot \frac{d(\cos\theta)}{dv_\parallel} dv_\parallel \\[2mm]
&= \quad \frac{1}{4\pi} \cdot (2\pi \sin\theta) \cdot \frac{-1}{\sin\theta} \cdot \frac{1}{v^0} dv_\parallel \\[2mm]
&= \quad -\frac{1}{2v^0} dv_\parallel \\[2mm]
&= \quad \text{const.} \cdot dv_\parallel
\end{aligned}
$$

The ideal GRID line $P_\tau(\Delta E_\gamma) \sim P(v_\parallel, 0)$ is constant within the possible range of Doppler shifts, and 0 elsewhere. Taking the instrumental response into account, the shape displayed in Fig. 5.1a) is obtained.

One neighbour

The situation with only one neighbouring atom is illustrated in Fig. 5.1b). If the neighbour is located in the direction of observation (<100>), the recoiling atoms moving towards the spectrometer are scattered by this neighbour. The scattering leads to a slowing down of the recoiling atom and to a deflection of its direction of movement. Both phenomena
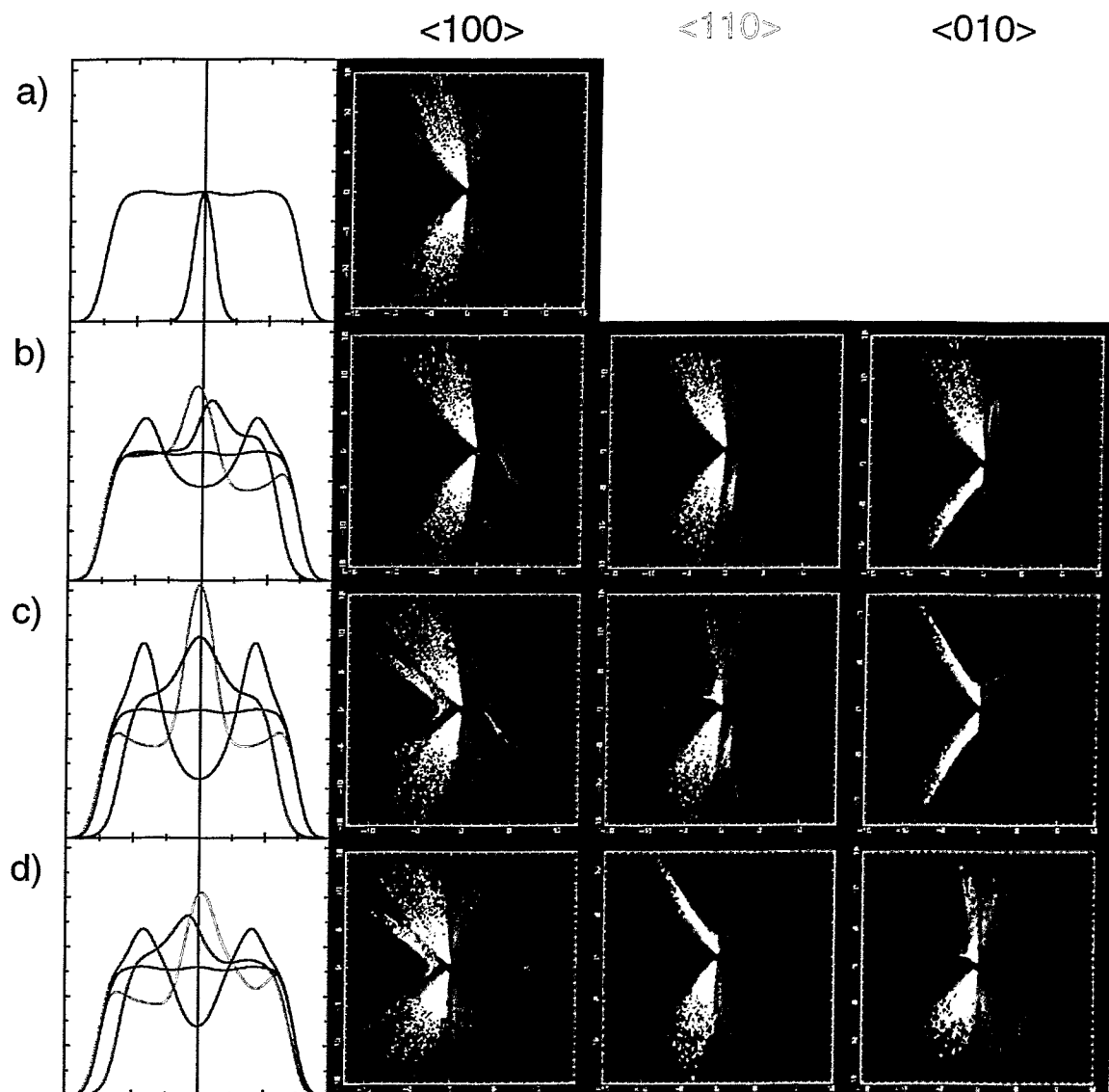
FIGURE 5.1: *GRID lines and emission points of secondary photons in 2-dimensional atom arrangements. Three different sample orientations are plotted: <100> (red GRID line), <110> (green), and <010> (blue). In the last three rows the orientations <100> and <010> are identical. The rows show the following atom configurations: a) no neighbours, b) 1 neighbour, c) 2 neighbours, d) 2 neighbours at different distances, e) 4 neighbours (1st neighbour shell), f) 4 neighbours (2nd neighbour shell), and g) 8 neighbours (1st and 2nd neighbour shells).*
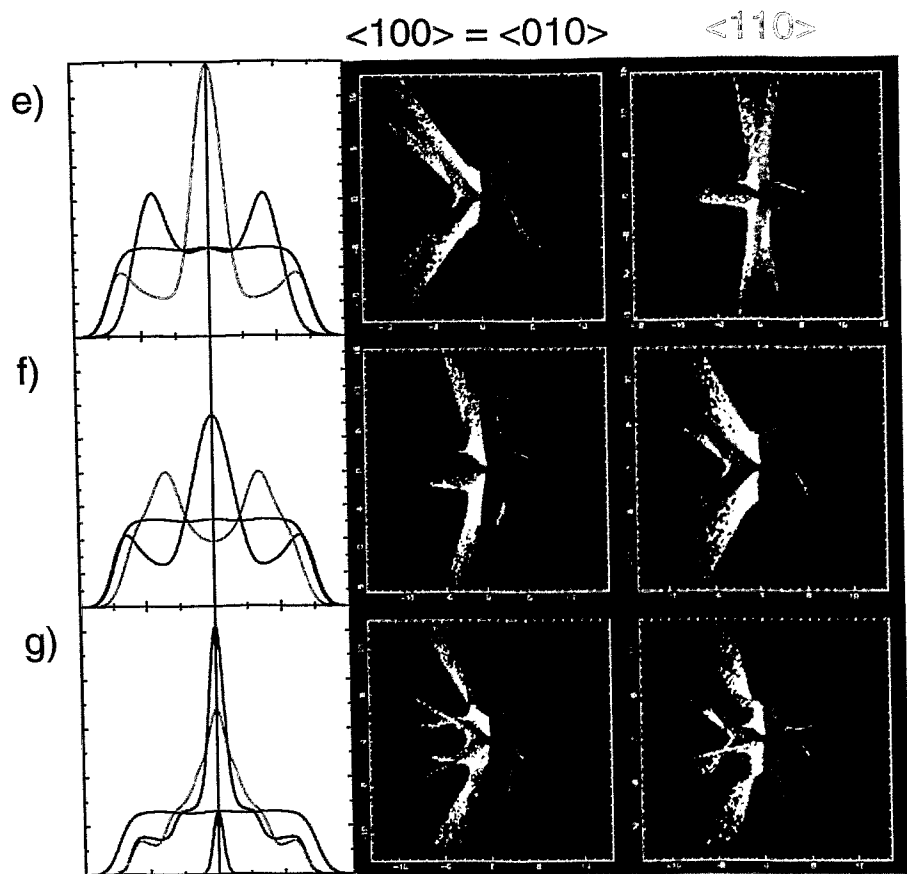
FIGURE 5.1: *(continuation of previous page)*

result in a reduced velocity projection. Nearly no secondary photons are emitted with the highest possible positive Doppler shift. The intensity in the GRID line is reduced at the right edge (red line) and enhanced towards smaller shifts.

If the neighbour is located perpendicular to the direction of observation (<010>), those recoiling atoms are scattered that initially move perpendicular to the direction of observation, i.e. that have a zero Doppler shift. Again, the scattering leads to a slowing down of the atoms. However, the zero Doppler shift cannot be further reduced. The deflection of the trajectories leads to an enhanced velocity projection. Secondary photons of the scattered atoms are observed at non-zero Doppler shifts. The corresponding GRID line has less intensity in the centre and enhanced intensity to both sides of the minimum (blue line).

In the third case, a neighbour placed 45° from the direction of observation (<110>), the situation is in between the two previous cases. Intensity is reduced at medium Doppler shifts and enhanced for lower Doppler shifts due to the slowing down (green line). Besides the central peak, a second peak can be seen at the maximum positive Doppler shift. It is related to two phenomena. First, the atoms initially moving towards the observer are nearly uninfluenced by the neighbour and thus continue to contribute photons with maximum Doppler shift. Second, some atoms are scattered into a direction towards the

spectrometer, yielding higher velocity projections despite the slowing down.

Summarizing the three situations, it can be clearly seen that one neighbouring atom causes one region of reduced intensity, i.e. one valley, in the GRID line. This region can be located at any Doppler shift energy, not only in the centre or at the edge. Therefore, a single collision can cause multiple peaks.

Two neighbours

Fig. 5.1c) shows the case of two neighbouring atoms. The GRID lines can be explained in the same way as in the previous situation. Only now, the GRID lines are symmetric. In the <100> and <110> cases, the lines show two regions of reduced intensity as expected in the case of two neighbours, one for positive Doppler shifts, and one for negative. In the <010> orientation, where both neighbours scatter the recoiling atoms moving perpendicular to the direction of observation, only one minimum exists. It can be called *doubly degenerate*, as both neighbours contribute to the GRID line in the same way. They are indistinguishable in the chosen direction of observation.

Degeneracy always occurs for neighbours occupying lattice sites that can be transferred to each other by a rotation around the axis of observation. Crystal-GRID is insensitive to this angle of rotation, as the Doppler shift only depends on the projection of the recoiling atom's velocity.

A similar situation is shown in Fig. 5.1d). However, now, the set-up is asymmetric. The scattering of the atom further away from the atom under investigation has less influence on the GRID line, as it scatters fewer atoms due to the reduced solid angle as seen from the recoiling atom's initial site. Consequently, the regions of reduced intensity caused by the atom on the right are less pronounced. The simulated GRID lines are asymmetric (<100> and <110>). The topic of asymmetric GRID lines will be looked at in more detail in Section 5.3.

One neighbour shell (Four neighbours)

Simulations have been performed with the complete first neighbour shell consisting of four atoms (Fig. 5.1e)) as well as the second neighbour shell (Fig. 5.1f)). The two cases are almost identical if one turns the second shell by 45°. However, the atoms of the second shell are around 40% further away from the central atom. The GRID lines differ in that the minima are slightly more pronounced for the first neighbour shell. This can be seen in the larger offset at the edges of the line and at the higher central peak caused by slightly deeper valleys on both sides.

Let's look at Fig. 5.1e). In the <100> orientation – identical to the <010> case – the line should show three valleys (red line), as two atoms yield one degenerate valley. The two regions of reduced intensity at the edges of the line are clearly present. However, the doubly degenerate minimum expected in the centre of the line presents a small local maximum.

Due to the slowing down and the deflection of trajectories, the neighbours along the axis of observation lead to reduced intensity at the edges and "shift" this intensity to lower Doppler shifts (compare Fig. 5.1c) <100>). The two other neighbours reduce intensity in the centre and shift it to higher velocity projections (compare Fig. 5.1c) <010>). The two processes, slowing down and deflection of trajectories, however, have opposite effects;

the shifting is less efficient. The three valleys are perfectly present. However already in this simple situation they start to smear out.

In the <110> orientation, two doubly degenerate valleys can be seen.

Two neighbour shells (Eight neighbours)

Taking both neighbour shells together, five minima are expected, three doubly degenerate and two non-degenerate valleys. As can be seen from Fig. 5.1g), the two regions of missing intensity at the edges are clearly visible. Two further regions are present at medium shift energies. However, they are only resolved because a narrower instrumental response function is used in this calculation. The central minimum disappeared completely.

The more neighbours are present and contribute to the slowing down, the more photons are emitted from slowly moving atoms, thus having a small Doppler shift. The central peak starts dominating the GRID line and thereby hiding its fine structure.

Furthermore, the recoiling atom can now be successively scattered by different neighbours. The first neighbours focus a part of the recoiling atoms in the direction of the second neighbours so that the scattering efficiency of the second neighbour shell is enhanced.

Conclusion

The interaction of the recoiling atom with every single neighbour causes a region of reduced intensity to appear in the GRID line. Next to this valley, one or two peaks are created. The slowing down due to the scattering always reduces the absolute velocity projection; the deflection of the trajectories can both increase or decrease the projection. For atoms that are located on degenerate positions, degenerate valleys are formed so that in high-symmetric crystal orientations, the number of valleys is smaller than the number of neighbours.

As soon as several neighbours are taken into account, valleys and adjacent peaks start to mix and structure disappears. Only the missing intensity at the edges of the GRID line can always be attributed to recoils with neighbours in the direction of observation, without any doubt. The nearer a neighbour is located to the recoiling atom, the more influence it has on the GRID line.

5.2.2   Macroscopic look at Crystal-GRID lines

The shape of Crystal-GRID lines depends on a large number of properties. Jentschel extensively discusses this topic in his thesis [Jen 97a, Section 2.2]. He studies the influence of the sample crystal by varying the orientation of the crystal (direction of observation), the mass-ratio of its constituents, the charge number of the recoiling atom, the lattice constant, and the crystal structure. Also, the influence of nuclear properties has been investigated, namely the initial recoil velocity (recoil energy), the details of the decay cascade, and the nuclear level lifetime. Last but not least, an influence is observed by using different interatomic potentials.

As discussed in Section 3.5 and Appendix C, only very few transitions are actually suited for Crystal-GRID measurements due to the low efficiency of the spectrometers. Therefore, in this work, discussion will be limited to selected transitions.

For a given transition, the experimental Crystal-GRID line only depends on the direction of observation, i.e. on the sample crystal orientation. This dependence can be understood from the previous section. When calculating GRID lines theoretically, the nuclear level lifetime τ, as well as the interatomic potential V are varied in order to find the best estimates of these unknown quantities. Their influence is visualized by theoretical GRID lines, calculated for the studied transition $E_{\gamma_2} = 1.498\,\text{MeV}$ in TiO_2, depopulating the $3.261\,\text{MeV}$ nuclear level (compare Section 9.3).

Influence of level lifetime

Fig. 5.2 shows the crucial influence of the lifetime on a GRID line. For very short lifetimes, most secondary photons are emitted by the recoiling atom before any scattering occurs. Only very few atoms have experienced a scattering event and thus lead to a certain structure of the line.

For intermediate lifetimes, most recoiling atoms have scattered and a well-structured line is formed. The amount of observed structure depends mainly on the resolution of the spectrometer.

The structure disappears more and more for very long lifetime values, as many recoiling atoms have enough time to reach quasi-thermal velocities before emitting the secondary photons. This can be seen in the plot of the trajectories. A large central peak is obtained from these thermalized atoms with their nearly unshifted photons. Structure is still present on the wings. However, it is added to the wing of the central peak, so that the ratio of structured contributions to the monotonously increasing central peak intensity becomes very bad for large values of τ.

For many nuclear levels, lifetimes are reported in the literature. However, the reported (or neglected) errors of the lifetimes are of the order of 30%. Even values obtained by powder GRID measurements can not be taken as being more precise, due to the assumptions inherent in the MFPA approach and the use of the BM potential in the evaluation (compare Section 8.3.2). Therefore, the lifetime has to be considered as an unknown variable, when evaluating Crystal-GRID data.

Influence of interatomic potential

The main topic of this work is to check whether interatomic solid state potentials can be improved by Crystal-GRID measurements. What influence do they have on Crystal-GRID lines? Fig. 5.3 shows three lines derived from simulations using both the universal (ZBL) potential, one with the original screening length, and two with a reduced or increased screening length. The recoiling atom loses energy more quickly, the more repulsive the potential is, leading to the creation of a central peak in the line. If the centre peak becomes dominant, less structure is visible.

In the energy region under investigation, the ZBL potential is expected to be a relatively good approximation for the true interactions. A change of 25% of the screening length presents a drastic change. Even though many parameters can be varied in interatomic potential formulas, and many functional forms can be used, it is obvious that the interatomic potential has less influence on GRID lines than the nuclear level lifetime has.
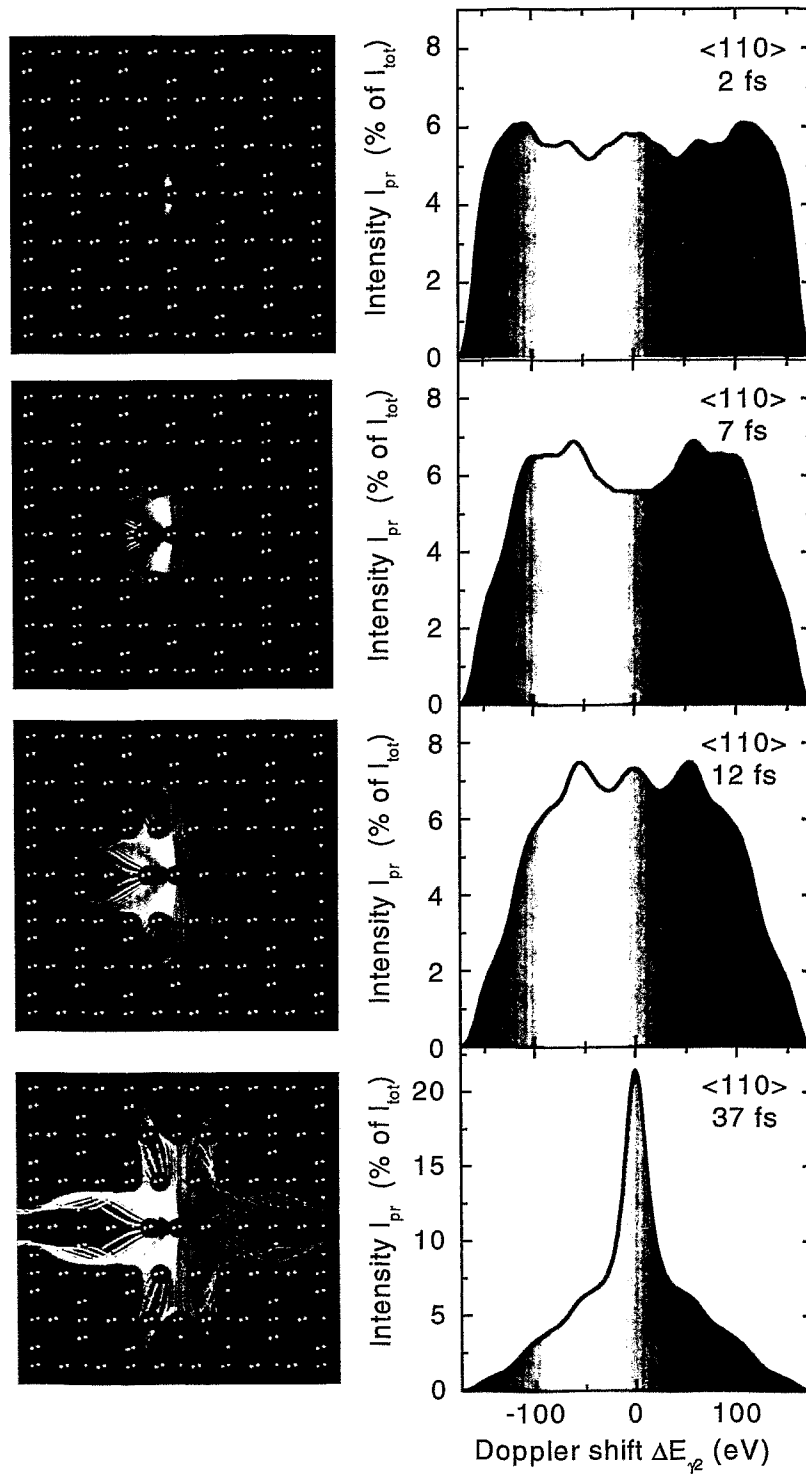
FIGURE 5.2: *Influence of nuclear level life time on Crystal-GRID lines. The longer the lifetime, the more atoms have slowed down to low velocitites and the higher the central peak becomes. Most structure is obtained for intermediate lifetimes.*
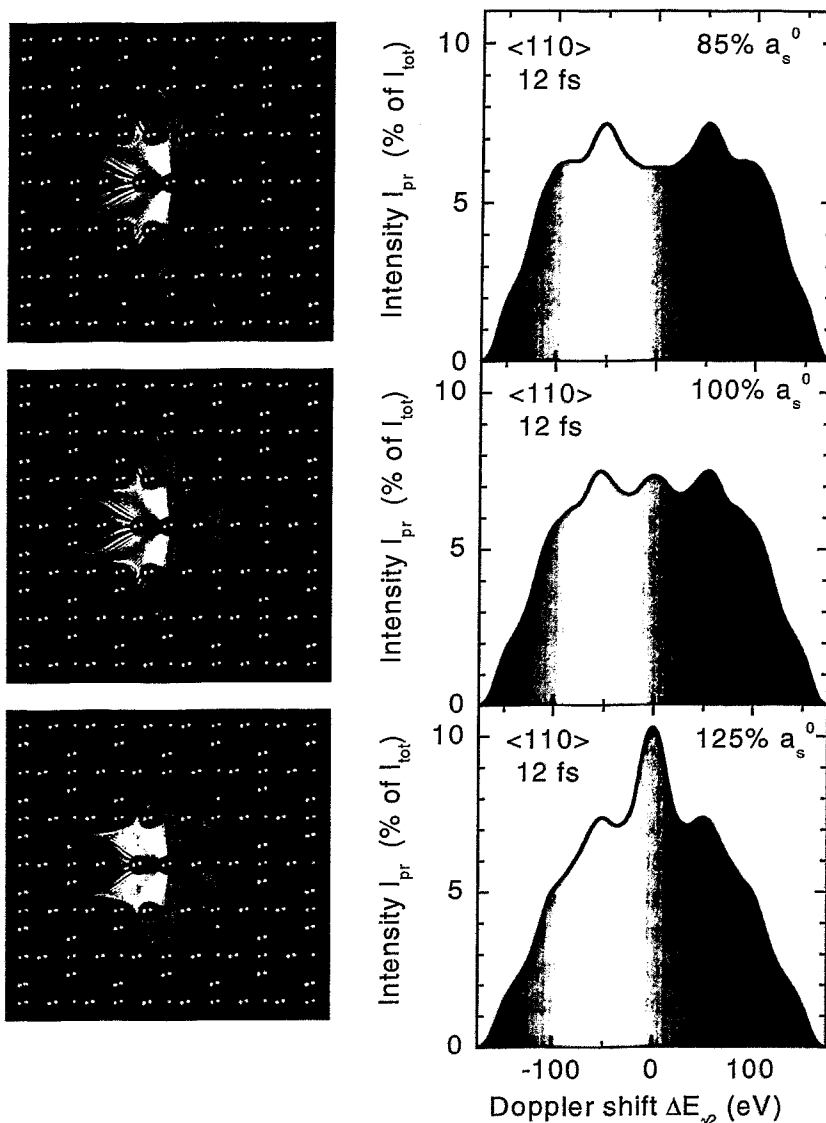
FIGURE 5.3: *Influence of the interatomic potential on Crystal-GRID lines. An enhanced screening length a_s leads to a faster slowing down and thereby to a higher central peak and less structure on the line.*

5.3 Asymmetric GRID lines

In previous powder GRID and Crystal-GRID measurements, the Doppler broadening was always symmetric with respect to the unshifted photon energy. This symmetry was due to the inversion symmetry in real space of the crystals. Crystals having an inversion symmetry yield symmetric lines for all orientations, because the recoiling atom slows down in the same way for an emission with velocity $+\mathbf{v}^0$ or $-\mathbf{v}^0$.

As stated before, the Crystal-GRID method is insensitive to rotations of the sample around the direction of observation. Therefore, a symmetric GRID line is also produced if
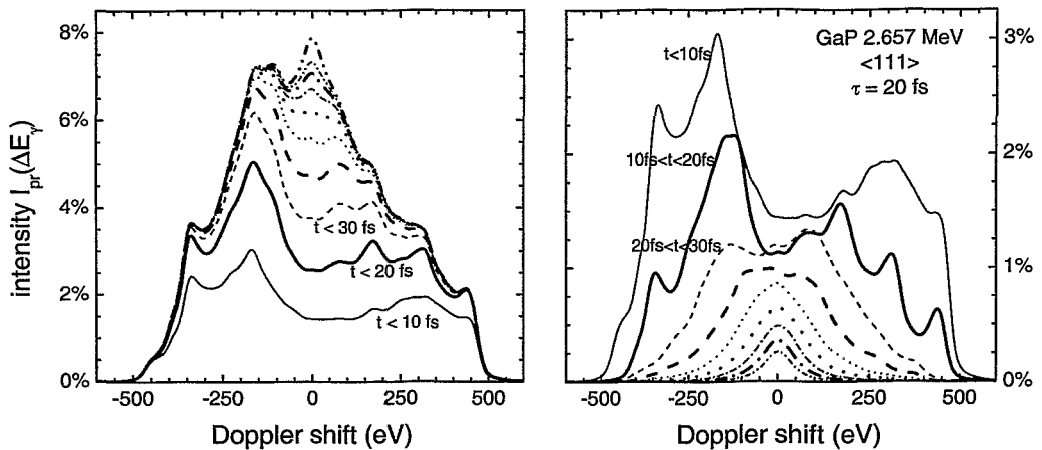
FIGURE 5.4: *Asymmetric Crystal-GRID line. The total GRID line is subdivided into its single contributions of intervals of 10 fs after the initial recoil. In the left picture, the contributions are added to each other so that the time-dependent "evolution" of the line can be seen. The right plot visualizes the single contributions seperately.*

the lattice only has a rotation-inversion symmetry around this axis. In a direction without rotation-inversion symmetry, however, an asymmetric line is predicted.

Fig. 5.4 illustrates the formation of an asymmetric Crystal-GRID line. In the right part the contributions to the total Doppler broadened energy spectrum belonging to secondary photons emitted within the first 10 fs, the second 10 fs, and so on, are plotted separately. On the left side, the contributions are added successively visualizing the "evolution" of the line. It can be clearly seen that the asymmetry is formed by the photons emitted soon after the initial recoil, i.e. by the atoms having undergone only few collisions. The asymmetry is directly related to the nearest neighbours of the initially recoiling atom. At later times, the correlation of the velocity to the first scattering event is lost and symmetric contributions are added to the line.

If the lifetime is higher than in the plotted case, more photons are emitted at late times and thus contribute a symmetric part to the line. The asymmetry, mainly present in the wings, becomes less visible.

From the very beginning of this work, it was one of the major aims to verify the existence of this asymmetry. The zinc blende structure, e.g., has no inversion symmetry if the two sub-lattices are occupied by different atomic species. A rotation-inversion symmetry exists for some axes, e.g. for the <100> and the <110> directions, but not for the <111> direction. Consequently the predicted Crystal-GRID line in the latter case is asymmetric. Results of measurements using ZnS single crystals are reported in Section 9.1.

5.3.1   Angular correlation and asymmetry

The question arises if angular correlation can influence the symmetry of Crystal-GRID lines. Symmetric lines are predicted in crystals having at least an inversion-rotation symmetry around the axis of observation. In this case, after application of the symmetry operators, to every trajectory $\mathbf{v}_i(t)$ a second trajectory $\mathbf{v}_j(t)$ exists where the initial re-

coil occurred in the opposite direction and the trajectory evolves in the identical but opposite way. If an inversion symmetry exists, $\mathbf{v}_j(t) = -\mathbf{v}_i(t)$; if only a rotation-inversion symmetry exists, a rotation around the axis of observation must be applied.

In both cases, $\mathbf{v}_j(t) \cdot \mathbf{n} = -\mathbf{v}_i(t) \cdot \mathbf{n}$, i.e. the two trajectories contribute at opposite velocity projections to the Crystal-GRID line. The angle ϕ between the emission directions of the two photons, $-\mathbf{v}(0)$ and $\mathbf{n}$, can be calculated using Eq. (2.9)

$$\cos\phi_i = \frac{-\mathbf{v}_i(0)}{v^0} \cdot \mathbf{n} = -\cos\phi_j \tag{5.11}$$

If angular correlation is considered in the calculation (compare Eq. (5.3)), the contribution of the trajectories is weighted by the factor $W'(\cos\phi)$. As seen in Section 2.4, this factor is symmetric with respect to 0. Consequently, it is identical for both trajectories, and the Crystal-GRID line remains symmetric.

It can not be proven, that asymmetric Crystal-GRID lines remain asymmetric when considering angular correlation. However, it is highly improbable that angular correlation exactly compensates the effect of the asymmetric slowing down. Therefore, in the general case, angular correlation does not influence the symmetry of a Crystal-GRID line.

Chapter 6

Fitting theoretical GRID lines to experimental scans

Crystal-GRID measurements are performed in order to determine potential parameters and nuclear level lifetimes. For this purpose, the theoretical Crystal-GRID line $I_{\mathrm{pr}}\left(\Delta E_{\gamma_2}\right)$ (Eq. (5.7)) is fitted to the experimental scans consisting of count values c_i^k (Eq. (3.9)) taken at angular positions θ_i^k of the second spectrometer crystal. Here, k numbers the K scans within a series of scans and i numbers the measuring points of a single scan. Due to the slight drift of the spectrometer, it is not possible to directly convert θ_i^k to an absolute energy with sufficient precision. For that reason, the theoretical line is always given as a function of the Doppler shift $\Delta E_{\gamma_2} = E_{\gamma_2} - E_{\gamma_2}^0$. The Doppler shift $\left(\Delta E_{\gamma_2}\right)_i^k$ at the measuring angle θ_i^k can be obtained by converting the angular difference $\theta_i^k - \theta_{\mathrm{c}}^k$, where θ_{c}^k is a fit parameter, the so-called *centre position* of scan k, corresponding to unshifted photons.

$$\left(\Delta E_{\gamma_2}\right)_i^k = \left(\theta_i^k - \theta_{\mathrm{c}}^k\right) \cdot \underbrace{\left(\frac{\Delta E_{\gamma_2}}{\Delta \theta}\right)}_{\text{conversion factor (Eq. (3.7))}} \tag{6.1}$$

As discussed in Section 5.1, the theoretical line I_{pr} is normalized to the total yield I_{tot} of photons belonging to the transition under study. Consequently, the GRID line to be fitted to the experimental scans, also called *model function* $m_{\mathbf{a}}$, depending on the J parameters $\mathbf{a} = (a_1, a_2, ..., a_J)$, can be obtained by multiplying the theoretical GRID line I_{pr} with I_{tot} and adding the constant background I_{bg}.

$$m_{\mathbf{a}} = I_{\mathrm{pr}} \cdot I_{\mathrm{tot}} + I_{\mathrm{bg}} \tag{6.2}$$

Often, it is more convenient to explicitly use the height I_{c} in the centre of the GRID line for scaling.

$$I_{\mathrm{c}} = I_{\mathrm{pr}}(0) \cdot I_{\mathrm{tot}} \tag{6.3}$$

$$\Longrightarrow m_{\mathbf{a}} = \frac{I_{\mathrm{pr}}}{I_{\mathrm{pr}}(0)} \cdot I_{\mathrm{c}} + I_{\mathrm{bg}} \tag{6.4}$$

For the actual fitting, the value of the model function at the angular position θ_i^k needs to

be known.

$$m_{\mathrm{a}}\left(\theta_i^k\right) = \frac{I_{\mathrm{pr}}\left(\left(\Delta E_{\gamma_2}\right)_i^k\right)}{I_{\mathrm{pr}}\left(0\right)} \cdot I_{\mathrm{c}}^k + I_{\mathrm{bg}}^k$$

$$= \frac{I_{\mathrm{pr}}\left(\left(\theta_i^k - \theta_{\mathrm{c}}^k\right) \cdot \left(\frac{\Delta E_{\gamma_2}}{\Delta \theta}\right)\right)}{I_{\mathrm{pr}}\left(0\right)} \cdot I_{\mathrm{c}}^k + I_{\mathrm{bg}}^k \tag{6.5}$$

As can be seen, three parameters need to be determined for every scan k: the height I_{c}^k in the centre of the line (or, alternatively, the total yield I_{tot}^k), the constant background level I_{bg}^k, and the centre position θ_{c}^k of the experimental scan. These so-called *local* parameters are only related to the data within one scan. For clarity, the upper index k will be dropped if the discussion only focuses on a single scan.

The nuclear level lifetime τ and the potential parameters are physical constants and are thus identical for all the scans. These so-called *global* parameters also need to be determined by the fit. Consequently, if looking at K scans, the total number of parameters to be fitted is $3K + 1 + L$ where L is the number of potential parameters.

The distinction of local and global parameters suggests to separate the fitting procedure. First, the GRID line corresponding to a trial value of the global parameters is fitted to all the scans separately by varying the three local parameters and looking for the best consistency between model function and experimental counts.

Second, the nuclear level lifetime is varied. For every new trial value of the lifetime, the corresponding GRID line is calculated and again fitted to every single scan in order to optimize the local parameters. The best estimate of the lifetime is found as soon as the simultaneous consistency between the model function and all experimental scans is reached.

These two steps are performed by the fitting codes `griddle` and `gravel` (see Section 6.3). The consistency is judged by the statistical variable χ^2, as discussed in Section 6.1.

In a third step, the parameters of the interatomic potential will be optimized. For every set of parameters, a new simulation of the slowing down becomes necessary. As these simulations may take several days, a straightforward optimization within a fitting code, as done for the lifetime, is not possible. Instead, the two-step fitting, as described before, is applied to every simulation separately. Afterwards, the results are compared in order to judge on which potential parameters are best. As this comparison brings about several problems, the next Chapter will be entirely dedicated to the optimization of potential parameters.

6.1 Statistics

The estimation of parameters is the main aim of fitting model functions to experimental data. It is called *point estimation* in statistics literature. In order to judge which parameters are best, a so-called *statistic* is used. A statistic is a measure of the consistency of the model and the experimental data.

Two more quantities can be estimated from the fit in order to get an idea about the reliability of the parameters. First, a measure of the errors or uncertainties needs to be

determined using the so-called *interval estimation*. A typical measure is the standard deviation σ of the parameter.

Parameter and error estimation are sufficient if the underlying model is known to be correct. Otherwise, a statement on the validity of the model is needed, the so-called *goodness-of-fit* needs to be calculated, as presented in Section 6.1.5. In statistics this is called the *test of hypothesis*. It tells how probable it is that the data have occurred if the assumed model was true.

Three different statistics are presented in the following, two well-known χ^2 methods, as well as the maximum likelihood estimation (MLE) using Poisson distributed data. Maximum likelihood approaches are numerically more costly than χ^2 methods. With modern computers, however, this difference becomes meaningless. In Section 6.5 and Appendix D, the different statistics will be applied and compared, in order to understand under which circumstances which statistic can be used. For more details see [HauJen 01].

6.1.1 χ^2 statistics

The classical χ^2 statistics base on the χ^2 density which is defined as

$$\chi^2 = \sum_i \frac{(c_i - m_a(\theta_i))^2}{\sigma_i^2} \tag{6.6}$$

where $(c_i - m_a(\theta_i))$ is normally (Gauss) distributed with the known variance σ_i^2. When counting random events, however, the number of counts per given time is not Gauss but Poisson distributed around the true value $t(\theta_i)$. It is necessary to check whether χ^2 statistics can be used, anyhow.

For Poisson distributed data, it can easily be shown that the variance is equal to the true value, i.e. $\sigma_i^2 = t(\theta_i)$. As this true value is not known, it must be approximated. Depending on what approximation one uses, the statistic can be represented by one of the classical chi-square forms:

$$\chi_P^2 = \text{Pearson's } \chi^2 = \sum_i \frac{(c_i - m_a(\theta_i))^2}{m_a(\theta_i)} \tag{6.7}$$

$$\chi_N^2 = \text{modified Neyman's } \chi^2 = \sum_i \frac{(c_i - m_a(\theta_i))^2}{\max(c_i, 1)} \tag{6.8}$$

The fitting code griddle uses the modified Neyman's χ_N^2. Originally, Neyman's χ_N^2 has been defined with c_i in the denominator. As this expression is undefined if any measured value c_i is zero, Eq. (6.8) has been widely used [Awa 79, BevRob 92, Whe 95]. It is identical to the original Neyman's χ_N^2, if all c_i are non-zero.

6.1.2   Maximum likelihood estimation (MLE)

An intuitive way of extracting information from measured data is to ask the question whether it is probable that the data have occurred given a set of parameters and a model. The idea of maximum likelihood estimation (MLE) is to maximize this probability, called "likelihood". In its simplest form it can be used to determine the expectation value of an observable if the latter has been measured several times.

Stoneking and Den Hartog state that "for non-normal uncertainty distributions such as the Poisson distribution, minimizing χ^2 does not maximize the likelihood that the fitted parameters reflect the data" [StoDen 97].

The likelihood L_P is given by the combined probability of measuring a set of c_i counts at positions θ_i where the model predicts $m_\mathrm{a}(\theta_i)$ counts. In the case of Poisson distributed data,

$$L_P\left(\mathbf{c}|m_\mathrm{a}\right) = \prod_i P_P(c_i; m_\mathrm{a}(\theta_i)) = \prod_i \frac{[m_\mathrm{a}(\theta_i)]^{c_i}}{c_i!} e^{-m_\mathrm{a}(\theta_i)} \qquad (6.9)$$

where $P_P\left(c_i; m_\mathrm{a}\left(\theta_i\right)\right)$ is the Poisson probability that a measurement gives c_i counts if the true value is $m_\mathrm{a}(\theta_i)$ and $\mathbf{c} = (c_1, c_2, ..., c_N)$ is the set of N measured count values [BevRob 92, p. 111]. If m_a depends on the J parameters a_j, then the likelihood L_P needs to be maximized with respect to these parameters in order to find their best estimates.

It is easier to use the logarithm of this expression. Minimising $-2 \ln L_P$ leads to the same parameters as maximising L_P.

$$-2 \ln L_P\left(\mathbf{c}|m_\mathrm{a}\right) = 2 \sum_i \left[m_\mathrm{a}\left(\theta_i\right) - c_i \ln m_\mathrm{a}\left(\theta_i\right) + \ln c_i!\right] \qquad (6.10)$$

A similar equation has been derived several times. In 1979, Awaya presented it as a "new method" and called it G [Awa 79]. In the same year, Cash published his C statistic [Cas 79]. Further formulations can be found in [Gre 91, JadRii 96][BloLoh 98, p. 191]. If no analytic expression of the model function m_a exists, as in the case of GRID lines, numerical methods are used to find the minimum.

6.1.3   Likelihood ratio test

The log-likelihood of Eq. (6.10) does not have the typical properties of a χ^2 distribution. It can be extended, however, by using the so-called *likelihood ratio test* [Wil 63, section 13] (see also [Cas 79][BakCou 84][Hoe 54, p. 189][Ead 71, p. 230ff][Bra 99, p. 228]).

The (maximum) likelihood ratio λ was first introduced by Neyman and Pearson and defined as [NeyPea 28]

$$\lambda = \max_\mathrm{a} \lambda^* = \frac{\max_\mathrm{a} L_P\left(\mathbf{c}|m_\mathrm{a}\right)}{\max L_P\left(\mathbf{c}|\mathbf{m}'\right)} \qquad (6.11)$$

The numerator gives the likelihood $L_P\left(\mathbf{c}|m_\mathrm{a}\right)$ that the experimental data $\mathbf{c}$ occurred if the model m_a was true, and maximized with respect to the parameters $\mathbf{a}$. The denominator gives the likelihood $L_P\left(\mathbf{c}|\mathbf{m}'\right)$ that the experimental data $\mathbf{c}$ occurred, maximized without having any restriction on the model, where $\mathbf{m}' = (m_1', m_2', ..., m_N')$ is the set of parameter-independent model values. As the denominator is constant and independent of the model, the quantity λ^* has been introduced. Parameters can be estimated by maximising its value. It is evident that the ratio λ, as well as λ^*, can only take on values between 0 and 1.

The likelihood in the numerator is given by Eq. (6.9). The global maximum of L in the denominator is found by calculating

$$\frac{\partial}{\partial m_j'} \left[-2 \ln L_P\left(\mathbf{c}|\mathbf{m}'\right)\right] \overset{!}{=} 0 \qquad (6.12)$$

where the parameter-independent m_i' replaces $m_a(\theta_i)$ in the likelihood function L_P (see Eq. (6.9)).

$$\implies \quad 2 \cdot \left[1 - \frac{c_j}{m_j'}\right] \overset{!}{=} 0 \tag{6.13}$$

$$m_j' = c_j \qquad \forall j \tag{6.14}$$

The best possible estimation of the counts $\mathbf{c}$ is the counts themselves, i.e. $\max L_P(\mathbf{c}|\mathbf{m}') = L_P(\mathbf{c}|\mathbf{c})$. Even though this sounds trivial, it is *not* a general result.

One can now define a "maximum likelihood $\chi^2_{\lambda,P}$" as

$$\begin{aligned} \chi^2_{\lambda,P} &= -2\ln\lambda^* \\ &= 2\ln L_P(\mathbf{c}|\mathbf{c}) - 2\ln L_P(\mathbf{c}|m_a) \end{aligned} \tag{6.15}$$

$$= 2\left[\sum_i (m_a(\theta_i) - c_i) - \sum_{\substack{i \\ c_i \neq 0}} c_i \ln\left(\frac{m_a(\theta_i)}{c_i}\right)\right] \tag{6.16}$$

This equation will be referred to as *Poisson MLE*.

As $0 < \lambda^* \leq 1$, the maximum likelihood $\chi^2_{\lambda,P}$ can not become negative. A theorem of Wilks shows that $\min_a \chi^2_{\lambda,P}$ asymptotically follows a χ^2 distribution with $N - J$ degrees of freedom [Wil 63, p. 419] except for a deviation varying as $1/N$ which is important if the number N of data points is small.

As the first term in Eq. (6.15) does not depend on the parameters to be estimated, minimising $\chi^2_{\lambda,P}$ with respect to one parameter is identical to minimizing $-2\ln L_P(\mathbf{c}|m_a)$. Thus, the parameter estimation is unchanged if using $\chi^2_{\lambda,P}$ instead of $-2\ln L_P$. In addition, however, $\chi^2_{\lambda,P}$ should be applicable to check the consistency of the model and the data by a goodness-of-fit test (see Section 6.1.5).

6.1.4 Error estimation

Estimating parameters is only useful if one can also state the error of the newly obtained value. It is well known that for χ^2 statistics the 1σ error of non-correlated parameters can be obtained by looking for their values where χ^2 is increased by 1.

For sufficiently large event samples, the likelihood (not the distribution of the single measurements) becomes Gaussian centred on those values a_j' that minimize its function [BevRob 92, p. 144] (see also [Ead 71][BloLoh 98, p. 189]). Near the minimum, the likelihood L_P can be approximated by

$$L_P = A\exp\left[-\frac{1}{2}\left(\frac{a_j - a_j'}{\sigma_j}\right)^2\right] \tag{6.17}$$

where A is a function of the parameters $a_1, a_2, ..., a_{j-1}, a_{j+1}, ..., a_J$. Calculating the negative logarithm of Eq. (6.17) yields

$$-2\ln L_P = \left(\frac{a_j - a_j'}{\sigma_j}\right)^2 + \text{const.} \tag{6.18}$$

$$\chi^2_{\lambda,P} = \left(\frac{a_j - a_j'}{\sigma_j}\right)^2 + \text{const.} \tag{6.19}$$

showing that a variation of the parameter a_j by $n\sigma_j$ $(a_j = a'_j \pm n\sigma_j)$ leads to an increase of the Poisson MLE $\chi^2_{\lambda,P}$ by n^2. In order to extract the 1σ error limit, one can vary the parameter until $\chi^2_{\lambda,P}$ is increased by 1, just as one would do for a classical χ^2 statistic.

This derivation is correct in the case where only one parameter is fitted. In the GRID fitting procedure, the local parameters are optimized for every value of τ. Thereby the fitting problem is separated into K sub-problems with 3 parameters, and one fit with 1 parameter, the lifetime. Consequently, it is correct to look for the increase of χ^2 by 1 to find σ_τ [BevRob 92, p. 212].

6.1.5 Goodness-of-fit estimation

Up to this work, the consistency of theoretical GRID lines and experimental data was roughly judged by the so-called *reduced* χ^2

$$\chi^2_\nu = \chi^2/\nu \tag{6.20}$$

where the number ν of degrees of freedom is equal to the number N of measuring points minus the number of fitted parameters. For a good fit, the value of χ^2_ν must be close to 1. However, the meaning of the term "close" depends strongly on the number of degrees of freedom. Increasing the number of scans, e.g., χ^2_N comes closer to 1 without any change to the model.

For that reason, a better-defined variable is chosen in this work, the so-called *goodness-of-fit Q*

$$Q\left(\chi^2_{\min}, \nu\right) = \frac{1}{\Gamma\left(\frac{\nu}{2}\right)} \int_{\chi^2_{\min}/2}^\infty \exp\left(-t\right) \, t^{\frac{\nu}{2}-1} \, dt \tag{6.21}$$

where Γ is the Gamma function. $Q\left(\chi^2_{\min}, \nu\right)$ gives the probability that an observed χ^2 exceeds the value $\chi^2_{\min}$, obtained for the best potential, by chance *even* for a correct model. In other words, assuming that the model were correct, then Q is the probability that the consistency between *any* experimental data and the model line is worse than the consistency of the measured data with this model.

If the goodness-of-fit $Q > 10\%$, approximately, the model can be accepted, if $Q < 0.1\%$ the model is very likely to be wrong [Pre 89, p. 160-165]. For a correct model, Q is independent of the number of data points and of the number of counts. If the model is not quite correct, however, Q decreases with increasing statistics, showing that the model needs to be further improved.

6.2 Summing experimental data

The typical fine structure of a Crystal-GRID line can only be observed in the experimental data after summing several scans, because the intensity of every single scan is usually so small that the statistical noise hides all details. The so-called *experimental sum scan* is also needed if one wants to present the measured data, as often more than 100 scans are measured.

The scans need to be aligned with respect to each other using the centre positions θ^k_c in order to correct for the slight drift of the spectrometer. After the alignment, the scans

overlap in a certain energy range. Ideally, all scans cover at least the full Doppler broadened line and extend slightly into the background to the right and left of the spectrum. Within this common range, a set of summation points θ_i^* needs to be defined. The first summation point is fixed at one edge of the common interval. The remaining points are defined iteratively, by using the average spacing of the measuring points in the single scans at the previous angle. For most scans, no measurement has been performed exactly at the positions θ_i^*. For that reason, the number of counts in every single scan is intra-polated in between the two nearest measuring points.

By using the fitted centre positions θ_c^k for the alignment, however, the experimental sum scan depends on the model applied during the fitting procedure. Theory and experimental data are not clearly distinguished.

Alternatively, it has been tried to perform a theory-independent summation by a self-consistent fit of the experimental sum scan. How does this work? A first alignment of the scans is obtained by looking for the highest count rate of every single scan, averaged over three adjacent measuring points to reduce statistical noise. Summing the aligned scans, a first experimental sum scan is obtained.

In the following iterations, the experimental sum scan is used as model function, after subtracting the background. It is fitted just like a theoretical model function to every single scan by varying the three local parameters. The experimental sum scan for the next iteration is obtained by summing the single scans shifted with respect to their fitted centre positions. The background to be subtracted is given by the sum of the fitted background terms I_{bg}^k of the single scans. After several iterations, the procedure converges and the theory-free experimental sum scan is determined.

The correctness of the described algorithm has not been rigorously proven. However, test calculations for the solids studied within this work show that, within the errors, the theory-free experimental sum is identical to the experimental sum from the model-dependent fit. As the experimental sum scan is only needed for visualisation, the minor differences are of no importance.

6.3   The fitting codes gravel and griddle

Up to this work, the evaluation of GRID data was done with the fitting code griddle [RobJol 90]. The original version of griddle used the MFPA theory of the slowing down for the calculation of GRID lines. Jentschel extended the code to the case of Crystal-GRID where the slowing down is calculated by an MD or RMD simulation [Jen 97a]. The fitting code calculates the model GRID line and fits this line to the experimental scans as described before, using the modified Neyman's χ_N^2 statistic.

Summing up the experimental scans as well as the fitted theoretical GRID lines, one finds that the theoretical sum lies far outside the error bars of the summed experimental data points. This can be seen in Fig. 6.1a) where the summed theoretical GRID line is plotted with a dashed line (χ_N^2). For every single scan, the theoretical GRID line lies within the errors of the single data points (see Fig. 6.1b). The obvious disagreement only becomes visible after summing many scans.

Two questions arise at that point. Where does the disagreement come from? And, does it have any influence on the parameters to be determined, i.e. on the nuclear level lifetime, and in a later step, on the interatomic potential?
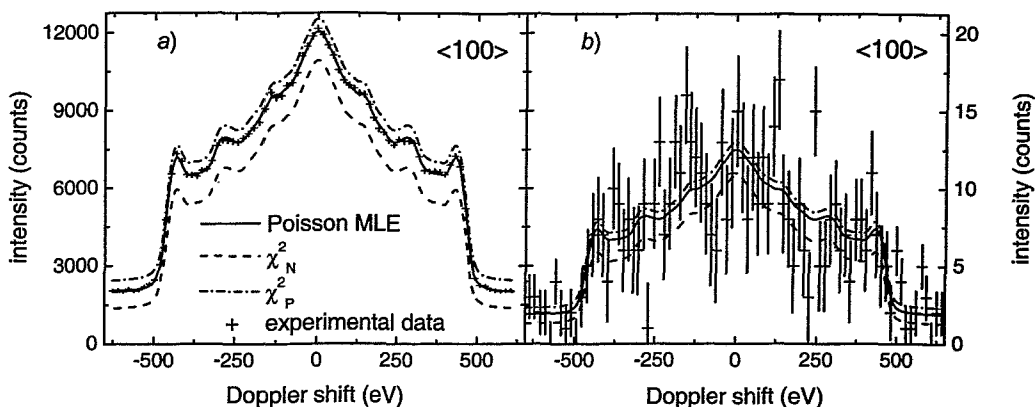
FIGURE 6.1: *Comparison of fitted theoretical lines and artificial experimental data. (a) The sum of 1000 artificial scans (centre height $I_c = 10$ on a background $I_{bg} = 2$) is compared to the sum of the fitted lines. It is most evident, that Neyman's χ^2_N, as used in* griddle, *and Pearson's χ^2_P do not reproduce the data at all. (b) The inconsistency can not be seen in the plot of a single scan.*

The implementation of the theory-free experimental sum, as discussed in the previous section, allowed to fit theoretical GRID lines to the sum scan. It is observed that thereby, the disagreement can be reduced. However, the sum scan should not be used to determine parameters. The measured data are given by the single scans and not by the sum scan. Only in the optimal case, i.e. if the summation algorithm is rigorously correct and has perfectly converged, the experimental sum scan contains as much information as all the single scans.

Looking deeper into detail, it turned out that the disagreement is related to the statistic used for the evaluation. In statistics literature, it is well known that χ^2_N and χ^2_P are not suited to estimate the area under a peak or simply the mean of Poisson distributed values (for details see Appendix D). As can be seen in Fig. 6.1, only the Poisson MLE $\chi^2_{\lambda,P}$ leads to a good agreement of summed fitted lines and experimental sum scan.

The question whether other parameters are also influenced will be answered in Section 6.5, where it will be shown that the Poisson MLE also is the best statistic to estimate the nuclear level lifetime.

6.3.1 Short description of the new fitting code gravel

The implementation of the fitting procedure in the code griddle only allows to work with symmetric GRID lines. As in this work, the existence of asymmetric Crystal-GRID lines should be proven, a new fitting code, called gravel, has been developed. Five different statistics have been implemented in this code in order to check the applicability of the different statistics.

When starting gravel, the general input file fit_input.dat, the scan files, the instrumental response function, the symmetry operators of the crystal, as well as the trajectories (MD input file) are read in. Amongst others, it can be chosen whether the summation shall be performed with or without using the theory (compare Section 6.2), which statistic is to be used for the fitting (compare Section 6.1), and if the lifetime shall be fitted or

stepped through with a constant step size in order to obtain the dependence $\chi^2\left(\tau'\right)$.

During the run of the program, the file `fit_protocol.dat` is generated, containing a detailed protocol of the fit. At the same time, the experimental data, theoretical lines, sum scans, and the calculated χ^2 values are displayed on the screen, so that the fitting procedure can be easily supervised.

The first three iterations are performed using the trial values $\tau_0'/1.3$, $\tau_0' \cdot 1.3$, and τ_0' for the lifetime where τ_0' is read in from the input file. First guesses for the local parameters are calculated for every scan: The background $I_{\rm bg}^k$ is estimated by averaging the lowest counts within the scan, the centre height $I_{\rm c}^k$ by searching for the highest number of counts, averaged over three adjacent measuring points, and the centre position $\theta_{\rm c}^k$ by a simple least-squares fit of the model line to the scan.

For every trial value τ', the theoretical Doppler broadened line is calculated by multiplying the radioactive decay law with the pre-calculated distribution $P(v_\parallel, t)$ (Eq. 5.4). The local parameters are then optimized, scan by scan, by minimizing the statistical variable χ_k^2 using a Levenberg-Marquardt algorithm (compare Appendix E). After all scans have been fitted, the global χ^2 can be calculated as

$$\chi^2 = \sum_{k=1}^{K} \chi_k^2 \tag{6.22}$$

The χ^2 values of the last three iterations are connected by a parabola as a function of τ'. The minimum of this parabola determines the next trial value for the lifetime. Convergence is assumed as soon as the extrapolated minimum is very near to the last calculated value.

After convergence to the value τ, the standard deviation σ_τ is calculated from the parabola, and seven further iterations are performed at the trial values $\tau \pm 3\sigma_\tau$, $\tau \pm 2\sigma_\tau$, $\tau \pm \sigma_\tau$, and τ. This allows to plot the function $\chi^2\left(\tau'\right)$ and to visualize the convergence to the value τ as well as its error σ_τ (see e.g. Fig. 7.1).

6.3.2 Improvements in gravel compared to griddle

Besides the implementation of different statistics and the possibility to fit asymmetric Crystal-GRID lines, several minor improvements have been implemented, all of them related to the calculation of the theoretical GRID line on the basis of an MD input file.

1. The calculation of GRID lines is much faster as the probability distribution $P(v_\parallel, t)$ (Eq. (5.2)) is only calculated once from the MD input file. During the fitting procedure the theoretical line is calculated by multiplying the radioactive decay law (Eq. (5.4)) basing on the pre-calculated distribution.

2. As discussed in Section 5.1, the trajectories are only simulated up to $t_{\rm end} \approx 5\tau$. Up to this work, the remaining part of the trajectories was completely neglected. All decays occurring after $t_{\rm end}$ did not contribute to the theoretical GRID line. Therefore, the central peak was always underestimated by a few percent, and consequently, the fitted lifetime was always too high. Now, the remaining part is approximated by the velocity distribution at the last time step (Eq. (5.5)). If the quasi-thermal regime is reached, this approximation is exact on the considered time scale, and the lifetime

is correctly estimated. Otherwise, it predicts too many decays at velocities above the thermal regime, and too few at thermal velocities. The centre peak is slightly smeared out, eventually entailing a small error of the lifetime. In any case, the error is smaller than in `griddle`. If necessary, it can be further reduced by increasing t_{end}.

3. During the simulation, the recoiling atom's velocity is recorded with a constant time step Δt. The integral of Eq. (5.4) is approximated by a sum over these discrete values. In `gravel`, a minor improvement was implemented, in that the values $P(v_{\parallel}, 0)$ are only considered for half a time step. Thereby, instead of calculating the upper sum of the integral, a better approximation to the integral is performed. Compared to the old fitting code, the theoretical GRID line and the estimate of the level lifetime is slightly improved.

6.4 Generating artificial (Monte Carlo) data

Real experimental data are not well suited for methodical studies of the data evaluation, as needed, e.g., to compare the different statistics implemented in the fitting code `gravel`. The true interatomic interactions are not known and need to be approximated. Many other variables may also have an uncontrolled influence on the studied phenomenon. Furthermore, Crystal-GRID experiments suffer from the low efficiency of the spectrometer. For that reason, it was tried, for the first time, to generate and to apply artificial GRID data, i.e. Monte Carlo data, allowing to ignore any problem of low efficiency, insufficient measuring time, limited stability of the instrument, and others. In that sense, artificial data can be considered as ideal experiment and show up principle limits of the GRID method.

Working with artificial data, the model is completely known, so that it is possible to concentrate on selected parameters. For that reason, artificial data are extensively used in this work. On the one hand, the comparison of different statistics, as discussed in Section 6.5, largely bases on these data. On the other hand, investigations have been performed in order to study the influence of angular correlation, to predict the sensitivity of Crystal-GRID to potential parameters and the level lifetime, to predict the size of expected uncertainties and to compare the different approaches, MD, RMD, and MFPA, with respect to their estimation of level lifetimes. All of this will be discussed in Chapter 8. Furthermore, complementary investigations using artificial data are done for the true experiments using ZnS and Si single crystals, as discussed in Chapter 9.

How can artificial data be generated? First, the theoretical Crystal-GRID line is calculated for a given interatomic potential V and a given nuclear level lifetime τ. As in a true experiment, the number of measuring points and their spacing needs to be defined. The spacing must be chosen so that in all scans, several background data points are present on both sides of the Doppler broadened spectrum. The centre position of the line is randomly chosen within a range of approximately 2 fringes, in order to account for a slight drift between the scans. Drift within the scans is not considered in the generated data, even though this could be easily done for an assumed drift function.

Once the centre position and the sampling points are defined, artificial data can be generated by a Monte Carlo approach. At every sampling point θ_i, a random number of counts c_i is taken from the Poisson distribution around the model value $m_a(\theta_i)$ of the
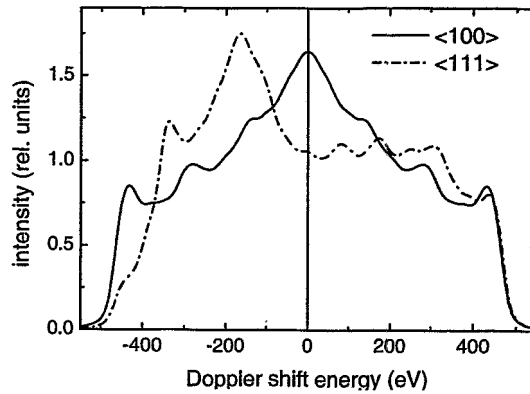
FIGURE 6.2: *Crystal-GRID lines for two directions of observation in GaP single crystals derived from MD simulations based on idealised assumptions about the decay cascade. The nuclear level lifetime is taken to be $\tau = 8$ fs.*

Crystal-GRID line at the sampling point. The algorithm used, is described in [Pre 89, Section 7.3, p. 207].

Investigating artificial data allows to freely chose the constant background I_{bg}, the centre height I_c, the number of scans, the number of data points in each scan, and the spacing of these data points. Furthermore, it is possible to generate data for any desired potential and any value of the level lifetime.

The newly developed computer code for generating artificial data is subdivided into two parts. The program `ad_prepare` generates the sampling points for all the scans, `ad_make` calculates the GRID line from an MD input file and determines the random numbers at the given sampling points.

Sometimes, artificial data corresponding to a real experiment are needed. In this case, the second program uses the experimental data files as input for the sampling points. The intensity can be scaled in order to simulate a higher efficiency of the spectrometer in an otherwise unchanged measurement.

6.5   Testing statistics with artificial data

6.5.1   Parameter and error estimation

For the purpose of testing the different statistics, artificial data are generated for GaP. The decay cascade is idealised, the details of which are of no importance to the following. Two directions of observation are investigated, along the <100> and <111> crystal orientations, respectively. The major difference is related to the symmetry of the lines. The lines for the fixed lifetime of 8 fs are displayed in Fig. 6.2.

The artificial data are generated by scaling the line with $\tau = 8$ fs so that the centre height I_c is equal to 6, 10, 18, 30, 60, 100, 180, 300, 600, or 1000 counts, and afterwards adding a constant background of 2 counts. A total of 100 equidistant points (distance: 0.13 fringes ≈ 13.8 eV) are chosen within the line as well as in the background region to the right and left of the line.
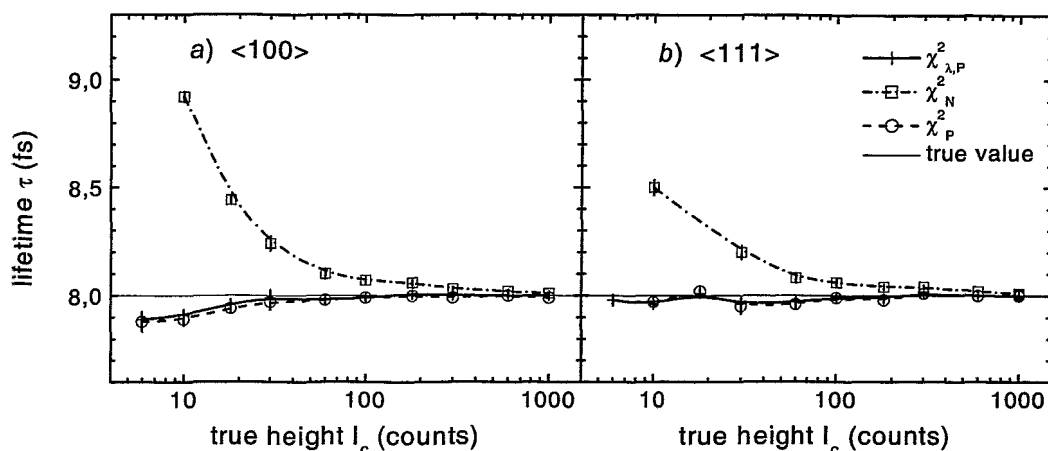
FIGURE 6.3: *Resulting lifetime when fitting the model line to artificial data generated using the true lifetime of 8 fs. The fit has been performed using scans for an observation a) in <100> direction, and b) in <111> direction, respectively.*

For each centre height, 1000 artificial scans are generated, for $I_c \leq 18$, 5000 scans are used, as convergence is not easily obtained. The model GRID line is fitted to these scans in order to determine an estimate for the lifetime. Ideally, the true value of 8 fs should be reproduced.

The result of the fit can be found in Fig. 6.3(a-b) where the values of the fitted lifetime corresponding to the minimum χ^2 are displayed versus the true centre height in a single scan. In the case of the modified Neyman's χ^2_N statistic, the resulting lifetime is too high, especially at low values of I_c. The Poisson MLE statistic, as well as Pearson's χ^2_P, lead to nearly identical results. The estimates of τ are consistent with the true value in the case of <111> orientation, they are slightly too small for small centre heights in the <100> orientation.

Why is the true value of the lifetime not at least within one or two standard deviations σ_τ of the estimated value? The fitting procedure separates the fits of the local parameters from the lifetime fit. Consequently, the statistical error σ_τ does not include the uncertainties of the local parameters which can be regarded as systematic error related to the way of fitting. The statistical error σ_τ of the lifetime can be reduced to an arbitrarily small value by adding further and further scans. Yet, the accuracy of the local parameters is not increased. For low centre heights, the statistical error may become negligible compared to the systematic one.

The fitted centre position $\langle \theta_c^k \rangle$ of scan k deviates from the known true one θ_c^k by $\Delta\theta_c^k = \langle \theta_c^k \rangle - \theta_c^k$. The average deviation, as well as their spread or standard deviation are displayed in Fig. 6.4. It can be seen that the average deviation is very small for any centre height and any statistic, but that there is a large spread $\sigma_{\Delta\theta_c}$, especially for small centre heights. If one summed up the single scans centred around the wrong centre positions, the obtained "experimental" sum scan is smeared out in comparison to the true one.

In a second step, it is checked whether this deviation entails the observed error in the determination of the lifetime. The centre position in every scan is fixed to the correct value, so that besides the lifetime only I_c^k and I_{bg}^k have to be fitted as local parameters.
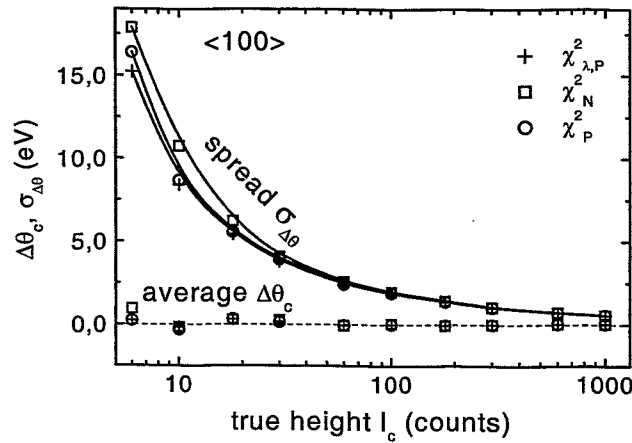
FIGURE 6.4: *Average deviation of the fitted centre positions from the true values and its spread when fitting a model line to a large number of scans for an observation in <100> direction. On average, all statistics estimate the correct positions, the deviation from the true values is very small. However, a large spread (standard deviation) exists, especially for true centre heights up to* 30 *counts. A similar result is found for the <111> orientation.*
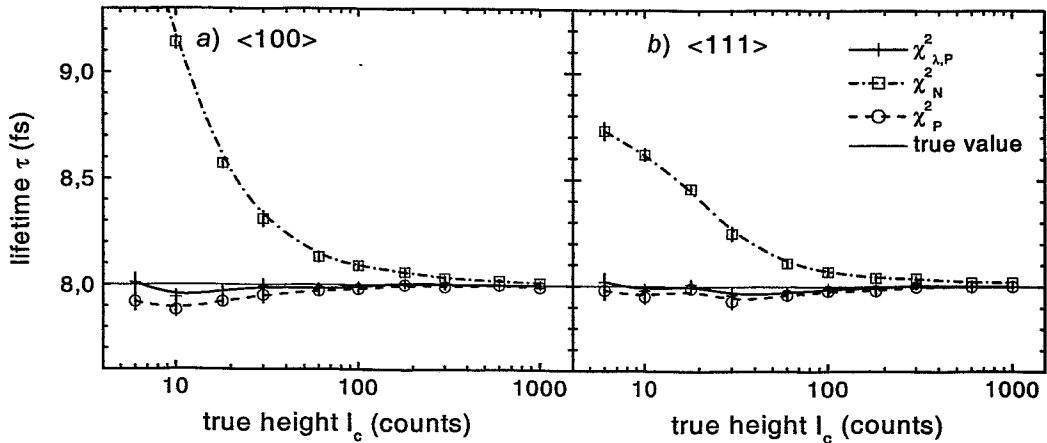
FIGURE 6.5: *Resulting lifetime when fitting the model line to artificial data generated using the true lifetime of 8 fs with the centre positions fixed at their true values during the fit. The fit has been performed using scans for an observation a) in <100> direction, and b) in <111> direction, respectively.*

The resulting lifetimes are plotted in Fig. 6.5(a-b).

In this case, the deviation of the lifetime estimates derived from the Poisson MLE statistic is slightly smaller, the true value of the lifetime can be obtained within $2\sigma_\tau$. The modified Neyman's χ_N^2 again yields incorrect results. If the Pearson's χ_P^2 estimates are better than without fixing the centre positions, it is difficult to say.

6.5.2 Goodness-of-fit test

Which statistic is suited for a goodness-of-fit test? The goodness-of-fit Q is a true probability and can be calculated using Eq. (6.21), if the statistical variable follows a χ^2 distribution. The general χ^2 statistic fulfils this requirement, if all terms in the sum are independent and Gauss distributed with variance 1 [Ead 71, p. 64]. For counting experiments this is only approximately fulfilled. The likelihood ratio, as presented in Section 6.1.3, is supposed to extend the maximum likelihood approach for this purpose.

If the statistic follows a χ^2 distribution, the expectation value $\langle \chi^2 \rangle$ should be equal to the number ν of degrees of freedom. In the following, this necessary condition is checked for the estimation of a mean value, where a sufficiently high value of Q indicates that the measured data really belong to a Poisson distribution around one value, whereas a low value is a sign for a systematic error. If the experimental conditions have changed during the measurement, e.g., the correct description might be a superposition of two Poisson distributions around different mean values.

The expectation value of χ^2 is calculated by

$$\langle \chi^2 \rangle = \sum_{c_i=0}^{\infty} N \cdot P_P\left(c_i; \mu\right) \cdot \chi^2\left(c_i | \mu\right) \tag{6.23}$$

where $P_P\left(c_i; \mu\right)$ is the Poisson probability of obtaining c_i counts if the true mean value is μ, and $\chi^2\left(c_i | \mu\right)$ is the appropriate statistical variable.

The deviation of $\langle \chi^2 \rangle$ from $\nu = N - 1$ is shown in Fig. 6.6 for the three statistics presented in Section 6.1. It can be clearly seen that only Pearson's χ_P^2 leads to the correct estimation. All the other statistics deviate from the theoretical expectation value at least for small values of μ and can therefore not be used for a goodness-of-fit test. This behaviour has also been found by Mighell (see Fig. 2 in [Mig 99]), but he does not draw any conclusions from the disagreement.

The result is very interesting as the wide application of the χ^2 methods is often explained by their applicability to goodness-of-fit estimation. It can be clearly seen, however, that the Neyman approximation does not give the correct expectation value in the case of Poisson distributed data, i.e. that it is not distributed following a χ^2 distribution.

The maximum likelihood approach, as well, leads to incorrect results. This is astonishing as the textbooks do not mention any deviation from the χ^2 distribution for small numbers. Deviations for small data sets exist and possible corrections are discussed for example in [KenStu 67, p. 233] or originally by Lawley [Law 56b, Law 56a]. He proposes to correct the obtained χ^2 by multiplying a factor $\nu / \langle \chi^2 \rangle$.

6.5.3 Conclusion

Within this section, it could be shown that the Poisson MLE $\chi_{\lambda,P}^2$ statistic is best suited to estimate the nuclear level lifetime. Not only do the theoretical and experimental sum scans coincide (Fig. 6.1), but also the estimates of the lifetime reproduce the true values. For very small centre heights, a small systematic deviation may exist. The modified Neyman's χ_N^2 statistic, as implemented in the old fitting code griddle, is not suited at all. Pearson's χ_P^2 yields estimates of the lifetime that are nearly as good as using the Poisson MLE statistic. However, the summed theoretical lines overestimate the experimental sum, so that this statistic should also be avoided.
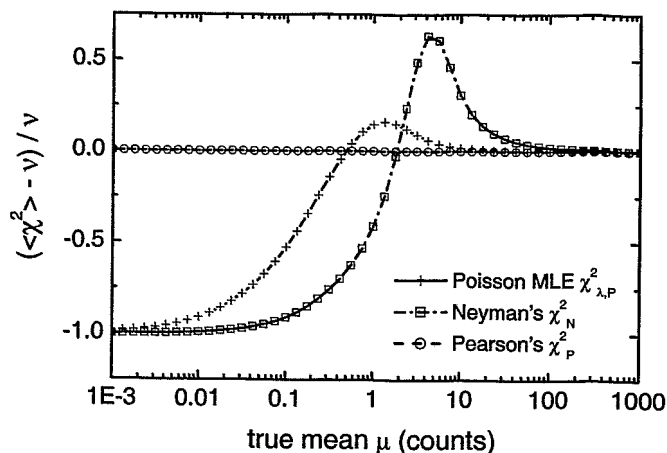
FIGURE 6.6: *Normalised expectation values for χ^2 calculated for different mean values of a Poisson distribution. If the statistic is distributed following a χ^2 distribution, the expectation value $\langle \chi^2 \rangle$ should be equal to the number ν of degrees of freedom, therefore $(\langle \chi^2 \rangle - \nu)/\nu$ should vanish. Only Pearson's χ^2_P shows this behaviour for all mean values. A goodness-of-fit estimation based on the other statistics would lead to incorrect results for the consistency.*

Pearson's χ^2_P is the only statistic yielding a correct expectation value for χ^2, however. Consequently, the goodness-of-fit test needs to be performed on the basis of the χ^2_P value determined at the parameter values estimated with the Poisson MLE statistic.

It is worth noting that Pearson's χ^2_P does not take on its minimum there. As seen from Fig. 6.7, its value is larger than its minimum value, obtained when using χ^2_P for the parameter optimization, as well. If using this minimum value of χ^2_P for a goodness-of-fit estimation, the consistency of the model with the data would be overestimated.
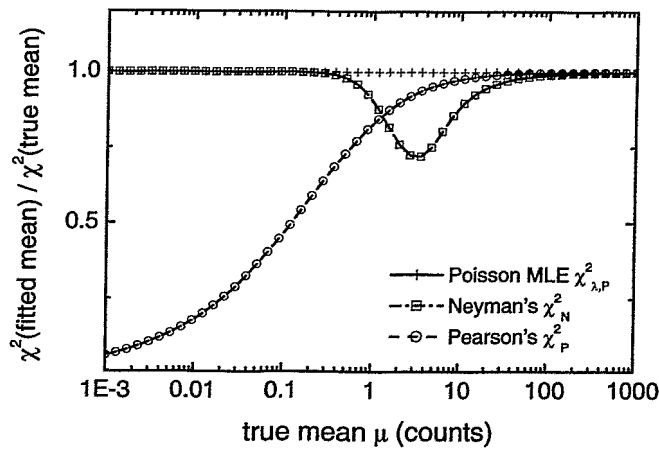
FIGURE 6.7: *Comparison of χ^2 calculated at the true and at the estimated mean of a Poisson distribution. The maximum likelihood statistic leads to correct estimates for the mean. Consequently, the two χ^2 values are identical. Both, Pearson's χ^2_P and Neyman's χ^2_N, however, yield wrong estimates. In some range of μ, the values of χ^2 calculated at these incorrect parameter values are significantly smaller than χ^2 at the true mean.*

Chapter 7

Improving interatomic potentials

"A detailed study of the validity of different possible interatomic potentials has been started recently and is in itself certainly one of the very challenging issues which can be addressed with the GRID/MD method." [BörJol 93]

GRID lines mainly depend on two quantities, the nuclear level lifetime τ and the interatomic potential V. The lifetime is a physical constant. Interatomic potentials, however, are developed in order to approximately describe the atomic interactions. They are presented in arbitrary functional forms with several parameters that, unlike the lifetime, have no physical meaning by themselves. For that reason, the study of interatomic potentials is much more complicated than the determination of a level lifetime.

The study of interatomic potentials includes two main topics. On the one hand, different reported interatomic potentials can be compared. On the other hand, one or more potential parameters of a single interatomic potential can be optimized. Both approaches will be summarized as "improving interatomic potentials", they will only be distinguished if necessary.

By what means is it possible to improve potentials? For every potential (or set of potential parameters), a separate MD simulation is performed. As described in Chapter 6, fitting the derived GRID line to the experimental scans, yields an estimate of the nuclear level lifetime as well as a minimum value of the Poisson MLE $\chi^2_{\lambda,P}$ for each potential. Arguing in the same way as for the determination of the lifetime, the lowest value of $\chi^2_{\lambda,P}$ belongs to the best potential. This straightforward approach, called χ^2 *criterion* in the following, has not been used until very recently. Instead, the fitted estimate of the lifetime has often been compared to reported values or to values from other GRID measurements. This approach will be called *lifetime criterion*. A complete survey of first attempts to improve interatomic potentials using GRID measurements is given in Section 7.1.

Section 7.2 deals with the error of the statistical variable χ^2 itself and reports on convergence tests. This error needs to be known before comparing different potentials using the χ^2 criterion. Once the best potential is found, the question arises whether it sufficiently well describes the slowing down. Both, the goodness-of-fit test and the lifetime criterion can be used in order to judge the quality of the obtained best potential (see Section 7.3). In the last section of this chapter, it will be discussed which part of the interatomic potential, Crystal-GRID is most sensitive to.

7.1 History of potential investigation via GRID

Already in 1988, Börner *et al.* mentioned the possibility to investigate the slowing-down mechanism and the model used for the slowing down if the lifetime of an investigated level is known by other methods [Bör 88].

A first try has been published by Jolie *et al.* in 1989 [Jol 89] dealing with two nuclear levels in Ti. The slowing down was described by the MFPA theory using a Born-Mayer potential with two different sets of potential parameters. In order to judge which set is better, measurements were performed using the two poly-crystalline materials Ti and TiC and comparing the estimates of the lifetime from the two different measurements. Identical estimates are a necessary condition for a correct description of the slowing down. In this very measurement, the estimates are consistent within the error using one set of parameters, but differ by about two standard deviations using the other set. Even though a difference of two standard deviations is very small, this work can be seen as the first indication that interatomic potentials at intermediate distances can be studied using the GRID technique.

In his thesis, Ulbig studies the influence of the potential on the estimate of nuclear level lifetimes in order to make a statement on the reliability of the GRID method with respect to lifetime measurements [Ulb 91a, p. 92-94]. Two different interatomic potentials are used in the MFPA theory, the universal (ZBL) and a Born-Mayer (BM) potential. A series of GRID measurements is compared via their estimates of the nuclear level lifetime. Ulbig finds that the estimates obtained with the ZBL potential are systematically higher than the BM estimates. Especially for short-lived levels, the difference reaches up to 60%.

In order to decide on which lifetime is correct, and thus on which potential yields a better description, it was tried to compare the estimates to results from Doppler shift attenuation (DSA) measurements. However, this comparison did not help to discriminate the two potentials, as the errors of the DSA measurements are quite large, multiple measurements differ strongly from each other, and the DSA evaluation also includes assumptions on the slowing down.

In 1991 and 1992, a series of papers was published by Kuronen and Keinonen who first used MD calculations to simulate powder GRID lines [Kur 91, Kei 91, Kur 92]. Kuronen studied the dependence of the simulated energy spectra on the interatomic potential by comparing three potentials [Kur 91], the universal (ZBL) potential, a Born-Mayer (BM) form with parameters from Abrahamson, and a pair potential based on effective-medium theory (EMT) by Jacobsen. As all of these potentials are only repulsive, a Morse potential was added for the equilibrium region. MD simulations were performed for poly-crystalline Ti. The calculated GRID lines were found to be insensitive to the exact form of the attractive potential. The repulsive part is important, however. The estimates for the lifetime strongly depend on the interatomic potential. The lifetime obtained for the 3.261 MeV level (1.499 MeV transition) is (9.6 ± 0.5) fs with the BM, (15.9 ± 1.6) fs with the ZBL, and (18.1 ± 0.7) fs with the EMT potential. A decision on which potential is best was not drawn, however, as no accurate non-GRID value of the lifetime is reported which could be used as a reference.

Keinonen *et al.* compared three interatomic potentials using GRID measurements of KCl and NaCl, namely the universal (ZBL) potential, an interatomic potential by Gordon and Kim, and a newly developed *ab initio* potential basing on density functional theory (DFT) atomic cluster calculations [Kei 91]. In the first two cases, Coulomb forces were

additionally taken into account. The best fits of the simulated GRID lines resulted in similar estimates of the lifetime using any of the potentials. All estimates of the lifetime are further compatible with a reported value of (61 ± 4) fs from DSA measurements. Keinonen points out that "despite of the remarkable differences between the potentials similar slowing-down times (...) are obtained as total effects." He prefers the newly derived *ab initio* potential "as it is based on a minimum number of approximations and contains no adjustable parameters."

The observation of similar lifetimes from very different potentials is astonishing. It is difficult to judge today, if the calculation has been done with sufficient care. The simulation cell only contained 216 atoms. This is very small, as long-range Coulomb forces are considered, and the level lifetime is very long. The insensitivity to the potential, however, might also be related to the very long and thus unsuited lifetime of around 60 fs.

Until then, only powder samples were used. For every nuclear transition, only one Doppler broadened spectrum could be recorded. In 1992, Heinig and Janssen presented the idea to use single crystals, instead [HeiJan 92]. They predicted an orientation-dependent fine structure of the Doppler broadened energy spectra. Different GRID lines were predicted for different crystal orientations. This should allow to determine more accurate lifetimes, to make more decisive tests of interatomic potentials, and to extract both information from one GRID measurement.

As discussed in the previous chapter, the estimates of the lifetime are obtained by a χ^2 optimization during the fit of the theoretical line to the experimental data. Jentschel first proposed to use χ^2 also for the investigation of interatomic potentials [Jen 96b]. The lowest value of χ^2 is supposed to belong to the best potential among the ones under study. In his work, Jentschel compares RMD simulations using different potentials, mainly the universal (ZBL) and the Krypton-Carbon (KrC) potential. Jentschel further made first efforts to improve interatomic potentials by varying parameters [Jen 97a]. He optimized the screening length of the ZBL potential via the parameters x and y, by minimizing χ^2.

Finally, Stritt *et al.* investigated interatomic potentials in metals [Str 99b, Str 99c, Str 99a]. The slowing down was calculated by MD simulations using a large number of different potentials. Best potentials were found by only considering those potentials that yield a lifetime compatible with reported values, and comparing the remaining potentials via their χ^2. As this approach is questionable and as the evaluation still used the old fitting code `griddle`, the measurements are re-analysed within this work (see Section 9.4).

7.2   Accuracy of the statistical variable χ^2

The model line to be fitted to experimental data analytically depends on the local parameters background, centre height, and centre position. For a given set of trajectories, the dependence on the nuclear level lifetime is also analytic. For these parameters, χ^2 can be easily minimized. The estimate of the parameter and its statistical error can be directly given, as illustrated in Fig. 7.1a). As the dependence is analytic, the fitting procedure is very fast and can be followed to any precision wanted.

When optimizing potential parameters, different simulations are performed. Even if using the same series of random numbers in the MD simulation, different rounding errors occur, and the dependence of the derived GRID line on the potential parameters is not analytic. Plotting χ^2 as a function of a potential parameter, as the relative screening
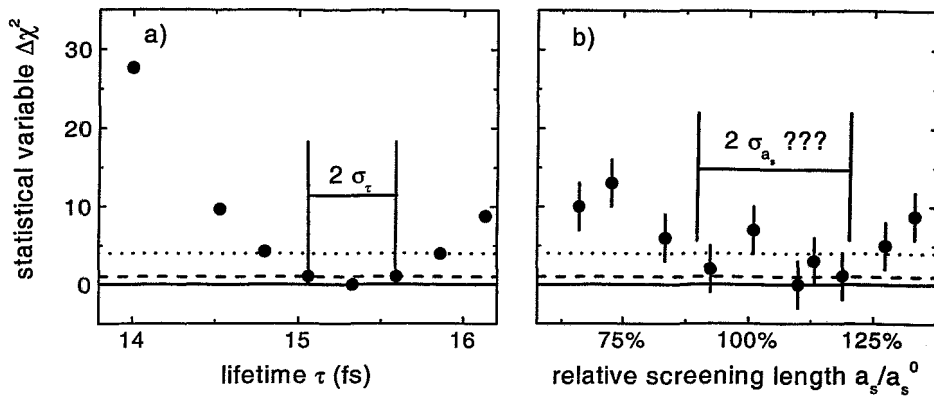
FIGURE 7.1: *Typical dependence of χ^2 on the level lifetime τ and on potential parameters. Whilst the dependence on τ easily allows to determine the best estimate and the error σ_τ, the dependence on potential parameters is less clear. It is often not easy to determine a best estimate and the standard deviation $\sigma_{p.p.}$ for potential parameters.*

length, e.g., often the dependence is not as nice as in the previous case. This is illustrated in Fig. 7.1b). The statistical variable χ^2 itself must be attributed an error, as plotted in the figure.

The influence of a potential parameter on the GRID line is partly compensated by the lifetime τ. As this latter variable is optimized for every set of potential parameters, the variation of χ^2 with a potential parameter is reduced. Sometimes, χ^2 does not significantly change its value at all, when varying one parameter within reasonable limits. In this case, the measurement was not sensitive to this parameter. By repeating the same procedure with artificial data containing more scans or higher peaks, it is possible to estimate if the Crystal-GRID measurement with this material is not sensitive at all or if the non-sensitivity is only due to an insufficient total number of counts.

The error of χ^2 itself is directly related to the accuracy of the simulated GRID lines. One MD simulation consists of a large number of independent trajectories calculated in a finite simulation cell. Two technical parameters influence the accuracy of the GRID line: the cell size and the number of calculated trajectories. In order to limit the computing time, it is necessary to chose relatively small numbers. For good accuracy, the numbers must be high.

The size of the simulation cell influences the results, as in small cells the recoiling atom can penetrate a damaged region due to the periodic boundary conditions, even though it should reach an undisturbed crystal. The number of calculated trajectories determines the statistical error of the calculated line. The less events one calculates, the more noise is present.

Convergence tests have been performed for the ZnS measurements as described in Section 9.1. The estimates of the lifetime are plotted in Fig. 7.2, the minimum values of the Poisson MLE $\chi^2_{\lambda,P}$ in Fig. 7.3. For every cell size, 6000 trajectories have been simulated (5000 for 3^3 unit cells). They have been grouped in sets of 1000, 2000, 3000, and 6000 trajectories, so that one can get an idea of the spread of the values when using different random numbers.
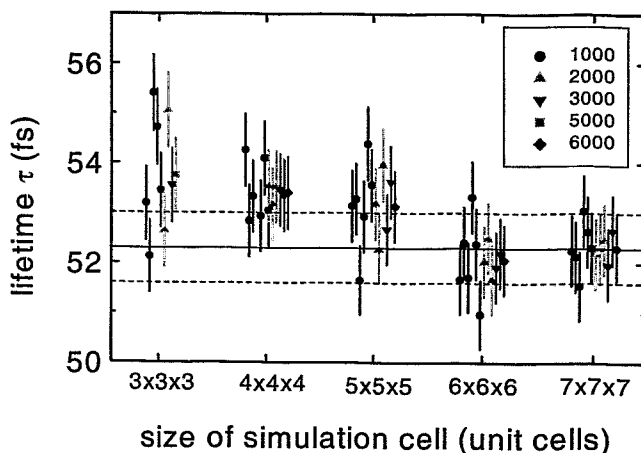
FIGURE 7.2: *Estimates for the lifetime for different sizes of the simulation cell and different numbers of trajectories. For sufficiently large cells ($\geq 6^3$), all simulations yield identical estimates within the error.*
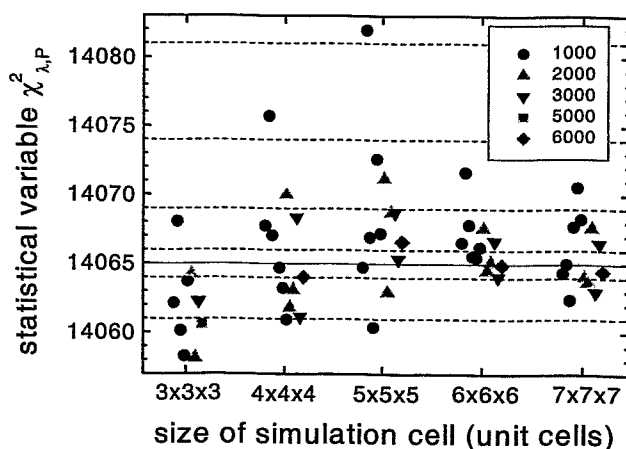
FIGURE 7.3: *Statistical variable χ^2 for different sizes of the simulation cell and different numbers of trajectories. Even in sufficiently large cells, the spread of χ^2 when calculating only 1000 or 2000 trajectories is quite large.*

As can be seen from Fig. 7.2, the estimate of the lifetime slightly drifts with increasing cell size. The two cases of 6^3 and 7^3 unit cells, yield similar results. Estimates of the lifetime from different sets of trajectories are mostly consistent within one or at maximum two standard deviations. Consequently, a cell size of 6^3 unit cells seems to be sufficient, in this case.

Looking at Fig. 7.3, the spread of the values of χ^2 seems to be more or less independent of the cell size, perhaps slightly enhanced for smaller cell sizes. However, the spread largely depends on the number of trajectories. For 1000 trajectories, the standard deviation σ_{χ^2} is about 5, even in the largest cell; for 2000 trajectories, it is still of the order of 3.

Typically, no more than 2000 trajectories are simulated for every set of parameters,

because full MD simulations take a lot of time. Consequently, an error of ± 3 should be taken as the standard deviation σ_{χ^2}. This is important, as a variation of χ^2 by 1, gives the standard deviation for the parameter under study; a variation by 4 gives the 2σ error (compare Section 6.1.4). Including the error of χ^2 itself, a cautious approach is to always state the 2σ error as the statistical error of parameters extracted from GRID measurements.

Special care is necessary when comparing different potentials, as in this case, no error can be attributed to a potential parameter. A potential should only be judged "best" if the appropriate χ^2 is significantly lower compared to the other potentials. A difference of 4 should be the absolute minimum, before making any statement.

Of course, it is possible to use more trajectories and to reduce the error of χ^2. However, also the feeding of the nuclear level and the angular correlation is often not perfectly known, and small rounding errors are present in the MD simulation as well as in the calculation of the GRID line. In order to avoid false conclusions from Crystal-GRID measurements, one should never publish decisive results, if the difference in χ^2 is very small, even if $10,000$ trajectories have been calculated.

7.3 Quality check for best potential

After determining a best potential or a best set of potential parameters, it is essential to quantitatively check the quality of this potential. This check is necessary, as it is impossible to vary all parameters of a potential and to use all imaginable functional forms when improving the potential. How can the quality be checked? Two approaches can be used: the purely statistical goodness-of-fit test and the physical lifetime criterion.

On the one hand, a goodness-of-fit test using Pearson's χ_P^2 should be performed. As discussed in Section 6.1.5, this test gives a quantitative statement about the consistency of the theoretical GRID line with the experimental data. If the goodness-of-fit estimator Q is well above 0.1%, the model is sufficiently good to describe the measured data. This does not automatically mean that the potential well describes the slowing down, but only that the actual set of measured data is sufficiently well reproduced, within the error of the experiment. Perhaps, if continuing the measurement and thereby reducing the statistical error of the data, Q decreases. If Q is below 0.1%, then the potential is very likely to be no good approximation. In this case, the potential needs to be further improved.

On the other hand, if reliable values for the lifetime have been obtained by other GRID or non-GRID measurements, a comparison of the newly derived GRID estimate with these reported values should also be performed.

This lifetime criterion has been extensively used in the past. However, it is not needed to decide on which potential is best, as the statistical variable $\chi_{\lambda,P}^2$ gives an unambiguous and doubtless result. Furthermore, reported lifetimes have large errors and are sometimes not reliable or not independent of a description of the slowing down, as in the case of Doppler shift attenuation (DSA) measurements.

If two or more GRID measurements have been performed with one nuclear level using different single crystals, the obtained estimates of the lifetime should coincide within one or two standard deviations for a good potential. If they don't, the potential probably does not well describe the slowing down. However, by no means, a potential that yields a significantly higher value of χ^2 should be preferred only because the estimates of the

lifetime coincide, in this case. Instead, it should be tried to further optimize the potential, e.g. by varying additional parameters.

If one GRID measurement is compared to reported values of the lifetime, one should be even more cautious. If the estimates, obtained with the best potential, coincide with the reported value, and the goodness-of-fit is sufficiently high, the results can be trusted within the precision of the measurement. If the values do not agree within one or two standard deviations, but the goodness-of-fit indicates good consistency, one should, on the one hand, question the reported value and the size of its error, and on the other hand, try to vary some of the potential parameters. It is possible that a potential parameter is strongly correlated with the lifetime, leaving the value of χ^2 more or less unchanged while changing the potential parameter. In this case, further measurements are needed in order to get a result, both for the interatomic potential and the nuclear level lifetime.

7.4 Which part of the potential function most influences GRID lines?

In a Crystal-GRID experiment, the velocity projections of recoiling atoms are measured via the Doppler shift of the photon energy. The trajectory, and thus the velocity, of the recoiling atom is determined by the interaction with the neighbouring atoms, i.e. by the interatomic forces or the interatomic potential. For two-body interactions, it is equivalent to say that the recoiling atom underlies a certain force, a certain potential or is located at a certain distance of one neighbour.

The nearest possible approach of the recoiling atom to a neighbour is realized in a head-on-collision. If the neighbour atom was fixed at its lattice position, this nearest approach would be given by the distance corresponding to the recoiling atom's initial kinetic energy E_{kin}^0 (typically several hundreds of eV) minus the small binding energy (about 5 eV). The approaching atom repels its neighbour, however, so that some of the energy is transferred to kinetic energy of the neighbour.

As shown in Fig. 7.4, the maximum potential energy is reduced by a factor of 2, approximately, in the case of Si where the two colliding particles have almost equal masses. The figure shows the interatomic BM-SW potential, the theoretical nearest approach corresponding to three different initial kinetic energies, and the true nearest approaches obtained by simulating a head-on-collision. It can be concluded that the part of the potential energy function above this critical value does not influence the resulting GRID line, and is not tested by the Crystal-GRID method.

Most of the time, the recoiling atom moves at "large" distances to its neighbours. The forces exerted by its neighbours are small, and the trajectories are only little altered. The recoiling atom is influenced by the low-energy part of the potential curve. Due to the high initial recoil energy, the moving atom can approach other atoms up to relatively small distances in central collisions. In this case, the velocity is heavily changed. Admittedly, only few recoiling atoms undergo (almost) central collisions. The influence of the high-energy part of the potential is very strong, but occurs rarely.

The interaction of the recoiling atom with one lattice atom is no simple two-body interaction, however. The lattice atom is coupled to its (first) neighbours via the equilibrium part of the potential. This can be regarded as an *effective mass effect* and represents
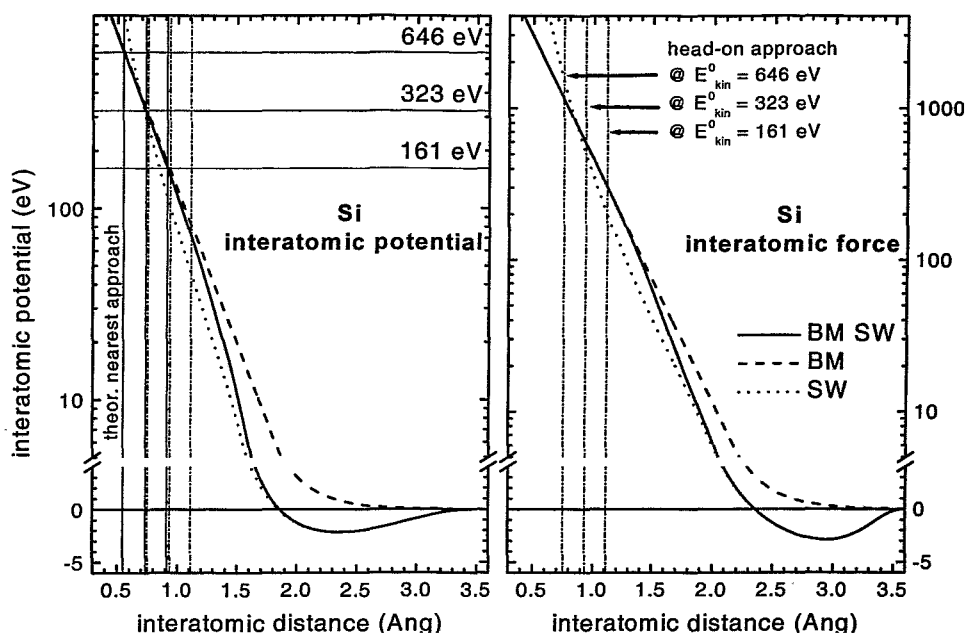
FIGURE 7.4: *Interatomic potential and force in Si. The Born-Mayer (BM) force (dashed line) is switched over to the Stillinger-Weber (SW) force (dotted line). The combined BM-SW potential is obtained by integrating the combined force. The straight horizontal lines give three different initial kinetic energies E^0_{kin}. The intersection with the potential curve determines the theoretically nearest approach. As the colliding atom is not fixed at its lattice position, the true nearest approach, obtained in a head-on-collision, is significantly smaller. The distances are indicated by dash-dotted lines for the three initial energies. Only the potential curve to the right of these true nearest approaches is tested by the measurements.*

a second order contribution. This interaction is neglected in the RMD calculation, but automatically taken into account in a full MD calculation.

After some time, the recoiling atom is slowed down to quasi-thermal velocities. Especially for long lifetimes, many recoiling atoms reach this regime. Now again, the dynamics is determined by the low-energy part of the potential.

The equilibrium parts of interatomic potentials, especially when also including many-body interactions as in the case of ZnS (Stillinger-Weber potential), are often optimized for one crystal structure. In this case, the applicability of this potential to the low-energy interactions between the recoiling atom and the lattice atoms is doubtful. At the beginning, the recoiling atom is quickly moving through the crystal. It can *not* be found on a lattice site where the potential yields a correct description. Later, in the thermal regime, at least some of the recoiling atoms are located at interstitial positions, i.e. at shorter distances to their first neighbours than expected by the potential. In this case, the potential will lead to a relaxation. However, one should be cautious about conclusions to be drawn, as the potential is only valid for the perfect crystal structure.

Chapter 8

Results on the basis of artificial data

Due to the low experimental yield, methodical studies for Crystal-GRID were not possible or very difficult to perform until this work. Precise knowledge about methodical topics was often replaced by assumptions from hand-waving arguments. The use of artificial data finally allows to address these studies. In Section 8.1, several assumptions about the sensitivity of Crystal-GRID measurements are analysed that largely influence the way of how Crystal-GRID measurements are performed. The analysis is performed for GaP, where nicely structured lines are obtained. However, the main conclusions can be transferred to other materials. The question whether angular correlation has a significant influence on experimental results will be discussed in Section 8.2.

The last section will be dedicated to a comparison of the different descriptions of the slowing down, mainly MD and RMD simulations. Furthermore, the use of artificial data finally allows to compare predictions from the MFPA theory to the less approximate predictions from MD simulations, fundamentally clarifying the inadequacy of the MFPA for a general description of the slowing down.

8.1 Sensitivity of Crystal-GRID to the nuclear level lifetime and to potential parameters

8.1.1 Influence of separation into scans

Due to the slight drift of the spectrometer, GRID measurements are separated into many scans. An upper limit for the measuring duration of a single scan is given by the drift stability, a lower limit by the necessity to have a sufficient number of counts per scan in order to correctly fit the centre positions.

In order to check whether the error of fitted parameters depends on the number of scans into which the total measuring time is subdivided, artificial data have been generated for GaP with different centre heights[1] I_c (10, 30, 60, 100, 300, 600, 1000, 3000). The background I_{bg} was chosen to be 10% of the centre height I_c. The model line has been fitted to the artificial data, in order to determine an estimate for the lifetime τ and its error σ_τ. The result is displayed in Fig. 8.1. For different summed centre heights, it can

---

[1]The centre height refers to the <100> orientation. Lines for other orientations have been normalized so that they correspond to an identical measuring time.

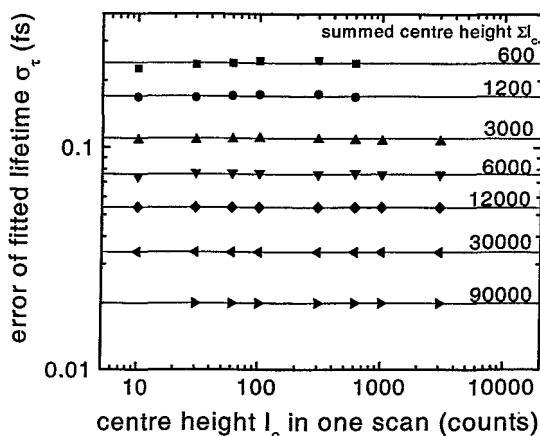FIGURE 8.1: *Error σ_τ of the fitted lifetime. The error σ_τ does not depend on the number of scans into which the total measuring time is subdivided. For a summed centre height of 600 counts, e.g., calculations have been performed using 60 scans with $I_c = 10$, 20 with $I_c = 30$, and so on. The plotted results have been obtained for single crystals oriented in <111> direction. Similar results are obtained for other orientations or with a powder sample.*

be shown that σ_τ does not depend on the number of scans into which the total measuring time is subdivided.

A single scan consists of many measuring points, typically 60 to 100. Keeping the total measuring time for a single scan constant, it could be further shown that the number of measuring points within a scan does not significantly influence the result, as long as the number is sufficiently high to correctly determine the centre positions of the lines. For this investigation, artificial data have been used for three different orientations of single crystalline samples, going from 200 measuring points ($I_c = 10$, $I_{bg} = 1$) to 10 points ($I_c = 200$, $I_{bg} = 20$). In the case of only 10 measuring points, convergence could not be obtained. However 25 points turned out to be sufficient. The correct lifetime is always found within the standard deviation σ_τ. The standard deviation σ_τ slightly increases with decreasing number of measuring points. In this case, an increase by about 3% from 200 to 25 measuring points was observed.

The standard deviation σ_τ turned out to be proportional to the square root of the total number of counts which itself is proportional to $\sum I_c$ for a constant number of measuring points (see Fig. 8.2)

$$\sigma_\tau \sim \sqrt{\sum I_c} \qquad (8.1)$$

The variance σ^2 of a number of counts always equals the (model) number of counts c in a counting experiment. Consequently, the above result is not surprising. It shows, however, that the basic proportionality $\sigma^2 \sim c$ is also valid for the error of the lifetime, even though the calculation of GRID lines uses MD simulations.
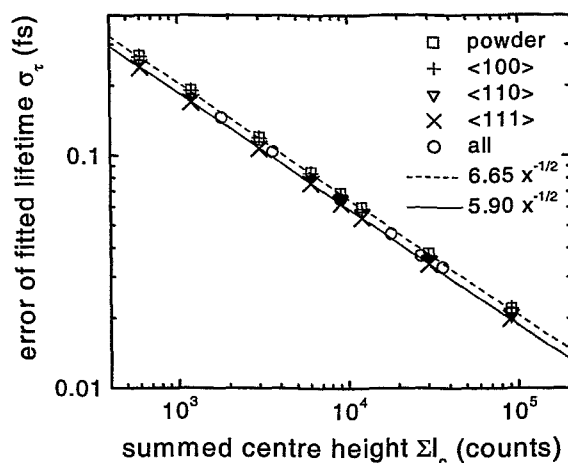
FIGURE 8.2: *Error σ_τ of the fitted lifetime. The error σ_τ depends on the total number of measured counts. Different orientations of the sample crystals yield errors that differ by only 10%, approximately. A powder sample is nearly as well suited as a crystal. Combining different orientations does not improve the statistical error of the lifetime.*

8.1.2   Determination of level lifetime

Comparing different sample orientations, it is found that the error *of the lifetime* — for a given interatomic potential — only slightly depends on the orientation of the sample. As can be seen in Fig. 8.2, the error obtained by fitting data of the <111> orientation is slightly lower than for other orientations; the difference between best and worst case is about 10%. Furthermore, using a powder sample, the standard deviation is of the same size as when using a single crystal. The general assumption that combining measurements of different crystal orientations ("all" in the figure) would reduce this error, could not be verified.

The error σ_τ depends on the value of the level lifetime, as the lifetime drastically influences the fine structure of a GRID line (compare Section 5.2). Artificial GaP data for different values of the true level lifetime have been evaluated. The obtained errors σ_τ are plotted in Fig. 8.3. In this case, the optimal lifetime lies around 20 fs. The dependence of the relative error σ_τ/τ^0 on τ^0 is almost similar for the three different crystal orientations. Only for the powder sample, σ_τ varies more strongly with the true value τ^0 of the lifetime.

Consequently, for a given system, artificial data can be used to calculate which crystal orientation is best and to estimate the expected statistical uncertainty as a function of the total number of counts.

8.1.3   Determination of potential parameters

What about the potential parameters? Using 30 artificial scans for GaP with a centre height of 100 counts on a background of 10 counts, the screening length a_s has been fitted. The results are shown in Fig. 8.4 for artificial data belonging to true values of the level lifetime of 8 fs (a-b) and 20 fs (c-d), respectively. Similar results are obtained with 150 scans with a centre height of 20 counts on a background of 2 counts.
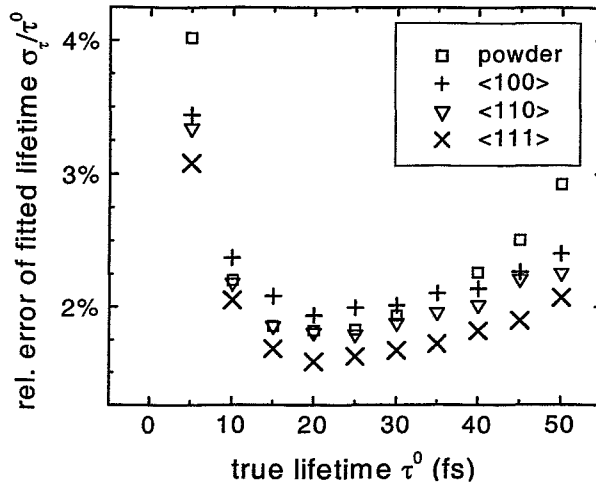
FIGURE 8.3: *Relative error σ_τ/τ^0 of fitted lifetime for different sets of artificial GaP data. In this case, the smallest error can be obtained for a true lifetime τ^0 of 20 fs. The error increases especially for very small lifetimes. The three single-crystalline samples show a similar behaviour. The dependence of σ_τ on the true lifetime is stronger in the case of a powder sample.*

As can be seen in Fig. 8.4a) and 8.4c), single-crystalline samples are much more sensitive to the screening length than a powder sample in which case χ^2 hardly changes at all when varying a_s. The sensitivity depends on the sample crystal orientation. This is related to the fine structure of the lines which depends on the orientation (compare Section 5.2). The best sensitivity, i.e. the smallest error is obtained for the asymmetric <111> orientation.

For the first time, it could be shown that the asymmetry by itself improves the sensitivity. For that purpose, the <111> GRID line has been symmetrized, and artificial data have been generated for both, the original <111> orientation and this so-called <111>* orientation. As obvious from Fig. 8.4a) and 8.4c), the sensitivity is drastically reduced for the symmetrized line.

Contrary to expectations prior to this work, the sensitivity is *not* improved by combining measurements with different crystal orientations. The size of the error σ_τ is similar to the error obtained when measuring one crystal orientation the whole time (compare Section 9.2).

A second prediction could also *not* be verified. It was assumed that only with the correct potential, the lifetime estimates obtained from the measurement of different orientations should coincide. If the estimates did not agree, the potential would not be suited and it could be excluded. As can be seen in Fig. 8.4b) and 8.4d), the lifetime estimates do not differ strongly from each other when varying the screening length within a wide range. A difference of two standard deviations is not sufficient to exclude a set of potential parameters. As discussed in Section 7.3, this additional criterion is not necessary, as the best set of potential parameters also yields the lowest value of χ^2.
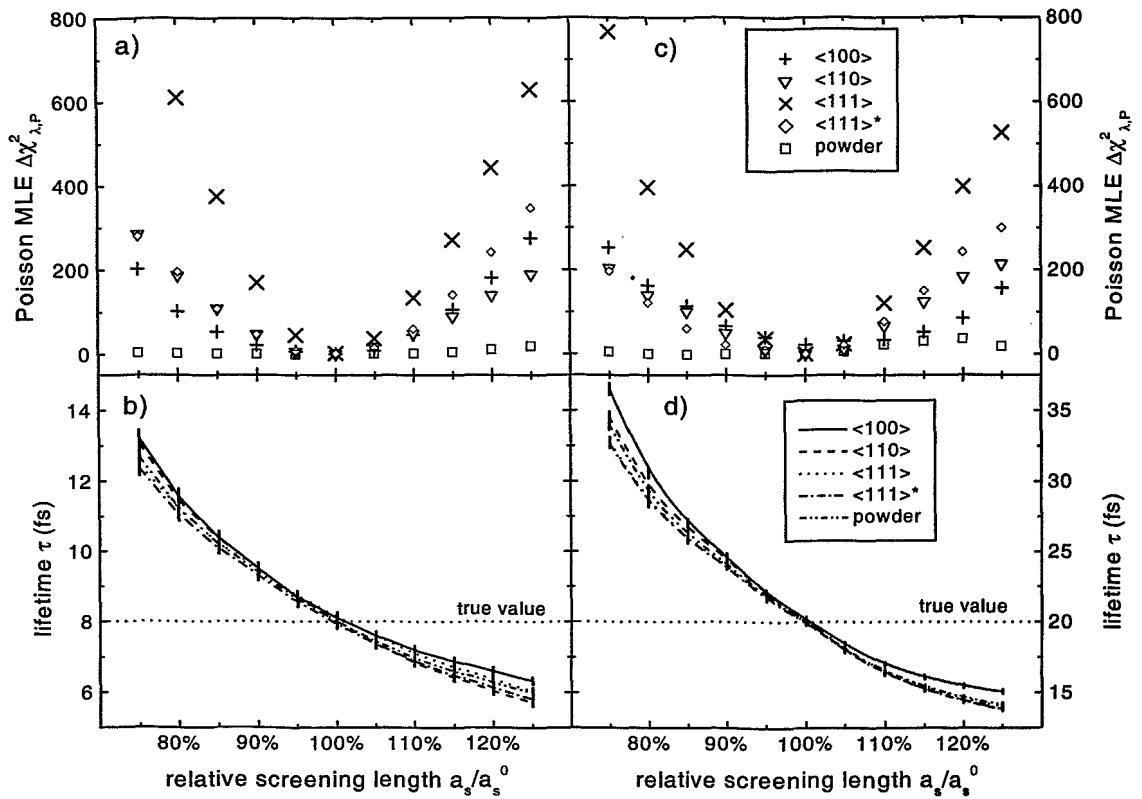
FIGURE 8.4: *Optimization of screening length for artificial GaP data with a true level lifetime of 8 fs (a+b) and 20 fs (c+d). The sensitivity to the screening length depends on the orientation of the sample (<111>* refers to a symmetrized <111> Crystal-GRID line). Different orientations yield lifetime estimates that do not differ a lot. Consequently, potential parameters can not be excluded due to inconsistent estimates from different measurements.*

8.2　Importance of angular correlation

The angular correlation function can only be calculated if the nuclear spin states of the cascade under study are known. Otherwise, the unknown coefficients have to be fitted during the GRID evaluation. However, this enlarges the number of free parameters and thus the needed accuracy of the measurement. For that reason, it would be nice if angular correlation could be neglected when calculating GRID lines.

Jolie states that angular correlation is only important for "very short lifetimes" [Jol 92, p. 32]. After some collisions, the correlation of the recoiling atom's initial direction with the actual direction of motion is lost, and the γ–γ correlation washes out. Fig. 8.5 shows Crystal-GRID lines of the 4.934 MeV transition[2] in ^{29}Si for the <100> crystal orientation. For every value of the lifetime τ, two lines have been calculated, correctly taking into account the angular correlation, and neglecting its influence, respectively. For the short lifetime of 5 fs, the two lines differ strongly. The difference decreases with increasing τ. However, even for a comparatively long lifetime of 35 fs, the theoretical lines differ

---

[2] This transition has been studied experimentally within this work (compare Section 9.2).
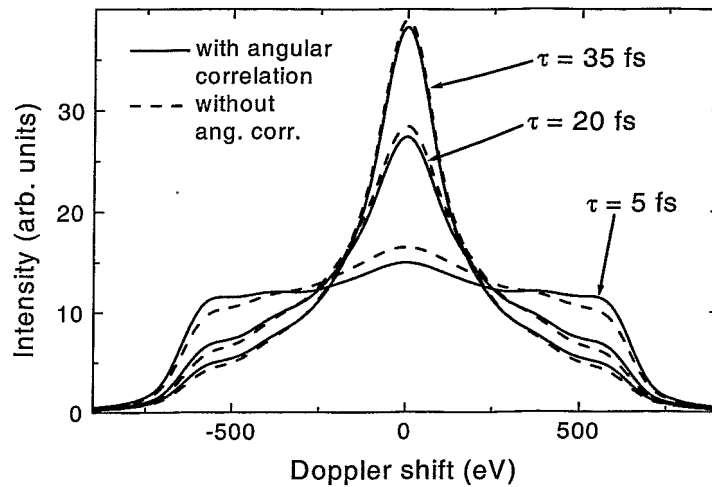
FIGURE 8.5: *Crystal-GRID lines of the 4.934 MeV transition in ^{29}Si calculated for different values of the lifetime τ. For each value, two lines are plotted, one taking the angular correlation into account, one neglecting it. Even for relatively long lifetimes, the lines are not identical (calculation with KrC potential, <100> orientation, $\sigma_{ew} = 0.172$ fringes, diffraction order (1/2)).*
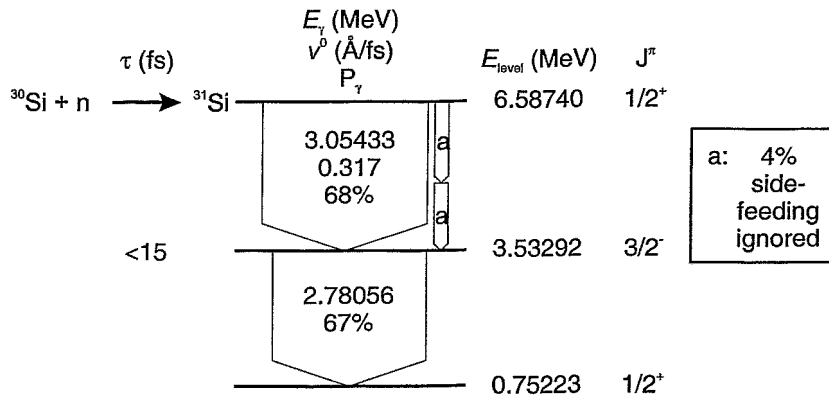
FIGURE 8.6: *Deexcitation cascade in ^{31}Si [Ram 92]. For each level of energy E_{level}, the reported lifetime τ [End 90] and the spin parity J^{π} are given. For the transitions, the photon energy E_{γ}, the corresponding initial recoil velocity v^0 of the Si nucleus, and the absolute intensity P_{γ} of the transition are indicated (% refers to the number of neutrons captured). Only the main feeding is used in the calculations.*

significantly.

In order to get an idea of how experimental results are influenced if angular correlation is neglected, artificial data have been generated for the 2.781 MeV transition in ^{31}Si. The corresponding decay cascade is shown in Fig. 8.6, the angular correlation of the two photons is given by the factor $W'(\cos\phi) \sim 1 + \frac{1}{8}\left[3\left(\cos\phi\right)^2 - 1\right]$.

Data have been generated for single crystals in <111> orientation and for a powder sample at six different values of the lifetime, namely, 5 fs, 10 fs, 15 fs, 20 fs, 30 fs, and 40 fs. The background I_{bg} has been set to 30 counts, the total number I_{tot} of diffracted photons
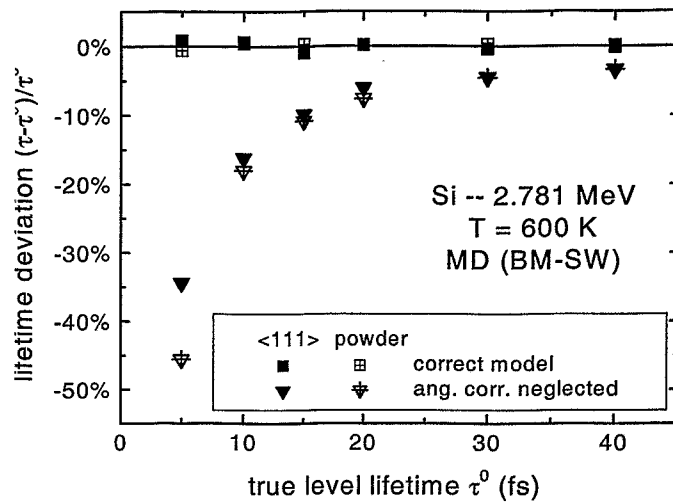
FIGURE 8.7: *Deviation of the fitted lifetime τ from the true value τ^0 if angular correlation is neglected in the evaluation. Both, for powder and single crystals, the simulation neglecting angular correlation underestimates the nuclear level lifetimes significantly. Even for relatively long lifetimes, the deviation is still around 5%.*

to 900, corresponding to a centre height I_c in between 90 and 230 counts, depending on the lifetime[3].

The GRID lines have been derived from an MD calculation using a combined BM-SW potential; the switching between the two forces is performed by the power-switch function with parameters $r_0 = 1.6$ Å, and $\xi = 12$ (compare Fig. 7.4). The simulation cell contained 6^3 unit cells, i.e. 1728 atoms.

Fig. 8.7 shows the estimates of the nuclear level lifetime obtained when fitting theoretical GRID lines to these artificial data. While the correct values are reproduced within the error when taking the correct model, the estimates become drastically wrong if neglecting the angular correlation. As expected, the largest deviation is observed for the shortest lifetime. Until this work, it was commonly assumed that angular correlation is of no importance above 15 fs. As can be seen, the estimate of the lifetime is wrong by about 10% at $\tau = 15$ fs. Even for $\tau = 30$ fs, the error is still of the order of 5%. At least in this cascade, angular correlation can not be neglected even for longer lifetimes. Yet, the result is not general, as the strength of the angular correlation depends on the nuclear spin states.

A 5% error for longer lifetimes may be regarded as very small compared to other sources of errors in nuclear level lifetime measurements. However, on the one hand, it must be included in the error given for the lifetime. And on the other hand, for Crystal-GRID measurements with the aim of improving interatomic potentials, it is necessary to describe the GRID lines as well as possible. The neglect of the angular correlation may partly compensate the weak influence of the interatomic potential and thereby lead to incorrectly determined potential parameters.

---

[3]The Crystal-GRID lines for the <111> orientation are displayed in Figure 8.8.

8.3 Comparing different descriptions of the slowing down

8.3.1 MD versus RMD

As discussed in Section 4.2, MD simulations are very time-consuming. A significant gain in time can be obtained by performing restricted MD (RMD) calculations where only the interactions of the recoiling atom with its neighbours are considered. Until this work, it could not be finally shown if this approximation is justified or if it alters the outcome of a GRID experiment.

In full MD calculations, all atoms are stabilized at their lattice positions by the interaction with their further neighbours. In a head-on-collision, e.g., the impinging atom is strongly slowed down. In the case of equal masses of the collision partners, the kinetic energy is maximally transferred. The recoiling atom occupies the lattice site of its neighbour which itself starts moving through the lattice. The observed Doppler shift (almost) vanishes.

In RMD calculations, the first neighbour only underlies the interaction with the recoiling atom itself. It is repelled without having a restoring force. Consequently, the scattering leads to a stronger acceleration of the neighbour and a weaker deceleration of the recoiling atom. Furthermore, once the scattered atom has left the interaction sphere of the recoiling atom, it can move freely through the crystal without being slowed down by any further neighbour. The initially recoiling atom continuous moving through the lattice which now has one vacancy but is perfect otherwise. In a full MD calculation the scattered atom would be slowed down by the further neighbours, entailing a cascade and thus a significantly changed crystal arrangement.

Furthermore, using the same full potential in RMD simulations, as would be used in full MD calculations, including an equilibrium part, Jentschel observed that the recoiling Cl atom in NaCl attracts the neighbouring Na atoms and pulls them through the crystal (unpublished). This phenomenon that could be called "vacuum-cleaner effect", occurs due to the long-range attractive forces in ionic crystals. Of course, this behaviour is far from being real and only related to the neglected interactions among the sample atoms. This effect is not observed in Si where the attractive forces are short-range.

In full MD calculations, the equilibrium part of a potential is essential in order to keep the crystal structure in the simulation cell stable. In RMD calculations, no interactions between the sample atoms are taken into account, and therefore, Jentschel decided to apply only purely repulsive potentials in RMD simulations. Besides the enormous gain in computer time, this presents a second appealing advantage. The universal (ZBL) potential only depends on the atomic charge numbers Z of the atoms involved and can thus be used to simulate Crystal-GRID lines in any material. It would not be necessary to look for adapted equilibrium potentials which differ from material to material.

In this case, however, an inverse effect has been observed within this work. After reaching quasi-thermal velocities, all neighbours are repelled due to the missing attractive part of the potential. In simulations for ZnS, no neighbours are left in the neighbour shell of the recoiling atom after about 100 fs, the recoiling atom moves freely.

A purely repulsive potential seemed to be sufficient to describe the slowing down of the recoiling atom. However, it must be emphasized that the interatomic potential differs

for energies below 100 eV, approximately. This can be seen in Fig. 7.4 in the case of Si.

Within this work, comparative investigations have been performed for the 2.781 MeV transition in ^{31}Si. For this transition, GRID lines have been derived from three different simulations: a full MD calculation with the combined BM-SW potential, an RMD calculation with the same potential, and an RMD calculation with the purely repulsive BM potential. In order to study the influence of the initial recoil energy, further simulations use the same decay cascade, but with the initial kinetic energy of the recoiling atom enhanced by a factor of 2 and 4, respectively.

The derived GRID lines for six values of the level lifetime are plotted in Fig. 8.8–8.10. What can be seen? The three different approaches yield quite similar lines. However, some obvious differences exist. The different lines for the short lifetimes (5 fs and 10 fs) disagree in many details. For longer lifetimes, the central peak becomes more and more dominant, and the main difference between the three approaches becomes obvious in the height of this central peak. The RMD simulation using the combined BM-SW potential always yields a central peak that is lower than the peak derived from the full MD calculation. The RMD simulation using only the BM potential slightly overestimates the height of the central peak.

In the case of a low initial kinetic energy (Fig. 8.8), some BM (RMD) lines coincide almost exactly with the full MD ones. Also for the highest kinetic energy (Fig. 8.10), the consistency with the correct MD lines is generally better compared to the lines derived from the BM-SW (RMD) simulations. Only for the intermediate energy (Fig. 8.9), this is not the case.

The average velocities calculated from the different simulations are plotted in Fig. 8.11, the distribution of velocities in the case of a full MD calculation ($E_{\text{kin}}^0 = 161$ eV) is illustrated in Fig. 8.12. The interaction of a recoiling atom with its first neighbour, located at 2.4 Å from the initial lattice site, e.g., entails a decrease of the average velocity. Most atoms are only slightly slowed down, as they pass far from the neighbour's lattice site. However, some of them undergo a strong collision, their velocity drops quickly (see Fig. 8.12).

In the case of NaCl, Jentschel had found that MD and RMD calculations show a similar time-dependence of the average velocity of recoiling Cl atoms in NaCl down to velocities of about 0.02 Å/fs, neglecting the equilibrium part of the potential in the RMD approach [Jen 97a, Jen 00].

The actual investigation shows that for high velocities, i.e. high kinetic energies, the average velocities in the three approaches are very similar. The approximations of the RMD approach only little influence the slowing down (see Fig. 8.11c), $t < 20$ fs).

For later times ($t < 100$ fs), the average velocity obtained from RMD simulations with the BM-SW potential is systematically too high, leading to the underestimated height of the central peak in the GRID lines. Using the purely repulsive BM potential in the RMD simulation, the average velocity comes closer to the result of the full MD calculation up to 100 fs, approximately. The approximations of the RMD approach are partly compensated by the more repulsive potential (compare Fig. 7.4). Depending on which influence is more pronounced, the average velocity is sometimes higher and sometimes lower than the full MD average velocity. A good equilibration is reached in the last case (Fig. 8.11c), the average velocity is always too small in the second case (Fig. 8.11b), it oscillates around the MD average velocity in the first case (Fig. 8.11a). The two effects are of varying
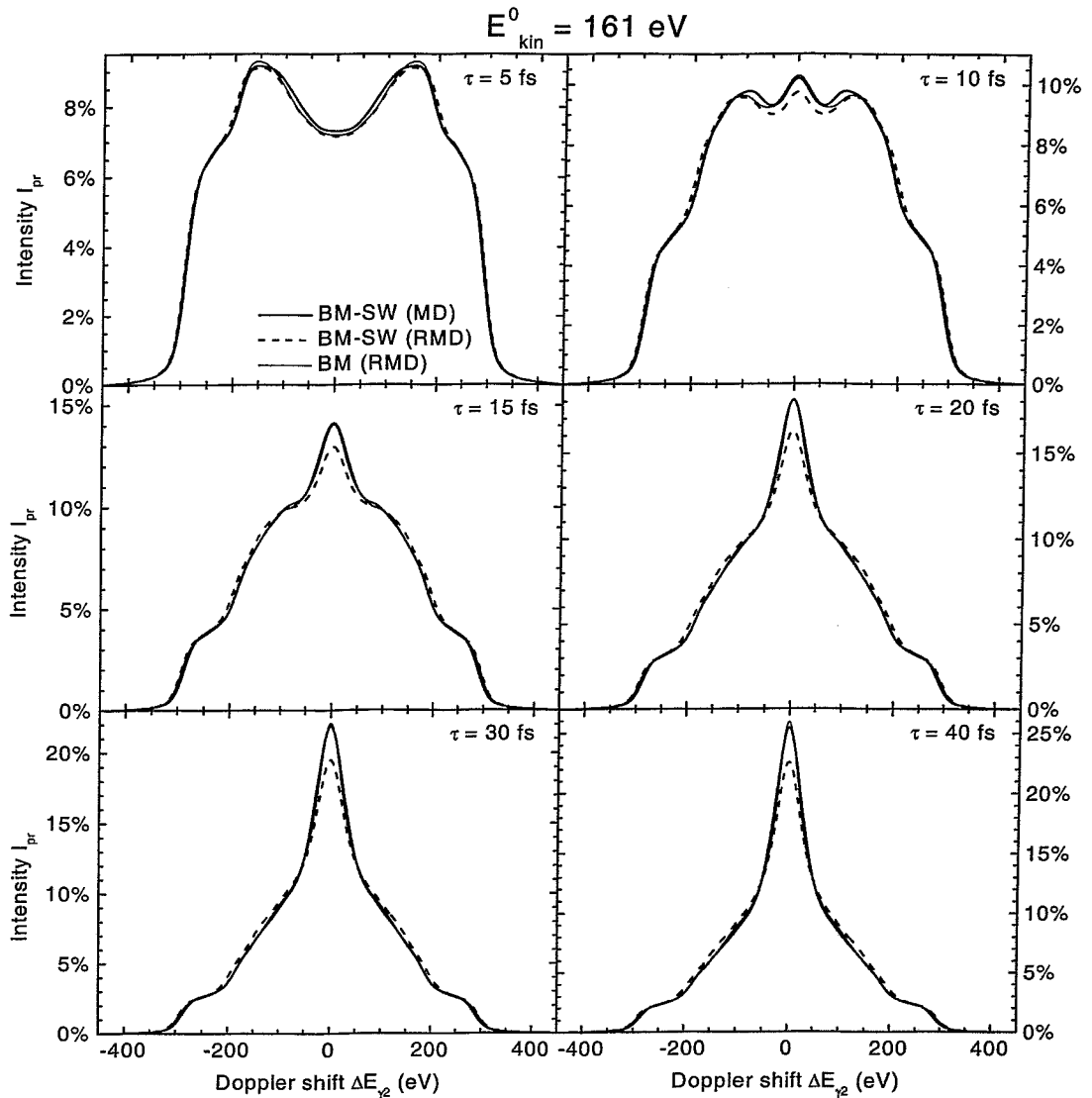
FIGURE 8.8: *Theoretical Crystal-GRID lines for the* 2.781 MeV *transition in* [31]Si *for the* <111> *crystal orientation. Angular correlation is taken into account, side feeding disregarded. The lines are plotted for different values of the lifetime and using three different simulations.*

importance. Consequently, a general conclusion about the influence on GRID lines is not possible.

For times $t > 100$ fs, the RMD simulation using the BM potential results in too small average velocities, the central peaks of the derived GRID lines is too high. However, only few atoms decay at very late times, and thus, the influence on the GRID lines is not very pronounced.

In order to estimate the influence on parameters to be determined, the derived GRID lines from the three approaches are fitted to artificial data that have been generated on the basis of the full MD calculation (compare previous section). The resulting deviations
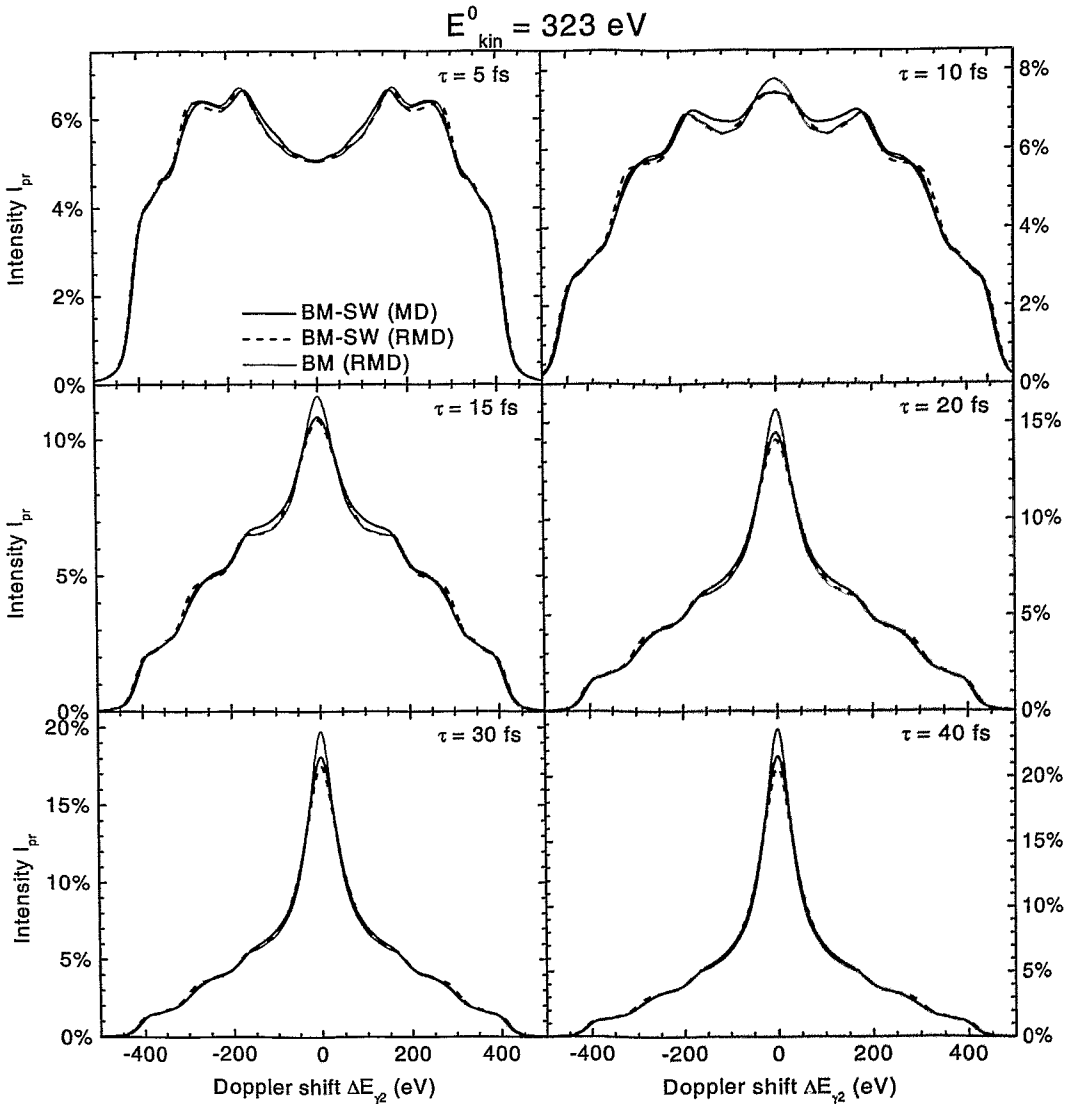
FIGURE 8.9: *Theoretical Crystal-GRID lines for the* 2.781 MeV *transition in* ^{31}Si *with enhanced initial kinetic energy* $E^0_{kin} = 323$ eV *for the* <111> *crystal orientation. Angular correlation is taken into account, side feeding disregarded. The lines are plotted for different values of the lifetime and using three different simulations.*

of the lifetime estimates τ from the true values of the lifetime τ^0, used when generating the artificial data, are shown in Fig. 8.13.

As expected, the full MD calculation reproduces the true values τ^0 quite well, both using a powder sample and an oriented single crystal. The small deviations are related to the error of fitting the local parameters of the single scans, as discussed in Section 6.5. The RMD simulation using the combined BM-SW potential overestimates the lifetime. The deviation becomes generally bigger, the longer the true lifetime is, and reaches values of 10% to 20% (see Fig. 8.13a) and 8.13c)).
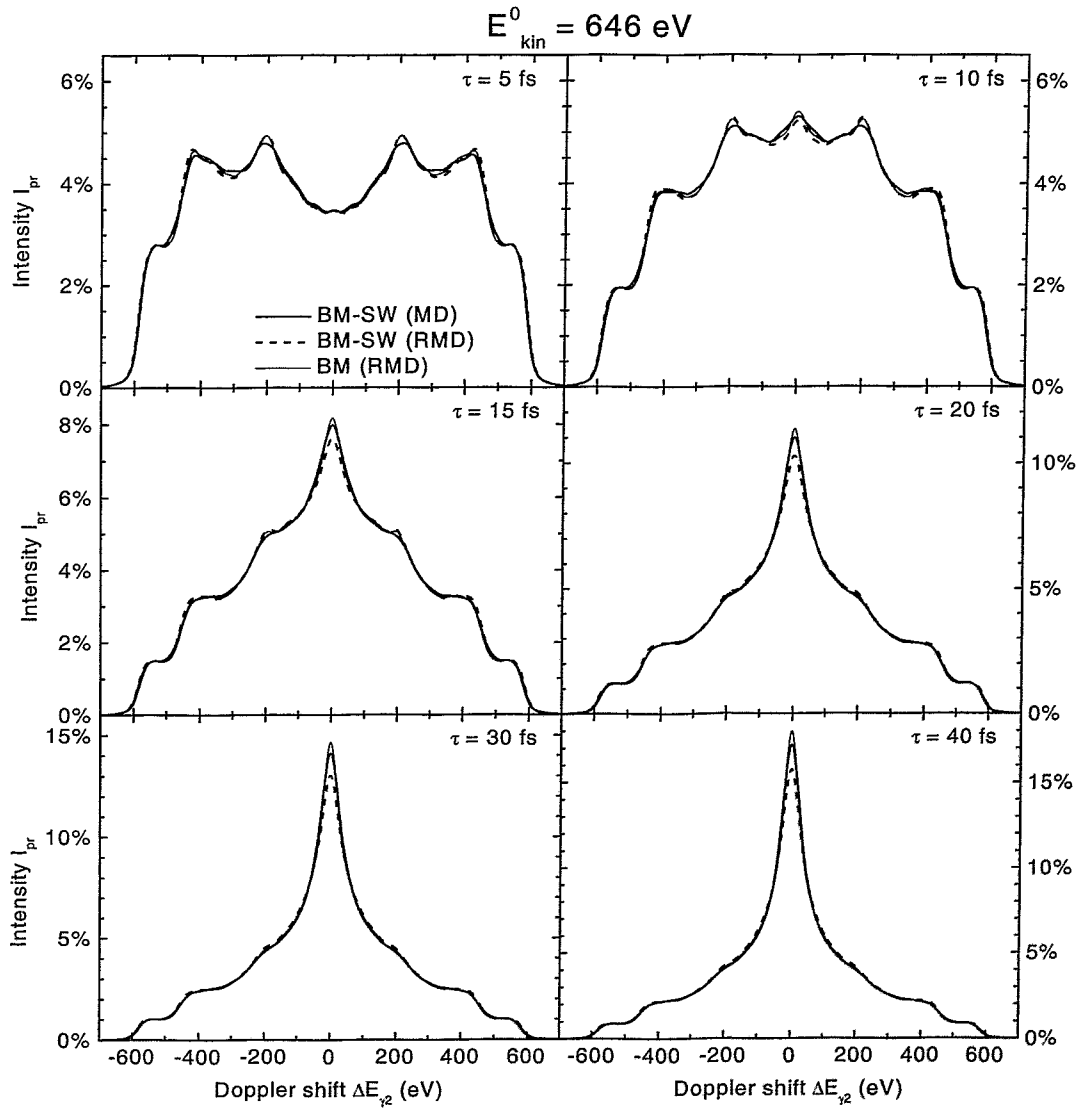
FIGURE 8.10: *Theoretical Crystal-GRID lines for the* 2.781 MeV *transition in* [31]Si *with enhanced initial kinetic energy* $E_{kin}^0 = 646$ eV *for the* <111> *crystal orientation. Angular correlation is taken into account, side feeding disregarded. The lines are plotted for different values of the lifetime and using three different simulations.*

The RMD calculation using the BM potential mostly yields estimates that are wrong by less than 3%. Only for $\tau^0 = 5$ fs in the first, and for $\tau^0 \geq 30$ fs in the second case, the deviations are larger (5% to 7%). The observed deviations quantify the differences in the GRID lines.

This work mainly focuses on semiconductors, and consequently, Si has been chosen for the investigation. Similar studies can be easily performed for any solid of interest. However, basing on the above results, some general conclusions can be drawn for GRID
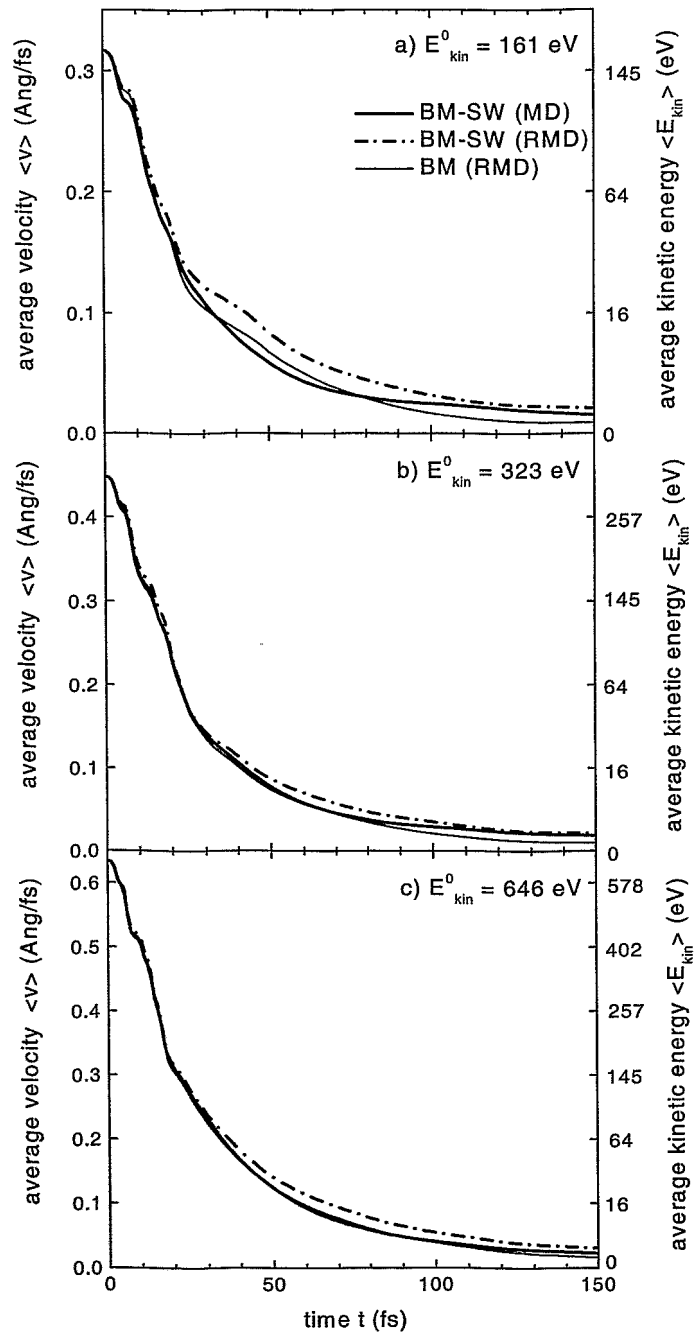
FIGURE 8.11: *Average velocity* $\langle v \rangle$ *of the recoiling atoms as a function of the time t for three different initial kinetic energies* E_{kin}^0. *The three curves are calculated from MD and RMD simulations, respectively, using the combined BM-SW or the purely repulsive BM potential. The average is based on 2000 trajectories.*
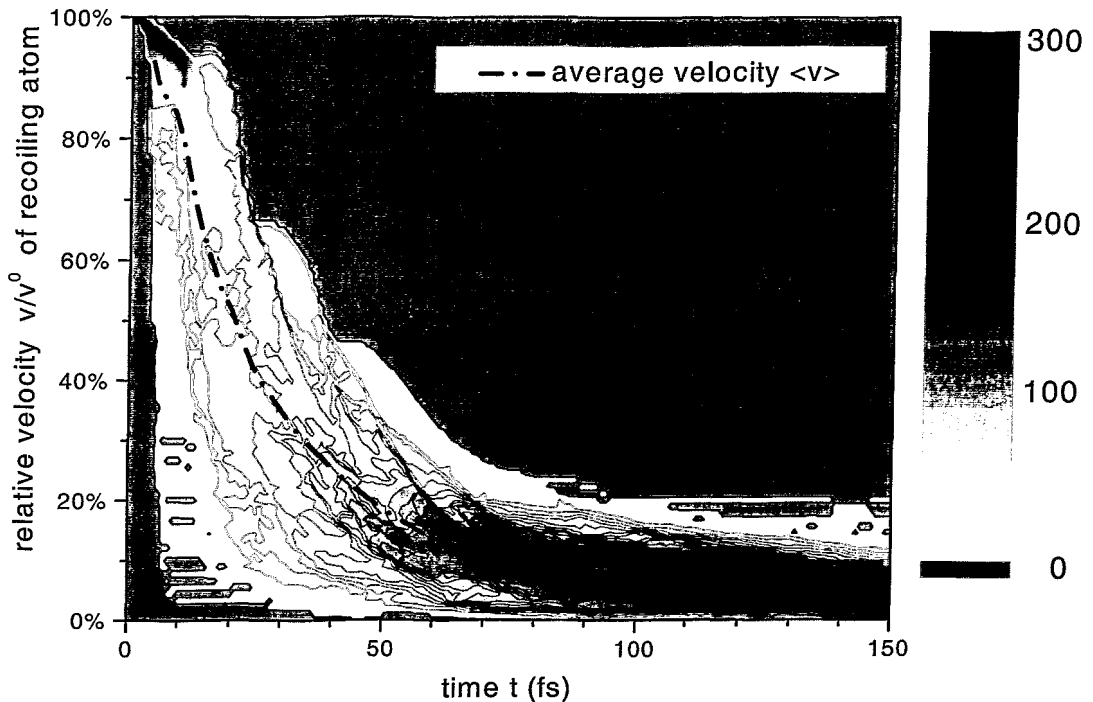
FIGURE 8.12: *Velocity distribution of* 2000 *recoiling atoms starting with an initial kinetic energy* $E^0_{kin} = 161$ eV *(black=many atoms, white=few atoms). The recoiling atoms that move in the direction of their first neighbour undergo a first collision after a few fs. The head-on collision leads to a drastic reduction of the recoiling atom's velocity. Most atoms, however, pass the first neighbour shell with almost unchanged velocity (black spot in the upper left corner). As they are focused by the first neighbours in the direction of the second neighbours, most of them undergo a strong collision at the second shell. Further collisions can be recognized in the velocity distribution. After about* 100 fs, *most atoms reach quasi-thermal velocities.*

and Crystal-GRID measurements. When performing GRID measurements with the aim of determining nuclear level lifetimes, only one simulation with a well-suited interatomic potential needs to be performed. If an adapted interatomic potential is reported in the literature, it is absolutely possible to perform a full MD calculation avoiding additional errors. Otherwise, RMD simulations using a purely repulsive potential, as the ZBL potential, seem to quite well reproduce the GRID lines and lifetime values, at least for lifetimes up to 20 fs or 30 fs. A 5% error is acceptable for the determination of nuclear level lifetimes. RMD calculations should, however, not be performed using the full potential, as this approach may lead to big errors, as seen for Si.

When performing Crystal-GRID measurements with the aim of improving interatomic potentials, many simulations are needed. RMD calculations would be of big advantage. As seen before, RMD simulations with the full potential may yield errors of up to 20% for the lifetime, and would consequently yield errors for potential parameters to be determined. Whether they are better suited for other crystals, as metals, e.g., it can be checked by a similar investigation using artificial data.

When neglecting the equilibrium part and using a purely repulsive potential in RMD
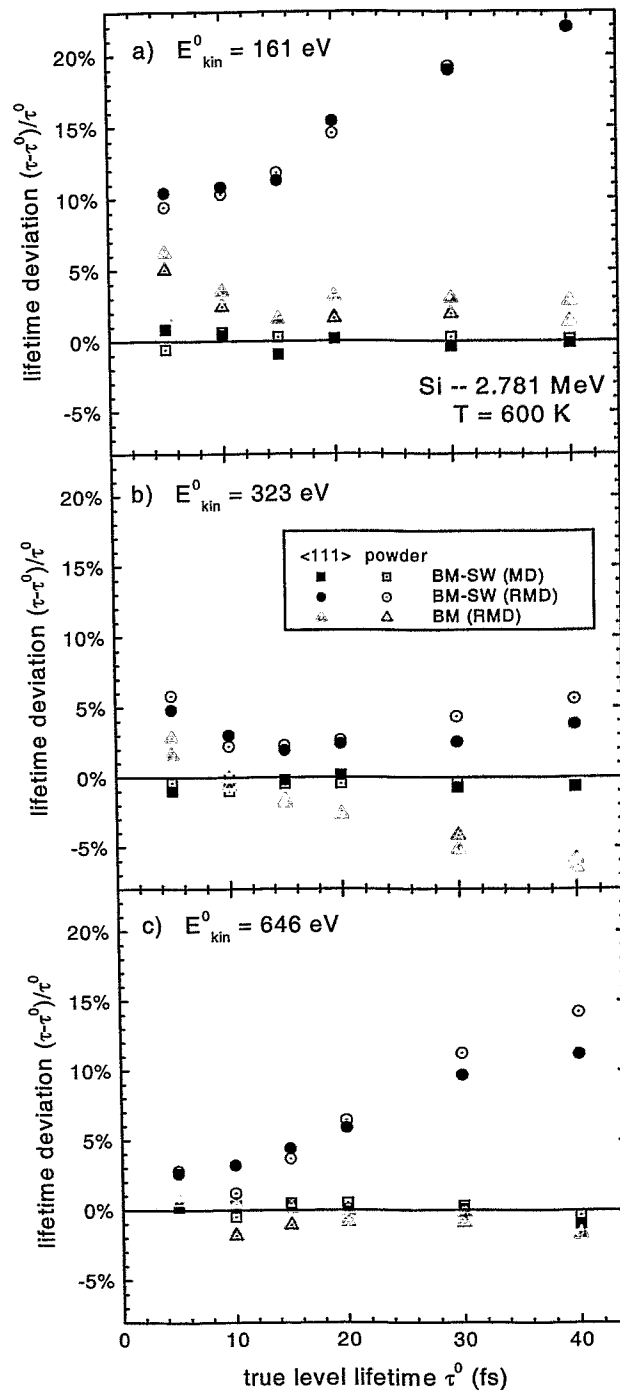
FIGURE 8.13: *Deviation of fitted lifetime τ from true lifetime τ^0 for different sets of artificial data. Simulations have been performed at 600 K, using the BM-SW potential (MD and RMD) as well as the purely repulsive BM potential (RMD). A similar investigation at 0 K comes to identical results.*

simulations, instead, the error of the simulation itself is partly compensated by a more repulsive potential. As it is the aim to learn more about the interatomic potential, however, this compensation is clearly undesired. Reported potentials are quite good already, and only small corrections to some parameters are needed. Consequently, if one wants to further improve a potential, it is absolutely necessary to perform full MD calculations.

There is one exception. Interatomic potentials are improved for computer simulations. If the improved potential is to be used in an RMD calculation in the same energy range, it may be better to improve the potential parameters also using a similar RMD calculation. However, it must be clearly stated, that the potential is not the best potential that could be fitted to the data, but that it is the best potential to be used in the approximate RMD approach.

The difference between the two RMD simulations may also be used to further explain the discrepancy in the two studies of range distributions after ion bombardment of Si, as presented in Section 4.2. In the round-robin test [Gär 95], the purely repulsive ZBL potential was used in the RMD simulations. In this case, Gärtner comes to the conclusion that RMD and MD simulations yield similar results. Posselt and Heinig [PosHei 95], on the other hand, used a combined ZBL-SW potential to describe the interaction. They found a disagreement between MD and RMD. Gärtner explained the difference by the different masses of the impinging ions, B in the first case and Si in the second case. Basing on the investigation described in this section, the difference might also be explained by the different potentials applied in the RMD simulations. The two studies present no contradiction in themselves.

8.3.2   MFPA versus MD

The mean free path approach (MFPA) has been developed in the late 1980s by Jolie *et al.* in order to theoretically describe the slowing down of recoiling atoms in GRID experiments [Jol 92, pp. 26-30]. The MFPA bases on many approximations and is therefore less suited to describe GRID lines than computer simulations. Nevertheless, the approach is still commonly applied for the evaluation of powder GRID experiments. Jentschel, e.g., states that "in order to obtain a very fast qualitative estimation of the slowing down the MFPA presents the best suited approach" [Jen 97a, p.60].

Even though MFPA is not suited for the evaluation of Crystal-GRID experiments, as it does not consider the crystal structure and as it is thus not able to predict orientation-dependent properties of GRID lines, it is worth comparing MFPA to MD simulations by looking at powder samples. It is the aim of this section to use artificial data to finally and clearly present the discrepancies of the MFPA approach.

It has been reported since long that MFPA yields different estimates for the level lifetime compared to MD simulations. The general conclusion was that MFPA lifetimes are approximately 30% higher than MD lifetimes. Comparing a large number of MD lifetime estimates in the range of 10 fs ... 100 fs to published MFPA values, Kuronen *et al.* found an average scaling of

$$\tau_{\text{MD,ZBL}} = 0.69\, \tau_{\text{MFPA,BM}} \tag{8.2}$$

with a large "scatter of necessary scaling factors" for different materials [Kur 92].

The comparison mixes two different things, however. MFPA is a theoretical approach to describe the slowing down just as MD does. But both, theory and simulation, base
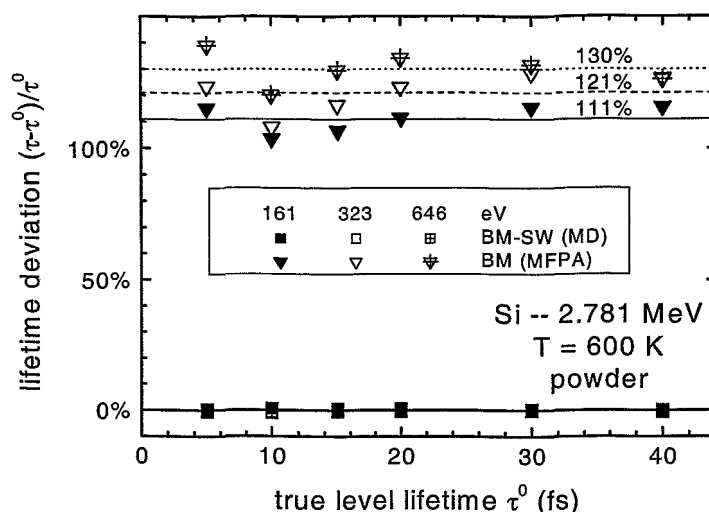
FIGURE 8.14: *Comparison of MFPA and MD estimates of the lifetime. Theory and simulation are both based on the BM potential. In the considered case, MFPA yields a deviation of more than 100% of the true value.*

on an interatomic potential. In the MFPA approach, the BM potential with parameters from Abrahamson is used [Abr 69], as it was supposed to be "the best empirical potential appropriate for the description of the interaction of identical atoms at separations between 0.5 Å and 2 Å" [Jol 92, p. 28]. The MD calculations, however, commonly use the universal (ZBL) potential which is said to be the best-suited potential by the ion-beam community [Eck 91, p. 62]. Therefore, the scaling factor corrects for two things at the same time, the different approach and the different interatomic potential.

Using the ZBL potential in the MFPA approach, Ulbig found that the newly obtained estimates for the lifetime are up to 60% higher than with the BM potential [Ulb 91a, p. 92]. Kuronen cites this work and concludes that MFPA yields lifetimes by about a factor of 2 longer than the ones obtained in the MD simulations, this time using the ZBL potential in both cases [Kur 92]. Despite this work, the factor of 0.69 became common knowledge [BörJol 93, Jen 97a].

In this work, MD and MFPA calculations are compared, using artificial data basing on the BM potential (as generated in Section 8.2). Both evaluations use the BM potential to describe the slowing down. As can be seen in Fig. 8.14, the MFPA overestimates the lifetime by $(111 \pm 5)\,\%$ for the original decay cascade with $E_{\mathrm{kin}}^{0} = 161\,\mathrm{eV}$. Increasing the recoiling atom's initial velocity, the estimates become even worse, they are too long by $(121 \pm 8)\,\%$ or $(130 \pm 7)\,\%$, respectively. The energy-dependence of the deviation shows that it is *not* possible to give a universal correction factor as previously tried.

Why does the MFPA yield that wrong estimates? MFPA uses two basic assumptions for the iterative calculation of the recoiling atom's velocity: i) The recoiling atom moves with *unchanged energy* for a distance equal to the energy-dependent *mean free path* $R_{\mathrm{MFP}}\,(E_{\mathrm{kin}})$ and ii) it loses *half of its energy* at this point. The mean free path R_{MFP} is taken to be the length of a cylinder of base $\pi\,[d_{\mathrm{min}}]^{2}$ and volume V, where d_{min} is the distance of closest approach at a given kinetic energy E_{kin}, and V is the average volume per atom in the
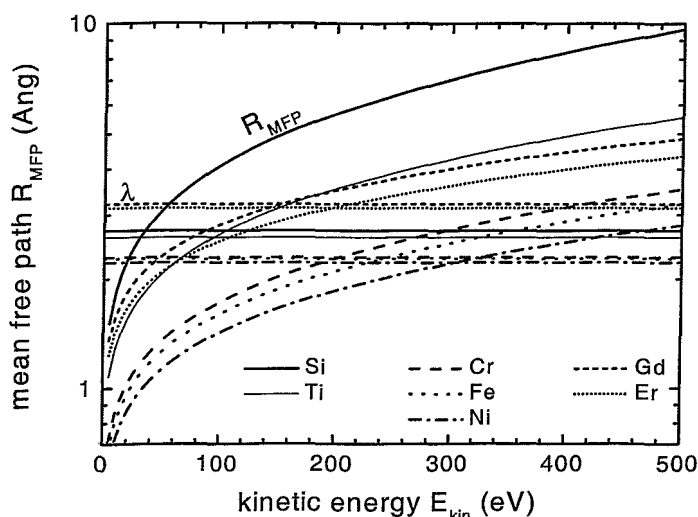
FIGURE 8.15: *Energy-dependent mean free path R_{MFP} used in the MFPA calculation of powder GRID lines for typical materials used in GRID experiments. For comparison, the mean free path λ (liquid model) is also given.*

sample [Jol 92, pp. 26-30].

$$R_{\mathrm{MFP}}\left(E_{\mathrm{kin}}\right) = \frac{V}{\pi\left[d_{\min}\left(E_{\mathrm{kin}}\right)\right]^{2}} = \frac{V}{\pi\left[B_{\mathrm{BM}}\ln\left(2A_{\mathrm{BM}}/E_{\mathrm{kin}}\right)\right]^{2}} \qquad (8.3)$$

In Eq. 8.3, the distance $d_{\min}$ is calculated using the BM potential where A_{BM} and B_{BM} are the potential parameters. The mean free path R_{MFP} is visualized in Fig. 8.15 for commonly used, monatomic GRID samples. The straight lines represent a mean free path λ calculated as the third root of the volume per atom (liquid model)

$$\lambda = \sqrt[3]{V}$$

The plot drastically shows why the MFPA method fails in the case of Si. Even at the low initial kinetic energy of 161 eV, the first mean free path in the MFPA calculation is about 5 Å. This value is much larger than the nearest neighbour distance of 2.35 Å or than $\lambda = 2.72$ Å. For increased initial kinetic energies, the mean free path $R_{\mathrm{MFP}}\left(E_{\mathrm{kin}}^{0}\right)$ becomes even longer; the discrepancy from a reasonable size is further enhanced. Consequently, the slowing down is not well described. This can be seen in Fig. 8.16, where the average velocity in the MD/RMD calculation is compared to the MFPA velocity which is a step function.

In fact, Jolie mentions that the approximation of considering the energy loss only after the atom has travelled the distance R_{MFP}, is only valid if $R_{\mathrm{MFP}}\left(E_{\mathrm{kin}}^{0}\right)$ is of the order of the interatomic distances [Jol 92, p. 30]. This condition is not fulfilled in the case of Si. It is, however, also not fulfilled in many other cases where it has been applied (compare Fig. 8.15).

Basing on these considerations, it becomes clear that the MFPA approach should not be used at all, unless a better formulation for the mean free path is found. RMD
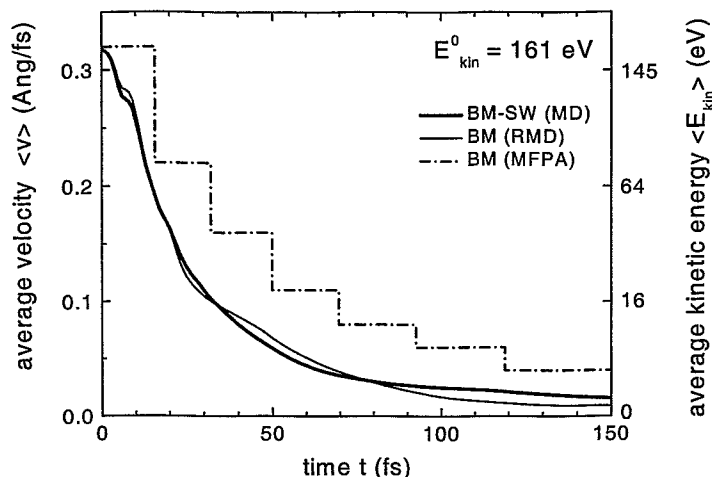
FIGURE 8.16: *Average velocity $\langle v \rangle$ of recoiling atom determined from MD and RMD calculations as well as taken from the MFPA theory in the case of Si with $E^0_{kin} = 161\,eV$. The MFPA underestimates the slowing down drastically. If taking all mean free pathes to be only half as long, a good consistency would be obtained, in this case.*

calculations using the purely repulsive ZBL potential can be easily performed for all GRID measurements up to about 100 fs. For longer times, a different treatment is needed, as RMD does no longer sufficiently describe the recoiling atom's velocity. In the MFPA approach, a Maxwell distribution around the measured sample temperature is used as soon as thermal velocities are reached. With some additional work, a similar approximation could also be implemented in the RMD code.

If a well-suited interatomic potential exists, an evaluation by a full MD simulation is, of course, preferable. With modern computers it should be no problem to perform a full MD simulation even for lifetimes up to the ps range. As slowly moving recoiling atoms only emit almost unshifted photons, the simulation can even be made more efficient by stopping the calculation of a trajectory as soon as the recoiling atom is very slow. However, investigations for this range of lifetimes are beyond the scope of this work.

Chapter 9

Experimental Results

Crystal-GRID experiments have been performed at the high-flux reactor of the ILL in Grenoble. The use of the ILL facilities requires the submission of proposals which are then handled in a subcommittee of the Scientific Council, corresponding to their scientific content. The proposals are evaluated for scientific merits, assigning priorities and beam time to accepted proposals. Actually, around 70% of the submitted proposals are accepted[1]. On average, seven months pass in between the submission of a proposal and the actual measurement.

When I first started working on the investigation of interatomic potentials using Crystal-GRID, two proposals had already been submitted by my supervisors and accepted by the Scientific Council, dealing with gallium phosphite (GaP) and iron (Fe) single crystals, respectively.

The proposed measurements using single-crystalline iron (Fe) were scheduled only a few days after I started working on Crystal-GRID. As a second group, from the Université de Fribourg in Switzerland, had proposed similar measurements, it was decided that this Fe experiment would be evaluated by the Fribourg group, and that I would focus on semiconductors.

Predictive computer simulations had shown that GaP should be ideal to prove the existence of asymmetric Crystal-GRID lines. However, the study of expected count rates, as reported in Appendix C, shows that the transition in P, originally selected for the GaP measurement, is to weak to yield good results. Furthermore, no more than one GaP crystal can be brought in the reactor, as the β activity of Ga would be too high in case of an emergency extraction of the samples. Instead, it was decided to use ZnS single crystals, even though the reported lifetime of $\tau = (40 \pm 12)$ fs is at the upper limit of measurability. Results are reported in Section 9.1.

Silicon (Si) is certainly the technically most important semiconductor. Improving its interatomic potential would be of great interest. A new potential could immediately be applied, e.g. in standard process simulation software. Unfortunately, the only transition that might actually be measurable has a reported lifetime of $\tau = (1.22 \pm 0.18)$ fs (compare Appendix C) which is too small for Crystal-GRID measurements. As reported lifetimes are often not very reliable, test measurements have been performed with Si single crystals in order to verify the value. Experimental results as well as results using artificial data are reported in Section 9.2.

---

[1] http://www.ill.fr/SCO/

Both, the measurements with ZnS and Si, did not yield very promising results. Therefore, further measurements were performed using the insulator titanium dioxide (TiO_2). The studied transition in Ti had already been applied several times in powder GRID measurements. As first Crystal-GRID data had been taken by Jentschel during his thesis [Jen 97a], it was known that well-structured lines would be obtained. The results of these measurements are reported in Section 9.3.

The Fe experiment, as well as measurements with Cr and Ni, have been evaluated by Stritt *et al.* (Fribourg). After the detailed studies presented in Chapters 6 and 7, a re-evaluation of these measurements became necessary. The results are presented in the last section of this chapter.

9.1 Results – Zinc Sulphide (ZnS)

Zinc sulphide (ZnS) is a II-VI semiconductor with a comparatively wide band gap (3.7 eV). The material is especially interesting because of its optoelectric properties. Examples for its application are electro-luminescent devices [Bri 94] or planar waveguides [Won 91]. Diodes and transistors can also be produced on the basis of ZnS.

During three measuring periods, ZnS crystals have been investigated with the <100>, <110>, and <111> directions oriented towards the spectrometer, respectively. The measurements used the $E_{\gamma_2}^0 = 2.380$ MeV transition in the ^{33}S nucleus, depopulating the 3.221 MeV level. This level is mostly directly fed, 91% of the nuclei decay directly from the capture state (see Fig. 9.1). Two two-step cascades further contribute to the feeding [Ram 85]. Their influence is small but taken into account in the simulations. The energy E_{γ_1} of the primary photon in the main feeding is 5.421 MeV, corresponding to an initial recoil energy of the excited S nucleus of 478 eV, i.e. an initial recoil velocity v^0 of 0.529 Å/fs. The nuclear state has a reported lifetime τ of (40 ± 12) fs [Fir 96].

The two spectrometers, GAMS 4 and GAMS 5, were used in flat-crystal mode. For all orientations, one measurement has been performed with one crystal in first, the other in second diffraction order. Two further measurements have been done with both crystals in second diffraction order leading to a higher resolution at the cost of intensity. For each measurement, a large number of scans (16 to 47) has been recorded, containing about 90 data points each. Details can be found in Table 9.1.

As discussed in Section 3.4, the experimental setup is not absolutely stable, and a small drift is present in the scans. For that reason, short reference scans of the long-lived, highly intensive 0.841 MeV transition have been measured in between the long scans. Fitting the centre positions of these scans allows to approximate the drift function and to correct the drift. A linear correction algorithm has been used in slowly drifting regions. Scans including a strong drift have been neglected in the evaluation. The centre positions of both, the reference scans and the scans of interest, are plotted in Fig. 9.2 for the <100> measurement at GAMS 5.
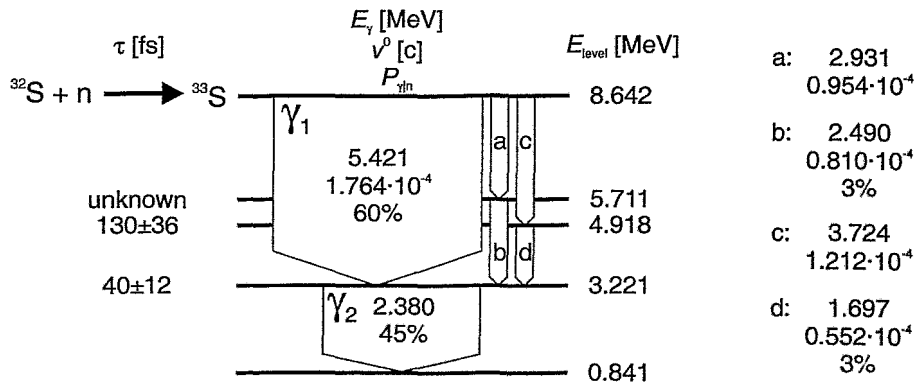

FIGURE 9.1: *Partial level scheme of ^{33}S [Ram 85]. For each level of energy E_{level}, the reported lifetime τ is given [Fir 96]. For the transitions, the photon energy E_γ, the corresponding initial recoil velocity v^0 of the S nucleus, and the absolute intensity $P_{\gamma|n}$ of the transition (% refers to the number of captured neutrons) are given.*

orient. <hkl>	GAMS	order (n/m)	no. scans	m. time / point (min)	centre h. $\sum I_c$ (counts)	backg. $\sum I_{bg}$ (counts)	excess width σ_{ew} (GAMS 4-fringe)
<100>	5	(1/2)	47	235	1347	113	0.259 ± 0.016
<110>	4	(1/2)	33	176	906	380	0.281 ± 0.013
<110>	5	(2/2)	19	190	299	58	0.263 ± 0.014
<$\bar{1}\bar{1}\bar{1}$>	4	(1/2)	33	176	908	333	0.252 ± 0.015
<111>	5	(2/2)	16	160	290	44	0.164 ± 0.016

TABLE 9.1: *Details of the five measurements using the* 2.380 MeV *transition in* ^{33}S. *For every measurement, the orientation of the ZnS crystals, the used spectrometer, the diffraction order of the spectrometer crystals, the number of performed scans (90 measuring points each), the time of measurement per point, the summed centre height over background, the summed background level as well as the fitted excess width are given. The excess width is given in GAMS 4-fringes for all measurements, conversion to eV can be obtained with the factor* 113.9 eV/fringe.

The sum scans of the five measurements are plotted in Fig. 9.3. Only a small part of the background is shown, the single scans extend further in the background region. The straight lines are the summed fitted theoretical GRID lines. The dashed lines show the instrumental response functions.

All GRID lines have a significant peak around zero, confirming that the nuclear level lifetime is rather long. The wings contain fine structure which differs significantly comparing the five measurements. However, the dominant peak leads to a strong statistical noise, thus hiding a lot of the fine structure. Even though many scans have been taken, the statistics of the measurement is not sufficient.

The resolution in the measurements, which are displayed on the right side of Fig. 9.3, is much better compared to the other three measurements. The main peak is narrower and the fine structure becomes slightly more pronounced.

9.1.1   First measurement of asymmetric Crystal-GRID line

Besides the improvement of the interatomic potential, the actual experiments aimed to observe for the first time a theoretically predicted asymmetry of the Doppler broadened line for the <111> crystal orientation.

Under normal conditions, zinc sulphide has the zinc-blende structure (point group $F\bar{4}3m$). The two constituents are found on two face-centred cubic sub-lattices, respectively, displaced with respect to each other by one forth of the diagonal of the cubic unit cell (see Fig. 9.4). Every atom has 4 first neighbours of the opposite atom sort at a distance $d_1 = \sqrt{3}a/4 \approx 43\% \, a$ (tetrahedral positions), and 12 second neighbours of the same atom sort at $d_2 = a/\sqrt{2} \approx 71\% \, a$ where a is the lattice constant.

The zinc-blende structure has no inversion symmetry. A rotation-inversion symmetry exists for some axes, e.g. for the <100> and for the <110> directions, but not for the <111> direction. Consequently, the expected Crystal-GRID line in the latter case should be asymmetric (compare Section 5.3).

This asymmetry could be verified experimentally, as can be seen in Fig. 9.3. Due to the long lifetime, the asymmetry of the Crystal-GRID lines is not very pronounced (compare
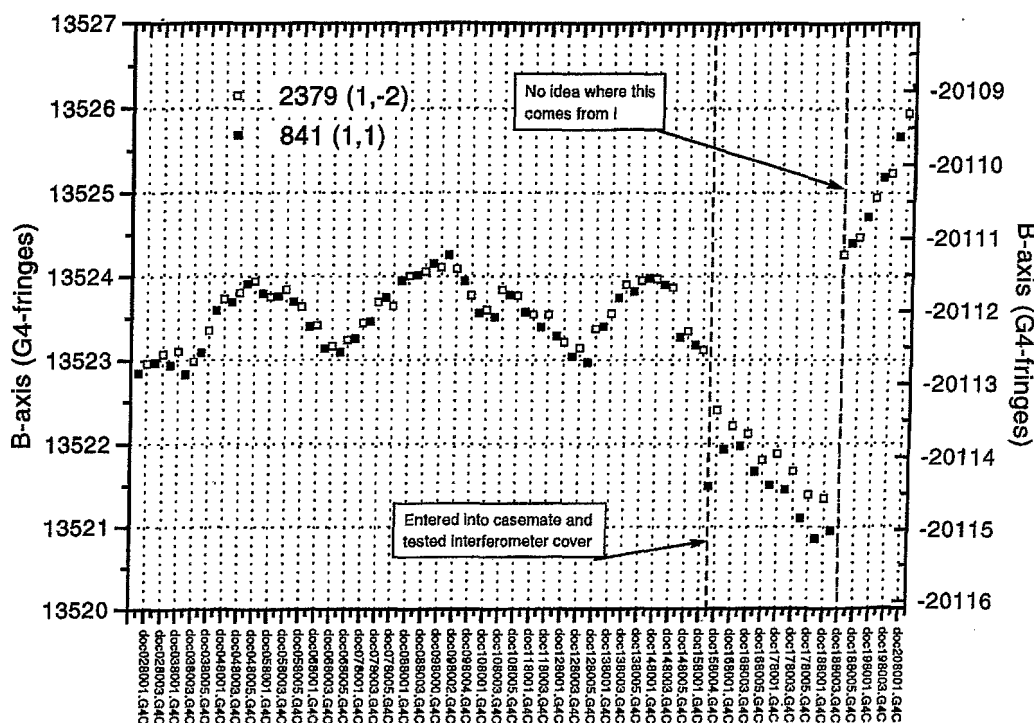
FIGURE 9.2: *Drift of spectrometer monitored by the fitted centre positions of short reference scans (0.841 MeV, diffraction order $(1, -1)$, left scale, solid square) and of the scans of the transition under study (2.380 MeV, diffraction order $(1, 2)$, right scale, hollow square). The x-axis gives the names of the scan files (oc=october, 02=2nd, 8=1998, 001=file 1). (plot by Jentschel)*

Section 5.3). However, especially, the slope around 200 eV differs significantly for positive compared to negative energy shifts. As the two spectrometers are placed on opposite sides of the beam tube (see Fig. 3.2), i.e. of the sample, the asymmetry is mirrored comparing the measurements at the two spectrometers.

The existence of the asymmetry is also confirmed statistically by fitting theoretical Crystal-GRID lines for both, the <111> and the <$\bar{1}\bar{1}\bar{1}$> orientations, to the same experimental scans, and comparing the obtained values of $\chi^2_{\lambda,P}$. A difference in $\chi^2_{\lambda,P}$ corresponding to more than 4σ for GAMS 5 and more than 6σ for GAMS 4 is obtained, proving that the line is asymmetric.

9.1.2 Improving the interatomic potential (RMD)

As MD simulations are very time consuming, RMD simulations with purely repulsive potentials have been performed to get a first impression of how the interatomic potential can be improved on the basis of the measured data.

First, the universal (ZBL) potential is used. The screening lengths of the potentials for all three interactions (Zn–S, S–S, and Zn–Zn) are simultaneously varied in order to find an optimal value. The original value, as defined in Eq. (1.6), will be called a_s^0 in this context. In principle, it would also be possible to separately optimize the screening lengths of the
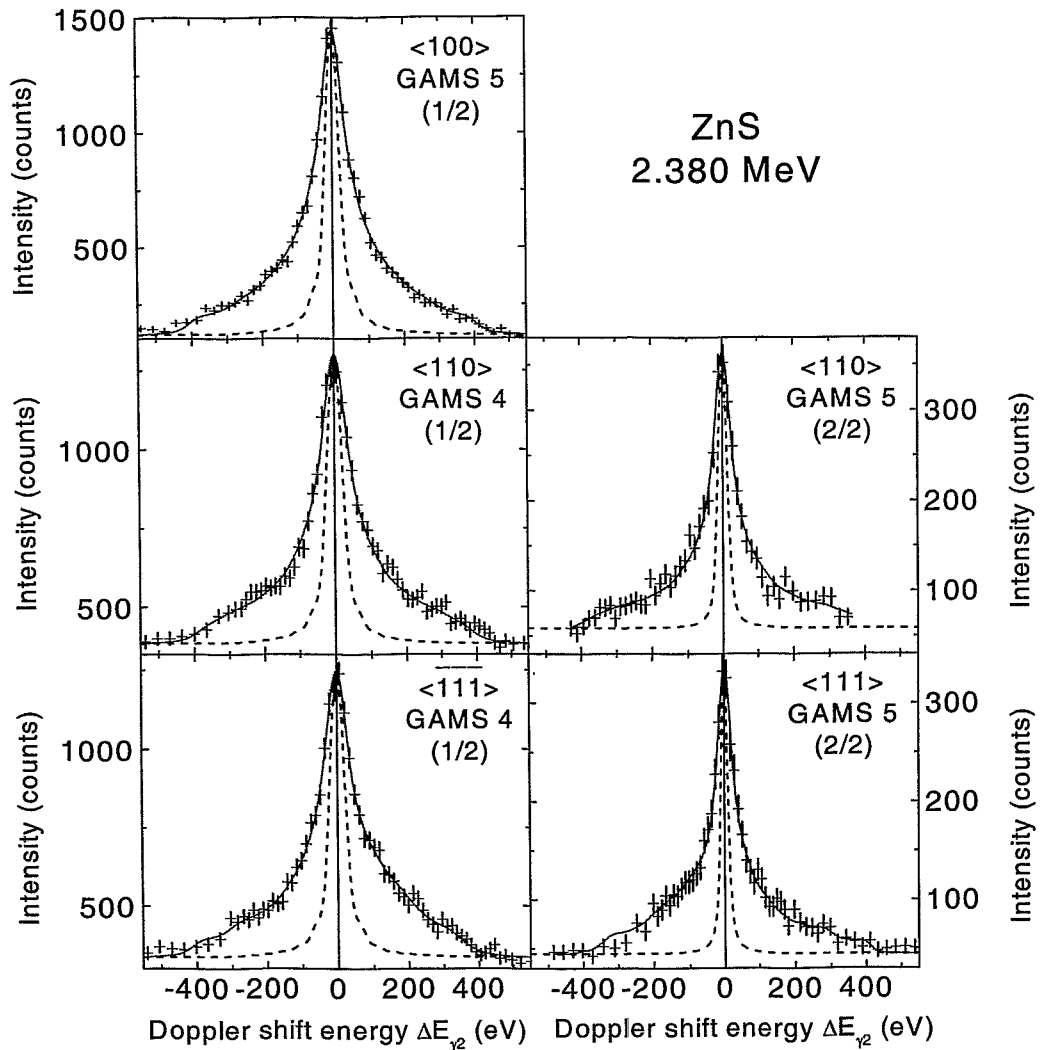
FIGURE 9.3: *Experimental results for ZnS. The sum scans are plotted together with the summed theoretical GRID lines (straight lines) and the instrumental response functions of the spectrometers (dashed lines). The measurements with one spectrometer crystal in first, one in second diffraction order are shown on the left side, the measurements with both crystals in second order are shown on the right side.*

three interactions. However, in this case, a three-dimensional parameter space would have to be treated. Furthermore, the recoiling S atom is not or only very little influenced by the Zn–Zn potential. The Zn–S potential is the most important, as the first neighbour shell consists of Zn atoms. Due to the long lifetime, also the S–S potential plays an important role for the movement of the recoiling S atom.

Second, the Gärtner-Hehl potential is used. The screening functions for the three combinations Zn–S, S–S, and Zn–Zn, have been calculated by Gärtner [Gär 98]. They should, in principle, yield a better description than a mean potential, as ZBL. As the function is given numerically, it is difficult to vary the potential for an optimization. Only
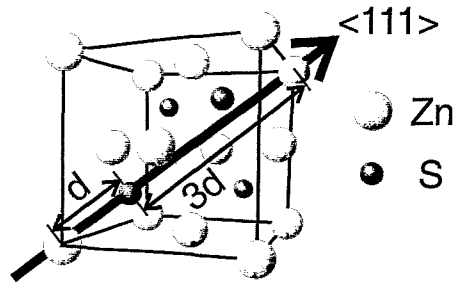
FIGURE 9.4: *The ZnS lattice consists of two inter-penetrating fcc lattices, shifted by one forth of the lattice diagonal and occupied by two different atom sorts. The lattice has no rotation-inversion symmetry along the <111> crystal orientation, along which the S atom has a Zn neighbour at a distance of $d = \sqrt{3}a/4$ in one direction and 3d in the other direction.*

data	potential	optimized a_s/a_s^0	minimum $\chi_{\lambda,P}^2$	Q	τ (fs)
original	GH		14051	0.007%	(51.6 ± 0.7)
	ZBL	$(98 \pm 11)\%$	14065	0.005%	(54.8 ± 0.8)
drift-corrected	GH		14057	0.005%	(51.7 ± 0.7)
	ZBL	$(97 \pm 11)\%$	14071	0.004%	(55.7 ± 0.8)

TABLE 9.2: *Results of ZnS measurement evaluated with RMD simulations. The error given for the screening length corresponds to a 2σ error, the error for the lifetime τ is purely statistical (due to the total number of counts).*

the originally calculated functions are used.

The simulated GRID lines have been fitted to both, the original and the drift-corrected data. The resulting values of the statistical variable $\chi_{\lambda,P}^2$ are plotted as a function of the relative screening length in Fig. 9.5. It can be seen that the original data are slightly more consistent with the model lines than the drift-corrected data, the values of $\chi_{\lambda,P}^2$ are smaller[2]. Obviously, the linear drift correction did not improve the consistency[3]. Consequently, the drift correction is ignored in the following, the small additional error can be neglected compared to the statistical error. A similar conclusion can be drawn from the evaluation using full MD simulations (compare Fig. 9.12).

The screening length a_s of the universal (ZBL) potential can be optimized. Its optimized value is $(98 \pm 11)\%$ of the original value, i.e. the original value is correct within this 2σ error. The GH potential is slightly better suited for RMD simulations than the optimized ZBL potential. The results are summarized in Table 9.2.

Looking at the goodness-of-fit, one gets aware that both potentials are not sufficient to describe the data, as Q is only of the order of 0.005%. Usually, for $Q < 0.1\%$, the model is rejected (see Section 6.1.5). The inconsistency becomes only visible when considering all data in the evaluation. Every single series of scans is sufficiently well described by the

---

[2]The drift-corrected data ($\nu = 12835$) contain five data points less than the original data ($\nu = 12840$). Consequently, the expectation value of $\chi_{\lambda,P}^2$ is reduced by 5 compared to the original data. This further enhances the observed difference in $\chi_{\lambda,P}^2$ between the two data sets.

[3]Rigourously speaking, it is not clear whether the drift correction is correct. $\chi_{\lambda,P}^2$ is a statistical variable describing the consistency of data and model. Of course, it is possible that the correctly drift-corrected data are less consistent with the model. However, this is not very probable.
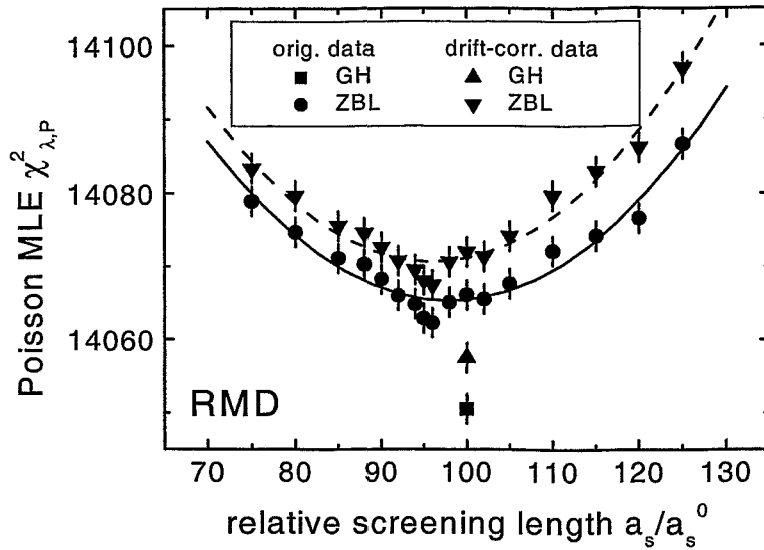
FIGURE 9.5: *Minimum values of the statistical variable $\chi^2_{\lambda,P}$ obtained by fitting theoretical GRID lines (RMD) to the data. The original data lead to smaller values of $\chi^2_{\lambda,P}$ than the drift-corrected data, showing that the drift correction is not suited. The GH potential leads to a slightly better consistency than the ZBL potential. The screening length a_s of the ZBL potential can be optimized.*

orientation	GAMS	$\chi^2_{\lambda,P}$	goodness-of-fit Q
<100>	5	4626	0.9%
<110>	4	3149	0.6%
<111>	4	2949	24%
<110>	5	1835	8%
<111>	5	1489	9%

TABLE 9.3: *Comparison of the five measurements evaluated with RMD simulations on the basis of the GH potential.*

potentials, Q is in the range from 0.6% to 24% (see Table 9.3).

Due to the large number of scans, the statistical error $\sigma_\tau \approx 0.7\,\text{fs}$ is very small. However, this error does not include the uncertainty due to the potential. This explains the comparatively large discrepancy between the GH and the ZBL estimates for the lifetime. Including the 2σ uncertainty of the screening length a_s in the error σ_τ, a reasonable estimate of the lifetime, basing on RMD calculations, becomes $(55 \pm 11)\,\text{fs}$.

9.1.3   Improving the interatomic potential (MD)

Due to the long lifetime, many secondary photons are emitted by slowly moving atoms. However, the equilibrium state of ZnS is not reflected in RMD simulations.

As discussed in Chapter 1, the high-energy part of the interatomic potential is well described by one of the screened Coulomb potentials, namely ZBL, KrC, or GH. This has been tested experimentally for high energies. The equilibrium state is well described by
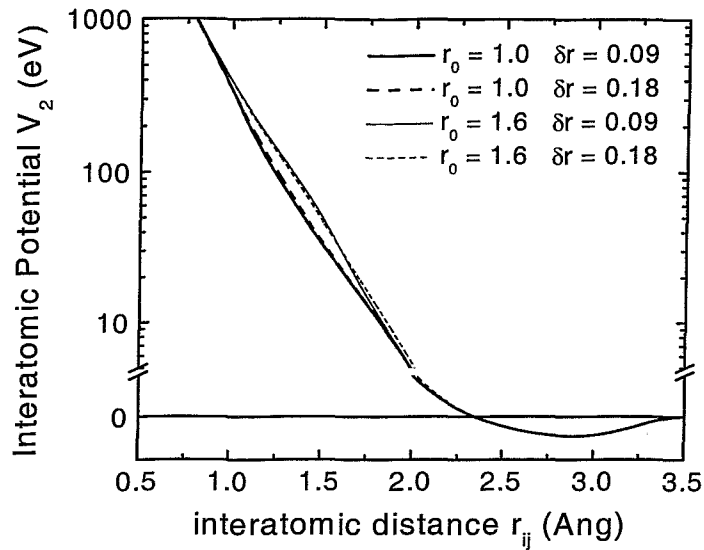
FIGURE 9.6: *Two-body term V_2 of the combined interatomic KrC–SW potential for the Zn–S interaction used in the evaluation of the ZnS Crystal-GRID data. Potential functions are plotted for the highest and lowest values of the two parameters. As can be seen, the switch centre r_0 has a larger influence than the parameter δr. The V_2 axis is linear below 4 eV and logarithmic above 5 eV.*

equilibrium potentials. For ZnS, Stillinger-Weber (SW) potential parameters have been adjusted within this work (compare Appendix B). This potential should be well suited for the description of the bound state.

The aim of Crystal-GRID is to improve the intermediate region. The studied recoiling atoms have an initial kinetic energy of 478 eV. The nearest approach corresponds to an energy of about 300 eV, i.e. the potential energy function can only be studied for energies below 300 eV, approximately. For this reason, it is first tried to optimize the parameters of the switch function (see Section 1.3).

Simulations are performed using a combined KrC–SW potential for the Zn–S interaction. A total of 1500 trajectories is calculated using a simulation cell of 6^3 unit cells, i.e. 1728 atoms. The cell is equilibrated at a temperature of 900 K.

The potential is optimized by varying the adjustable parameters r_0 and δr of the switch function s_1, as defined in Eq. (1.15) and (1.19). The parameter r_0 is the switch centre, i.e. the position where both potentials are added with an equal weight of 50%. It determines which of the two potentials, SW or KrC, is more important in the intermediate region. The switch parameter δr defines the steepness of the transition. The smaller δr, the faster the switching occurs.

The two-body terms V_2 of the combined interatomic potentials are plotted in Fig. 9.6 for the maximum and minimum values of the parameters.

In the following, often the value

$$\sqrt{\Delta \chi^2_{\lambda,P}} \equiv \sqrt{\chi^2_{\lambda,P} - \chi^2_{\lambda,P}\big|_{\min}} \qquad (9.1)$$

is plotted instead of the statistical variable itself. As shown in Section 6.1.4, a variation of the parameter a_j by $n\sigma_j$ corresponds to an increase of the Poisson MLE $\chi^2_{\lambda,P}$ by n^2. Consequently, $\sqrt{\Delta\chi^2_{\lambda,P}}$ gives the number of standard deviations that a trial value of a parameter is worse than its best value. Due to correlation, this is not perfectly correct when varying more than one parameter. However, the quantity is still better suited for visualization than $\chi^2_{\lambda,P}$, itself.

Fitting the theoretical Crystal-GRID lines derived from full MD simulations using the combined KrC–SW potential to the experimental data by optimizing the local parameters as well as the nuclear level lifetime τ, best values of the statistical variable $\chi^2_{\lambda,P}$ and estimates for the lifetime are obtained for every set of parameters r_0 and δr. The values $\sqrt{\Delta\chi^2_{\lambda,P}}$ are plotted in Fig. 9.7, the corresponding estimates of the lifetime in Fig. 9.8.

As can be seen, the value of $\chi^2_{\lambda,P}$ varies only little for the different switch parameters. The difference between best and worst $\chi^2_{\lambda,P}$ is about 10, corresponding to little more than 3 standard deviations. Furthermore, no clear minimum can be distinguished. The parameter-dependent variation of $\chi^2_{\lambda,P}$ is, if present, completely hidden by the statistical noise. An optimization of the parameters is not possible.

Indeed, the variation of the parameters did change the slowing down of the recoiling atoms. This can be seen in Fig. 9.8. The estimates of the lifetime show a clear dependence on the potential parameters, they increase from $\tau \approx 46\,\mathrm{fs}$ for $r_0 = 1.6\,\text{Å}$ up to $\tau \approx 50\,\mathrm{fs}$ for $r_0 = 1.0\,\text{Å}$. This variation is significant, as the statistical error σ_τ is only 0.7 fs. The non-sensitivity to the switch parameters is clearly linked to the correlation of nuclear level lifetime and interatomic potential.

The absolute values of $\chi^2_{\lambda,P}$, as well as the goodness-of-fit Q, have similar values as in the evaluation basing on RMD simulations. Hence, the added equilibrium part of the potential did not significantly improve the consistency of model GRID lines and experimental data.

The fitted estimates of the lifetime are smaller, now. This is related to the use of the KrC potential which is slightly more repulsive than the ZBL or GH potential, leading to a faster slowing down of the atoms. Due to the correlation of lifetime and slowing-down time, this leads to a shorter estimate of the lifetime.

Obviously, it is necessary to more strongly change the interatomic potential in order to see a significant variation of $\chi^2_{\lambda,P}$ with a potential parameter. Therefore, simulations are performed with a combined ZBL–SW potential where the screening length a_s of the ZBL potential, as well as the switch centre r_0 are varied. Again, the forces are linked, but using the power switch function s_2, this time (see Eq. (1.16)). The second switch parameter is fixed at the value $\xi = 10$. The potentials for various values of the screening length are plotted in Fig. 9.9.

To reduce statistical noise, 2000 trajectories are calculated for every set of potential parameters. One further calculation is performed using the combined GH–SW potential with switch parameters $r_0 = 1.2\,\text{Å}$ and $\xi = 10$. In this case, 4000 trajectories are calculated.

The result of the parameter variation is shown in Fig. 9.10 and 9.11. Again, the switch centre r_0 does not significantly influence the consistency of model and data. However, the variation of the ZBL screening length leads to large changes in $\chi^2_{\lambda,P}$. A sectional view of Fig. 9.10 for $r_0 = 1.4\,\text{Å}$ is plotted in Fig. 9.12.

This latter figure additionally shows the results of fitting the drift-corrected data, as well as the results for the GH–SW potential. As in the RMD evaluation, the drift-corrected
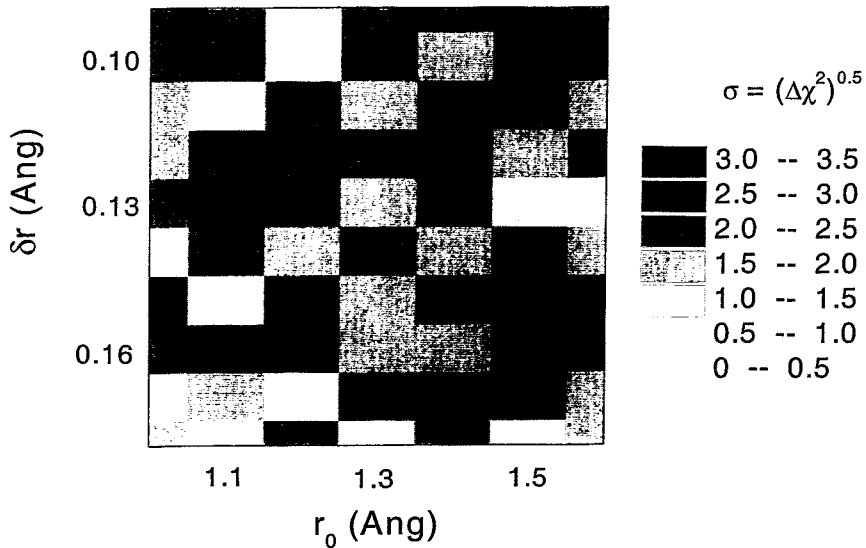
FIGURE 9.7: *Result of fitting model GRID lines to original data. The variation of the switch parameters r_0 and δr does not yield significant differences in the statistical variable $\chi^2_{\lambda,P}$. A minimum can not be found. The measurement is not sensitive to the parameters.*
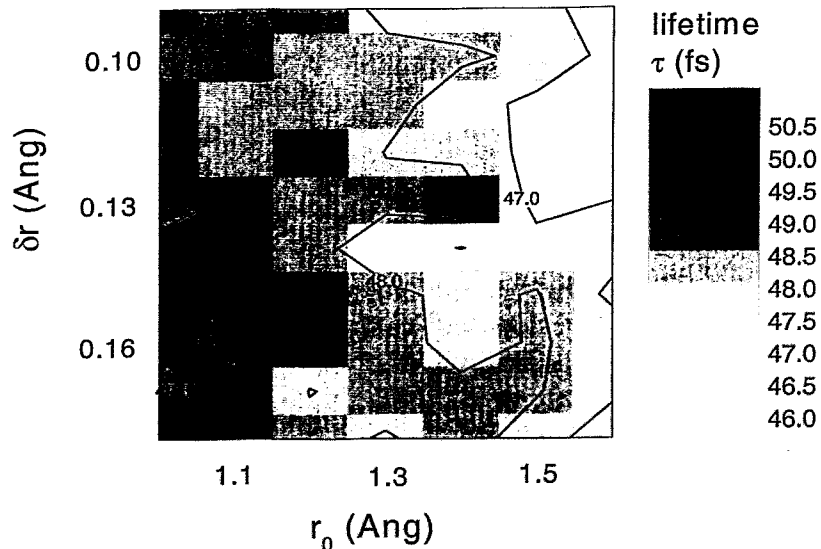
FIGURE 9.8: *Estimated lifetimes τ for different values of the switch parameters r_0 and δr. A correlation between r_0 and τ can clearly be seen. This correlation compensates the change of $\chi^2_{\lambda,P}$ with r_0 when fitting model lines to the data.*
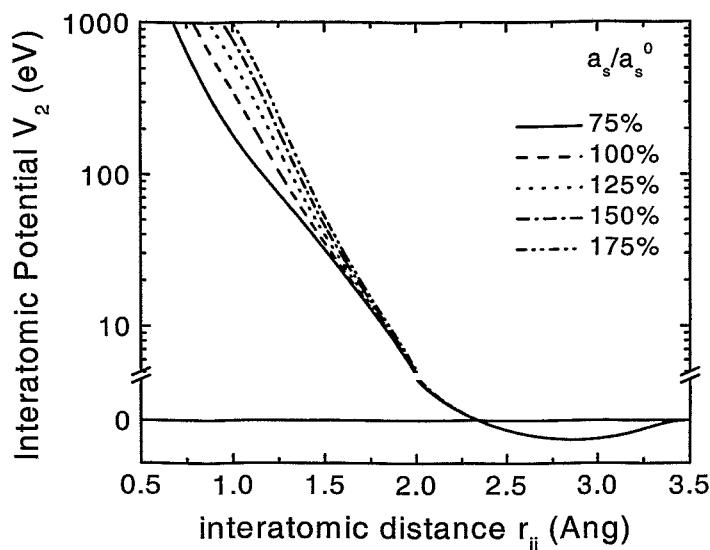
FIGURE 9.9: *Interatomic potentials for the Zn–S interaction. The combined ZBL–SW potentials are plotted for different values of the screening length a_s. The V_2 scale is linear up to 4 eV and logarithmic above 5 eV. The potential with $a_s = 50\% \cdot a_s^0$ is certainly unsuited due to its unusual run. This will also turn out in the evaluation.*

data	potential	optimized a_s/a_s^0	minimum $\chi^2_{\lambda,P}$	Q	τ (fs)
original	GH–SW		14059	0.006%	(50.3 ± 0.7)
	ZBL–SW	$(101 \pm 11)\%$	14055	0.007%	(50 ± 0.7)
	KrC–SW		14057	0.006%	$(46...50)$

TABLE 9.4: *Results of ZnS measurement evaluated with MD simulations. The error given for the screening length corresponds to a 2σ error, the error for the lifetime τ is purely statistical (due to the total number of counts).*

data are less consistent with the model GRID lines than the original data. They will not be regarded.

The optimization of the screening length leads to a value of $(101 \pm 11)\%$ of the original value a_s^0. Due to the large error, the variation with r_0 can be neglected. The resulting value of a_s is consistent with the original value of the screening length, the stated error corresponds to the 2σ error. The obtained values of $\chi^2_{\lambda,P}$, Q, and τ are listed in Table 9.4.

As evident from Fig. 9.11, the screening length is strongly correlated to the slowing-down time, i.e. to the interatomic potential. The very high values for $a_s = 50\% \cdot a_s^0$ are not precise, as the trajectories are cut off at 250 fs. However, even between 75% and 200%, the estimates of the lifetime vary between 75 fs and 25 fs, approximately.

Including the variation of a_s in the error of the lifetime, a reasonable estimate of the 3.221 MeV nuclear level lifetime is (50 ± 8) fs. This result is compatible with the reported value of (40 ± 12) fs [Fir 96]. Unfortunately, it is at the upper bound of the previously reported interval. As Crystal-GRID lines become less structured for long lifetimes, the newly obtained value of the lifetime shows that ZnS is not well suited for the investigation of atomic interaction using the Crystal-GRID method.
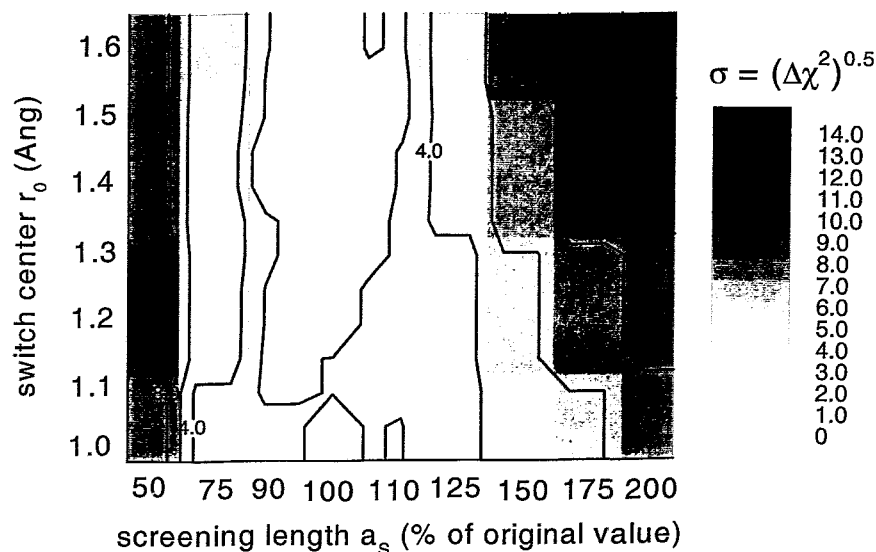
FIGURÉ 9.10: *Optimizing the screening length a_s and the switch parameter r_0 in the combined ZBL–SW potential by fitting model GRID lines to the original ZnS data. The clear dependence of $\chi^2_{\lambda,P}$ on the screening length allows to optimize the latter variable. The experiment is, however, not sensitive to the switch parameter r_0.*
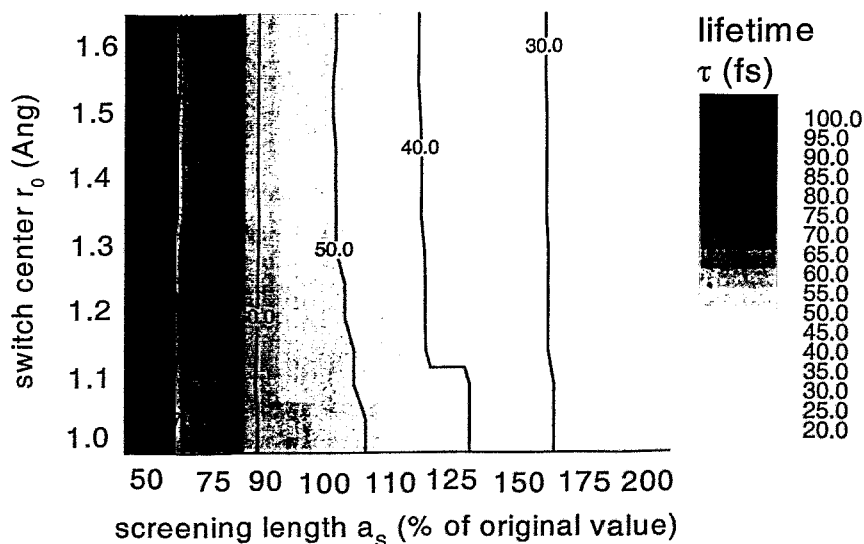
FIGURE 9.11: *Estimates of the lifetime when fitting GRID lines using the combined ZBL–SW potential to the experimental ZnS data. A strong correlation can be seen between the screening length a_s and the estimate of the lifetime τ.*
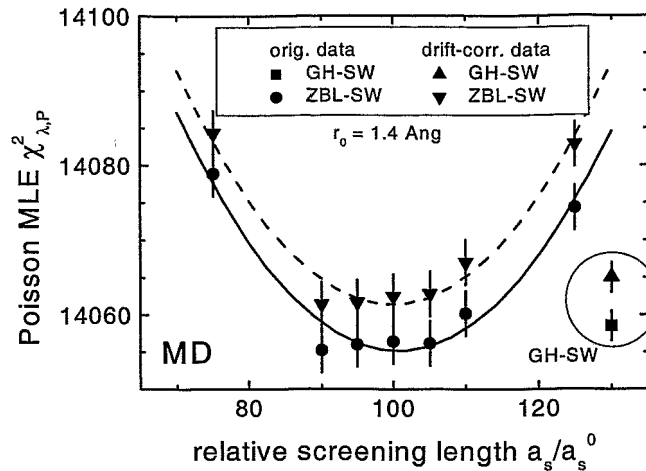
FIGURE 9.12: *Optimization of the screening length in the combined ZBL–SW potential for a fixed switch parameter $r_0 = 1.4\,\text{Å}$. For comparison, the minimum values of the GH–SW potential are also indicated. The original ZnS data lead to a better consistency than the drift-corrected data.*

As said before, the correlation between level lifetime and slowing-down time leads to a reduced dependence of $\chi^2_{\lambda,P}$ on the potential parameters. This is emphasized in Fig. 9.13 and 9.14 for an RMD and MD calculation, respectively. If the true value of the lifetime was known, it would be much easier to optimize potential parameters. As this is not the case, large errors must be attributed to the parameters, as long as the total number of counts can not be drastically enhanced.

The correlation is stronger for the RMD calculation. This is not surprising, as the MD simulation uses a combined potential where the equilibrium part is identical for all values of the screening length. In the RMD calculation, the purely repulsive screened Coulomb potential is applied for the complete range.

The actual ZnS measurement allows to optimize the screening length to within an error of about 10%, showing that the original choice is good. The screening length has a comparatively strong influence on the potential. Therefore, it must be expected that the present data do not allow for further results, and it has not been tried to optimize other, less important parameters.

Furthermore, investigations with artificial data show that the total number of counts in this measurement is not sufficient to optimize parameters such as r_0 and δr. This has been found by fitting the model functions to artificial data, generated on the basis of the known KrC–SW potential with known switch parameters. Drastically increasing the total number of counts, the true switch parameters can be estimated[4]. However, even in this case, the variation of $\chi^2_{\lambda,P}$ with the parameters is very noisy. The optimization is easier possible if the true lifetime were shorter.

Why is the goodness-of-fit that small? A value of 0.007% indicates that the model is not well suited to describe the data. A bad value of Q usually indicates a wrong estimation of

---

[4]Artificial data with $\sum I_c = 30,000$ were not sufficient, while data with $\sum I_c = 1,000,000$ allowed to find the minimum.
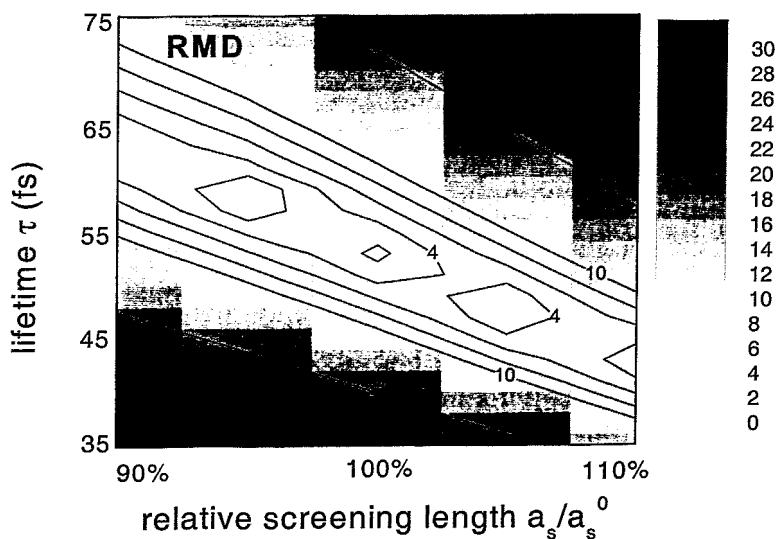
FIGURE 9.13: *Correlation of nuclear level lifetime τ and screening length a_s in the case of an RMD evaluation of the original ZnS data using the purely repulsive GH potential. If the lifetime was previously known, the screening length could be much better estimated by Crystal-GRID measurements.*
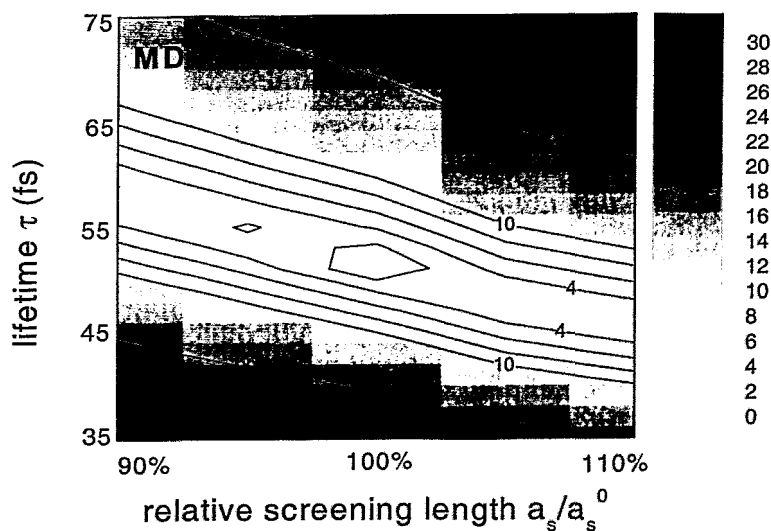
FIGURE 9.14: *Correlation of nuclear level lifetime τ and screening length a_s in the case of a full MD evaluation of the original ZnS data using the combined GH-SW potential. The correlation is weaker than in Figure 9.13, as the SW part of the potential is unchanged when varying the screening length.*

potential parameters. The fact that all simulations, MD or RMD, using a purely repulsive or a combined potential, using a mean potential like ZBL or a specially calculated one like GH, yield nearly identical values of the minimum $\chi^2_{\lambda,P}$ and of the goodness-of-fit urges to look for a different explanation.

- The drift correction did not improve the consistency of the data with the theoretical GRID lines. However, a drift within the scans is present. Using an improved algorithm for the drift correction, the goodness-of-fit might eventually be improved.

- The SW potential has been developed for the diamond or zinc-blende structure of crystal. It is not at all evident that it is adapted for the S atom moving through the crystal and therefore being part of a completely different atomic configuration. Especially, the three-body term is only valid near the equilibrium, tetrahedral structure. Also for late times, where a quasi-thermal equilibrium at high temperature is reached, the SW potential may be a fundamentally wrong approach to describe the atomic movement. If these points have a significant influence on the results, however, an investigation of interatomic potentials using Crystal-GRID would be impossible from general considerations.

- The switching to the SW potential is only applied for the Zn–S interaction. The S–S interaction as well as the Zn–Zn interaction are described by the purely repulsive screened Coulomb potentials in all simulations. This is certainly not justified. The equilibrium part of the Zn–S interaction stabilizes the sample lattice and is thus the most important equilibrium part. Nonetheless, an equilibrium potential for the S–S interaction should not be neglected. Atoms that have slowed down to low velocities are influenced by this potential. However, the same problems as mentioned for the SW potential would arise. The Zn–Zn interaction is of nearly no importance for the recoiling S atom.

These points are not further investigated within this work. Due to the insufficient statistics, a significant improvement with respect to the study of interatomic potentials can not be expected.

The central peak of the ZnS Crystal-GRID lines mainly originates from slowly moving atoms. On the one hand, a good equilibrium potential is needed to well describe the crystal structure. On the other hand, the method is not very sensitive to the very low energies.

This problem could eventually be avoided by masking the central peak in the fit and fitting only the wings. Of course, the total number of counts in the peak must be included as boundary condition. Thereby, it might be possible to concentrate on the potential range above a certain threshold energy. This approach has not been tested, however, as the fine structure in the wings of the ZnS measurement is too much washed out.

9.2 Results – Silicon (Si)

Silicon is one of the actually most important materials for industrial applications. Its use as basic material for the semiconductor industry makes it very interesting for the application of ion beam techniques. An investigation of the interatomic solid state potential by Crystal-GRID would be of big interest.

Only one transition in silicon has a sufficiently high effective cross section (see Table C.2) to allow a measurement with the crystal spectrometers GAMS 4/5 in flat crystal mode. This transition depopulates the 4.934 MeV state in ^{29}Si towards the ground state (see Fig. 9.15).

The lifetime of the 4.934 MeV level is reported to be (1.22 ± 0.18) fs [End 90]. This lifetime would be too short to study atomic motion with Crystal-GRID, as most of the γ-rays are emitted before the first atomic collision could occur. However, reported values of lifetimes are often not very precise. As will be seen in Section 9.2.2, a value of about 3 fs would already allow to perform Crystal-GRID studies. For that reason, it was tried to verify the reported value of the lifetime. Experimental results will be reported in Section 9.2.3.

9.2.1 Angular correlation of 4.934 MeV transition in ^{29}Si

As shown in Section 8.2, angular correlation has a large influence on Crystal-GRID lines, especially for small values of the lifetime (compare also Section 2.4). For the studied 4.934 MeV transition in ^{29}Si, the spin and parity values in the two-step cascade are $\frac{1}{2}^{+} \rightarrow \frac{3}{2}^{-} \rightarrow \frac{1}{2}^{+}$ (see Fig. 9.16). The emitted radiation is of type E1, electric dipole radiation. For
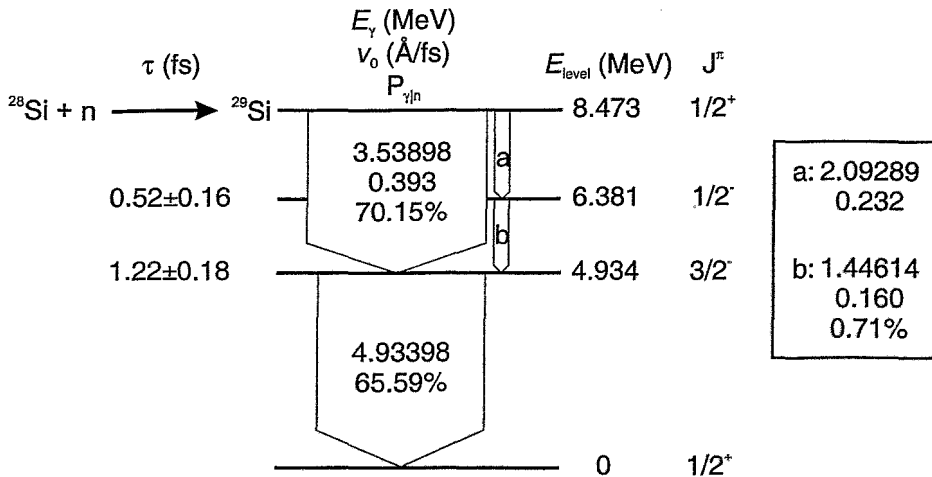
FIGURE 9.15: *Deexcitation cascade in ^{29}Si [Ram 92]. For each level of energy E_{level}, the reported lifetime τ [End 90] and the spin parity J^{π} are given. For the transitions, the photon energy E_{γ}, the corresponding initial recoil velocity v^0 of the Si nucleus, and the absolute intensity $P_{\gamma|n}$ of the transition are indicated (% refers to the number of neutron captures).*
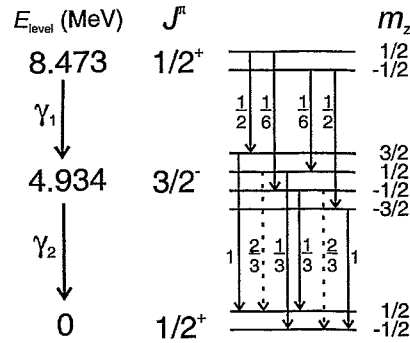
FIGURE 9.16: *Directional correlation of Si cascade. If the first photon is observed along the quantisation axis, only transitions with $\Delta m = \pm 1$ can occur (solid arrows). The second photon γ_2 is detected under the angle ϕ to the first direction, transitions with $\Delta m = \pm 1$ (solid arrows) and $\Delta m = 0$ (dashed arrows) are allowed. The relative intensities are shown. The energy levels for different quantum numbers m_z have been drawn separately even though they have the same energy.*

this radiation, the directional distribution functions $F_{\Delta l}^{\Delta m}$ are (for details see [FraSte 65])

$$
\begin{aligned}
F_1^0(\phi) &= 2 - 2P_2(\cos\phi) \\
F_1^{\pm 1}(\phi) &= 2 + P_2(\cos\phi)
\end{aligned}
\tag{9.2}
$$

If the direction of the first photon emission is chosen to be the quantisation axis, only transitions with $\Delta m = \pm 1$ are possible; the relative intensities are shown in Fig. 9.16. With this knowledge, the angular correlation function W or W' can be calculated [FraSte 65]:

$$
\begin{aligned}
W(\phi) &\sim 1 + \frac{1}{4}P_2(\cos\phi) = 1 + \frac{1}{8}\left(3\cos^2\phi - 1\right) \\
W'(\cos\phi) &\sim 1 + \frac{1}{8}\left(3(\cos\phi)^2 - 1\right)
\end{aligned}
\tag{9.3}
$$

These functions are illustrated in Fig. 9.17. As the Doppler shift energy ΔE_{γ_2} is proportional to $\cos\phi$, a GRID line of a non-interacting particle would look exactly like $W'(\cos\phi)$. This is realized in the limiting case $\tau \longrightarrow 0$, i.e. for very short lifetimes.

9.2.2   Results using artificial data

A theoretical study is performed to check whether it would be possible to investigate the Si interatomic potential with Crystal-GRID if the lifetime τ was slightly longer. Artificial data are generated for three assumed true values τ^0 of the lifetime, 1 fs, 3 fs, and 5 fs. For every lifetime and three different crystal orientations, <100>, <110>, and <111>, 120 scans are used with a centre height $I_c = 30$ counts on a background $I_{bg} = 10$. Furthermore, 30 scans are generated with $I_c = 120$ on $I_{bg} = 40$, i.e. for an identical total measuring time subdivided into fewer scans.

Theoretical GRID lines are derived from RMD simulations using the ZBL potential with the screening length varied in between 75% and 125% of its original value a_s^0. These
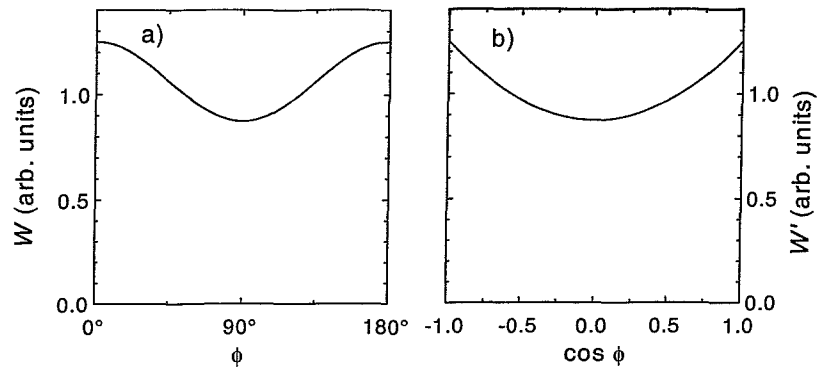
FIGURE 9.17: *Angular correlation function W or W' for electric dipole transition with spin states $\frac{1}{2}^+ \rightarrow \frac{3}{2}^- \rightarrow \frac{1}{2}^+$ a) as a function of ϕ b) as a function of $\cos\phi$.*
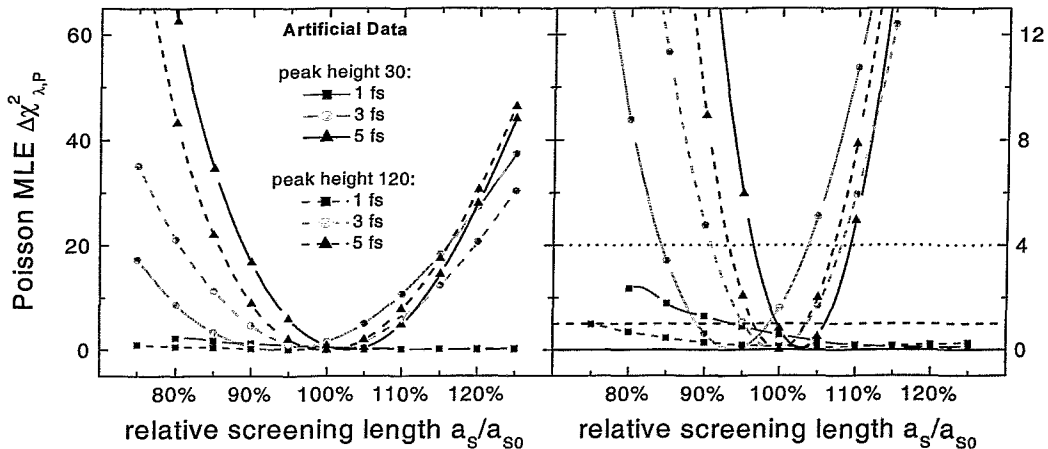
FIGURE 9.18: *Statistical variable $\Delta\chi^2_{\lambda,P}$ as a function of the relative screening length a_s/a_s^0. Theoretical GRID lines basing on potentials with different screening lengths have been fitted to three sets of artificial data. The 1 fs data are insensitive to the screening length, $\chi^2_{\lambda,P}$ does not change its value significantly. The two other sets show a clear dependence. The figure on the right gives an enlarged view.*

lines are fitted to the artificial data generated for $a_s = a_s^0$. The resulting values of $\Delta\chi^2_{\lambda,P} = \chi^2_{\lambda,P} - \chi^2_{\lambda,P}\big|_{min}$ are plotted in Fig. 9.18.

As expected, the data corresponding to a lifetime $\tau^0 = 1\,\text{fs}$ are insensitive to the screening length. The statistical variable $\chi^2_{\lambda,P}$ remains almost constant within the studied range. If one wanted to state a best value of the relative screening length, it is found to be much larger than the true 100%. However, the true value lies within the 1σ error. The value of $\Delta\chi^2_{\lambda,P}$ corresponding to a 1σ error is indicated by a straight dashed line in the enlarged view on the right side of Fig. 9.18, the straight dotted line corresponds to the 2σ error.

The sensitivity of the data to the screening length is significantly enhanced for higher

values of the lifetime. Both, for 3 fs and for 5 fs, the parameter can be optimized, i.e., already for a value of 3 fs, the interatomic potential becomes accessible. Consequently, a verification of the reported lifetime is very useful.

As already shown in Section 8.1, the sensitivity does not significantly depend on the number of scans into which the total measuring time is subdivided. It can be seen, however, that the screening length is better estimated by the data corresponding to a longer measuring time per scan ($I_c = 120$). For all three values of the lifetime, the estimate is closer to the true value than the estimate coming from the $I_c = 30$ data which, however, are also correct within two standard deviations.

9.2.3   Experimental Results

Encouraged by the theoretical results, a test measurement of the 4.934 MeV transition has been performed. Before the experiment, it was not possible to estimate the background intensity that largely influences the obtainable statistics, because the measured energy represents the highest energy ever measured in a GRID experiment. The spectrometer works at extremely small Bragg angles, which make a good shielding of the detector against the direct beam and small angle scattered photons very difficult. A certain fraction of the beam time was spent on the optimization of the shielding. Despite this effort, the background was still much higher than in prior experiments.

Data were taken at the GAMS 4 spectrometer with thick spectrometer crystals (4.41 mm and 6.95 mm, respectively) mounted to increase the efficiency. 15 scans (600 s per measuring point per scan) in diffraction order (1,2) were recorded during six days of measurements. For technical reasons, GAMS 5 could not be used at the time of the experiment.

Due to the low intensity of the studied transition as well as to the high energy of the photons to be detected, the experimental number of counts at a given measuring point is determined by adding the full-energy, single-escape and double-escape peaks of the Ge detector (compare Section 3.1). The experimental sum scan is plotted in Fig. 9.19a), showing that a signal-to-noise ratio of 530/340 ($\sum I_c \approx 190$, $\sum I_{bg} \approx 340$) is obtained.

To further enhance the number of counts, a second set of experimental data is defined by additionally considering the Compton scattered photons from the full-energy and the single-escape peaks, i.e. by counting all photons that are detected by the Ge detector in an energy window $\left[E^0_{\gamma_2} - 1.022\,\text{MeV}, E^0_{\gamma_2} \right]$. In this case, the background intensity is drastically enhanced, a signal-to-noise ratio of 4500/3850 ($\sum I_c \approx 650$, $\sum I_{bg} \approx 3850$) is obtained. The sum scan is displayed in Fig. 9.19b).

The collected intensity is very low, the background very high, in both cases. For comparison, the investigation using artificial data in the previous section assumed a summed centre height $\sum I_c = 3 \cdot 3600$ on a background $\sum I_{bg} = 3 \cdot 1200$.

Theoretical Crystal-GRID lines are calculated on the basis of RMD simulations using different interatomic potentials. Fitting these model lines to the two sets of experimental data, estimates of the level lifetime τ and minimum values of $\chi^2_{\lambda, P}$ are obtained. As can be seen in Table 9.5, the results are very similar for the different applied interatomic potentials.

However, comparing the two different sets of experimental data, the estimates of the lifetime are not identical. Neglecting the Compton scattered photons, a lifetime of about (3.5 ± 1.1) fs is obtained; including the additional counts, a value of $\left(2.2^{+0.9}_{-1.0}\right)$ fs is extracted.
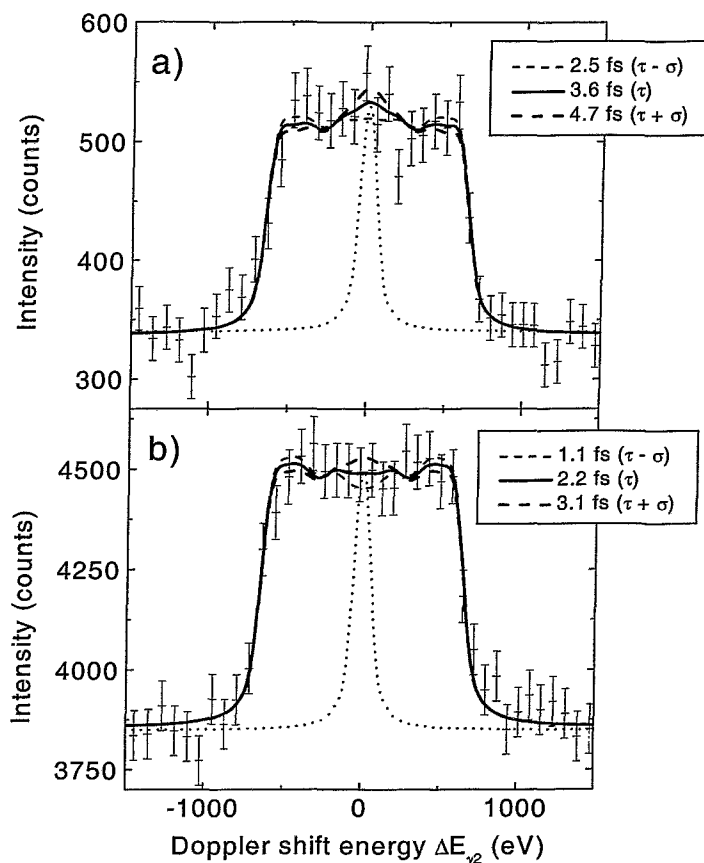
FIGURE 9.19: *Measurement of the 4.934 MeV transition in ^{29}Si, using single crystals oriented along the <100> direction. a) The experimental data contain the full-energy, single-escape, and double-escape peaks of the detector. Three different theoretical lines (simulated using the ZBL potential) are plotted — for the fitted lifetime τ as well as for the lifetimes $\tau \pm \sigma_\tau$. The statistical errors of the data points are larger than the details of the structure. b) The experimental data are formed by additionally including the Compton scattered photons. The fitted lifetimes of the two approaches overlap within the statistical errors.*

		KrC	KrC–SW	ZBL	goodness-of-fit Q
sum of peaks	τ (fs)	3.4 ± 1.0	3.4 ± 1.0	3.6 ± 1.1	45%
	$\chi^2_{\lambda,P}$	(1142.2)	(1142.4)	(1142.4)	
sum of peaks + Compton	τ (fs)	$2.2^{+0.9}_{-1.0}$	2.2 ± 0.9	$2.2^{+0.9}_{-1.1}$	25%
	$\chi^2_{\lambda,P}$	(1154.9)	(1154.6)	(1155.0)	

TABLE 9.5: *Resulting estimates of the lifetime and minimum values of $\chi^2_{\lambda,P}$. The evaluation is performed with two sets of experimental data, using RMD simulations on the basis of three different interatomic potentials.*

Even though the difference is quite large, the estimates are consistent, as their 1σ errors overlap.

The GRID lines corresponding to the fitted lifetime τ, as well as to $\tau + \sigma$, and to $\tau - \sigma$, are also plotted in Fig. 9.19. It can be clearly seen that the statistical errors of the data points are larger than any fine structure in the theoretical lines.

Full MD simulations are not performed, as the error due to the RMD approximation (compare Section 8.3.1) is much smaller than the intrinsic error σ_τ of the measurement related to the insufficient statistics (30%...50%).

Due to the large error of the lifetime estimates, it can not finally be decided whether the reported lifetime of the 4.934 MeV nuclear level, $\tau = (1.22 \pm 0.18)$ fs, is incorrect. However, it is probable that the true lifetime is longer by a factor of 2 or 3.

As the study of atomic motion in silicon is an extremely important task, the experiment is continued. Unfortunately, the measurements could not be finished before the end of this work. It can be estimated that the determination of the nuclear level lifetime to an error[5] $\sigma_\tau = 0.3$ fs necessitates a total number of counts increased by a factor of 10 (compare Eq. (8.1)). This can be achieved by using both spectrometers during a measuring period of approximately one month.

---

[5]purely statistical error, disregarding the influence of the unknown potential

9.3 Results – Titanium Dioxide (TiO$_2$)

The aim of this work is to show whether interatomic potential functions can be optimized by Crystal-GRID measurements. The measurements using ZnS or Si single crystals did not finally answer this question, as they were not or only very little sensitive to the potential. For that reason, a better suited solid was needed. As can be seen from Fig. 3.8 (compare also Appendix C), Cl and Ti are the nuclei that yield the highest count rates.

The 1.498 MeV transition in ^{49}Ti has already been used in a number of powder GRID experiments. This transition is emitted from the 3.261 MeV level, which is mostly primarily fed (95%) [Bur 95]. The relevant part of the decay cascade is shown in Fig. 9.20.

The lifetime of the 3.261 MeV level was found to be about 15 fs [Bör 88, Kur 91]. However, the estimate of the lifetime depends on the assumptions of the slowing down. As usual, the evaluation of powder GRID measurements is performed using the MFPA theory on the basis of a BM potential.

The 1.498 MeV transition has also been used in the very first Crystal-GRID measurements using single crystals of SrTiO$_3$ in three different crystal orientations, as well as TiO$_2$ in one orientation [Jen 96b, Jen 97a]. Nicely structured lines were obtained. However, statistics was not good enough to extract precise information on the lifetime, as well as on the interatomic potentials. Furthermore, the Crystal-GRID experiments using SrTiO$_3$ showed inconsistencies because different lifetime values were measured for different crystal alignments [Jen 97a].

The aim of the current experiment is to optimize the interatomic potential and to determine the nuclear level lifetime, at the same time. This would be the final prove that Crystal-GRID is, in principle, suited for the investigation of interatomic potentials. Furthermore, it will be checked whether the lifetime estimates for different crystal orientations are consistent and the unknown angular correlation function will be determined.
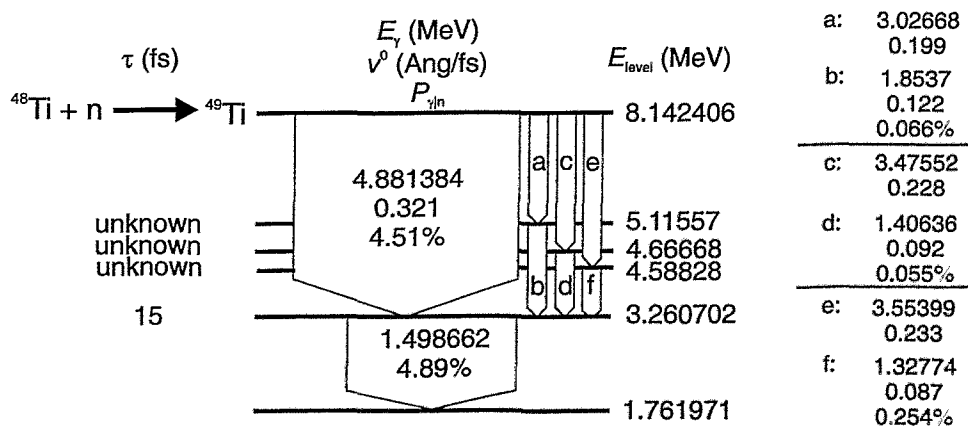
FIGURE 9.20: *Partial level scheme of ^{49}Ti [Bur 95]. For each level of energy E_{level}, the reported lifetime τ is given (if known). For the transitions, the photon energy E_γ, the corresponding initial recoil velocity v^0 of the S nucleus, and the absolute intensity $P_{\gamma|n}$ of the transition (% refers to the number of captured neutrons) are given.*
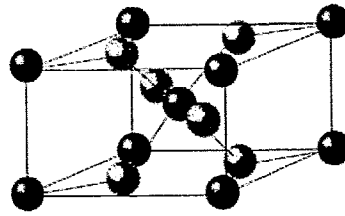
FIGURE 9.21: *Unit Cell of TiO₂ in the rutile structure (figure taken from [Jen 97a]).*

orient. <hkl>	GAMS (year)	order (n/m)	numb. scans	m. time per point (min)	centre h. $\sum I_c$ (counts)	backg. $\sum I_{bg}$ (counts)	excess w. σ_{ew} (fringes)
<110>	4 (1996)	(2/2)	21	112	322	339	0.203
<100>	4 (1999)	(2/2)	56	318	2075	1010	0.311
<100>	5 (1999)	(2/2)	51	204	830	52	0.213
<001>	4 (1999)	(2/2)	21	84	628	148	0.299
<001>	5 (1999)	(2/2)	53	265	871	62	0.141
<110>	4 (2000)	(2/2)	30	150	793	370	0.181
<110>	5 (2000)	(2/2)	46	184	928	88	0.171

TABLE 9.6: *Details on the measurements with TiO₂ single crystals using the 1.499 MeV transition in ^{49}Ti. The first row gives the details of the 1996 measurement by Jentschel. Conversion from fringe to eV is possible by the factor 33.88 eV/fringe for GAMS 4 and 27.12 eV/fringe for GAMS 5.*

9.3.1 Experimental Details

New measurements have been performed within this work, using three different crystal orientations of TiO₂. Fig. 9.21 shows the unit cell of rutile, the stable crystal structure of titanium dioxide in the relevant temperature range. Details about the measurements are summarized in Table 9.6. The first row corresponds to the 1996 measurement of Jentschel, showing that the signal-to-noise ratio has been improved drastically within the last four years. Especially, GAMS 5 yields a very low background intensity. Due to this, the fine structure of the Crystal-GRID lines becomes more pronounced in the new measurements.

As in the case of ZnS, intensive reference scans have been measured in between the scans of the transition under study. Applying a linear drift correction for the <110> measurements at both spectrometers, the consistency of model lines and data decreases. The goodness-of-fit is reduced from 53% to 24% for the GAMS 4 measurement and from 25% to 21% for GAMS 5. Obviously, the linear approximation to the drift function does not allow to improve the data. As the drift within the scans is expected to have only little influence on the results, it has not been tried to apply higher order corrections. Instead, the drift correction is disregarded in the evaluation.

A single scan is displayed in Fig. 9.22. The Doppler broadening can be clearly seen, the fine structure, however, is mostly hidden by the statistical noise. It becomes visible in the experimental sum scans, as shown in Fig. 9.23. As predicted, symmetric shapes are found that differ strongly for the different crystal orientations.
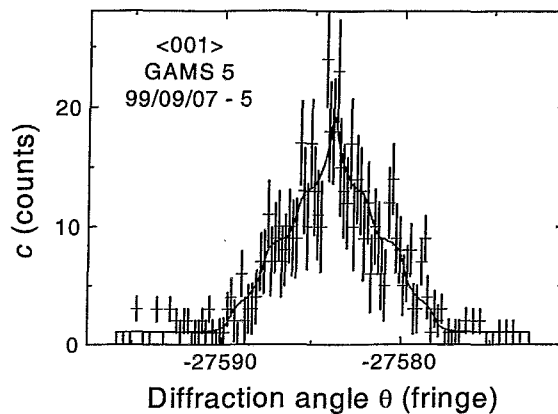
FIGURE 9.22: *Single scan (no. 99/09/07–5) of the* 1.499 MeV *transition in* [49] *Ti measured with the GAMS*5 *spectrometer. The Doppler broadening can be seen in a single scan, most of the fine structure is hidden by the statistical noise, however.*

9.3.2 Improving the interatomic potential (RMD)

RMD calculations are performed with the purely repulsive screened Coulomb potentials ZBL, KrC, and GH. The screening length of the first two potentials is varied in the range of 75% to 125% of the original value a_s^0. The GH potentials for the interactions Ti–O, Ti–Ti, and O–O have been calculated by Gärtner [Gär 00].

Fitting the derived theoretical Crystal-GRID lines to the experimental data by optimizing the local parameters as well as the nuclear level lifetime, minimum values of the Poisson MLE $\chi^2_{\lambda,P}$ and estimates of the lifetime are obtained. As can be seen in Fig. 9.24a), the screening length of both, the KrC and the ZBL potential can be optimized to a good precision. Within the range of screening lengths studied, the difference between lowest and highest value of $\chi^2_{\lambda,P}$ is of the order of 300. This is ten times more than in the ZnS measurement (compare Fig. 9.5), immediately showing that TiO$_2$ is much better suited for an investigation of interatomic potentials.

The result of the GH potential is nearly indistinguishable from the result for the KrC potential with the original screening length. It yields a slightly worse description than the optimized KrC or ZBL potential.

The optimized values of the screening length are listed in Table 9.7. Including the angular correlation (assumption of pure M1 transition, see Section 9.3.4), the goodness-of-fit is slightly reduced. However, the resulting values of the optimized screening length do not change significantly.

Fig. 9.24b) plots the values of $\chi^2_{\lambda,P}$ as a function of the estimated lifetime. It can be seen that a consistent value of the lifetime is obtained for both optimized potentials. A similar observation has already been made by Jentschel basing on only one measurement [Jen 97a, Figures 6.6 and 6.7]. He further showed that the optimized potentials have a similar functional run. Whether the value of the lifetime is reliable, it can only be said after optimizing an interatomic potential for the full energy range using full MD simulations.

As in ZnS, the lifetime and the screening length are strongly correlated (see Fig. 9.25). Increasing the screening length, the potential becomes more repulsive. The recoiling atoms
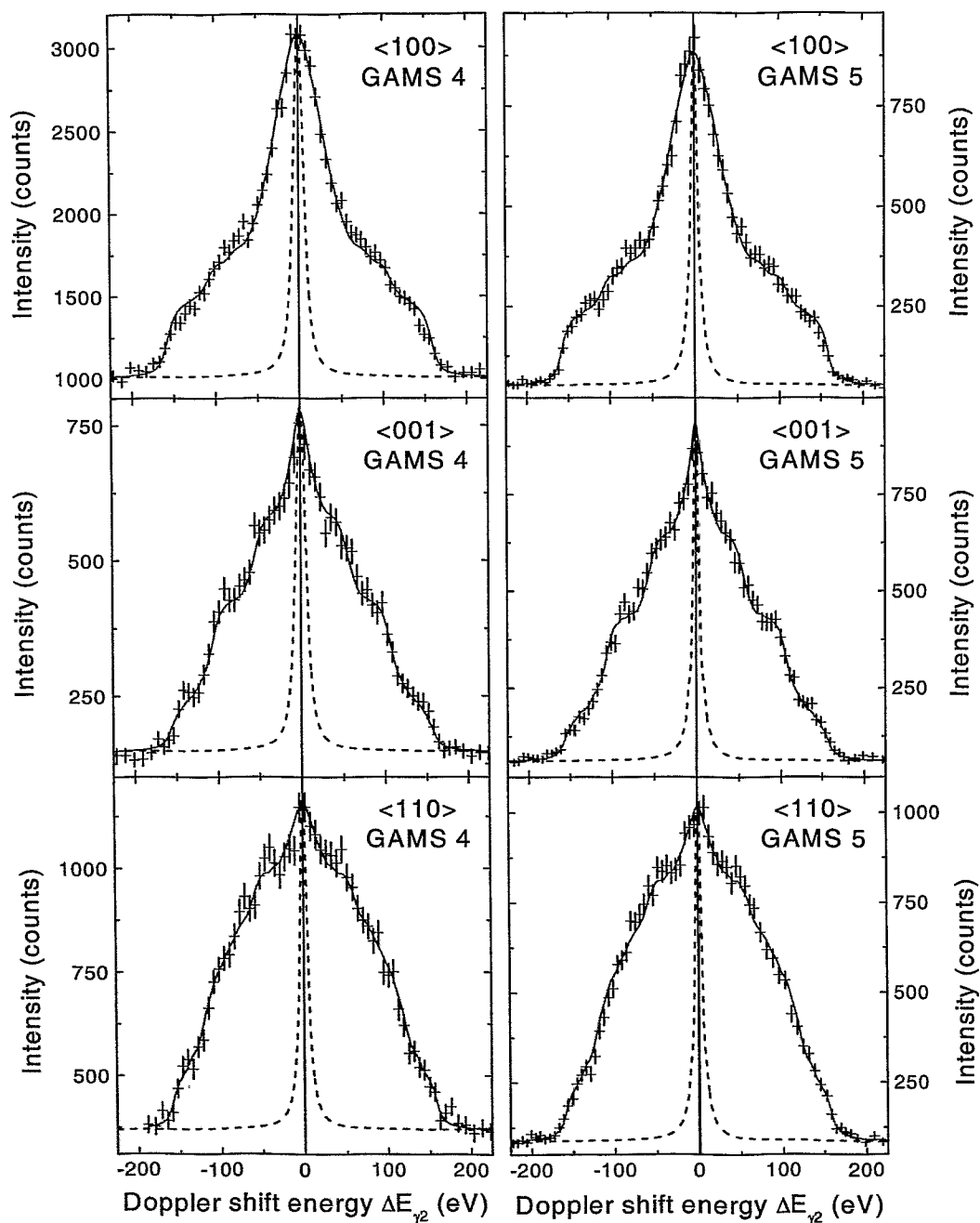
FIGURE 9.23: *Sum scans of the six new measurements with TiO₂ single crystals. The summed fitted Crystal-GRID lines are plotted with straight lines, the instrumental response functions with dashed lines. The measurements yield nicely structured sum scans that differ strongly in the different crystal orientations.*
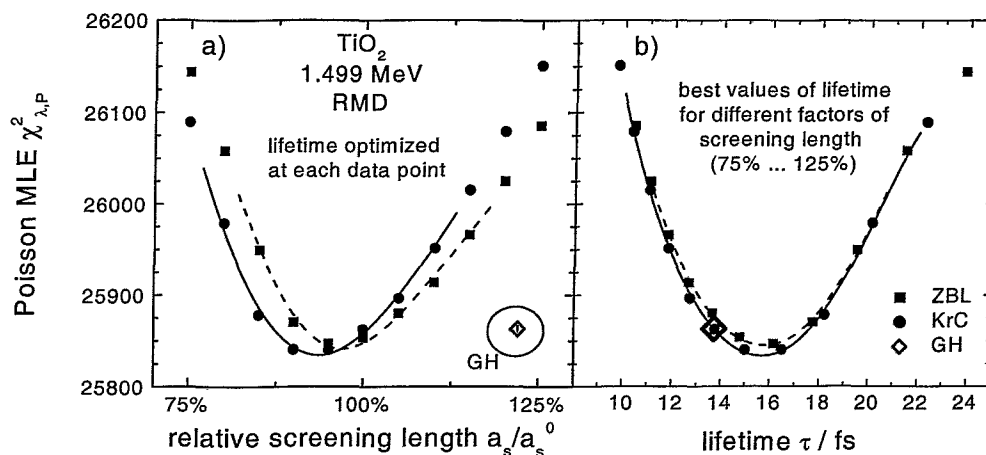
FIGURE 9.24: *Optimization of the screening length using RMD simulations by fitting model lines to the experimental TiO$_2$ data. a) The Poisson MLE $\chi^2_{\lambda,P}$ shows a clear dependence on the screening length a_s. The optimized KrC and ZBL potentials slightly better reproduce the experimental TiO$_2$ data than the GH potential. b) Both, the optimized KrC and ZBL potentials, yield consistent values of the lifetime. The GH result is almost indistinguishable from the result of the original (100%) KrC potential.*

ang. corr.	potential	optimized a_s/a_s^0	$\chi^2_{\lambda,P}\vert_{\min}$	Q
neglected	KrC	$(92.6 \pm 2.6)\,\%$	25837	23%
	ZBL	$(95.8 \pm 2.6)\,\%$	25845	22%
	GH		25863	20%
M1	KrC	$(91.9 \pm 2.4)\,\%$	25855	21%
	ZBL	$(95.3 \pm 2.4)\,\%$	25870	20%
	GH		25888	18%

TABLE 9.7: *Results of the optimization of the screening length a_s using RMD simulations. The data have been evaluated, both neglecting and taking into account the angular correlation. The errors of the optimized screening lengths correspond to 2σ errors.*

are slowed down more quickly leading to an enhanced intensity in the centre of the simulated Crystal-GRID line. Reducing the nuclear level lifetime, the central intensity is reduced and a compensation can be obtained. However, the studied scans are sufficiently structured and intense, in order to determine both parameters, the screening length and the lifetime, at the same time.

Values of the goodness-of-fit Q above 20% indicate that the purely repulsive screened Coulomb potentials applied in the RMD simulations are already suited to describe the slowing down. Even the mean ZBL potential with its original screening length gives a relatively good approximation to the true interaction.

This is astonishing, as the initial kinetic energy E_{kin}^0 of the recoiling atom is only 261 eV. Consequently, the maximum potential energy tested by the actual measurement is less than 75 eV for the Ti–O interaction, and less than 130 eV for the Ti–Ti interaction, the potential energies obtained in a head-on-collision with the neighbouring atoms. It can be expected
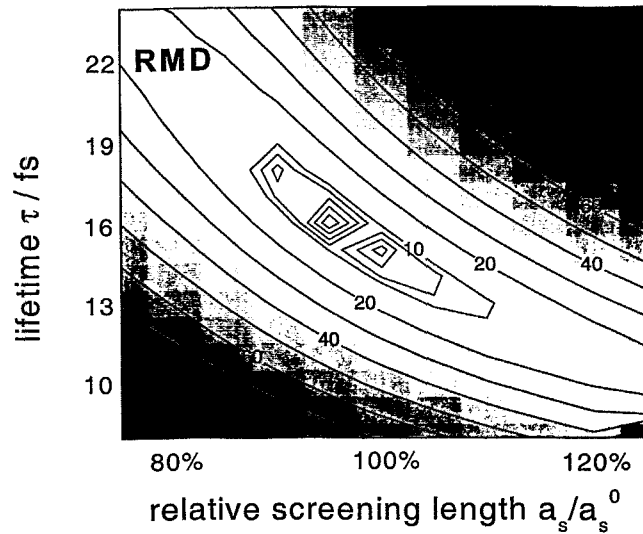
FIGURE 9.25: *Correlation of the nuclear level lifetime τ and the screening length. The numbers within the line give the quantity $\sqrt{\chi^2 - \chi^2|_{min}}$, i.e. the number of standard deviations that the actual parameter values are worse than the optimal choice. Even though a strong correlation exists between the lifetime and the screening length, both parameters can be simultaneously determined. A global minimum can be found as seen in Figure 9.24.*

that using an adopted equilibrium part for the low-energy region and performing full MD calculations, the agreement of theoretical lines and data can be further improved.

However, long-range Coulomb interactions have to be considered in MD simulations for ionic materials. This requires to use the Ewald method in the MD simulations. As this technique is not implemented in the code developed within this work for the simulation of semiconductors, first full MD simulations for TiO_2 have been performed by Jentschel who had studied ionic compounds during his thesis [Jen 97a]. Due to the application of the Ewald technique, the MD simulations are very slow. Until the end of this work, only a small number of simulations could be finished, each of them consisting of no more than 1000 trajectories in the main branch. The optimization of the switch parameters and of the ZBL screening length is actually in progress.

9.3.3   First results from MD simulations

An equilibrium potential for TiO_2 has recently been published by Kim *et al.* [Kim 96]. First full MD simulations have been performed using this potential for the equilibrium part and the universal (ZBL) potential for the high-energy part. The switching is performed by the switch function s_1 (Eq. (1.15)). It has been started to optimize the presumably most important switch parameters, namely r_0 of the Ti–Ti and Ti–O interactions. By varying both values between $0.8\,\text{Å}$ and $1.1\,\text{Å}$, the statistical variable $\chi^2_{\lambda,P}$ is changed by about 400, showing that the measurement is sensitive to these parameters. However, a final best set of parameters could not yet be found. In the following, the values as given in Table 9.8 will be used. They currently lead to the best consistency of model lines and experimental data.

interaction	r_0 (Å)	δr (Å)
Ti–Ti	0.9	0.10
Ti–O	0.7	0.05
O–O	0.7	0.20

TABLE 9.8: *Switch parameters used in the MD simulations for TiO₂.*
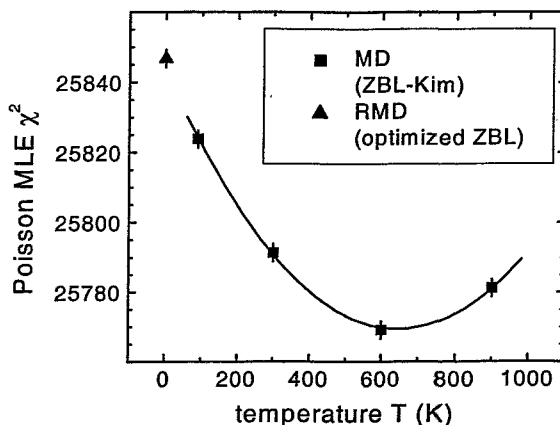
FIGURE 9.26: *Determination of the sample temperature by fitting theoretical Crystal-GRID lines for different sample temperatures to the experimental TiO₂ data. The result of the RMD simulation at 0 K is also plotted.*

First of all, the sample temperature is determined. Usually, the temperature of GRID samples is estimated from the thermal broadening of a very long-lived level. However, the thermal broadening only reflects the "temperature" of the recoiling atoms which is not necessarily identical to the sample temperature. The recoiling atoms deposit energy in their environment. Even for long-lived levels, with lifetimes of typically a few 1000 fs, the heat is not completely dissipated, the surrounding rests at enhanced temperatures. Throughout this work, this situation is called "quasi-thermal".

Furthermore, many recoiling atoms will take on interstitial lattice sites after several hundreds of fs. It is far from obvious that the temperature, i.e. the average kinetic energy, of interstitial atoms is identical to the temperature of atoms in the optimal lattice.

The temperature of the TiO₂ samples is determined in a different way. Trajectories for the transition under study are calculated in simulation cells, equilibrated at different temperatures. Fitting the derived Crystal-GRID lines to the experimental data, the true sample temperature is expected to yield the best consistency, i.e. the lowest value of $\chi^2_{\lambda,P}$. As shown in Fig. 9.26, the temperature can be determined to 600 K, approximately. For comparison, the 0 K RMD result is also plotted. The sample temperature has only a small influence on Crystal-GRID lines. A more precise determination, e.g. by repeating the above calculation for the optimized potential, is not necessary.

The temperature can only be determined from full MD simulations, as RMD simulations do not consider the interactions among the sample atoms, they do not correctly describe the bulk sample. The MD values of $\chi^2_{\lambda,P}$ obtained from the MD simulations are better than the RMD values for all temperatures, proving that the combined ZBL–Kim
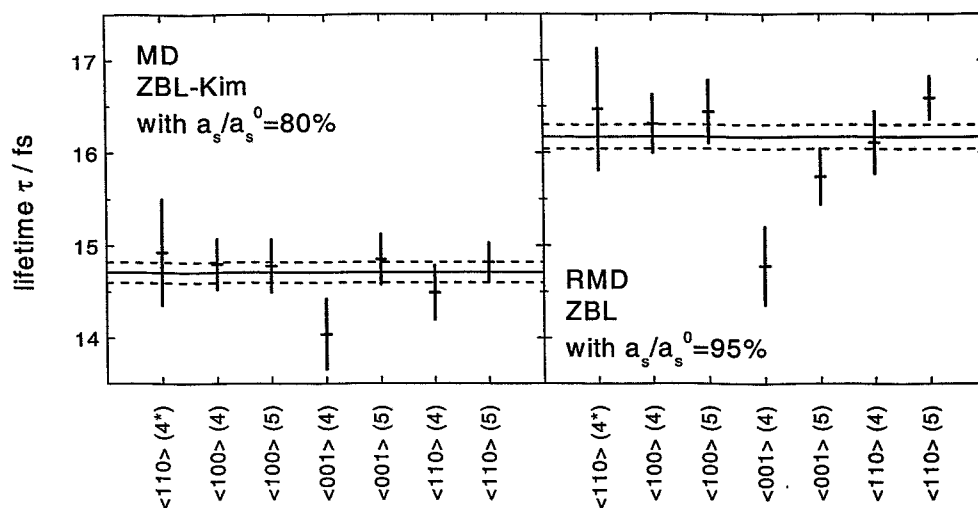
FIGURE 9.27: *Lifetime estimates when fitting the series of scans separately. The lifetime esti-mates are consistent, only one value of the RMD evaluation lies more than two standard devia-tions away from the global estimate indicated with a straight line (dashed line = error of global estimate). Also, the old measurement of 1996 (<110> (4*)) is consistent with the new mea-surements. The lifetime estimates of the MD approach are systematically lower than the RMD estimates. This is mainly related to the different potentials applied. As the MD potential is not yet optimized, the lifetime estimates of the MD are only preliminary.*

potential is even better suited to describe the slowing down of the recoiling atoms than the purely repulsive screened Coulomb potentials. The goodness-of-fit is $Q = 32\%$ for the 600 K measurement.

As said before, Jentschel had observed inconsistencies in his $SrTiO_3$ measurements. Evaluating the series of scans for different crystal orientations separately, the derived values of the lifetime were not consistent. Since these measurements, two major improvements have been realized: the signal-to-noise ratio of the spectrometers could be significantly enhanced, and, within this work, a new fitting code has been developed.

The resulting estimates for the seven series of TiO_2 scans are displayed in Fig. 9.27, evaluated using both, RMD and MD simulations. In the new measurements, the values coincide very well. Only one RMD estimate differs significantly from the global estimate which statistically is not impossible. As stated at the end of Section 8.1, lifetime estimates do *not* differ for different crystal orientations, even if the potential is not optimally suited, as the RMD potential in this case. The difference between RMD and MD estimates can mainly be explained by the different potential applied and the correlation between lifetime and potential. However, a final statement can only be made after the potential parameters of the combined potential have been optimized.

9.3.4 Angular Correlation

Until this work, angular correlation in Ti has always been neglected in the evaluation of GRID data, mainly because the correlation function is not exactly known. The spin
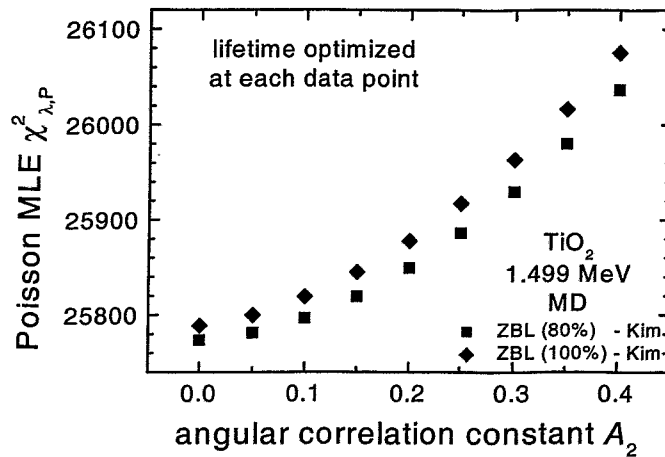
FIGURE 9.28: *Determination of angular correlation constant A_2. The consistency of model lines and experimental TiO$_2$ data increases with decreasing A_2. Consequently, the lowest possible value, namely $A_2 = 0.05$, best describes the data. The 1.499 MeV transition is a pure M1 transition. Astonishingly, the consistency is further enhanced by completely neglecting the angular correlation. This is to be verified with a further improved potential.*

states of the two-step cascade (compare Fig. 9.20) are $\frac{1}{2} \rightarrow \frac{3}{2} \rightarrow \frac{5}{2}$. In order to determine the angular correlation function W', it must be known which kind of transition occurs between the different states. This is not exactly known for the 1.499 MeV transition (γ_2). The most probable assumption is that this transition is purely M1. In this case, the angular correlation would be very weak. If the transition is 50% M1 and 50% E2, however, it would be much stronger [Leh 99].

$$ W'(\cos\phi) = \begin{cases} 1 + 0.05 \cdot P_2(\cos\phi) & \text{for } \gamma_2\text{: M1} \\ 1 + 0.41 \cdot P_2(\cos\phi) & \text{for } \gamma_2\text{: 50\% M1, 50\% E2} \end{cases} \qquad (9.4) $$

As can be seen, the constant A_2, as defined in Eq. (2.6), lies in between 0.05 and 0.41. In order to determine the correct correlation function and thereby the kind of transition between the two nuclear states, Crystal-GRID lines have been derived for different values of A_2. The resulting values of $\chi^2_{\lambda,P}$ are plotted in Fig. 9.28 for two different interatomic potentials, the combined ZBL–Kim potentials with relative screening lengths of 80% and 100%, respectively.

As can be seen in the figure, the best consistency of model lines and data is achieved for the lowest value of A_2. Consequently, the 1.499 MeV transition is found to be a pure M1 transition, and the correct value of $A_2 = 0.05$. Astonishingly, disregarding the angular correlation leads to a slightly better consistency than the pure M1 transition. However, the difference is small, much smaller than the difference to other possible values of A_2. It can be expected that for the optimized interatomic potential, the calculation yields a global minimum at $A_2 = 0.05$.

9.4   Results – Metals (Cr, Fe, Ni)

A series of Crystal-GRID measurements has been carried out mainly by Nicolas Stritt and Jan Jolie from the University of Fribourg in Switzerland. The results have been published in [Str 99a, Str 99b, Str 99c, Str 00]. The studied transitions are listed in Tables 9.9 and 9.10. For further details refer to the cited publications.

The data evaluation has been performed using the evaluation code `griddle` [RobJol 90] basing on Neyman's χ_N^2 statistic, thus possibly leading to partially incorrect results. For this reason, the results are re-evaluated with the new fitting code `gravel`, developed in this work and described in Section 6.3. As will be seen, especially the interpretation has to be revised after thoroughly looking at the absolute values of χ^2 instead of concentrating on the reduced χ^2, as defined in Eq. (6.20).

The aim of this section is to re-analyse the data of Stritt *et al.* with respect to the statistics applied and not to repeat the complete study of interatomic potentials. Consequently, the experimental data as well as most of the simulations are taken from Stritt *et al.* New simulations have only been performed occasionally, mainly to underline detected insufficiencies. If the side feeding, or the angular correlation have been neglected in the original evaluation, these approximation have also been adopted.

	E_{γ_1} (MeV)	E_{kin}^0 (eV)	$|v^0|$ (Å/fs)	E_{level} (MeV)	reported τ (fs)	reported τ (GRID) (fs)	prop. direct feed.	$E_{\gamma_2}^0$ (MeV)
^{54}Cr	6.64564	440	0.40	3.07410	<25 [a] $2.4^{+1.2}_{-1.0}$ [b]	12.9 ± 0.7 [A1] 10.3 ± 0.5 [A2]	98%	2.23907
^{54}Cr	5.99995	358	0.36	3.71991	<43 [a] 10^{+8}_{-5} [b]	31 ± 5 [A1] 24 ± 2 [A2]	97%	3.71984
^{57}Fe	5.92035	337	0.34	1.72542	36 ± 12 [c] 47 ± 9 [d]	62 ± 6 [B1] 38 ± 3 [B2]	91%	1.72529
^{57}Fe	4.21798	171	0.24	3.42767	<5 [d]	$4.3^{+0.9}_{-4.2}$ [B1]	100%	2.72117
^{59}Ni	6.58385	396	0.36	2.41497	48 ± 11 [e] 60 ± 30 [e]	79^{+12}_{-13} [C1]	95%	1.95005
^{59}Ni	4.85861	216	0.27	4.14034	none	$8.5^{+1.9}_{-1.7}$ [C1] 6.5 ± 1.4 [C2]	96%	3.67523

TABLE 9.9: *Studied transitions (Cr: [Jun 93], Fe: [Bha 98], Ni: [Bag 93]). The table gives the nuclei after neutron capture, the energy E_{γ_1} of the first photon entailing the recoil, the initial kinetic energy E_{kin}^0 and velocity $|v^0|$ of the recoiling nucleus, the intermediate nuclear level energy E_{level}, the reported values of the nuclear level lifetime, the proportion of direct feeding of this level, and the unshifted energy $E_{\gamma_2}^0$ of the second photon used in the measurement. — Non-GRID lifetimes from: a) DSAM [Stu 80], b) Gamma-Ray Induced Doppler Shift Attenuation (GRIDSA) [Kov 91] (see also [Kah 97]), c) DSAM in $(n,n'\gamma)$, d) centroid shift in $(d,p\gamma)$ [Ulb 89], e) DSAM [Pic 74] (see also [And 83]). — GRID lifetimes: A) GRID (called DSA in this paper) [Lie 88] [Ulb 91a, p. 54], B) GRID [Ulb 89] [Ulb 91a, p. 59], C) GRID [Ulb 91b] [Ulb 91a, p. 64] — 1) evaluation using MFPA approach with BM potential, 2) evaluation using MD simulation and ZBL potential [Kur 92].*

	E_{γ_2} (MeV)	orient. $<hkl>$	order (n/m)	no. scans	time / point (min)	$\sum I_c^k$ (c.)	$\sum I_{bg}^k$ (c.)	σ_{ew} (fr.)	conversion (eV/fr.)
^{54}Cr	2.239	$<100>$	(1/2)	36	120	781	457	0.242	100.8
		$<110>$	(1/2)	37	123	966	784	0.268	100.8
	3.719	$<100>$	(1/1)	5	33	256	36	0.242	417.5
		$<110>$	(1/1)	6	40	373	74	0.268	417.5
^{57}Fe	1.725	$<100>$	(2/2)	20	80	1051	335	0.248	44.91
		$<110>$	(2/2)	25	100	1092	384	0.234	44.91
		$<110>$	(2/3)	8 *)	43	185	86	0.234	35.9
	2.721	$<100>$	(1/1)	35	140	1059	220	0.248	223.4
		$<100>$	(1/1)	6	24	163	22	0.213	223.4
		$<110>$	(1/1)	27	108	714	68	0.234	223.4
^{59}Ni	1.950	$<100>$	(1/1)	7	19	337	12	0.256	114.7
		$<100>$	(1/2)	34	136	1363	117	0.256	76.48
		$<111>$	(1/2)	12	53	384	33	0.260	76.48
	3.675	$<100>$	(1/1)	12	60	203	51	0.256	407.5
		$<100>$	(1/2)	16	112	66	44	0.256	271.5
		$<111>$	(1/1)	15	75	217	56	0.260	407.5
		$<111>$	(1/2)	17	119	97	187	0.260	271.5

TABLE 9.10: *Experimental details of the Cr, Fe, and Ni measurements at GAMS4 measured in 1997 and 1998 by Stritt et al. The table lists the nucleus after neutron capture, the energy E_{γ_2} of the measured transition, the orientation of the metal crystals with respect to the spectrometer, the diffraction order of the spectrometer crystals, the number of scans, the total measuring time per data point summed over all scans (one scan contains approximately 60 to 100 data points), the fitted centre heights and background levels summed over all the scans as well as the excess width and the conversion factor needed to convert fringes to eV. *) Scans not considered in the evaluation.*

The MD simulations are mostly based on screened Coulomb or embedded-atom method (EAM) potentials, the applied interatomic potentials are listed in Table 9.11. As discussed in Section 1.2.2, the EAM potentials consist of two contributions, one for the equilibrium state and one for the short-range interactions. While the equilibrium part is individually designed for all of these potentials, different standard pair potentials with individually adjusted parameters are used for the repulsive pair interaction term. The potentials are applied in effective pair potential approximation, they are illustrated in Fig. 9.29. As can be seen, the run of the potential curves differs significantly, both, in the equilibrium region and for intermediate energies. Consequently large differences in the statistical variable χ^2 or in the correlated value of the lifetime τ are expected.

The initial kinetic energy E_{kin}^0 of the recoiling atom is of the order of 200 eV to 400 eV (see Table 9.9). For atoms of almost equal mass, the maximum potential energy in a head-on-collision equals approximately half of the kinetic energy of the moving atom. Consequently, the presented Crystal-GRID measurements are sensitive to energies below 100 eV to 200 eV, approximately. This energy is far above the range for which EAM potentials are developed. Consequently, the actual measurements test the low-energy

potential	potential form	Cr	Fe	Ni	authors (reference)
BM	$A_{BM} \exp\left(-r/B_{BM}\right)$	x 1)	x 1)	x 1)	Born, Mayer [Abr 69]
ZBL	$\sim \Phi\left(r\right)/r$	x 1)	x 1)	x 1)	Ziegler, Biersack, Littmark [Zie 85]
OMS	BM 3) + special		x		Osetsky, Mikhin, Serra [Ose 95]
OP	BM 3) + cubic	x	x		Ogorodnikow, Pokropivny [OgoPok 91]
PAIR	sum of cubic terms		x		Baskes, Melius [BasMel 79]
RAJ	sum of cubic terms		x		R. A. Johnson [Joh 64]
EAM ATVF	sum of cubic terms			x	Ackland, Tichy, Vitek, Finnis [Ack 87]
EAM BSS	BM 3)	x	x	x	Bhuiyan, Silbert, Stott [Bhu 96]
EAM FBD	$\sim \exp\left(-br\right)/r$			x	Foiles, Baskes, Daw [Foi 85, Foi 86]
EAM GA	sum of cubic terms	x	x		Guellil, Adams [GueAda 92]
EAM OJ	BM 3)			x	Oh, Johnson [OhJoh 88]
EAM PFS	polynomial	x 2)	x		Pasianot, Farkas, Savino [Pas 91]
EAM VC	Morse		x	x	Voter, Chen [VotChe 87]
EAM WB	special form	x 2)			Wang, Boerker [WanBoe 95]

TABLE 9.11: *Potentials used in the evaluation of the metal data. For the EAM potentials, the column "potential form" gives only the repulsive pair interaction Φ^{EAM}. — 1) As the BM and ZBL potentials are only repulsive, the potentials are switched to a Morse potential $(D\left[\exp\left(-2\alpha\left(r-r_0\right)\right)\right) - 2\exp\left(-\alpha\left(r-r_0\right)\right)]$ [GirWei 59]) for distances near the equilibrium distance. — 2) The repulsive part of the potential is insufficient to give reasonable results: a repulsive term of the BM type, called BM* in the text, with individually chosen parameters has been added to the potential. — 3) The parameters of the BM potential are individually adjusted for the potential.*

region of the repulsive pair interaction as well as the equilibrium part.

9.4.1   Chromium (Cr)

In chromium, two different nuclear transitions have been studied. The neutron capture entails the reaction $^{53}_{24}Cr(n,\gamma)^{54}_{24}Cr$. The capture state is 9.720 MeV. The details of the transitions are listed in Table 9.9.

Simulations have been performed by Stritt for seven different interatomic potentials (see Table 9.11) [Str 99c]. Theoretical GRID lines can easily be calculated from these simulations and be fitted to the experimental data. The sum scans of the measurements are displayed in Fig. 9.30 together with the summed fit and the instrumental response functions. The broadening of the 2.239 MeV transition is much larger than the instrumental response function (dashed line) which determines the resolution of the measurement. The measured sum scans clearly contain fine structure which differs significantly in the different crystal orientations. Consequently, this transition is better suited for GRID measurements than the measurements of the 3.719 MeV transition displayed in the same figure where the resolution is very low leading to non-structured sum scans.

Fig. 9.31 shows a comparison of the GRID lines calculated using the different potentials and fitted to the experimental data in the case of the <100> measurement of the 2.239 MeV transition. Obviously, it is impossible to judge with the naked eye which fit is best and thus which potential is best suited. As discussed in Section 7.3, two criteria are in principle
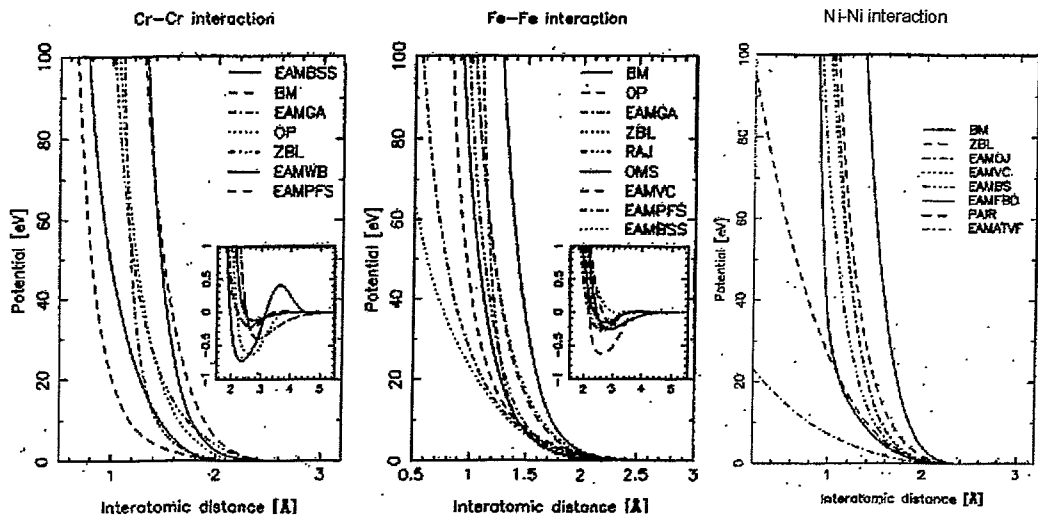
FIGURE 9.29: *Comparison of the interatomic potentials applied in the evaluation of the metal data. The potentials, supposed to describe one interaction, differ strongly, both in the equilibrium region and for intermediate energies. Consequently, significant differences in the consistency of deduced Crystal-GRID lines and experimental data are expected (figures taken from [Str 99c, Str 00]).*

applicable to choose among the different potentials. On the one hand, the best potential should yield the lowest value of $\chi^2_{\lambda,P}$. On the other hand, the value of the lifetime has to be consistent with reported values, experimentally determined by other methods. In the case of chromium, only reliable upper limits for the lifetimes have been measured by other means than GRID measurements. One Gamma-Ray Induced Doppler Shift Attenuation[6] (GRIDSA) measurement has been published in [Kov 91]. The reported lifetimes are given in Table 9.9, they are systematically lower than other values. As they have only been published in a one-page conference publication without any explanation, the values are only little credible.

In Fig. 9.32, the results for the 2.239 MeV transition, obtained within this work, are opposed to the ones by Stritt *et al.* The values of the level lifetimes do not differ more than their standard deviation in most of the cases. The incorrectness of the statistic used in the old evaluation has no strong influence on these values. However, the values of χ^2 change. As discussed by Stritt *et al.*, the original potentials EAM WB and EAM PFS did not "give reasonable values" [Str 99c]. Therefore, a BM potential with freely chosen parameters, called BM* in this work, has been added by Stritt *et al.* As can be seen in the upper left picture of Fig. 9.32, the minimum χ^2 was obtained with the BM*/EAM WB potential according to the old evaluation. The new evaluation shows that the BM*/EAM PFS potential leads to a slightly better fit.

Besides comparing different potentials, Stritt *et al.* optimized the screening length of the ZBL potential by varying the parameter x (see Eq. (1.6)). In the upper right picture of Fig. 9.32, χ^2 is plotted as a function of the relative screening length, a function of x. Stating the 1σ error, the new evaluation leads to a minimum at $a_s/a_s^0 = \left(83^{+5}_{-7}\right)\%$,

---

[6]This is not GRID, but a DSA technique.
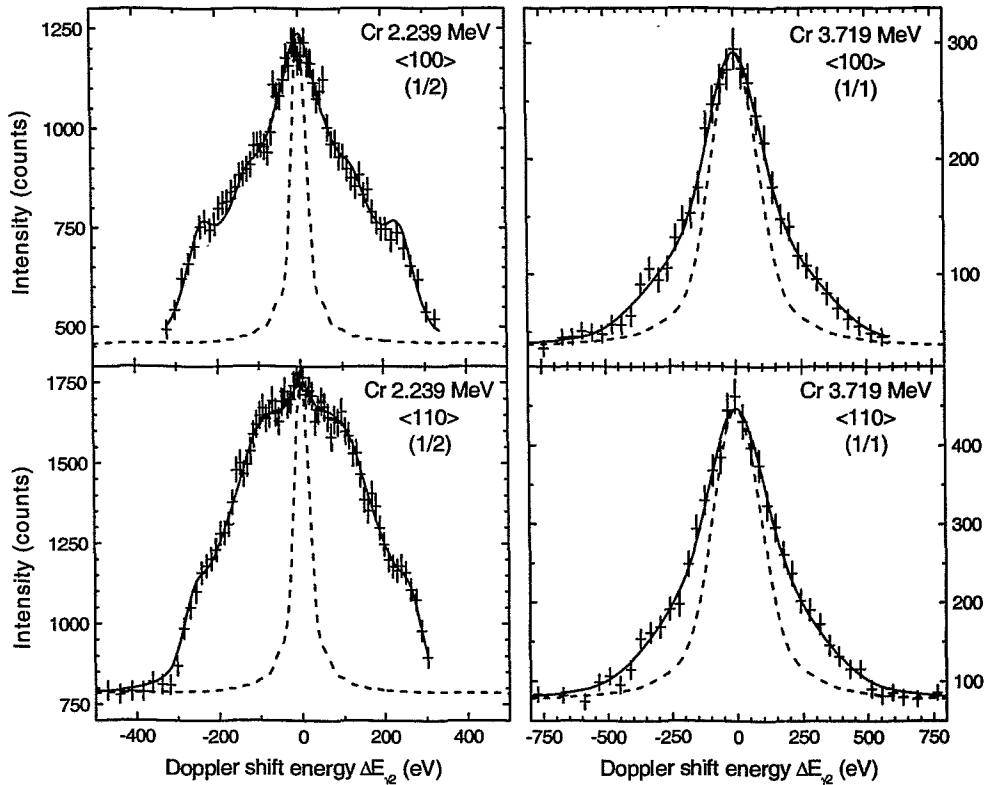
FIGURE 9.30: *Summed experimental data of the measured transitions in Cr. The solid line gives the summed best fit, the dashed line the instrumental response function of the spectrometer. The 2.239 MeV yield nicely structured sum scans, while the resolution of the 3.719 MeV GRID lines is not sufficient.*

corresponding to $x = 0.29^{+0.03}_{-0.02}$. Including the error of approximately ± 3 of χ^2 itself, a conservative estimate of the error limits would be twice as big. Even in this case, however, the standard value ($x = 0.23$, relative screening length 100%) lies outside the obtained range. The old evaluation by Stritt *et al.* gives a value of $x = 0.31 \pm 0.02$. Even though this value is consistent with the new evaluation, the new evaluation leads to a much smoother run of the curve $\chi^2 (a_s)$, especially around the minimum and for relative screening lengths below 60%.

Taking into account the error of approximately ± 3 of χ^2 itself, the modified embedded-atom potentials BM*/EAM WB and BM*/EAM PFS as well as the ZBL potential optimized with respect to the screening length (called 'ZBL (aS)' in the plot) lead to similarly good fits.

A huge spread is found when looking at the estimates for the nuclear level lifetime obtained with the different potentials (see lower part of Fig. 9.32). The minimum value of (5.1 ± 0.1) fs is obtained with the EAM BSS potential, the maximum value of (22.7 ± 0.5) fs with the BM*/EAM PFS potential. In the literature, only a reliable upper limit of 25 fs determined with DSA can be found [Stu 80]. The results of *all* fitted potentials are consistent with this upper limit. Only by varying the relative screening length of the ZBL potential below 55%, the limit can be violated. The published value of $\left(2.4^{+1.2}_{-1.0}\right)$ fs [Kov 91]
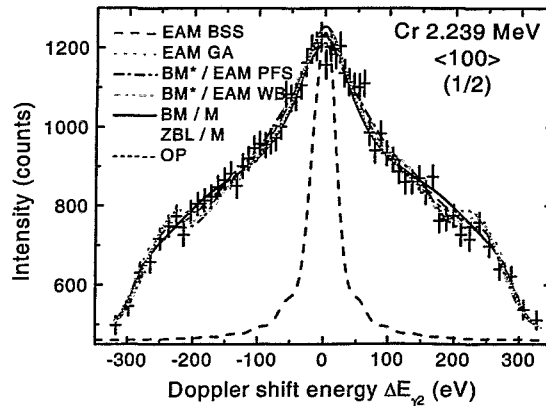
FIGURE 9.31: *Comparison of the best fits using seven different interatomic potentials. The fit has been performed to the 2.239 MeV transition in Cr. All models seem to yield a good agreement with the experimental data. With the naked eye, a distinction is not possible.*

can not be reproduced by any potential.

The lower right picture of Fig. 9.32 compares the lifetimes obtained for the two orientations when they are fitted independently. For the evaluation, the ZBL potential is applied with varied values of the screening length. A comparison with the data by Stritt *et al.* is omitted, as the values are very similar. As discussed in Section 8.1, the selection of a best potential was originally thought to be possible by looking for the parameter value where the independently fitted estimates of the lifetime for different crystal orientations coincide. Also in Cr, however, the estimates coincide for any value of the screening length within the error. The same behaviour can be found when looking at the other potentials studied. Only in one case, the difference is about two standard deviations.

The optimized ZBL potential gives a lifetime of $\left(12^{+4}_{-3}\right)$ fs taking into account the 2σ error of the screening length. The other two "best" potentials yield (14.4 ± 0.3) fs (BM*/EAM WB) and (22.7 ± 0.5) fs (BM*/EAM PFS), respectively. The latter two errors are purely statistical. As can be seen in Fig. 9.29, the "best" potentials are very different from each other. The discrepancy of the lifetimes shows that it is insufficient to compare reported potentials and that the optimization needs to be continued.

In order to check which value is correct, and thus to obtain a best interatomic potential, the potentials need to be optimized. As the BM*/EAM PFS estimate of τ differs strongly from the other two values, it is tried to optimize its BM potential parameters. The reported values for the parameters are $A^0_{BM} = 10606$ eV and $B^0_{BM} = (1/3.58663)$ Å $= 0.278813$ Å in the case of Cr [Abr 69]. Instead of switching between the high-energy and the equilibrium parts, Stritt added a BM potential with the parameters $A^0_{BM} = 3606$ eV and $B^0_{BM} = 0.17882$ Å [Str 99c]. These values are not motivated within the publications.

MD simulations are performed using the BM/EAM PFS potential with the two original BM parameters multiplied independently by a factor in the range of 50% to 150%. For a good comparison to the results of Stritt *et al.*, the two potentials are added. The resulting values $\sqrt{\Delta\chi^2_{\lambda,P}}$ are displayed in Fig. 9.33. A similar behaviour is obtained in RMD simulations using only the repulsive BM potential. The best consistency is obtained for values $A_{BM} \approx 70\% \cdot A^0_{BM}$ and $B_{BM} \approx 75\% \cdot B^0_{BM}$. For a precise determination of best values,
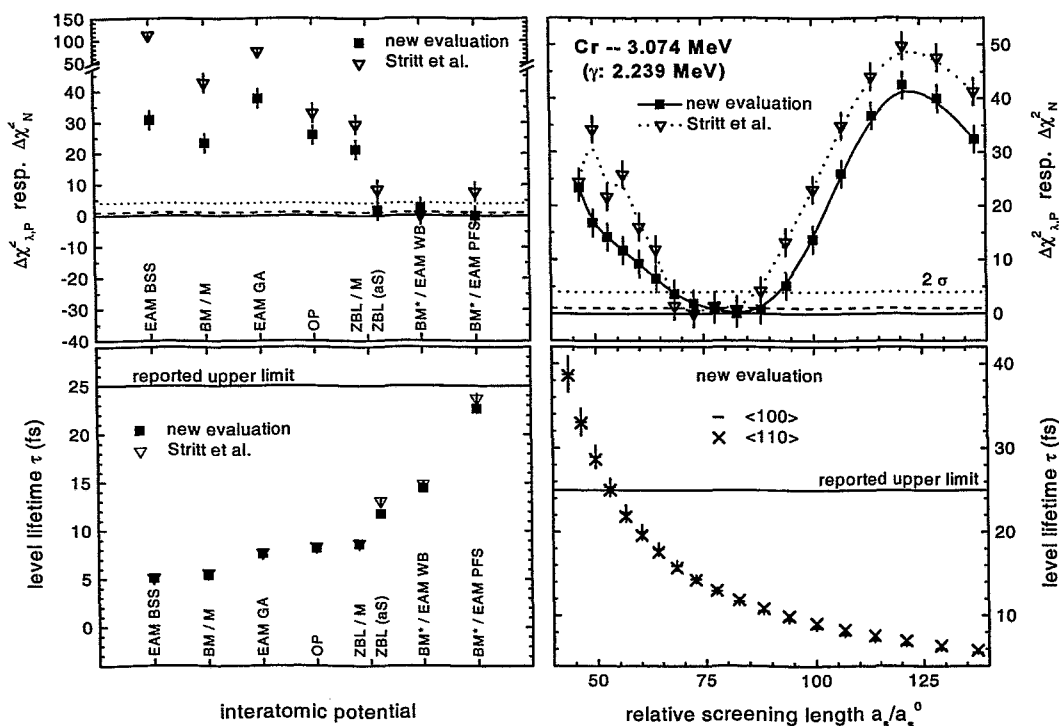
FIGURE 9.32: *Results of the fit – 2.239 MeV transition in Cr. The consistency of the model GRID lines deduced from different potentials with the data is judged by the Poisson MLE $\chi^2_{\lambda,P}$ (new evaluation) or by χ^2_N (Stritt et al.) Different potentials are compared (top left) and the screening length of the ZBL potential is optimized (top right). The corresponding estimates of the lifetime are plotted in the lower half. For further details refer to the text.*

further simulations are necessary. However, it can already be shown that this potential better describes the data than the one used by Stritt *et al.*, the absolute value of $\chi^2_{\lambda,P}$ is smaller by 30, approximately.

As the ZBL potential is said to be the best mean potential for the high-energy part, a further investigation is based on a combined ZBL/EAM PFS potential. As usual, the two potentials are combined by the switch function s_2, the parameters are chosen to $r_0 = 1.4\,\text{Å}$ and $\xi = 10$. Varying the screening length a_s of the ZBL potential, an optimization can be achieved, the best value of the screening length is found to be $a_s/a_s^0 = (91 \pm 15)\,\%$ stating the 2σ error. The result is shown in Fig. 9.34. The lifetime is determined to a value of $(12 \pm 2)\,\text{fs}$, including the 2σ error due to the uncertainty of the potential parameters.

The optimized BM/EAM PFS potential yields a lifetime estimate of $\left(12^{+3}_{-2}\right)\,\text{fs}$. The obtained values of $\chi^2_{\lambda,P}$ for the two series of simulations are plotted as a function of the lifetime estimates in the right part of the figure, underlining that both parameter optimizations yield consistent values of the lifetime. The value, obtained by Stritt *et al.*, is also plotted. Obviously, the parameters of the added BM potential were not optimally chosen. The obtained lifetime is higher by a factor of 2 than for the optimized potentials.

This example proves that in order to optimally extract information from Crystal-GRID data, it is necessary to optimize the potential parameters of the different interatomic
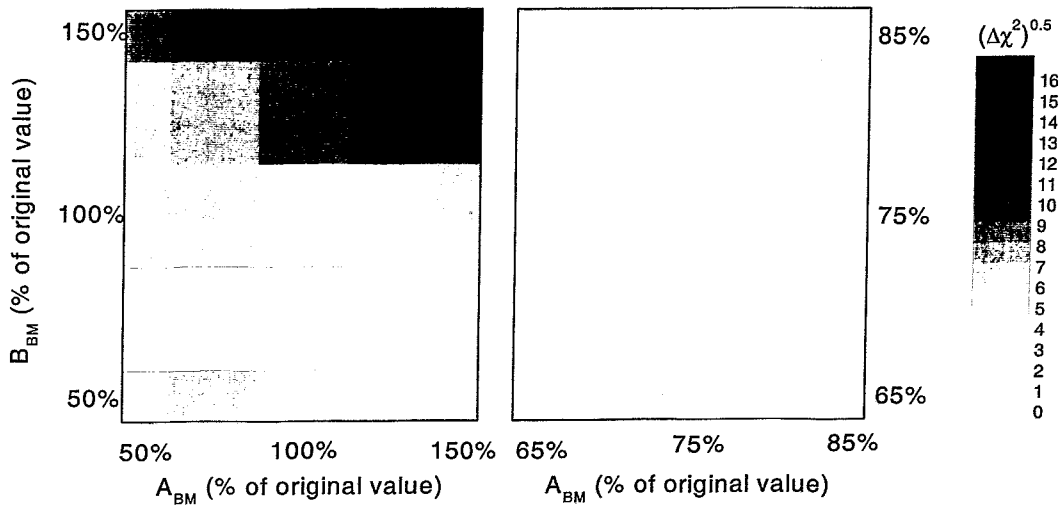
FIGURE 9.33: *Optimization of BM parameters - 2.239 MeV transition in Cr. Simulations are performed with modified BM/EAM PFS potentials where the two parameters A_{BM} and B_{BM} are varied between 50% and 150% of their published values. The picture shows $\sqrt{\Delta\chi^2_{\lambda,P}}$ as a function of the two parameters. On the right side, a close view around the optimal parameters is given. It can be clearly seen that the original values are not optimal in the studied energy range. The parameters, chosen by Stritt et al. lie outside the studied region.*
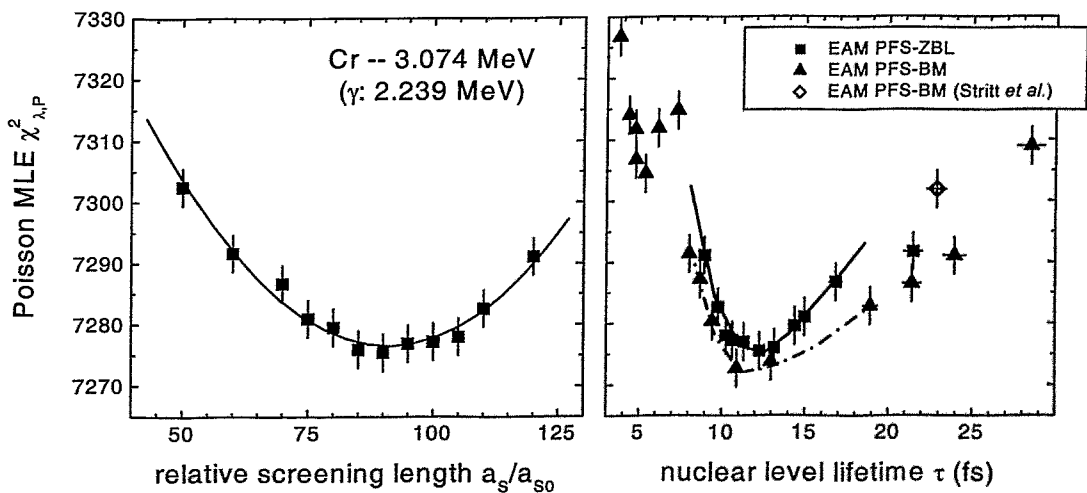
FIGURE 9.34: *Optimization of potential parameters of potentials basing on the EAM PFS potential. The screening length of the ZBL potential can be optimized (left side). Plotting the obtained values of $\chi^2_{\lambda,P}$ as a function of the estimates of the lifetime, a consistent value of the lifetime can be determined to (12 ± 2) fs for both optimized potentials.*
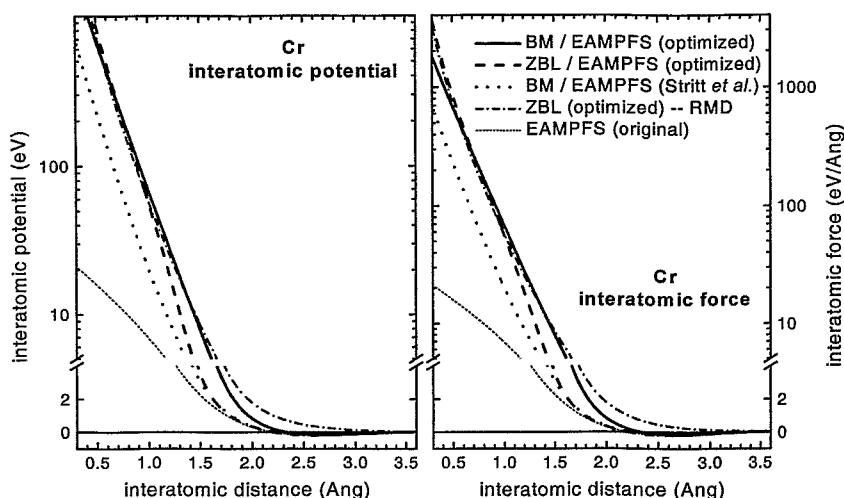
FIGURE 9.35: *Optimized interatomic potentials in Cr. The newly optimized potentials differ significantly from the one found 'best' by Stritt et al. and to the original EAM PFS potential. The two optimized full potentials BM / EAM PFS and ZBL / EAM PFS are close to each other, even though differences exist due to the different functional forms.*

potentials to be compared. Some of the potentials are plotted in Fig. 9.35. It can be seen that the optimized potentials are relatively close to each other. Of course, differences due to the functional form still exist. The original EAM PFS potential as well as the improved BM*/EAM PFS potential as used by Stritt *et al.* differ strongly from these newly found potentials.

The second transition studied was the 3.719 MeV transition. The results are displayed in Fig. 9.36. All potentials lead to similar values of χ^2, a selection following this criterion, as done by Stritt *et al.*, is not possible. Consequently, an optimization of the ZBL screening length is not performed, no sufficient variation of χ^2 is expected. The 'ZBL (aS)' value in the figure corresponds to the optimized screening length of the 2.239 MeV transition. The obtained values of the lifetime vary in a range going from (16 ± 1) fs to (74 ± 4) fs. Again, the reported GRIDSA value of $\left(10^{+8}_{-5}\right)$ fs [Kov 91] is much lower than the estimated values.

Only the BM*/EAM PFS potential, with the BM parameters as chosen by Stritt *et al.*, leads to a value significantly higher than the reported upper limit of 43 fs [Stu 80]. This can be explained by the unsuited parameters of the BM potential, that also lead to a wrong lifetime in the previous evaluation.

Stritt *et al.* concluded that the BM*/EAM WB potential is best suited and thus adopted the corresponding estimates of τ for both nuclear levels, i.e. a value of (14.8 ± 0.3) fs for the 3.074 MeV level, and (44 ± 3) fs for the 3.719 MeV nuclear level. As discussed, this result is not correct. Furthermore, the error margin is taken only from one potential. As shown for the 2.239 MeV transition, the potentials need to be further optimized. Still neglecting the angular correlation, the new value for the 3.074 MeV level lifetime is (12 ± 2) fs, including the uncertainty of the potential parameters.

The goodness-of-fit Q for the 2.239 MeV and 3.719 MeV transitions is 3% and 19%, re-
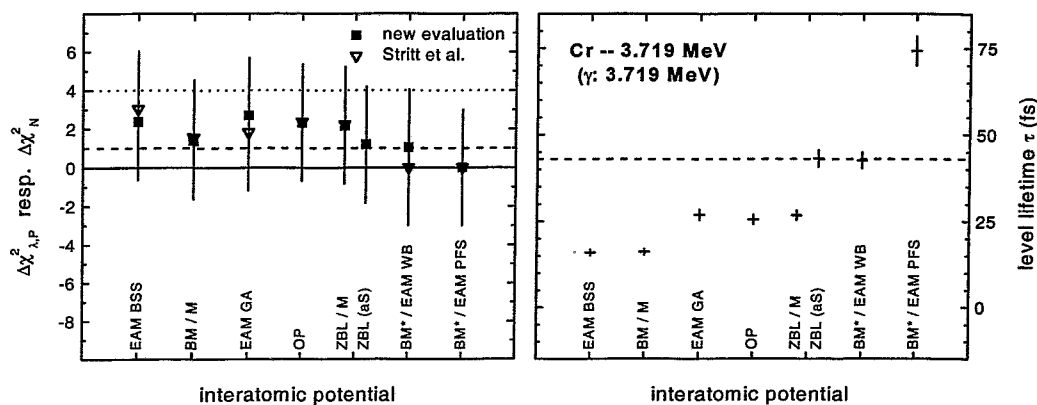
FIGURE 9.36: *Results of the fit – 3.719 MeV transition in Cr. All models yield similarly good fits (left side). However the estimated values for the nuclear level lifetime vary in a huge range. All estimates but one are consistent with the reported upper limit of 43 fs.*

spectively. Both values indicate that the model is sufficient to describe the data. However, a further optimization may be possible.

9.4.2 Iron (Fe)

Two transitions have been chosen for Crystal-GRID measurements using iron (Fe) single crystals. The 2.721 MeV transition is emitted from a level with a short lifetime below 5 fs, the 1.725 MeV transition originates from a level with a lifetime of approximately 45 fs (see Table 9.9). In the first case, the initial recoil velocity is 0.24 Å/ fs (see Table 9.9). Most of the secondary photons are emitted before the recoiling atoms could collide with the nearest neighbour which is 2.5 Å away. Their velocity is therefore only little altered. The expected GRID line resembles a lot the free-atom box-like structure (compare Section 5.2.1).

The second nuclear level treated is rather long-lived. Many nuclei can travel far through the crystal, finally reaching quasi-thermal velocities, and contributing only to the un-shifted, central peak of the GRID line. Much of the fine structure in the wings is hidden by the dominant central peak.

The described features can be found in the sum scans shown in Fig. 9.37. The GRID lines of the 2.721 MeV transition differ for the two crystal orientations. The plateau is broader in the <110> orientation. Hardly any difference can be detected for the 1.725 MeV transition, where the resolution is not sufficient to resolve any fine structure.

Fig. 9.38 shows the results of the 2.721 MeV transition. Within the error, all potentials lead to similar values of χ^2. The goodness-of-fit Q equals 18% which proves a good consistency of all model GRID lines with the data. Furthermore, all fitted values of the lifetime are consistent with the reported upper limit[7] of 5 fs [Ulb 89]. Only the EAM BSS potential yields a lifetime slightly larger, but within $2\sigma_\tau$ of the upper limit. No selection of a potential becomes possible from this measurement.

---

[7] The reported value of $\left(4.3^{+0.9}_{-4.2}\right)$ fs, cited in [Str 99c, Figure 4], originates from a GRID measurement, and is thus not independent of the new measurements.

FIGURE 9.37: *Summed experimental data of the measured transitions in Fe. The solid line gives the summed best fit, the dashed line the instrumental response of the spectrometer, i.e. the resolution of the measurement.*

Stritt *et al.* then tried to optimize the screening length of the ZBL potential. As can be seen in the upper right picture of Fig. 9.38, they find a minimum of χ^2 for a relative screening length of approximately $90\%^{+50\%}_{-20\%}$ ($x = 0.27^{+0.08}_{-0.16}$) [Str 99c]. Even though the given error, deduced from the increase of χ^2 by 1, is huge already, it does not include the error of χ^2 itself. The new evaluation does not even find a minimum. This drastically proves that it is not possible to draw any conclusions if the variations of χ^2 are as small as in this case.

In principle, for a lifetime as short as 4 fs, angular correlation needs to be considered. As the potentials cannot be distinguished by the measurement and all of them yield a good fit ($Q = 18\%$), no try will be made to determine the unknown angular correlation. No significant improvement of the results can be expected.

The investigation of the 1.725 MeV transition has been more successful, as can be seen in Fig. 9.39. Two interatomic potentials can be excluded due to their high values of χ^2, the EAM PFS and EAM BSS potentials. As in Cr, the EAM PFS potential does not yield "reasonable results". In this case, it was not tried to add a BM type potential, however. The EAM VC and BM/Morse potentials can probably also be excluded, however the difference in χ^2 is not as pronounced. The remaining potentials ZBL/Morse, OP, RAJ, EAM GA, and OMS all yield good consistency of the model GRID lines with the experimental data. The goodness-of-fit Q is about 17%, which quantitatively supports this conclusion.
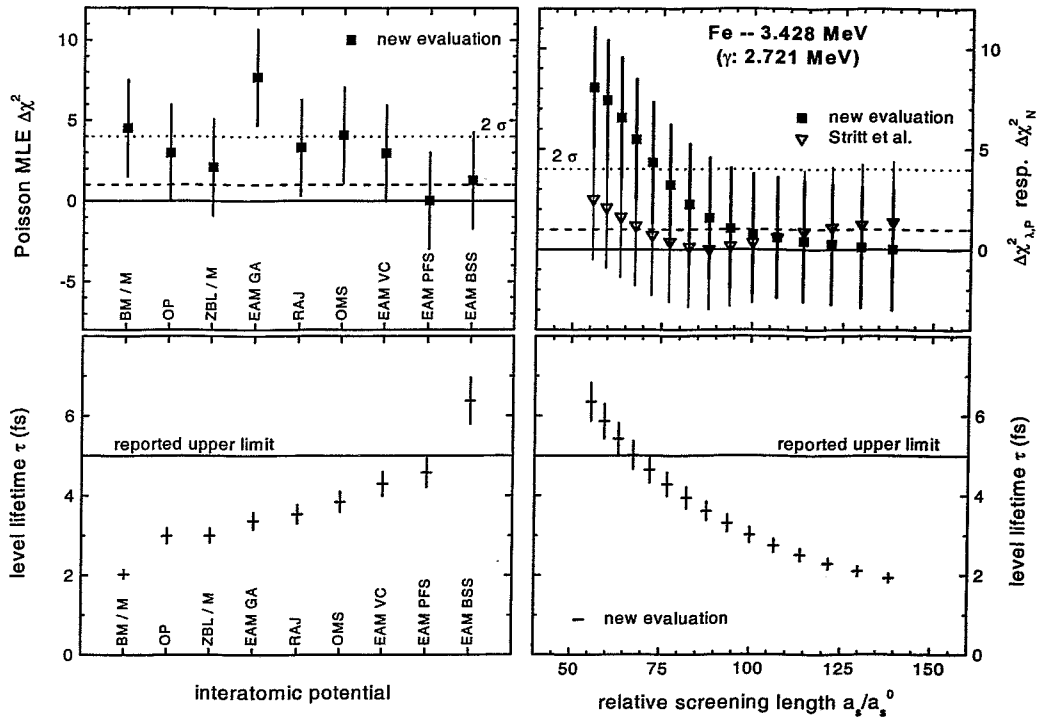
FIGURE 9.38: *Results of the fit – 2.721 MeV transition in Fe. The comparison of different potentials (top left) as well as the optimization of the screening length in the ZBL potential (top right) do not yield big differences for the Poisson MLE $\chi^2_{\lambda,P}$ (new evaluation) or χ^2_N (Stritt et al.) A discrimination of potentials is not possible. The related estimates of the 3.428 MeV level lifetime vary approximately from 2 fs to 6 fs (bottom). Nearly all estimates are consistent with the reported upper limit of 5 fs [Ulb 89].*

Again, the potentials have very different functional runs, and the similar values of χ^2 are only obtained due to the correlation of interatomic potential and nuclear level lifetime. An optimization of the single potentials seems to be necessary. A higher total number of counts would probably also allow to better discriminate between the potentials. Taking the five potentials as best candidates, a nuclear level lifetime for the 1.725 MeV level can be fixed to 38^{+7}_{-8} fs. Being more conservative and including the BM/Morse and EAM VC potentials in the error of the lifetime, a value of 38^{+16}_{-20} fs would be obtained. The reported lifetime is (36 ± 12) fs or (47 ± 9) fs from two different measurements [Bha 98], consistent with the newly obtained value.

Stritt *et al.* concluded in their paper that the EAM VC potential was the best even though six of the other potentials lead to a better agreement between theory and experiment. They did not look for the best χ^2 value but excluded all potentials but the EAM VC and OMS potential, because their estimates of the lifetime lie outside the reported error. As reference value, Stritt *et al.* used a reported lifetime of (48 ± 7) fs that is supposed to be extracted from [Bha 92] (value taken from [Str 99c, Figure 4]). However, the given reference lists multiple values for the 1.725 MeV level lifetime, as (61 ± 6) fs from GRID [Ulb 89], (36 ± 12) fs from DSA and (46 ± 9) fs from centroid shift in (d,pγ) [Ulb 89]. As
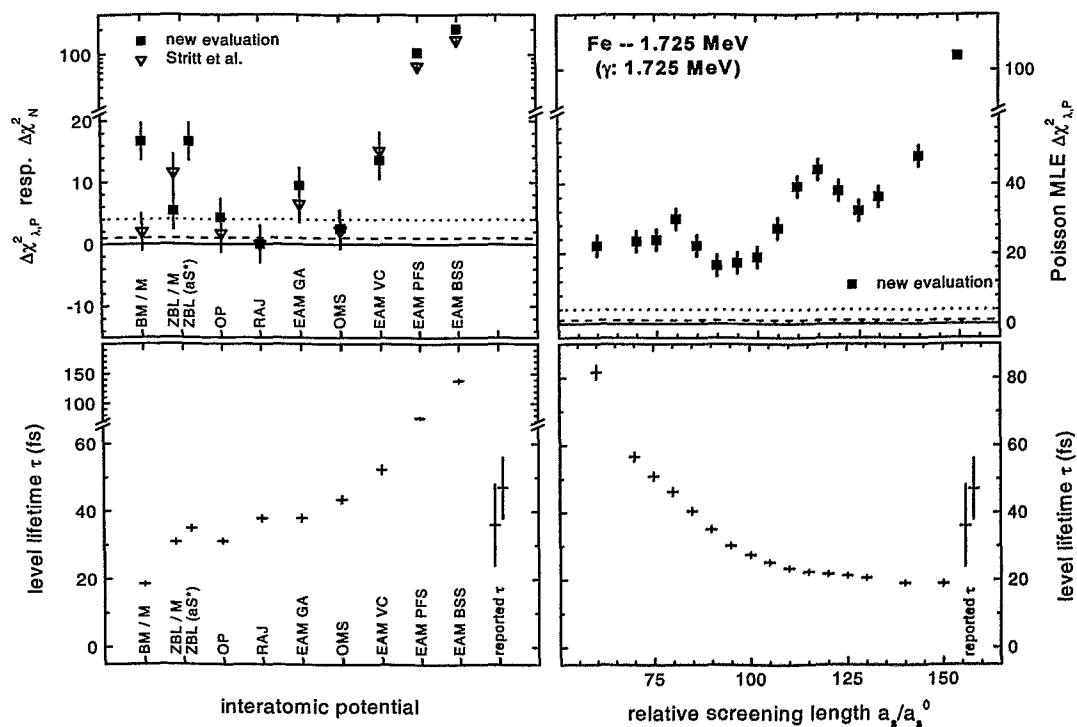
FIGURE 9.39: *Results of the fit – 1.725 MeV transition in Fe. Two potentials can be easily excluded due to their bad values of χ^2 (top left). Their estimates of the lifetime are also far away from the experiental values (bottom left). All the other potentials differ only little. The results previously obtained by Stritt et al. differ in some important details from the new ones (top left). An optimization of the ZBL screening length becomes possible (top right). However, the χ^2 values are worse than the best ones obtained with potentials including an attractive part.*

can be seen in the lower left picture of Fig. 9.39, most potentials yield lifetime estimates compatible with these experimental values. The lifetime criterion certainly has some relevance, in principle, but it is absolutely necessary to only exclude potentials that give estimates very far off the reported values, like for the EAM BSS potential. In this latter case, however, the χ^2 criterion comes to the same conclusion. The lifetime determined in [Str 99c] is (52 ± 3) fs. From the considerations presented here, the error given is much too small and even the value of the lifetime is probably wrong.

As the optimization of the screening length of the purely repulsive ZBL potential in the 2.721 MeV transition had not been successful, new RMD simulations have been performed for the 1.725 MeV transition. The result of the fitting is displayed in the right part of Fig. 9.39. A minimum can be found around a value of 90%. However, the $\chi^2(a_s)$ curve looks unusual due to three local minima. Furthermore, the RMD minimum of χ^2 using a purely repulsive potential is about 18 higher than the minimum χ^2 obtained with the best potential in a full MD calculation using potentials including an equilibrium part. This probably indicates that the equilibrium part of the potential is not negligible.

In all of the evaluation, only the main feeding of the 1.725 MeV level has been taken into account. A 9% side feeding by multiple transitions has been ignored. Stritt *et al.*
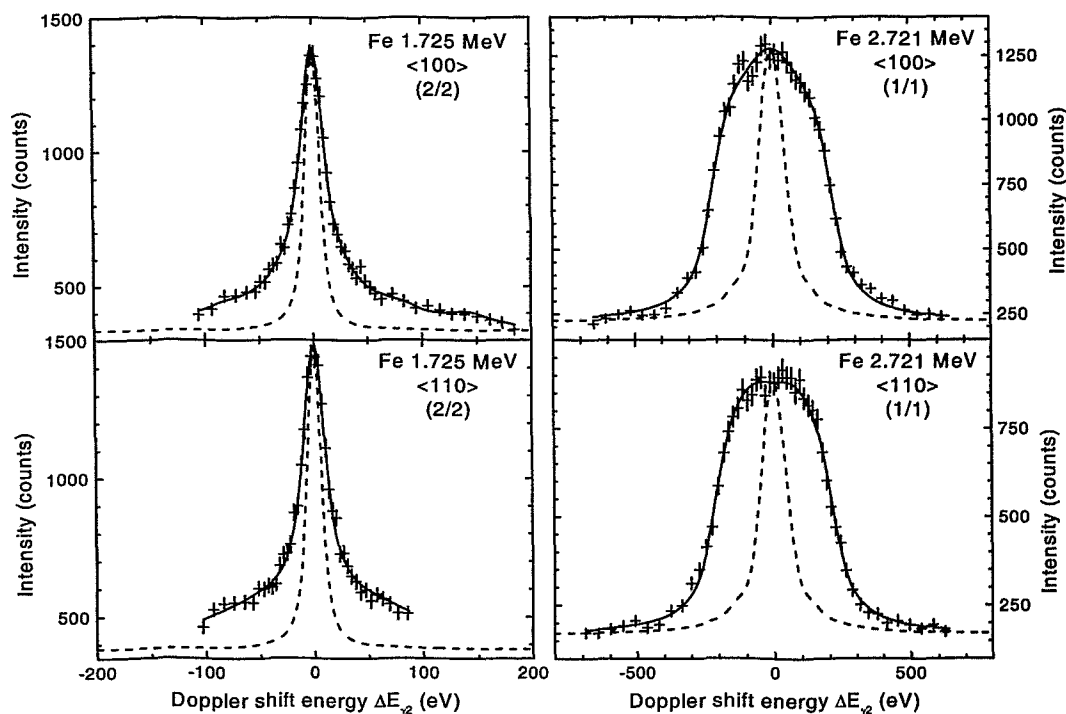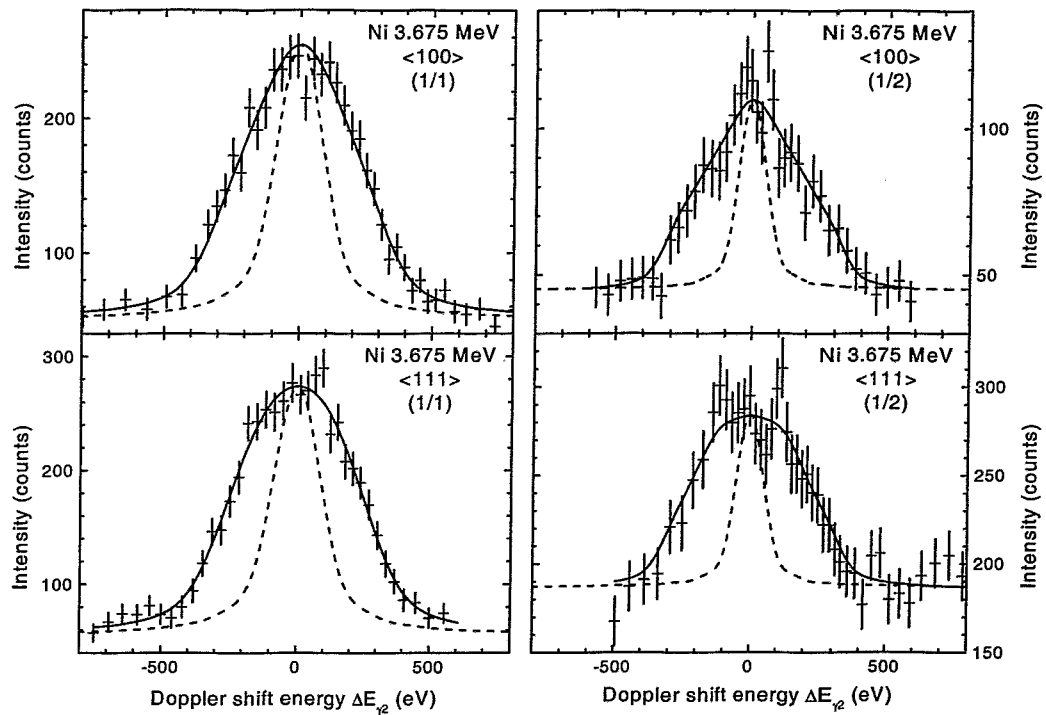
FIGURE 9.40: *Summed experimental data of the 3.675 MeV transition in Ni. The solid line gives the summed best fit, the dashed line the instrumental response function of the spectrometer. Statistics is much too low to unambigously detect any fine structure within the sum scans.*

state that the influence on the lifetime is only small. This has not been re-checked. For a correct determination of an interatomic potential, however, the side feeding should not be neglected.

9.4.3 Nickel (Ni)

Two different transitions have been investigated in nickel (Ni). Both transitions have been measured in two different crystal orientations, <100> and <111>, and in two different reflection orders, (1/1) and (1/2).

The sum scans of the different measurements are displayed in Fig. 9.40 and 9.41. The pictures on the right in Fig. 9.40 show that the GRID lines in the two different orientations differ significantly. However, the total number of counts is much too low in order to clearly see any fine structure. The first order scans, displayed on the left side, are smeared out by the reduced resolution. Looking at the 1.950 MeV transition (Fig. 9.41), one can see that the GRID lines are mainly influenced by the poor resolution. The different orientations do not show any difference. In order to extract any fine structure, one would have to switch to higher order. However, this is not possible, as the sensitivity of the setup would not be sufficient.

The new evaluation of the 3.675 MeV transition shows that all potentials lead to similar values of χ^2 (see Fig. 9.42). The fitted values of the lifetime, however, vary extremely, going from 4 fs to 28 fs. No reported lifetime value exists for the 4.140 MeV level except
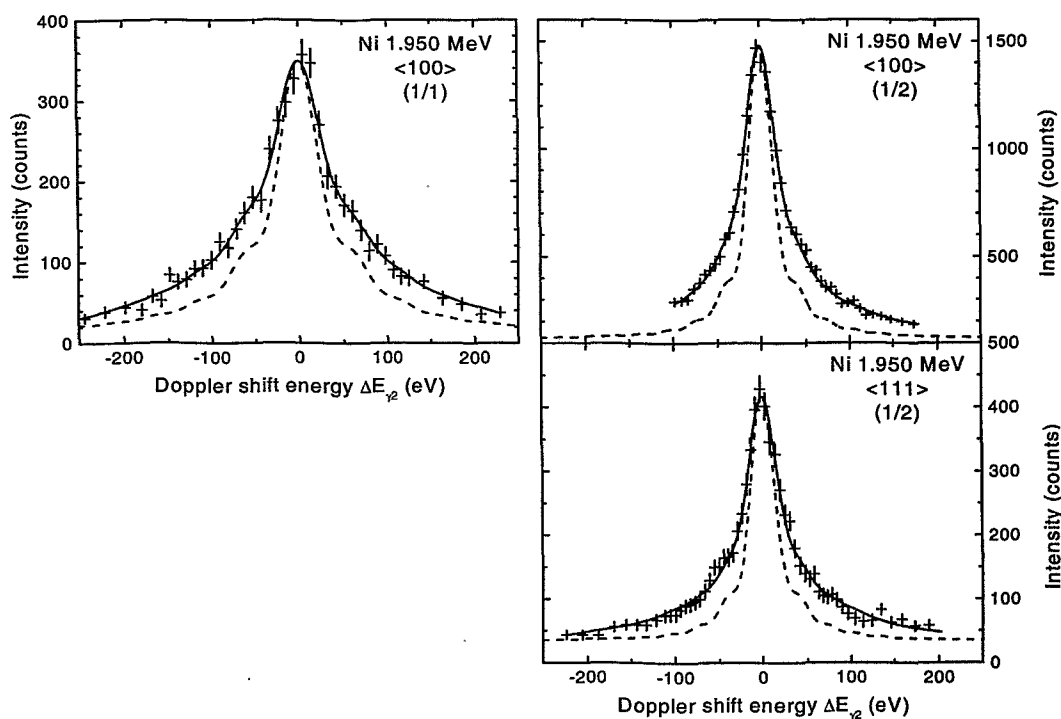
FIGURE 9.41: *Summed experimental data of the* 1.950 MeV *transition in Ni. The solid line gives the summed best fit, the dashed line the instrumental response function of the spectrometer. The resolution is very low, so that possible fine structure is smeared out.*

for GRID values that are not independent of the new measurements. The variation of the screening length comes to a similar result. By varying its value between 50% and 150% of the original value, the fitted lifetime can be "chosen" to any value between 4 fs and 21 fs. The statistical variable χ^2 does not vary by more than 2 in the whole range. This can be seen in the right part of Fig. 9.42. Consequently, no conclusions can be drawn from the measurement of this transition. At least, much more intensity would be needed. Before any repetition of the measurement, however, artificial data should be used to estimate whether the chosen transition is sensitive to the potential, at all.

The results of the 1.950 MeV transition are shown in Fig. 9.43. Again, all the potentials yield similar values of χ^2, with the only exception of the BM potential which then has been modified by switching to the Morse potential yielding a similar lifetime but a better fit. The reported value of the lifetime of the 2.415 MeV level has been measured with the Doppler shift attenuation method and been determined to (48 ± 11) fs or (60 ± 30) fs [Pic 74]. The fitted values vary between 26 fs and 89 fs. These values are all consistent with the reported lifetime, at least within two standard deviations. Furthermore, the reported error does not include any uncertainty of the stopping power needed in the evaluation [Pic 74]. Consequently, also this transition does not help to discriminate between the potentials tested or to determine a nuclear level lifetime.

Stritt *et al.* come to more positive results in their paper [Str 99b]. They argue that the ZBL, EAM VC, and EAM OJ potentials are the best due to the good agreement in
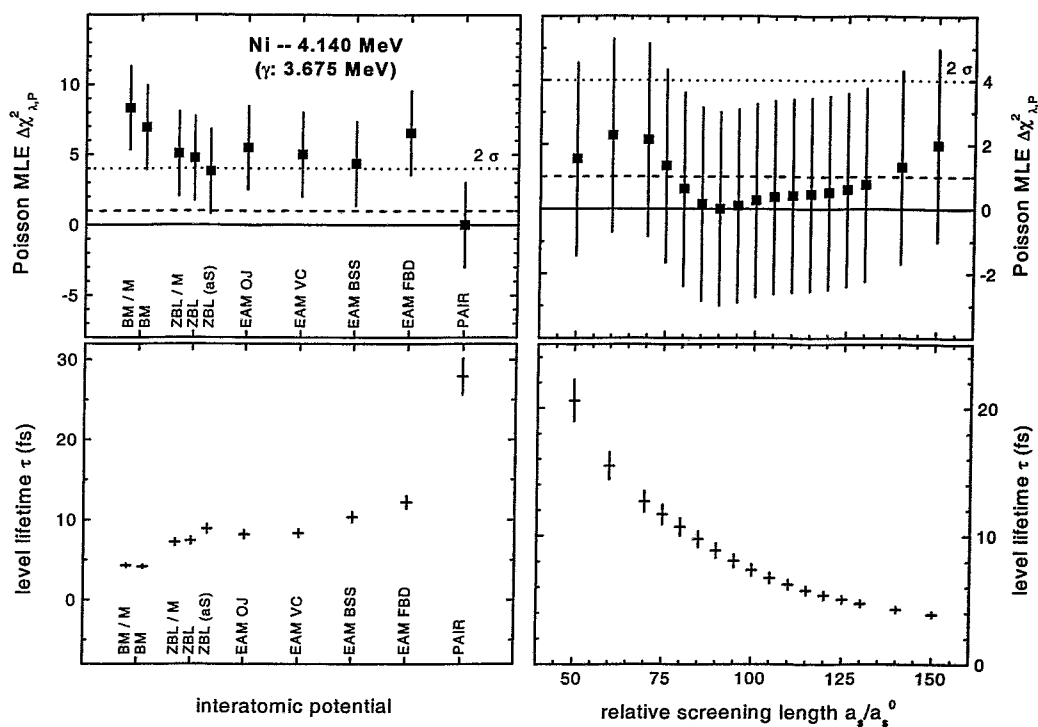
FIGURE 9.42: *Results of the fit – 3.675 MeV transition in Ni. No distinction becomes possible from the χ^2 values (top). All potentials yield similar values. An optimization of the ZBL screening length is also impossible. The 4.140 MeV level lifetime can not be determined, neither (bottom). The estimates differ by a factor of 7 from the lowest to the highest value.*

lifetime. To my opinion, it is impossible to exclude any potential as none of them lies far outside the reported error. They further argue that these potentials also give the best χ^2. Unfortunately not all χ^2 values are given in their paper. However, the new evaluation shows that the differences are very small and that it is not justified to exclude potentials on this basis, neither.

9.4.4 Conclusions

The aim of this chapter was to re-analyse the data of Stritt *et al.* with respect to the statistics applied and not to repeat the complete study of interatomic potentials. The new evaluation shows that only the 2.239 MeV transition in ^{54}Cr is well suited to study the atomic interaction and that, quite generally, different interatomic potentials need to be optimized before a comparison. For most of the other transitions, the differences between the reported potentials can be compensated by the nuclear level lifetime which is adjusted during the fit. A decision on which potential is best can not be made, the lifetime not be determined.

If the lifetimes of the studied nuclear states were known to a precision of 20% or better, a discrimination amongst the potentials would immediately become possible. If the potentials were known to a good precision, it would be possible to determine the level lifetimes within narrow limits. Due to the ignorance of both, a much higher total number
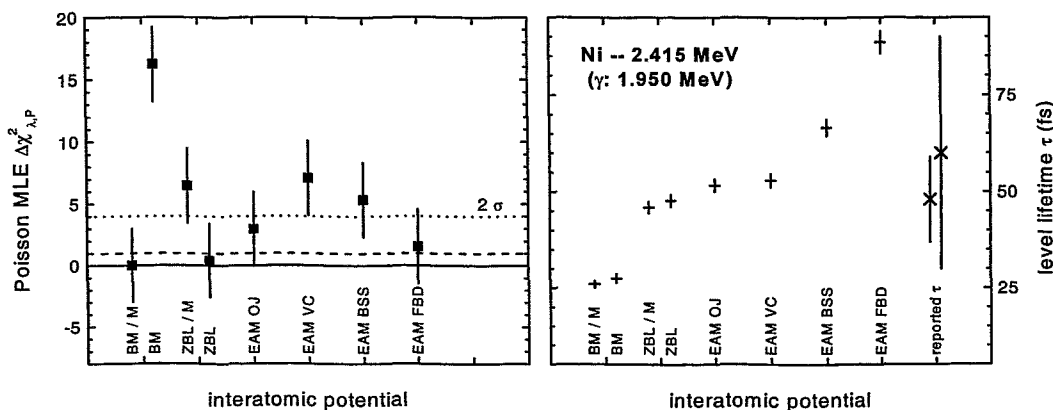
FIGURE 9.43: *Results of the fit – 1.950 MeV transition in Ni. Also in this transition, no distinction of the different potentials becomes possible. The estimates of the 2.415 MeV level lifetime cover a range from 26 fs to 89 fs, all consistent with the reported values. No new results can be obtained.*

of counts is necessary to extract valuable information.

In any case, conclusions about best potentials should be made much more carefully, and errors of nuclear level lifetimes should be given much bigger than this is the case in the papers of Stritt *et al.* The error of the fitted lifetime obtained for a single potential does never represent the final error of the lifetime. There always remains an uncertainty about the correct potential leading to an additional error.

The study of the 2.239 MeV transition in ^{54}Cr should be continued. Performing one further measurement during three weeks with both spectrometers, the total number of counts can be enhanced by a factor of 4. As shown for the BM*/EAM PFS potential, the different potentials can be further optimized. Thereby, a final value of the nuclear level lifetime and a decision on which potential is best should become accessible. Furthermore, the influence of angular correlation should be tested and it must be checked whether the effective pair potential approximation in the EAM simulations is justified. All of this, it could be done within the framework of a Diploma thesis.

Summary

The major aim of this work was to check if and to what extent Crystal-GRID can be used for the study of interatomic potentials under the actual conditions.

The major limitation of the Crystal-GRID method turned out to be the low yield of the flat crystal spectrometers GAMS 4/5. The systematic study of the applicability of Crystal-GRID showed that only very few solids can be investigated. Furthermore, sufficiently large single crystals are not available for many possible candidates. Both of these problems were expected to be partially solved when using the bent-crystal mode of GAMS 5. Unfortunately, sufficiently bent spectrometer crystals were not operational until the end of this work.

The major physical problem of the Crystal-GRID technique is the correlation of nuclear level lifetime and interatomic potential. Both have a similar influence on Crystal-GRID lines and are therefore difficult to separate. When fitting theoretical lines derived from different interatomic potentials to experimental scans, often similar values of χ^2 are obtained with extremely different estimates of the lifetime.

Measurements using TiO_2 single crystals finally prove that interatomic potential functions can be improved with Crystal-GRID. It can be shown that a global minimum on the χ^2 surface can be found if two criteria are fulfilled: the Doppler broadened line must be well structured and the total yield in the experiment must be sufficiently high. In this case, the relative screening length of the three interactions is optimized to $(95 \pm 3)\,\%$ for the ZBL potential using RMD simulations. Full MD simulations using a potential including an equilibrium part yield even better consistency with the data. Furthermore, it can be shown, for the first time, that the 1.499 MeV transition in ^{49}Ti is a pure M1 transition.

The first measurements within this work, using ZnS single crystals, only allowed to verify the original value of the screening length of the ZBL potential. The large error of about 10% can be explained by the correlation of interatomic potential and nuclear level lifetime. The measurement is insensitive to the parameters of the switch function which is used to interpolate between the high-energy and the equilibrium parts of the potential. The lifetime of the 3.221 MeV nuclear level is determined to $(50 \pm 8)\,\mathrm{fs}$, including the error of the screening length. The studied transition is not well suited for Crystal-GRID, as the measured lines contain only little structure due to this high value of τ.

The low numbers of counts in the experimental scans mainly determined the further steps within this work. First, the statistical basis of the evaluation had to be completely revised and second, artificial data have been intensively used for methodical studies in order to overcome the lack in intensity.

Until this work, the fitting code griddle, based on Neyman's χ^2_N statistic was used to evaluate GRID data. It is shown within this work that this statistic is not suited for

the evaluation of counting experiments. Especially for low-statistics data, the use of an accurate statistic is essential to obtain correct results. For this reason, the fitting code gravel has been developed, applying the Poisson MLE statistic $\chi^2_{\lambda,P}$ for the parameter and error estimation. Investigations using artificial data show that the true value of the lifetime can be found with this statistic. If the centre height in the single scans is very low, a small systematic error may be present due to the separated fits of local and global parameters.

A criterion is needed to judge which potential or which set of potential parameters is best suited to describe the experimental data. First attempts to apply GRID to the investigation of interatomic potentials mainly used the lifetime criterion, i.e. looked for a good agreement of the lifetime estimate with reported values or with estimates from other GRID measurements. However, consistent values of the lifetime are only a necessary condition but by no means a sufficient criterion for a good description of the atomic interaction.

Instead, a χ^2 minimization has to be used. A quantitative statement concerning the consistency of model and data can be given by the goodness-of-fit Q. It is shown, within this work, that the value of χ^2 is influenced by statistical noise due to the accuracy of the theoretical GRID line, i.e. mainly due to the limited number of simulated trajectories. This influence is significant for low total numbers of counts as obtainable with Crystal-GRID. Consequently, an error must be attributed to the statistical variable χ^2 itself, it is shown to be of the order of $\sigma_{\chi^2} \approx 3$ for a typical number of 2000 simulated trajectories. For that reason, errors for potential parameters have to be given as 2σ errors, corresponding to a change in χ^2 by 4. The *statistical* error of the nuclear level lifetime τ is often very small. It is essential, however, to additionally include the error of the estimated potential parameters.

In parallel to this work, measurements using Cr, Fe, and Ni single crystals have been performed by Stritt *et al.* However, the evaluation has several problems. On the one hand, it is based on Neyman's χ^2_N statistic, and neglects the error of χ^2 itself. On the other hand, the lifetime criterion is used to discriminate among different potentials, often taking the 1σ errors of reported lifetimes as exclusion criterion. For this reason, the measurements are re-evaluated within this work. The re-evaluation clearly shows that wrong conclusions were obtained due to the incorrect statistical model applied in the evaluation.

Only for the 2.239 MeV transition in Cr, where nicely structured sum scans were obtained, a meaningful investigation of the interatomic potential is possible. The total number of counts of the other measurements is too low. Often, the resolution is also insufficient to resolve the fine structure. By measuring in higher diffraction order, it is easily possible to enhance the resolution on the further cost of intensity.

The metal evaluation is based on a comparison of different potentials, reported in the literature. Often, similar values of χ^2 are obtained for several potentials, but the estimates of the lifetime differ strongly. While Stritt *et al.* applied the lifetime criterion to select the "best" potential, it can be shown in this work that a correct potential is only found if the potential parameters of the multiple potentials are optimized before the comparison. Optimized potentials yield consistent estimates of the lifetime for the 3.074 MeV level in Cr.

Methodical studies on the basis of experimental data are not possible due to the low

count rates. For this reason, artificial GRID data have been applied for the first time within this work. Artificial data present many advantages as the underlying model is completely known and any problem connected to low efficiency, insufficient measuring time or limited stability of the spectrometers can be ignored.

Artificial data have been applied to study the sensitivity of GRID measurements to certain parameters. It is shown that — for a given potential — the statistical error of the lifetime does not significantly depend on the orientation of the single crystals, even powder samples yield results of the same quality. As expected, the error of the lifetime depends on τ.

However, Crystal-GRID is much more sensitive than powder GRID to potential parameters. This is related to the fine structure. It can be shown, for the first time, that the sensitivity depends on the orientation of the sample crystals and thus, on the fine structure of the lines. It is furthermore proven that asymmetric lines are better suited than symmetric ones. In powder GRID measurements, most of the fine structure is averaged out. In this case, the correlation between lifetime and interatomic potential is even stronger and a simultaneous determination of both quantities is impossible.

Against prior assumptions, it is shown that combining measurements of different crystal orientations, as commonly done, does *not* enhance the sensitivity and that the lifetime estimates for different orientations do *not* strongly differ for different orientations even for unsuited potential parameters. Consequently, against prior expectations, the lifetime estimates from different crystal orientations can *not* be used to discriminate among different potentials.

Artificial data further show that a measurement with Si single crystals would be sensitive to potential parameters if the lifetime of the 4.934 MeV nuclear level was 3 fs instead of 1.22 fs, as reported. First test experiments had an insufficient total number of counts due to the very short allocated beam time. Even though a large error of the lifetime is obtained, it seems to be probable that the lifetime is in the range of 2 fs to 3 fs. The experiments are being continuing.

Due to the results obtained within this work, it becomes possible to better prepare Crystal-GRID experiments. The expected count rates can be easily estimated, the sensitivity to parameters can be checked beforehand using artificial data and the best crystal orientation can be chosen. Until this work, quantitative statements of this kind were not possible. Furthermore, it is no more necessary to perform multiple Crystal-GRID measurements with crystals oriented along different crystal directions. This saves money and makes better use of allocated beam time.

Three different approaches are used to derive theoretical GRID lines: i) MD simulations, ii) RMD simulations, and iii) the MFPA theory, only applicable to powder GRID experiments. The three approaches are compared within this work on the basis of artificial data.

As expected, the MFPA theory is found to be unsuited and should not be used at all. The estimated lifetimes are often wrong by a factor of 2. Only due to the application of the BM potential which is known to be too repulsive, a partial compensation is obtained reducing the error to about 30%. It can be shown that the error of the lifetime is related to the definition of the mean free path R_{MFP}.

MD simulations are performed with full potentials containing equilibrium and high-energy parts. RMD simulations, using the same potentials, often yield incorrect results; errors up to 20% are found for the lifetime within this work. RMD simulations, using purely repulsive potentials, instead, are usually better suited to determine the lifetime. The neglect of the interactions among the bulk atoms in the RMD approach is partly compensated by the different potential.

If GRID measurements are only used to determine a nuclear level lifetime within an error of about 10% and no MD potential is known, RMD simulations using the universal (ZBL) potential are probably a sufficient tool. They can also be applied to get an idea of the sensitivity of measurements or for a preliminary evaluation. However, correct results about interatomic potentials can only be expected from full MD simulations.

The present work clearly shows that the efficiency of the *actually* available spectrometers is not sufficient to investigate interatomic potentials of many solids. Apparently, only transitions in Ti and Cr, as well as in Cl seem to be well suited. As most of the Ti compounds are not available as sufficiently large single crystals, not many further Crystal-GRID studies are possible.

In the near future, it is necessary to finish the evaluation of TiO_2. The measured data are shown to be well suited to obtain optimized interatomic potentials below $100\,eV$, approximately. As the investigation of the interatomic potential in Si is very important, additional measurements are being performed.

Furthermore, new measurements of the $2.239\,MeV$ transition in Cr should be carried out and thoroughly evaluated. The re-evaluation within this work only gives an idea of possible steps towards the optimal interatomic potential. This task could be nicely done within the framework of a Diploma thesis.

In order to profit from the theoretical beauty of the Crystal-GRID technique, however, it is absolutely necessary to improve the efficiency of the GAMS spectrometers. This task turned out to be very difficult for the ILL instrument scientists during the last couple of years. Nevertheless, a wide application of the Crystal-GRID technique for the investigation of interatomic solid state potentials at intermediate energies is only possible with an optimized experimental setup.

Appendix A

Numeric relations for Crystal-GRID

The following relations allow to quickly calculate relevant quantities related to Crystal-GRID

Initial recoil velocity

$$v^0[c] = \frac{E_{\gamma_1}[\text{MeV}]}{m[\text{u}] \cdot 931.49} \tag{A.1}$$

$$v^0 \left[\frac{\text{Å}}{\text{fs}}\right] = \frac{E_{\gamma_1}[\text{MeV}]}{m[\text{u}] \cdot 931.49} * 2997.9 = \frac{E_{\gamma_1}[\text{MeV}]}{m[\text{u}]} * 3.2184 \tag{A.2}$$

using $uc^2 \approx 931.49\,\text{MeV}$ and $c \approx 2997.9\,\text{Å}/\text{fs}$

Initial kinetic recoil energy

$$E^0_{\text{kin}}[\text{eV}] = \frac{1}{2} \frac{\left(E_{\gamma_1}[\text{MeV}]\right)^2 \times 10^6}{m[\text{u}] \cdot 931.49} \tag{A.3}$$

Maximum Doppler shift

$$\Delta E_{\gamma_2}|_{\text{max}} = E^0_{\gamma_2} \frac{v_0}{c} = E^0_{\gamma_2} \frac{E_{\gamma_1}}{mc^2} \tag{A.4}$$

$$\Delta E_{\gamma_2}|_{\text{max}}[\text{eV}] = E^0_{\gamma_2}[\text{eV}] \cdot \frac{E_{\gamma_1}[\text{MeV}]}{m[\text{u}] \cdot 931.49} \tag{A.5}$$

Estimation of intensity

$$\begin{aligned} \dot{I}[\text{counts}/\text{min}] \approx\ & 8 \cdot \sigma_{A^*}[\text{barn}] \cdot c_{A^*}[\%] \cdot N_A[\text{mol}] \cdot \\ & P_{\gamma 2}[\%] \cdot R_{E_{\gamma 2,n,m}}(0)\,[1] \cdot P_{\gamma 2,\text{sp}}(\Delta E_{\gamma 2}) \end{aligned} \tag{A.6}$$

$$\begin{aligned} \bar{I}[\text{counts}/\text{min}] \approx\ & 8 \cdot \sigma_{A^*}[\text{barn}] \cdot c_{A^*}[\%] \cdot N_A[\text{mol}] \cdot \\ & P_{\gamma 2}[\%] \cdot R_{E_{\gamma 2,n,m}}(0)\,[1] \cdot \frac{\Delta E_{\text{res}}[\text{eV}]}{2\Delta E_{\gamma 2}|_{\text{max}}[\text{eV}]} \end{aligned} \tag{A.7}$$

with

$$N_A[\text{mol}] = \frac{m_s[\text{g}]}{xM_A[\text{g}\,/\,\text{mol}] + yM_B[\text{g}\,/\,\text{mol}]} \cdot x = \frac{\rho_s[\text{g}\,/\,\text{cm}^3] \cdot V[\text{cm}^3]}{xM_A[\text{g}\,/\,\text{mol}] + yM_B[\text{g}\,/\,\text{mol}]} \cdot x \quad (\text{A.8})$$

Appendix B

Stillinger-Weber parameters for ZnS

The Stillinger-Weber potential is applicable to crystals in the diamond or zinc-blende structure (compare Section 1.2.1). As the original SW potential was only designed for the application in Si, Ichimura extended the approach to some III-V compounds [Ich 96]. The SW parameters were obtained from the experimental lattice constant, the cohesive energy, and the elastic properties. The latter requirement was fulfilled by a comparison to the Keating potential which is supposed to correctly describe the elastic properties. Ichimura states that "the obtained potentials coincide with the Keating potentials for small distortion ($< 1\%$) but are more accurate for larger distortion".

Here, potential parameters for ZnS are derived by the same approach. The Keating parameters α and β, the cohesive energy ε per bond, and the lattice constant a_0 are used as input parameters. Their values are listed in Table B.1.

The Keating potential V^{K} was originally developed for the diamond type of crystals [Kea 66]. The potential energy function only uses the two independent parameters α and β. Just as the SW potential, V^{K} contains two-body and three-body terms. The interaction with atoms in the second-neighbour sphere is neglected.

The transfer to the zinc-blende structure was performed by Martin [Mar 70]. Eq. (9) in his paper gives the energy change ΔV^{K} relative to the ideal tetrahedral structure per primitive unit cell, i.e. for one Zn and one S atom.

$$\Delta V^{\mathrm{K}} = \frac{3}{8d^2} \left\{ \alpha \sum_{i=1}^{4} \left[\Delta \left(\mathbf{r}_{1i} \cdot \mathbf{r}_{1i} \right) \right]^2 + \beta \sum_{s=1}^{2} \sum_{i=1}^{3} \sum_{j=i+1}^{4} \left[\Delta \left(\mathbf{r}_{si} \cdot \mathbf{r}_{sj} \right) \right]^2 \right\} \qquad (B.1)$$

where d is the equilibrium bond length.

In the SW potential, the two-body term accounts for an isotropic expansion or compression, the three-body term is linked to a change of the bond angle. Stillinger-Weber

parameter			GaP		ZnS	
coh. energy	ε	eV/bond	1.78	[Ich 96]	1.58	[GolJeu 63]
lattice const.	a_0	Å	5.45	[Mad 82]	5.41	[Mad 82]
Keating par.	α	eV/Å^2	2.953	[Mar 70]	2.804	[Mar 70]
Keating par.	β	eV/Å^2	0.652	[Mar 70]	0.298	[Mar 70]

TABLE B.1: *Input parameters for the determination of Stillinger-Weber potential parameters.*

and Keating potentials are easily comparable, after transforming the above equation.

$$
\begin{aligned}
\Delta V^{\mathrm{K}} &= \frac{3}{8d^2}\left\{\alpha\sum_{i=1}^{4}\left[\Delta\left(r_{1i}\right)^2\right]^2+\beta\sum_{s=1}^{2}\sum_{i=1}^{3}\sum_{j=i+1}^{4}\left[\Delta\left(r_{si}r_{sj}\cos\theta_{isj}\right)\right]^2\right\}\\
&= \frac{3}{8d^2}\left\{\alpha\sum_{i=1}^{4}\left[2d\Delta r_{1i}\right]^2\right.\\
&\qquad\left.+\beta\sum_{s=1}^{2}\sum_{i=1}^{3}\sum_{j=i+1}^{4}\left[d\cdot\underbrace{\cos\theta_t}_{-\frac{1}{3}}\left(\Delta r_{si}+\Delta r_{sj}\right)+d^2\underbrace{\Delta\cos\theta_{isj}}_{\cos\theta_{isj}+\frac{1}{3}}\right]^2\right\}\\
&= \sum_{i=1}^{4}\frac{3}{2}\alpha\left(\Delta r_{1i}\right)^2+\sum_{s=1}^{2}\sum_{i=1}^{3}\sum_{j=i+1}^{4}\left[\frac{\beta}{24}\left(\Delta r_{si}+\Delta r_{sj}\right)^2\right.\\
&\qquad\left.+\frac{3}{8}\beta d^2\left(\cos\theta_{isj}+\frac{1}{3}\right)^2-\frac{\beta}{4}d\left(\cos\theta_{isj}+\frac{1}{3}\right)\left(\Delta r_{si}+\Delta r_{sj}\right)\right]\qquad\text{(B.2)}
\end{aligned}
$$

where $\theta_t\approx 109.47°$ is the ideal tetrahedral angle

The SW potential is defined in Eq. (1.8) to (1.10). The parameters a and γ keep their original values as given in [StiWeb 85]. The other parameters can be uniquely determined from the four conditions presented in the following. The derived values are listed in Table 1.2.

- First of all, the SW potential needs to reproduce the equilibrium bond length d of the ideal crystal. As the three-body term vanishes in the ideal tetrahedral structure (Eq. (1.9)), the correct bond length is given if

$$
\left.\frac{dV_2^{\mathrm{SW}}}{dr_{ij}}\right|_{r_{ij}=d} = 0
$$

$$
-\varepsilon A\left\{4B\frac{\sigma^4}{d^5}+\left[B\left(\frac{\sigma}{d}\right)^4-1\right]\left(\frac{d}{\sigma}-a\right)^{-2}\cdot\frac{1}{\sigma}\right\} = 0 \qquad\text{(B.3)}
$$

- Furthermore, the interatomic potential must yield $-\varepsilon$ for the ideal crystal structure where ε is the cohesive energy per first neighbour bond.

$$
V_2^{\mathrm{SW}}(d) = -\varepsilon
$$

$$
\varepsilon A\left[B\left(\frac{\sigma}{d}\right)^4-1\right]\exp\left[\left(\frac{d}{\sigma}-a\right)^{-1}\right] = -\varepsilon \qquad\text{(B.4)}
$$

- When changing a bond angle from the ideal tetrahedral angle θ_t while keeping the bond lengths unchanged, the Keating potential energy is increased by (compare Eq. (B.2))

$$
\Delta V_{\mathrm{bend}}^{\mathrm{K}}\left(\theta_{isj}\right) = \frac{3}{8}\beta d^2\left(\cos\theta_{isj}+\frac{1}{3}\right)^2 \qquad\text{(B.5)}
$$

In the Stillinger-Weber potential, the two-body term (Eq. (1.8)) is unchanged and the change in potential energy is given by

$$
\begin{aligned}
\Delta V_{\text{bend}}^{\text{SW}}\left(\theta_{isj}\right) &= V_3^{\text{SW}}\left(d, \theta_{isj}\right) - V_3^{\text{SW}}\left(d, \theta_t\right) \\
&= V_3^{\text{SW}}\left(d, \theta_{isj}\right) - 0 \\
&= \varepsilon\lambda\exp\left[2\gamma\left(\frac{d}{\sigma} - a\right)^{-1}\right]\left(\cos\theta_{isj} + \frac{1}{3}\right)^2 \quad (B.6)
\end{aligned}
$$

Both expressions have the same angular dependence. Consequently, the angular term of the Keating potential can be exactly converted to the SW potential.

$$
\begin{aligned}
\Delta V_{\text{bend}}^{\text{K}}\left(\theta_{isj}\right) &= \Delta V_{\text{bend}}^{\text{SW}}\left(\theta_{isj}\right) \\
\frac{3}{8}\beta d^2 &= \varepsilon\lambda\exp\left[2\gamma\left(\frac{d}{\sigma} - a\right)^{-1}\right] \quad (B.7)
\end{aligned}
$$

- Finally, an isotropic expansion or compression by Δd for all bonds is considered without changing the bond angles from their ideal values θ_t. In this case, an exact conversion is not possible for all values of Δd. Following Ichimura, the two expressions are set equal for a compression of $\Delta d = -0.4\% \cdot d$. Per ZnS primitive unit cell, the energetic change calculated from the Keating potential is given by

$$
\begin{aligned}
\Delta V_{\text{stretch}}^{\text{K}}\left(\Delta d\right) &= \left\{4\cdot\frac{3}{2}\alpha\left(\Delta d\right)^2 + 12\cdot\frac{\beta}{24}\cdot 4\left(\Delta d\right)^2\right\} \\
&= 4\cdot\frac{1}{2}\left\{3\alpha + \beta\right\}\left(\Delta d\right)^2 \quad (B.8)
\end{aligned}
$$

In the SW potential, the change in energy is given by the two-body term; multiplied by 4 for the four neighbouring atoms.

$$
\begin{aligned}
\Delta V_{\text{stretch}}^{\text{SW}}\left(\Delta d\right) &= 4\cdot\left\{V_2^{\text{SW}}\left(d'\right) - V_2^{\text{SW}}\left(d\right)\right\} \\
&= 4\cdot\left\{\varepsilon A\left[B\left(\frac{\sigma}{d'}\right)^4 - 1\right]\exp\left[\left(\frac{d'}{\sigma} - a\right)^{-1}\right] + \varepsilon\right\} \quad (B.9)
\end{aligned}
$$

where $d' = d + \Delta d$. Equating the two expression, the parameters can be determined.

$$
\begin{aligned}
\Delta V_{\text{stretch}}^{\text{K}}\left(\Delta d\right) &= \Delta V_{\text{stretch}}^{\text{SW}}\left(\Delta d\right) \\
\frac{1}{2}\left\{3\alpha + \beta\right\}\left(\Delta d\right)^2 &= \varepsilon A\left[B\left(\frac{\sigma}{d'}\right)^4 - 1\right]\exp\left[\left(\frac{d'}{\sigma} - a\right)^{-1}\right] - \varepsilon \quad (B.10)
\end{aligned}
$$

In order to check whether the derived potential fulfils some basic requirements, elastic constants are calculated. The constants are derived from MD total energy calculations. For details see Appendix A.1 in [Alb 98] and references therein. The resulting values are listed in Table B.2. They are compared to experimental values reported in [Mad 82], as well as to *ab initio* results, calculated using the Cerius code within this work.

The SW values deviate only slightly from the experimental values. This indicates that the new potential quite well describes the crystal. Only the value of c_{44} is wrong by a factor of 2, approximately. Comparing the SW values with the *ab initio* results, all data are consistent. The constant c_{44} is overestimated in both theoretical approaches.

parameter		experiment	ab initio	SW
c_{11}	GPa	98...105	105	109
c_{12}	GPa	59...65	68	74
c_{44}	GPa	34...46	78	89
$D = 2(c_{11} - c_{12})$	GPa	70...80	74	71
$B = (c_{11} + 2c_{12})/3$	GPa	72...82	80	86

TABLE B.2: *Elastic constants calculated using the new parameters of the Stillinger-Weber potential compared to experimental and ab initio results.*

Appendix C

Count rates in Crystal-GRID

Besides the necessity of a short-lived, mostly primarily populated nuclear level, the efficiency of the spectrometer actually presents the major limitation of the Crystal-GRID method. The expected count rate $\dot{I}\left(\Delta E_{\gamma_2}\right)$ for a transition γ_2,

$$\dot{I}\left(\Delta E_{\gamma_2}\right) = \frac{I\left(\Delta E_{\gamma_2}\right)}{t_{\mathrm{obs}}} \tag{C.1}$$

can be estimated from some fundamental quantities, multiplied by a normalization constant C determined from previous measurements. Here, t_{obs} is the time of observation.

C.1 Estimation of count rates

The simultaneous occurrence of four basic processes is required before a photon is counted by the detector of a GAMS spectrometer. First, a neutron must be captured by a sample nucleus. Second, the excited nucleus must de-excite via the decay cascade under study, i.e. under emission of a secondary photon of the studied transition. Third, the photon must be diffracted by the spectrometer crystals, and fourth, it must be detected by the Ge detector.

   In the following, the sample material will be assumed to be $X_x Y_y$, consisting of the two different atomic species A and B. The decay cascade under study de-excites the capture state of the isotope X^*.

1. The number of neutrons N_{n} captured by the sample is proportional to the number of capture centres, i.e. to the number N_{X^*} of atoms of isotope X^*, as well as to the (n,γ) capture cross section σ_{X^*} of this isotope.

$$N_{\mathrm{n}} \sim \sigma_{X^*} \cdot N_{X^*} = \sigma_{X^*} \cdot N_X \cdot c_{X^*} \tag{C.2}$$

where c_{X^*} is the isotopic abundance of the isotope X^*. The number N_X of atoms X in the sample can, of course, easily be calculated by

$$N_X = N_{X_x Y_y} \cdot x = \frac{m_s}{x M_X + y M_Y} \cdot x = \frac{\rho_s \cdot V_s}{x M_X + y M_Y} \cdot x \tag{C.3}$$

where m_s is the sample mass and M_X and M_Y are the atomic masses of atom sorts X and Y. If the sample mass m_s is not known, it can be calculated from the sample

density ρ_s and the total volume V_s of the crystals which is usually $V_s = 3 \cdot (17 \times 20 \times 2)\,\mathrm{mm}^3 = 2.040\,\mathrm{cm}^3$.

2. The probability $P_{\gamma_2|\mathrm{n}}$ that a photon of energy E_{γ_2} is emitted if a neutron is captured can be found in the literature for sufficiently strong transitions. Absolute intensities, referred to the total number of neutron capture events, can often be found in the original publications of measurements.

3. The reflectivity of the spectrometer is given by the instrumental response function $R^0_{E_\gamma,n,m}(\Delta\theta)$ (see Section 3.1). It depends on the energy E_{γ_2} of the photon to be measured, on the diffraction order (n,m), as well as on the thickness and the material (usually Si or Ge) of the spectrometer crystals, as discussed in the next section.

   The response function can be characterized by two quantities: the maximum reflectivity[1] $R^0_{E_\gamma,n,m}(0)$ with the second crystal in its correct m^{th} order position, and the resolution $\Delta\theta_{\mathrm{res}}$ or ΔE_{res} of the spectrometer (see Fig. C.1 and C.2).

   If the central peak of the response function is reasonably narrow, for instance, less than 20% of the width of the Doppler broadened line, it can be approximated by a box–like function of the same area and same height for the purpose of intensity estimation. The width of this box is called the "resolution" $\Delta\theta_{\mathrm{res}}$ or ΔE_{res} of the spectrometer in this context[2]

$$\Delta E_{\mathrm{res}} = \Delta\theta_{\mathrm{res}} \cdot \frac{\Delta E}{\Delta\theta} = \frac{\int d\theta\, R^0_{E_\gamma,n,m}(\Delta\theta)}{R^0_{E_\gamma,n,m}(0)} \cdot \frac{\Delta E}{\Delta\theta} \qquad (\mathrm{C.4})$$

   The conversion factor $\Delta E/\Delta\theta$ is given by Eq. 3.7, it also depends on the photon energy $E^0_{\gamma_2}$ and on the diffraction order (n,m).

   In a non-dispersive measurement, all photons of one transition, Doppler shifted or not, are diffracted simultaneously. In a dispersive scan, however, only some of the Doppler shifted photons fulfil the diffraction condition. Their proportion $I_{\mathrm{pr}}\left(\Delta E_{\gamma_2}\right)$ can be calculated for any given Doppler shift ΔE_{γ_2} using the computer code line4.

   The expected count rate $\dot{I}\left(\Delta E_{\gamma_2}\right)$ is proportional to $R^0_{E_\gamma,n,m}(0)$, i.e. to the maximum reflectivity, and to the proportion of diffracted photons.

$$\dot{I}\left(\Delta E_{\gamma_2}\right) \sim R^0_{E_\gamma,n,m}(0) \cdot I_{\mathrm{pr}}\left(\Delta E_{\gamma_2}\right) \qquad (\mathrm{C.5})$$

   In order to compare count rates from different transitions without calculating all the GRID lines, the average proportion $\overline{I_{\mathrm{pr}}}$, averaged over the whole line, seems to be a reasonable quantity. It can be approximated by

$$\overline{I_{\mathrm{pr}}} \approx \frac{\Delta E_{\mathrm{res}}}{2\Delta E_{\gamma_2}|_{\mathrm{max}}} \qquad \text{for } \Delta E_{\mathrm{res}} \ll \Delta E_{\gamma_2}|_{\mathrm{max}} \qquad (\mathrm{C.6})$$

---

[1]Xfneval gives the instrumental response $R^0_{E_\gamma,n,m}$ in arbitrary units, proportional to the reflectivity.

[2]The response function itself contains fine structure. In lifetime measurements of long-lived levels, this fine-structure can be measured. In this case, the resolution is not given by the total width of the response function but by the width of one of its peaks, i.e. much better. For Crystal-GRID, however, this enhanced resolution can not be used.
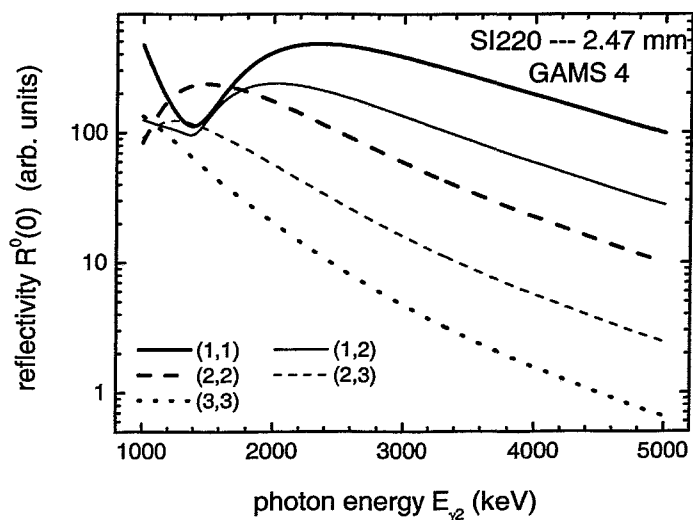
FIGURE C.1: *Reflectivity of GAMS 4 using the standard crystals (see Table C.1). The reflectivity $R_{E_{\gamma 2}, n, m}(0)$ is strongly energy-dependent. Especially for high energies the reflectivity in higher order diffraction becomes very small.*
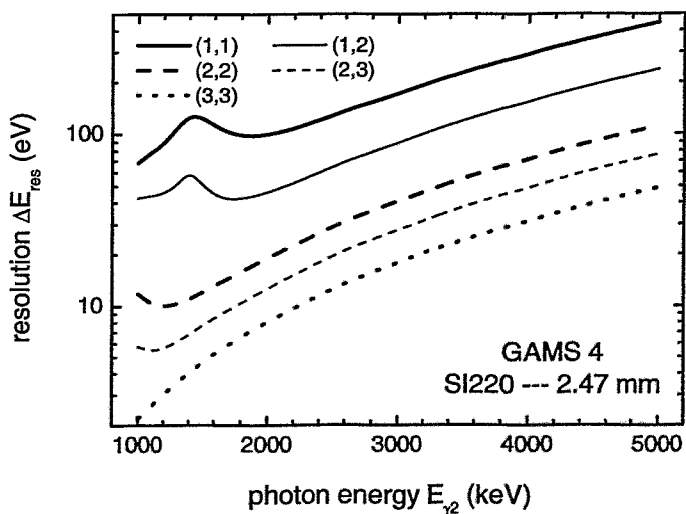
FIGURE C.2: *Resolution of GAMS 4 with standard crystals (see Table C.1). The resolution ΔE_{res} can be increased by using higher reflection order. In reflection order (2,2) the relative resolution $\Delta E_{res}/E_{\gamma 2}$ is about 10^{-5}.*

The average count rate $\overline{\dot{I}}$ is proportional to the maximum reflectivity $R^0_{E_\gamma,n,m}(0)$ and to the average proportion of diffracted photons $\overline{I_{\rm pr}}$.

$$\overline{\dot{I}} \sim R^0_{E_\gamma,n,m}(0) \cdot \overline{I_{\rm pr}} \qquad\qquad (C.7)$$

The broader the response function, i.e. the larger $\Delta E_{\rm res}$, the more counts are obtained, and the less the structure of the energy spectrum is resolved.

4. The detection efficiency of the detector depends slightly on energy. The efficiency decreases with increasing energy, a factor of two may occur in the relevant range of about 1 MeV to 3 MeV. The energy dependence is ignored in the following, the efficiency taken as constant and included in the constant C.

Combining the dependencies and introducing the calibration constant C to be determined, the count rate $\dot{I}\left(\Delta E_{\gamma_2}\right)$ and the average count rate $\overline{\dot{I}}$ can be written as (see also Appendix A)

$$\dot{I}\left(\Delta E_{\gamma_2}\right) = C \cdot \underbrace{\left[\sigma_{\rm X^*} \cdot N_{\rm X} \cdot c_{\rm X^*}\right]}_{N_{\rm n}} \cdot P_{\gamma_2|\rm n} \cdot \left[R^0_{E_\gamma,n,m}(0) \cdot I_{\rm pr}\left(\Delta E_{\gamma_2}\right)\right] \qquad (C.8)$$

$$\overline{\dot{I}} = C \cdot \underbrace{\left[\sigma_{\rm X^*} \cdot N_{\rm X} \cdot c_{\rm X^*}\right]}_{N_{\rm n}} \cdot P_{\gamma_2|\rm n} \cdot \left[R^0_{E_\gamma,n,m}(0) \cdot \frac{\Delta E_{\rm res}}{2\Delta E_{\gamma_2}|_{\rm max}}\right] \qquad (C.9)$$

In order to estimate the expected peak count rate $\dot{I}\left(\Delta E_{\gamma_2}=0\right)$ of a measurement, the GRID line must be calculated using a good estimate of the lifetime. The quantity $I_{\rm pr}\left(\Delta E_{\gamma_2}\right)$ also depends on the resolution function, i.e. on the diffraction order and on the excess width.

The calibration constant C is calculated from the TiO$_2$ measurements at GAMS 4 in 1999 and 2000 using the 1.498 MeV transition in diffraction order (2/2). The measurements are listed in chronological order.

orientation <hkl>	peak count rate $\dot{I}\left(\Delta E_{\gamma_2}=0\right)$ (min^{-1})	proportion of GRID line $I_{\rm pr}\left(\Delta E_{\gamma_2}=0\right)$	sample mass m_s (g)	calibration constant C (min^{-1} mol^{-1}barn^{-1})
<100>	6.53	14.0%	8.7	6.39
<001>	7.48	13.2%	8.63	7.82
<110>	5.29	8.4%	8.67	8.66

The efficiency of the spectrometers is being continuously improved. Since the 1996 TiO$_2$ measurement, it has been approximately doubled. Therefore, the calibration constant C can not be given precisely; its actual value is of the order of 8 min^{-1} mol^{-1}barn^{-1}. GAMS 5 is slightly more efficient. Due to the larger distance to the sample crystals (17 m instead of 15 m), however, it uses a smaller effective solid angle. The absolute count rates are very similar to those at GAMS 4.
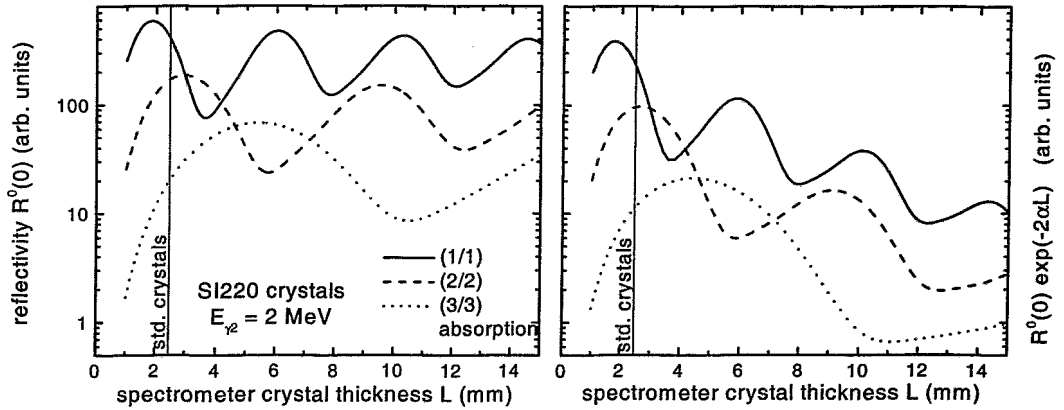
FIGURE C.3: *Reflectivity of GAMS spectrometer for 2 MeV photons. By optimizing the thickness of the spectrometer crystals, intensity can be gained. While in 2nd order diffraction, the standard crystals are near the optimum, in third order the efficiency can be improved by a factor of 3.5. The left part gives the reflectivities as calculated by Xfneval, the right part includes absorption within the spectrometer crystals.*

C.2 Optimization of Spectrometer Crystals

Usually two 2.47 mm thick Si crystals are used by the GAMS 4 spectrometer, two 2.72 mm thick Si crystals by GAMS 5. For a measurement of a known energy the spectrometer crystal thickness can be optimized. Fig. C.3 shows the dependence of the reflectivity on the spectrometer crystal thickness for 2 MeV photons.

Absorption is neglected in the code Xfneval, used to calculate the instrumental response functions. The left part of the Figure displays the reflectivity $R^0_{E_\gamma,n,m}(0)$ calculated. The right part includes absorption via the simple assumption that all photons travel twice the crystal thickness L within the crystal.

$$\text{reflectivity (including absorption)} \approx R^0_{E_\gamma,n,m}(0) \cdot \exp(-2\alpha L) \qquad \text{(C.10)}$$

The absorption coefficient is extrapolated to $\alpha = 0.12\,\text{mm}^{-1}$ for $E_{\gamma_2} = 2\,\text{MeV}$ from the data collection [Vei 71]. Absorption is 50% higher at 1 MeV, and becomes less important for higher energies.

Different crystals are available for the spectrometers, a list is given in Table C.1. For energies above 3 MeV, approximately, the combination of 4.41 mm and 6.95 mm thick Si crystals yields higher reflectivity *and* better resolution compared to the standard 2.47 mm crystals. Furthermore, the 1.27 mm Ge crystals yield a reflectivity increased by a factor of 2 at similar resolution if using a (2/-2) reflection instead of a (1/-2) with the standard crystals. An unpublished comparison of the available crystals with respect to reflectivity and resolution has been performed by Karmann [Kar 99].

Changing crystals takes about two days at GAMS 4 and is therefore rarely applied. At GAMS 5 it is now possible to change crystals within half a working day, so that future low-intensity Crystal-GRID measurements can use different crystals without losing too much time.

quantity	material	planes	thickness (mm)	comment
2	Si	(220)	1.6	
2	Si	(220)	2.47	standard GAMS 4
2	Si	(220)	2.72	standard GAMS 5
1	Si	(220)	4.41	
1	Si	(220)	6.95	
2	Ge	(220)	1.27	
2	Ge	(111)	4.26	

TABLE C.1: *Available spectrometer crystals for GAMS.*
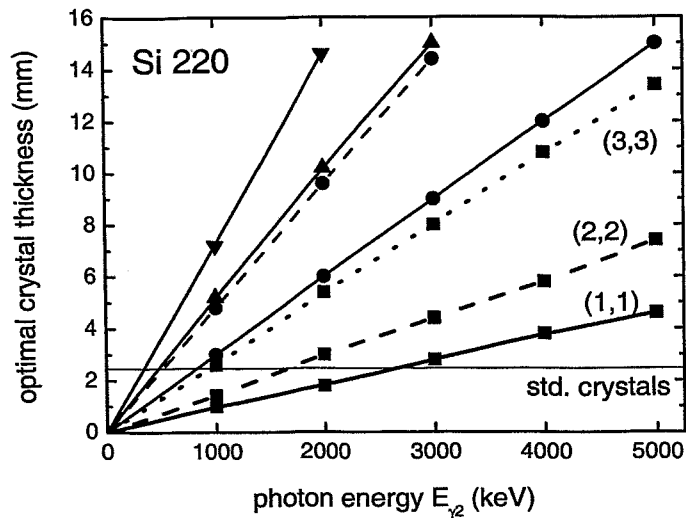
FIGURE C.4: *Spectrometer crystal thicknesses yielding maximum reflectivity. The thick lines, linking the boxes, represent the first and highest maximum in the reflectivity-versus-thickness curve (compare Figure C.3). The solid lines belong to diffraction order (1/1), the dashed to order (2/2), and the dotted to order (3/3).*

The optimal crystal thickness is linearly dependant on the photon energy (see Fig. C.4). As can be seen from Fig. C.3, the reflectivity oscillates as a function of the spectrometer crystal thickness. This is related to the interference of reflected waves from the top and back surfaces of the crystal. The reflectivity in the maxima is plotted in Fig. C.5. The height of the maxima decreases with crystal thickness due to enhanced absorption. Therefore, second or third maxima are most often not suited for measurements.

C.3   What can be measured?

Crystal-GRID measurements are only possible using single crystals containing an isotope with a mostly primarily populated short-lived level. The decay cascade after neutron capture must be sufficiently well known in order to simulate the recoil trajectories. Especially for heavy nuclei, knowledge of level schemes and γ transitions is very limited. Further-
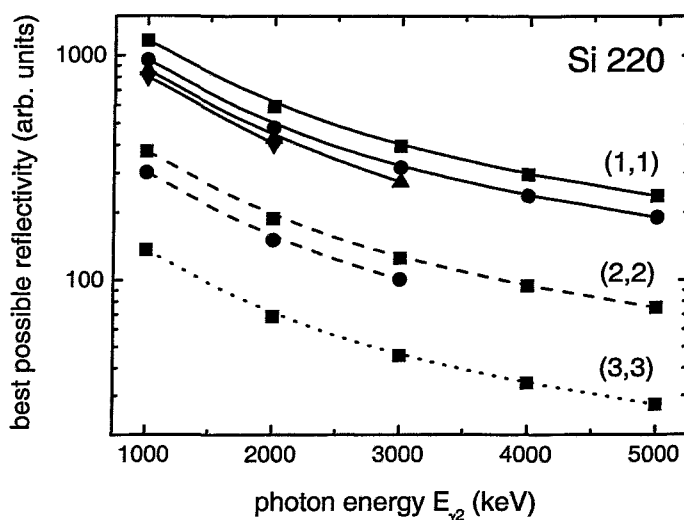
FIGURE C.5: *Reflectivity optimized by chosing optimal spectrometer crystal thickness. Absorption is neglected in this Figure. The different lines of same style belong to the different maxima (box = 1st, circle = 2nd, up triangle = 3rd, and down triangle = 4th maximum) in the reflectivity-versus-thickness plot (compare Figure C.3).*

more, nuclear level lifetimes in the interesting fs range are often not known, as only a few experimental methods exist.

A systematic search for suitable materials has been performed. It is limited to nuclei up to Kr (atomic number $A \leq 36$) as heavier nuclei generally have complicated feeding that is only partially known; noble gas nuclei are disregarded. Hydrogen is also not suited for GRID studies, as the de-excitation of deuterium ($^2_1$H) after neutron capture takes place via emission of a single photon.

The analysis mainly bases on the latest evaluations as listed in the Cumulated Index of the Nuclear Data Sheets, Vol. 90, No. 1, detailed references are given in Table C.2. Furthermore, a data collection containing the effective (n,γ) cross sections $\sigma_{A^*} \cdot c_{A^*}$ for most stable isotopes [Kis 94], as well as first studies concerning intensity estimation for Crystal-GRID performed by Karmann and Wesch [WesKar 98, Kar 00], have been used.

Odd-odd nuclei[3] usually do not have short-lived levels with lifetimes around 10 fs. The following nuclei have been excluded, as no short-lived levels are reported (e.g. in the standard data collection [Fir 96]): Sc, V, Mn, Co, Cu, Ga (one short-lived level exists, but cascade not known), As, Br. The same is true for the heavier nuclei ($A = 37...54$) Rb, Y, Nb, Rh, Ag, In, Sb, and I. All of these nuclei only have odd-odd isotopes after neutron capture, except for vanadium. The isotope $^{51}_{23}$V has a short-lived level, but the feeding is not sufficiently known.

Table C.2 lists all stable isotopes of the remaining nuclei together with their capture cross sections σ_{X^*}, isotopic abundances c_{X^*} [SE 81], and effective cross sections $\sigma_{X^*} \cdot c_{X^*}$ for neutron capture by a nucleus of isotope X*, as well as the binding energies S_{A+1} [Fir 96].

---

[3]Odd-odd nuclei are isotopes having an odd number Z of protons, and an odd number $(A - Z)$ of neutrons.

The best-suited transitions are listed in Table C.3. Besides the isotope after neutron capture, the level energy E_{level}, the level lifetime τ, and the amount of primary feeding, the secondary photon energy E_{γ_2}, its probability $P_{\gamma_2|n}$, and the derived effective cross section $\sigma_{X^*} \cdot c_{X^*} \cdot P_{\gamma_2|n}$ for emission of a photon γ_2, and the maximum Doppler shift $\Delta E_{\gamma_2}|_{max}$ are given. The amount of primary feeding may be wrong if transitions are missing in the reported cascades. This is probably the case for Se where many unplaced γ transitions are reported.

Some of the transitions in Table C.3 are at the limit of measurability for Crystal-GRID, as they depopulate levels with lifetimes that are very short (Si 4.934 MeV) or very long (Se, S, Al).

The average proportion $\overline{I_{pr}}$ of diffracted photons, the efficiency $R^0_{E_\gamma,n,m}(0)$ of the spectrometer, as well as the average expected count rates per mole $\overline{I}/N_A$ for all of these transitions are given in Table C.4. The calculation has been performed with the standard GAMS 4 crystals (2 times 2.47 mm Si) and for a combination of thicker crystals (4.41 mm and 6.95 mm Si, marked by * in the table). The higher yields of both are listed in the Table; the enhanced absorption by the thicker crystals has been neglected.

Once, suitable isotopes and transitions are found, one can calculate the expected count rates. The average expected count rates $\overline{I}$ for some materials are listed in Table C.5 for three different diffraction orders, basing on the most intense transition of Table C.4.

A viewgraph comparing the average count rates of the different nuclei and crystals is given in Chapter 3 (Fig. 3.8).

nucl. after capt. ^{A+1}X	n capt. cros.sec. σ_{X^*} [barn]	isotopic abund. c_{X^*}	X^* effect. cros.sec. $\sigma_{X^*} \cdot c_{X^*}$ [mbarn]	binding energy S_{A+1} [MeV]	comment	references (τ, cascade)
^{7}Li	0.038	7.5%	2.9	7.251	E	[AS 88]
^{8}Li	0.000050	92.5%	0.046	2.033	B, Z	[AS 88]
^{10}Be	0.0085	100%	8.5	6.812	A, C	[AS 88]
^{11}B	0.29	20%	58	11.454	D	[AS 90]
^{12}B	0.0055	80%	4.4	3.370	B	[AS 90]
^{13}C	0.0035	98.9%	3.5	4.946	ok	[AS 91]
^{14}C	0.0014	1.1%	0.015	8.176	A, F, Z	[AS 91]
^{15}N	0.075	99.63%	75	10.833	ok	[AS 91], [Jur 97]
^{16}N	0.000024	0.37%	0.000		Z	
^{17}O	0.000202	99.76%	0.202	4.143	A, E	[Til 93]
^{18}O	0.000538	0.04%	0.000	8.044	Z	σ_{A^*} from [AS 83]
^{19}O	0.00016	0.20%	0.000		Z	
^{20}F	0.0095	100%	10	6.601	ok	[Ram 96]
^{24}Na	0.53	100%	530	6.959	B, F	[End 90]+[EndvdLeu 78]
^{25}Mg	0.053	79%	42	7.331	ok	[End 90]
^{26}Mg	0.18	10%	18	11.093	B, D	[End 90]
^{27}Mg	0.038	11%	4.2	6.443	ok	[EndvdLeu 78]
^{28}Al	0.23	100%	230	7.725	ok	[End 90], [Sch 82]
^{29}Si	0.17	92%	156	8.474	ok	[End 90], [Ram 92]
^{30}Si	0.28	5%	13	10.609	ok	[End 90], [Ram 92]
^{31}Si	0.11	3%	3.4	6.587	ok	[End 90], [Ram 92]
^{32}P	0.18	100%	180	7.936	ok	[End 90], [Mic 89]
^{33}S	0.53	95%	504	8.642	ok	[End 90], [Ram 85]
^{34}S	0.14	0.75%	1.1		Z	
^{35}S	0.24	4.2%	10	6.986	Z	
^{37}S	0.15	0.02%	0.030		Z	
^{36}Cl	43	76%	32581	8.580	ok	[End 90], [Kru 82]
^{38}Cl	0.428	24%	104		Z	
^{40}K	1.96	93%	1827	7.800	ok	[End 90], [vEgi 84]
^{41}K	30	0.01%	3.0		Z	
^{42}K	1.46	6.7%	98		C, Z	[End 90]
^{41}Ca	0.4	97%	388	8.363	ok	[End 90], [GruSpi 67]
^{43}Ca	0.65	0.65%	4.2		Z	
^{44}Ca	6.2	0.14%	8.4		Z	
^{45}Ca	1	2.1%	21		Z	
^{47}Ca	0.7	0.004%	0.028		Z	
^{49}Ca	1.1	0.19%	2.1		Z	
^{47}Ti	0.6	8.2%	49		Z	
^{48}Ti	1.7	7.4%	126		Z	
^{49}Ti	7.8	74%	5756	8.142	ok	[Bur 95]
^{50}Ti	2.2	5.4%	119		Z	
^{51}Ti	0.179	5.2%	9.3		Z	

TABLE C.2: *List of stable isotopes (continued next page).*

nucl. after capt. ^{A+1}X	n capt. cros.sec. σ_{X*} [barn]	isotopic abund. c_{X*}	X* effect. cros.sec. $\sigma_{X*} \cdot c_{X*}$ [mbarn]	binding energy S_{A+1} [MeV]	comment	references (τ, cascade)
^{51}Cr	15.9	4.4%	692		Y	[Chu 97]
^{53}Cr	0.76	84%	637	7.939	B	[Jun 99]
^{54}Cr	18.2	9.0%	1638	9.719	ok	[Stu 80], [Jun 93]
^{55}Cr	0.36	2.4%	8.5		Z	
^{55}Fe	2.25	5.8%	131		Y	[Enc 85]
^{57}Fe	2.63	92%	2412	7.645	ok	[Ulb 89], [Bha 98]
^{58}Fe	2.48	2.2%	55		Z	
^{59}Fe	1.15	0.30%	3.5		Z	
^{59}Ni	4.6	68%	3140	8.999	ok	[Pic 74, Kur 92], [Bag 93]
^{61}Ni	2.8	26%	731		E or Y	[Bha 99]
^{62}Ni	2.5	1.1%	28		Z	
^{63}Ni	14.2	3.6%	510		Y	[Aub 79]
^{65}Ni	1.49	0.91%	14		Z	
^{65}Zn	0.78	49%	379		C	[Bha 93a]
^{67}Zn	0.85	28%	237		B, F	[Bha 91], [MoSen 83]
^{68}Zn	6.9	4.1%	283	10.198	B, F	[Bha 95], [Bha 88]
^{69}Zn	1.072	19%	202		C	[Bha 89]
^{71}Zn	0.0917	0.6%	0.550		Z	
^{71}Ge	3.2	21%	656	7.416	C	[Bha 93b]
^{73}Ge	0.98	27%	269	6.783	C	[KinCho 93]
^{74}Ge	15	7.8%	1170	10.196	C	[Far 95]
^{75}Ge	0.383	37%	140	6.505	C	[FarSin 99]
^{77}Ge	0.14	7.8%	11	6.072	C, Z	[FarSin 97]
^{75}Se	51.8	0.90%	466	8.028	ok, G	[FarSin 99]
^{77}Se	85	9.0%	7650	7.419	ok, G	[FarSin 97]
^{78}Se	42	7.6%	3192	10.498	B	[Rab 91]
^{79}Se	0.43	24%	101		Z	
^{81}Se	0.61	50%	303		C	[Bag 96]
^{83}Se	0.045	9.4%	4.2		Z	

TABLE C.2: *List of stable isotopes (continued). For every isotope, the capture cross section, the isotopic abundance, and the binding energy are given. Isotopes with comment 'ok' are, in principle, suited for Crystal-GRID. Other comments explain why the isotope is not suited.* **comments:** *A) decay cascade only partially known, B) decay cascade not (sufficiently) known, C) no short lifetime known, D) lifetimes not known, E) populated state lifetime too long, F) lifetimes good for Crystal-GRID, G) many transitions unplaced in level scheme, Y) isotope has much lower cross section for secondary photons* $(\sigma_{X*} \cdot c_{X*} \cdot P_{\gamma 2|n})$ *than other isotope of the same nucleus, Z) isotope has much lower natural cross section* $(\sigma_{X*} \cdot c_{X*})$ *than other isotope of the same nucleus.*

nucl. after capt. ^{A+1}X	level energy E_{level} [MeV]	level lifetime τ [fs]	prim. feed.	photon energy E_{γ_2} [MeV]	prob. of gam. $P_{\gamma_2|n}$	γ_2 effect. cros.sect. $\sigma_{X^*} \cdot c_{X^*} \cdot P_{\gamma_2|n}$ [mbarn]	max. D. shift $\Delta E_{\gamma_2}|_{\text{max}}$ [eV]
^{13}C	3.684	1.6(1)	100%	3.684	32%	1.1	384
^{15}N	7.155	18(8)	77%	1.885	19%	14	496
^{15}N	5.299	25(7)	92%	5.298	21%	16	2098
^{15}N	8.313	1.7(11)	100%	8.310	4%	3.0	1499
^{15}N	9.155	7+6-3	98%	2.000	4%	3.0	240
^{20}F	3.526	5.5(6)	95%	2.469	2%	0.190	408
^{25}Mg	3.414	16(6)	100%	2.824	59%	25	475
^{27}Mg	3.560	<10	100%	3.560	57%	2.4	408
^{28}Al	4.691	50(13)	100%	4.691	4.60%	11	546
^{28}Al	5.442	40(10)	100%	3.303	1.10%	2.5	289
^{28}Al	5.135	40(10)	100%	5.135	3%	6.9	510
^{28}Al	5.442	40(10)	100%	5.411	2%	4.6	474
^{29}Si	4.934	1.22(18)	99%	4.934	65%	102	647
^{30}Si	7.508	<35	100%	5.272	16%	2.1	585
^{30}Si	7.508	<35	100%	2.677	2.2%	0.288	297
^{31}Si	3.533	<15	95%	2.781	67%	2.3	294
^{32}P	2.658	<10	40%	2.658	2%	3.6	471
^{32}P	2.230	36(20)	35%	2.152	6.7%	12	412
^{32}P	3.444	35(15)	89%	1.215	0.5%	0.900	183
^{33}S	3.221	40(12)	85%	2.380	45%	227	420
^{36}Cl	2.864	<15	80%	2.864	6.55%	2134	488
^{40}K	2.787	<40	50%	2.757	1.9%	35	371
^{40}K	2.756	<30	57%	1.956	1.8%	33	265
^{40}K	2.756	<30	57%	2.727	1.6%	29	369
^{40}K	2.730	<40	80%	1.087	1.1%	20	148
^{40}K	2.730	<40	80%	1.930	0.5%	9.1	263
^{40}K	3.128	<30	61%	3.128	0.6%	11	392
^{41}Ca	3.945	<20	85%	2.001	19%	74	231
^{41}Ca	4.753	<35	100%	2.811	3.80%	15	266
^{41}Ca	4.753	<35	100%	2.290	1.60%	6.2	216
^{49}Ti	3.261	15	95%	1.498	5%	281	160
^{54}Cr	3.074	< 25	98%	2.239	10.20%	167	296
^{54}Cr	3.719	< 43	97%	3.719	3.60%	59	444
^{57}Fe	3.427	<5	100%	2.721	1.37%	33	216
^{57}Fe	1.725	36(12), 47(9)	91%	1.725	6.30%	152	192
^{59}Ni	2.415	48(11), 60(30)	95%	1.950	1.70%	53	234
^{59}Ni	4.140	6.5(1.4)	96%	3.675	0.96%	30	325
^{75}Se	1.590	72+20-12	100%	0.979	1.73%	8	90
^{77}Se	1.818	80+40-30	?	1.297	3.4%	260	101
^{77}Se	2.892	70+30-20	?	2.591	0.58%	44	164
^{77}Se	2.892	70+30-20	?	1.284	0.2%	15	81

TABLE C.3: *Suited Transitions for Crystal-GRID. Information on the nuclear level and the secondary gamma transition are given, as well as the maximum Doppler shift to be measured.*

nucl. after capt. ^{A+1}X	photon energy E_{γ_2} [MeV]	av. prop. diffr. γ_2 (1/1)	(1/2)	(2/2) $\overline{I}_{\mathrm{pr}}$		efficiency (1/1)	(1/2)	(2/2) $R^0_{E_\gamma,n,m}(0)$		av. count rate / mole (1/1)	(1/2)	(2/2) $\overline{I}/N_A$ [min^{-1}mol^{-1}]	
^{13}C	3.684	32%	11%	5%	243	107	76		0.11*	0.03*
^{15}N	1.885	10%	4%	2%	358	233	192	4.00	1.16	0.38
^{15}N	5.298	8%	4%	1%	148	93	45	1.42*	0.41*	0.08*
^{15}N	8.310	21%	12%	5%	91	30	12	*	0.08*	0.01*
^{15}N	2.000	21%	10%	4%	412	238	172		0.55	0.16
^{20}F	2.469	15%	8%	3%	471	198	104		0.02	0.01
^{25}Mg	2.824	16%	8%	4%	415	153	71		2.52	0.53
^{27}Mg	3.560	29%	11%	4%	264	101	76		0.20*	0.06*
^{28}Al	4.691	36%	11%	5%	122	109	58		1.03*	0.23*
^{28}Al	3.303	35%	18%	6%	314	104	73			0.08*
^{28}Al	5.135	31%	14%	6%	143	98	48	*	*	0.15*
^{28}Al	5.411	35%	16%	7%	150	89	43	*	*	0.11*
^{29}Si	4.934	24%	10%	4%	134	103	53	*	8.56*	1.85*
^{30}Si	5.272	27%	13%	5%	147	94	45	*	0.20*	0.04*
^{30}Si	2.677	24%	12%	6%	443	172	83		0.05	0.01
^{31}Si	2.781	26%	13%	6%	424	158	74			0.08
^{32}P	2.658	15%	8%	3%	446	174	85		0.38	0.08
^{32}P	2.152	13%	6%	3%	457	232	147	5.65	1.38	0.37
^{32}P	1.215	27%	13%	3%	254	113	188	*	0.10*	0.04
^{33}S	2.380	14%	7%	3%	476	209	115		26.72	6.52
^{36}Cl	2.864	16%	8%	4%	407	148	68		212.04	44.51
^{40}K	2.757	20%	10%	5%	429	161	76		4.60	0.99
^{40}K	1.956	19%	9%	3%	393	237	179		5.31	1.63
^{40}K	2.727	20%	10%	5%	434	165	79		3.92	0.85
^{40}K	1.087	26%	15%	4%	284	117	127			0.72
^{40}K	1.930	19%	8%	3%	381	236	184		1.46	0.46
^{40}K	3.128	24%	12%	4%	350	120	67		1.29	0.24*
^{41}Ca	2.001	21%	10%	4%	412	238	172		13.96	4.18
^{41}Ca	2.811	29%	15%	7%	418	155	72			0.58
^{41}Ca	2.290	26%	13%	6%	475	220	127		1.40	0.36
^{49}Ti	1.498	30%	12%	4%	410	263	238	*	72.23*	20.00
^{54}Cr	2.239	19%	9%	4%	471	225	134		27.33	7.09
^{54}Cr	3.719	29%	10%	4%	237	108	76		5.13*	1.45*
^{57}Fe	2.721	34%	17%	8%	435	166	79			1.64
^{57}Fe	1.725	26%	11%	4%	260	207	217		27.53	10.14
^{59}Ni	1.950	21%	10%	4%	390	237	180		9.73	3.01
^{59}Ni	3.675	38%	14%	5%	244	107	76		*	1.00*
^{75}Se	0.979	36%	22%	6%	533	146	161		*	0.66*
^{77}Se	1.297	36%	17%	5%	490	212	215	*	*	22.64
^{77}Se	2.591	41%	21%	9%	457	183	91			3.06
^{77}Se	1.284	47%	22%	6%	457	197	211	*	*	1.63

TABLE C.4: *Expected intensities for possible Crystal-GRID transitions. For every transition, the resolution, and efficiency of the spectrometer is given in the three different diffraction orders (1,1), (1,2), and (2,2). The derived expected average count rate per mole is listed if the relative resolution is better or equal 13%. The calculation has been performed for the standard 2.47 mm crystals as well as for a set of thicker crystals (4.41mm/6.95mm). The intensity is the maximum of both setups (* indicates thick crystals).*

material	atoms A in sample N_A [mol]	nucleus	gamma energy E_{γ_2} [MeV]	level lifetime τ [fs]	aver. count rate (1/1) | (1/2) | (2/2) $\bar{I}$ [counts/min]		
BN	0.1792	N	1.885	18(8)	0.72	0.21	0.07
TiN	0.1790				0.72	0.21	0.07
AlN	0.1620				0.65	0.19	0.06
InN	0.1089				0.44	0.13	0.04
Ca_3N_2	0.0735				0.29	0.09	0.03
CaF_2	0.1662	Ca	2.469	5.5(6)		0.004	0.001
AlN	0.1620	Al	4.691	50(13)		0.17	0.04
AlP	0.0845					0.09	0.02
AlAs	0.0753					0.08	0.02
Si	0.1692	Si	4.934	1.22(18)		1.45	0.31
$TiSi_2$	0.1569					1.34	0.29
CaSi	0.0715					0.61	0.13
TiP	0.1056	P	2.152	36(20)	0.60	0.15	0.04
AlP	0.0845				0.48	0.12	0.03
InP	0.0673				0.38	0.09	0.03
TiS_2	0.1228	S	2.380	40(12)		3.28	0.80
ZnS	0.0846					2.26	0.55
TiS	0.0983					2.63	0.64
NaCl	0.0757	Cl	2.864	<15		16.06	3.37
K_2TiO_3	0.0727	K	1.956	<30		0.40	0.12
$KNbO_3$	0.0526					0.39	0.12
CaO	0.1215	Ca	2.001	<20		1.70	0.51
Ca_3N_2	0.1102					1.54	0.46
CaSi	0.0715					1.00	0.30
CaC2	0.0707					0.99	0.30
$CaTiO_3$	0.0597					0.83	0.25
CaF_2	0.0831					1.16	0.35
CaTe	0.0592					0.83	0.25
TiN	0.1790	Ti	1.498	15		12.93	3.58
TiC	0.1680					12.13	3.36
TiO_2	0.1080					7.80	2.16
TiP	0.1056					7.63	2.11
TiS	0.0983					7.10	1.97
$TiSi_2$	0.0784					5.67	1.57
TiS_2	0.0614					4.43	1.23
$CaTiO_3$	0.0597					4.31	1.19
K_2TiO_3	0.0363					2.62	0.73
Cr	0.2801	Cr	2.239	< 25		7.65	1.99
Fe	0.2876	Fe	1.725	36(12), 47(9)		7.92	2.92
Ni	0.3096	Ni	1.950	48(11), 60(30)		3.01	0.93

TABLE C.5: *Intensity estimation for various crystals. The average count rate is given for three different diffraction orders if the relative resolution is better or equal 13%.*

Appendix D

Comparison of statistics: Estimation of mean values and areas under peaks

A common problem when dealing with χ^2 statistics is that the area under the measured peak is not identical to the area under the fitted curve. This problem does not arise with maximum likelihood methods. When using MLE, the areas are identical. As pointed out by Baker and Cousins, this is true as long as the overall scale in the fitting function can be freely varied during the fit, e.g. when estimating a constant background [BakCou 84].

D.1 Asymptotic behaviour

The estimation of a mean value μ is a special case of area determination. It is widely known that when trying to find the mean value of Poisson distributed data, the modified Neyman's χ_N^2 statistic underestimates the true mean and Pearson's χ_P^2 overestimates it. Similar results have been found or stated in several publications, e.g. [Awa 79, BakCou 84, Gre 91, Whe 95, JadRii 96, Mig 99, Mur 98]. In statistics, an estimator that does asymptotically lead to a wrong value is called *inconsistent* [Ead 71, p. 115]. The problem leading to the wrong values can be well explained qualitatively. Using $1/c_i$ as a weighting factor in Neyman's statistic, a stronger weight for all values $c_i < \mu$ will thus lead to an underestimation. On the other hand, using $1/\mu$ in Pearson's statistic, makes χ^2 smaller when μ is increased, thus leading to an overestimation.

The size of the inconsistency depends on the true mean of the Poisson distributed data. This can be seen in Fig. D.1. A set of $500,000$ Poisson distributed numbers with mean μ has been generated. Using the three statistics described in Section 6.1, best estimates $\langle \mu \rangle$ for the mean have been calculated using the relations given in Table D.1. This has been done for true mean values μ from 0.001 to 1000. The deviation from the true mean by -1 for χ_N^2, and 0.5 for χ_P^2, can be found for true mean values of approximately 10 or more. Using the MLE approach, the mean of Poisson distributed data is estimated correctly for any μ.

Baker and Cousins claim that the wrong "area", i.e. the wrong estimate of the mean, is due to the implicit assumption of Gauss statistic in the χ^2 methods [BakCou 84]. However, the maximum likelihood approach "Gauss MLE", based on the assumption that data are
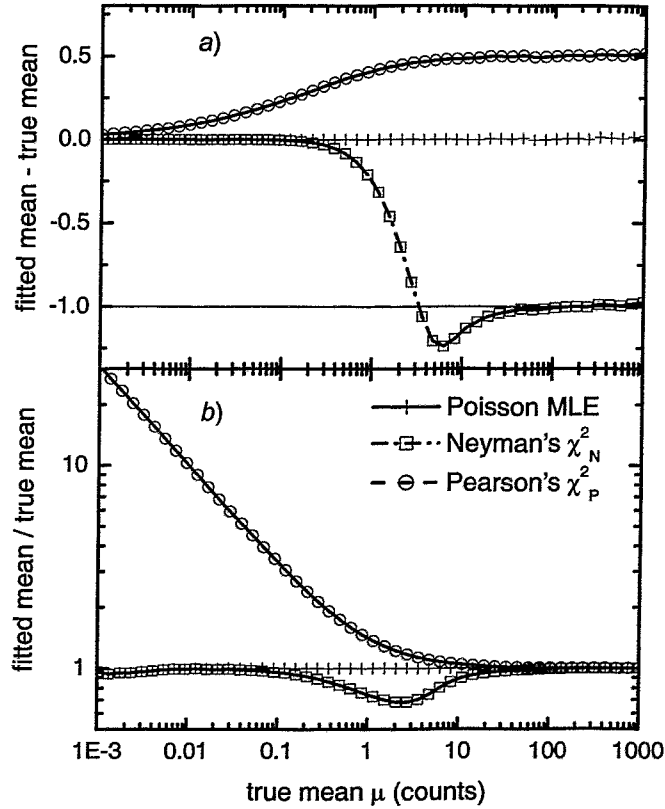
FIGURE D.1: *Deviation of fitted mean from true mean value when using the three statistics under study. (a) For large μ Pearson's χ_P^2 leads to an overestimation of 0.5 whereas Neyman's χ_N^2 underestimates the true mean by -1. (b) Looking at the ratio of fitted and true mean, one clearly sees that using Pearson's χ_P^2, the fitted mean deviates extremely from the true one for very small μ.*

statistic	$\langle \mu \rangle$	$\langle \mu \rangle$ (only 1 datum)	asymptotic mean
$\chi_{\lambda,P}^2$	$\frac{\sum c_i}{N}$	c	μ [HanTho 99]
χ_P^2	$\sqrt{\frac{\sum c_i^2}{N}}$	c	$\mu\sqrt{1+\frac{1}{\mu}}$ [JadRii 96]
χ_N^2	$\frac{\sum_{c_i \neq 0} 1}{\sum \frac{1}{\max(c_i,1)}}/$	c	$\frac{e^\mu - 1}{1+\sum_{k=1}^{\infty}\frac{\mu^k}{k(k!)}}$ [Mig 99]

TABLE D.1: *Relations giving the best estimate for the three statistics under study derived by setting $d\chi^2/d\mu = 0$. In the second column the general result is given. The third column gives the special case of only one measurement. The last column gives the asymptotic mean in the case of many observations.*

normally distributed, also estimates the correct mean if the variance is approximated by the fitted value. The calculation of the mean fails if the normalisation factor $(2\pi\sigma^2)^{-1/2}$ of the Gauss distribution is neglected as in χ_P^2 or artificially made independent of the mean to be fitted as in χ_N^2. The best possible derivation coming from the maximum likelihood method leads to additional terms $\ln m_a(\theta_i)$ compared to Pearson's χ_P^2 leading to a correct estimation of the mean even with Gauss statistic. [HauJen 01]

For large mean values, the Poisson distribution can be approximated by a normal distribution to high precision. This could explain the correctness of the Gauss MLE approach in the high-μ part. For low averages, however, this is not true. The overall correctness is due to the large number of Poisson distributed numbers used. The central limit theorem states that a variable is normally distributed if it is the sum of many independent identically distributed random variables. Consequently, averaging (summing) over a large number of Poisson data, a correct estimation of the mean becomes possible even with Gauss statistic.

Similar investigations have shown that inconsistent results are also obtained when fitting some pre-defined curve (e.g. a Gaussian or Lorentzian) to a peak in order to estimate a total intensity. If information about intensities is needed, the classical χ^2 methods are clearly not suited.

D.2   Convergence properties

In true experiments, only a limited number of measurements can be performed. Is it possible to estimate a correct mean when using only very few data points? The same 500,000 Poisson distributed numbers as used before, have been grouped by 1, 3, 9, ..., $3^6 = 729$ numbers. The estimate of every group can then be calculated by the equations given in Table D.1. Every group leads to a different result, of course, due to the random nature of the input data. However, it is possible to compare the distributions of results via their mean values and their spread.

It is important to note that the average has to be calculated without any weighting factor, as all the random numbers have been taken from a Poisson distribution around the same true value μ.

$$\langle\mu\rangle_{\text{average}} = \sum_{k=1}^{K} \frac{\langle\mu\rangle_k}{K} \tag{D.1}$$

The results of the calculations are displayed in Fig. D.2. For the modified Neyman's χ_N^2 and Pearson's χ_P^2 statistics, on average, the correct mean value μ is found if every datum is "fitted" separately (Fig. D.2b-c). This can be understood as, for a single datum, these statistics yield $\mu_i = c_i$. As soon as the inherent weighting of the statistics comes into play, i.e. as soon as more than one datum is fitted simultaneously, the correct value is no longer obtained on average. Combining many data finally leads to the deviation of -1 respectively, 0.5 for high values of μ. This proves that the failure of these two statistics can be understood as a problem with the weights used.

What about the asymptotically correct statistic? In the case of Poisson maximum likelihood estimation the average of the fitted results coincides with the true mean value for all values of μ and for any number of simultaneously fitted data points (Fig. D.2a).
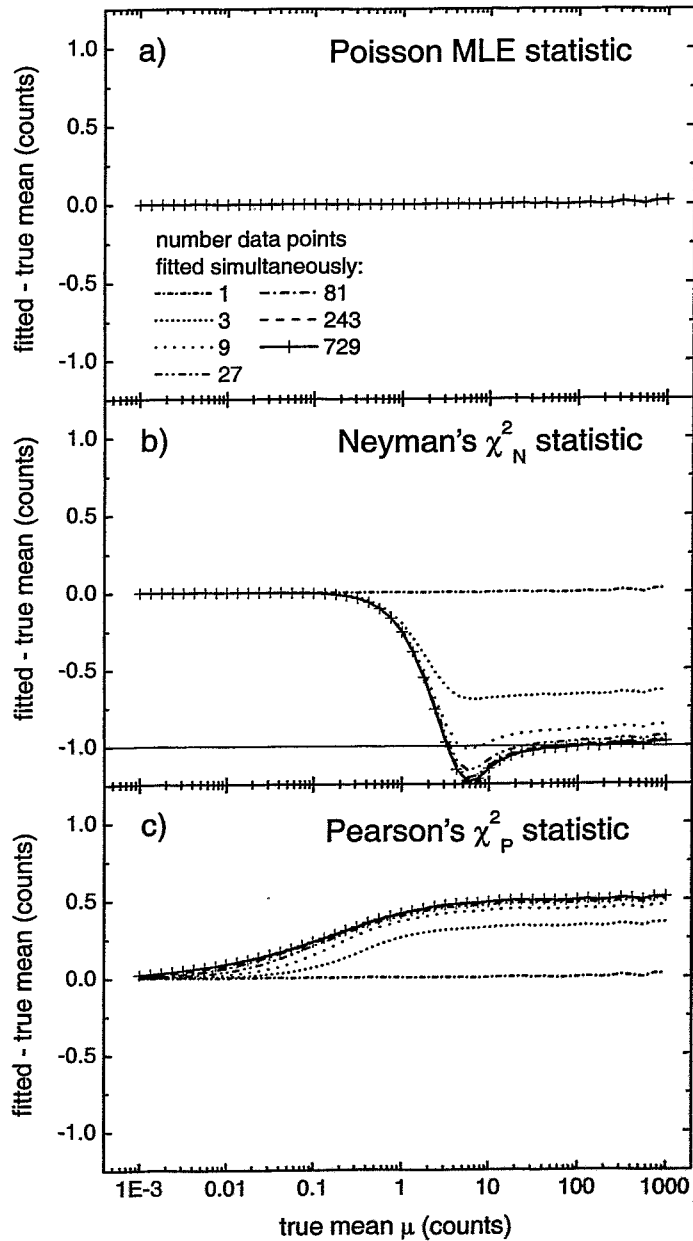
FIGURE D.2: *Convergence test for the three statistics under study: (a) Poisson MLE, (b) χ_N^2, (c) χ_P^2. Displayed is the deviation of the fitted mean from the known true mean value. The fitted mean has been obtained by averaging the fitted mean values of groups of 1, 3, ..., respectively $3^6 = 729$ random numbers (calculated by the relations given in Table D.1). Only the Poisson MLE approach finds the correct mean in all cases.*

D.3   Binned data – combining bins

Counting experiments often deal with binned data (histograms) and so do many publications. In GRID measurements, the theoretical function is sampled by taking measurements at different angles θ_i. This sequential way of measuring can be looked at as if all measurements were taken at the same time in different bins of identical size.

The χ^2 methods require, that the spread of the measured data is sufficiently well described by a normal distribution, i.e. that the number of counts in each bin is sufficiently large. Otherwise adjacent bins must be combined ("re-binning"). Many textbooks state that at least 5 counts must be in every bin (see e.g. [Ead 71, p. 257]). Combining bins, however, washes out the fine structure that may contain valuable information. Gumble already studied this phenomenon half a century ago using the χ^2_P statistic [Gum 43]. He finds that not only the χ^2 values but also fitted intensities and parameters may depend on the way of re-binning.

Appendix E

Application of the (Levenberg-)Marquardt method

The best estimate of a parameter is the value that minimizes the statistical variable χ^2. As in the case of GRID, the model function is not known analytically, a numeric method is used to find this minimum. The applied Levenberg-Marquardt algorithm, also called Marquardt algorithm, combines the advantages of two different approaches, the gradient (steepest descent) method and an approximate analytic (inverse Hessian) method.

Far away of the χ^2 minimum, the gradient method is used. The idea is to minimise χ^2 by changing the parameter vector $\mathbf{a}$ along the negative gradient of χ^2, i.e. in the direction of steepest descent [BevRob 92, p. 153]. As the gradient gives no information about how far to go, it has to be multiplied by a well-chosen number c. The change in parameters is

$$\delta a_j = -c \frac{\partial \chi^2}{\partial a_j} \quad \text{with} \quad c > 0 \tag{E.1}$$

Nearby the optimized values, a first order expansion of the theoretical function $m_{\mathbf{a}}$ about the point a_j' in the parameter increments $\delta a_j = a_j - a_j'$ is made in order to calculate the next step.

$$m_{\mathbf{a}}(\theta_i) \simeq m_{\mathbf{a}'}(\theta_i) + \sum_{j=1}^{m} \left[\left. \frac{\partial m_{\mathbf{a}}(\theta_i)}{\partial a_j} \right|_{\mathbf{a}=\mathbf{a}'} \cdot \delta a_j \right] \tag{E.2}$$

where $m_{\mathbf{a}'}(\theta_i)$ is the value of the fitting function with parameters a_j' and the derivatives are evaluated at this point. In this approximation, χ^2 can be expressed explicitly as a function of the parameter increments δa_j. Setting the derivative $\partial \chi^2 / \partial (\delta a_k) = 0$, a matrix equation of form

$$\boldsymbol{\beta} = \boldsymbol{\alpha} \cdot \delta \mathbf{a} \tag{E.3}$$

can be obtained with the matrix $\boldsymbol{\alpha}$ to be determined for every statistic, and

$$\beta_k \equiv -\frac{1}{2} \frac{\partial \chi^2}{\partial a_k} \tag{E.4}$$

as in the gradient part.

In the Levenberg-Marquardt method, the two approaches are combined in order to get a faster convergence. The parameter vector $\mathbf{a}$ is changed by $\delta\mathbf{a}$, calculated from

$$\delta\mathbf{a} = (\boldsymbol{\alpha}')^{-1} \cdot \boldsymbol{\beta} \quad \text{with} \quad \boldsymbol{\alpha}' = \boldsymbol{\alpha} + \lambda \cdot \mathbf{1} \tag{E.5}$$

where the diagonal elements of the matrix $\boldsymbol{\alpha}$ are increased by λ leading to the application of a pure gradient method for very high λ and a pure analytic solution for very small λ. A detailed description can be found in [BevRob 92, Pre 89], e.g. However, the discussion is usually limited to the application of a classical χ^2 statistic with known variances σ_i^2. When choosing $\sigma_i^2 = \max{(c_i, 1)}$, this becomes the modified Neyman's χ_N^2 statistic.

E.1   Neyman's χ_N^2

In the case of the modified Neyman's χ_N^2 statistic, the components of $\boldsymbol{\alpha}$ and $\boldsymbol{\beta}$ take on the following values.

$$
\begin{aligned}
\beta_k &= -\frac{1}{2}\frac{\partial \chi_N^2}{\partial a_k} = \sum_i \frac{c_i - m_{\mathbf{a}'}(\theta_i)}{\max{(c_i, 1)}} \cdot \left.\frac{\partial m_{\mathbf{a}}(\theta_i)}{\partial a_k}\right|_{\mathbf{a}=\mathbf{a}'} \\
\alpha_{kj} &= \sum_i \frac{1}{\max{(c_i, 1)}} \cdot \left.\frac{\partial m_{\mathbf{a}}(\theta_i)}{\partial a_k}\right|_{\mathbf{a}=\mathbf{a}'} \left.\frac{\partial m_{\mathbf{a}}(\theta_i)}{\partial a_j}\right|_{\mathbf{a}=\mathbf{a}'}
\end{aligned}
\tag{E.6}
$$

E.2   Pearson's χ_P^2

In the case of Pearson's χ_P^2, the statistical variable is given by Eq. (6.7)

$$\chi_P^2 = \sum_i \frac{(c_i - m_{\mathbf{a}}(\theta_i))^2}{m_{\mathbf{a}}(\theta_i)}$$

Using the expansion of Eq. (E.2), χ_P^2 can be written as a function of the parameter increments δa_j.

$$\chi_P^2 = \sum_i \frac{\left(c_i - m_{\mathbf{a}'}(\theta_i) - \sum_j \left.\frac{\partial m_{\mathbf{a}}(\theta_i)}{\partial a_j}\right|_{\mathbf{a}=\mathbf{a}'} \delta a_j\right)^2}{m_{\mathbf{a}'}(\theta_i) + \sum_j \left.\frac{\partial m_{\mathbf{a}}(\theta_i)}{\partial a_j}\right|_{\mathbf{a}=\mathbf{a}'} \delta a_j} \tag{E.7}$$

Minimising this function with respect to δa_j by setting its derivative equal to zero, the components of $\boldsymbol{\alpha}$ and $\boldsymbol{\beta}$ can be derived after applying the approximation $(1+\xi)^{-2} \simeq (1-2\xi)$ for $\xi \ll 1$

$$\frac{\partial \chi_P^2}{\partial \delta a_k} = \sum_i \left.\frac{\partial m_{\mathbf{a}}(\theta_i)}{\partial a_k}\right|_{\mathbf{a}=\mathbf{a}'} \left[1 - \frac{c_i^2}{\left(m_{\mathbf{a}'}(\theta_i) + \sum_j \left.\frac{\partial m_{\mathbf{a}}(\theta_i)}{\partial a_j}\right|_{\mathbf{a}=\mathbf{a}'} \delta a_j\right)^2}\right] \overset{!}{=} 0 \tag{E.8}$$

$$\implies \sum_i \left.\frac{\partial m_{\mathbf{a}}(\theta_i)}{\partial a_k}\right|_{\mathbf{a}=\mathbf{a}'} \left[1 - \left(\frac{c_i}{m_{\mathbf{a}'}(\theta_i)}\right)^2 \cdot \left(1 - \frac{2}{m_{\mathbf{a}'}(\theta_i)} \sum_j \left.\frac{\partial m_{\mathbf{a}}(\theta_i)}{\partial a_j}\right|_{\mathbf{a}=\mathbf{a}'} \delta a_j\right)\right] = 0 \tag{E.9}$$

$$\sum_i \frac{\partial m_{\mathrm{a}}(\theta_i)}{\partial a_k}\bigg|_{\mathrm{a=a'}} \left(\left[\frac{c_i}{m_{\mathrm{a'}}(\theta_i)}\right]^2 - 1\right) =$$

$$\sum_j \left[\sum_i \left(\frac{2c_i^2}{(m_{\mathrm{a'}}(\theta_i))^3} \frac{\partial m_{\mathrm{a}}(\theta_i)}{\partial a_k}\bigg|_{\mathrm{a=a'}} \frac{\partial m_{\mathrm{a}}(\theta_i)}{\partial a_j}\bigg|_{\mathrm{a=a'}}\right)\right] \delta a_j \quad \text{(E.10)}$$

This can be written in the form of Eq. (E.3) with components

$$\beta_k = -\frac{1}{2}\frac{\partial \chi_P^2}{\partial a_k} = \frac{1}{2}\sum_i \left[\left(\frac{c_i}{m_{\mathrm{a'}}(\theta_i)}\right)^2 - 1\right] \cdot \frac{\partial m_{\mathrm{a}}(\theta_i)}{\partial a_k}\bigg|_{\mathrm{a=a'}}$$

$$\alpha_{kj} = \sum_i \frac{c_i^2}{(m_{\mathrm{a'}}(\theta_i))^3} \cdot \frac{\partial m_{\mathrm{a}}(\theta_i)}{\partial a_k}\bigg|_{\mathrm{a=a'}} \frac{\partial m_{\mathrm{a}}(\theta_i)}{\partial a_j}\bigg|_{\mathrm{a=a'}} \quad \text{(E.11)}$$

E.3 MLE/Poisson

The MLE χ^2 for Poisson statistics is given by Eq. (6.16)

$$\chi_{\lambda,P}^2 = 2\sum_i [m_{\mathrm{a}}(\theta_i) - c_i \ln m_{\mathrm{a}}(\theta_i)] + \text{const.}$$

Using the expansion of Eq. (E.2) in this statistic, one obtains

$$\chi_{\lambda,P}^2 = 2\sum_i \left[\left(m_{\mathrm{a'}}(\theta_i) + \sum_j \frac{\partial m_{\mathrm{a}}(\theta_i)}{\partial a_j}\bigg|_{\mathrm{a=a'}} \delta a_j\right)\right.$$

$$\left. -c_i \ln\left(m_{\mathrm{a'}}(\theta_i) + \sum_j \frac{\partial m_{\mathrm{a}}(\theta_i)}{\partial a_j}\bigg|_{\mathrm{a=a'}} \delta a_j\right)\right] + \text{const.} \quad \text{(E.12)}$$

This function is minimised with respect to δa_k by setting its derivative equal to zero, leading to, if using the approximation $(1 + \xi)^{-1} \simeq (1 - \xi)$ for $\xi \ll 1$

$$\frac{\partial \chi_{\lambda,P}^2}{\partial \delta a_k} = 2\sum_i \frac{\partial m_{\mathrm{a}}(\theta_i)}{\partial a_k}\bigg|_{\mathrm{a=a'}} \left[1 - \frac{c_i}{m_{\mathrm{a'}}(\theta_i) + \sum_j \frac{\partial m_{\mathrm{a}}(\theta_i)}{\partial a_j}\big|_{\mathrm{a=a'}} \delta a_j}\right] \overset{!}{=} 0 \quad \text{(E.13)}$$

$$\sum_i \frac{\partial m_{\mathrm{a}}(\theta_i)}{\partial a_k}\bigg|_{\mathrm{a=a'}} \left[1 - \frac{c_i}{m_{\mathrm{a'}}(\theta_i)} \left(1 - \frac{1}{m_{\mathrm{a'}}(\theta_i)} \sum_j \frac{\partial m_{\mathrm{a}}(\theta_i)}{\partial a_j}\bigg|_{\mathrm{a=a'}} \delta a_j\right)\right] = 0 \quad \text{(E.14)}$$

$$\sum_i \frac{\partial m_{\mathrm{a}}(\theta_i)}{\partial a_k}\bigg|_{\mathrm{a=a'}} \left(\frac{c_i}{m_{\mathrm{a'}}(\theta_i)} - 1\right) =$$

$$\sum_j \left[\sum_i \left(\frac{c_i}{(m_{\mathrm{a'}}(\theta_i))^2} \frac{\partial m_{\mathrm{a}}(\theta_i)}{\partial a_k}\bigg|_{\mathrm{a=a'}} \frac{\partial m_{\mathrm{a}}(\theta_i)}{\partial a_j}\bigg|_{\mathrm{a=a'}}\right)\right] \delta a_j \quad \text{(E.15)}$$

This can be written in the form of Eq. (E.3) with components

$$\beta_k = -\frac{1}{2}\frac{\partial \chi^2_{\lambda,P}}{\partial a_k} = \sum_i \left.\frac{\partial m_{\mathbf{a}}(\theta_i)}{\partial a_k}\right|_{\mathbf{a}=\mathbf{a}'} \cdot \left(\frac{c_i}{m_{\mathbf{a}'}(\theta_i)} - 1\right)$$

$$\alpha_{kj} = \sum_i \frac{c_i}{(m_{\mathbf{a}'}(\theta_i))^2} \cdot \left.\frac{\partial m_{\mathbf{a}}(\theta_i)}{\partial a_k}\right|_{\mathbf{a}=\mathbf{a}'} \left.\frac{\partial m_{\mathbf{a}}(\theta_i)}{\partial a_j}\right|_{\mathbf{a}=\mathbf{a}'} \qquad\qquad (E.16)$$

Bibliography

[Abr 69]   A. A. ABRAHAMSON, *Born-Mayer-type interatomic potential for neutral ground-state atoms with $Z = 2$ to $Z = 105$*, Phys. Rev. **178** (1969) 76–79.

[Ack 87]   G. J. ACKLAND, G. TICHY, V. VITEK, AND M. W. FINNIS, *Simple N-body potentials for the noble metals and nickel*, Phil. Mag. A **56** (1987) 735–756.

[Alb 98]   K. ALBE, *Computersimulationen zu Struktur und Wachstum von Bornitrid*, PhD thesis, FZ Rossendorf, TU Dresden (1998).

[AllTil 87] M. P. ALLEN AND D. J. TILDESLEY, *Computer Simulation of Liquids*, Oxford University Press, Oxford (1987).

[And 83]   P. ANDERSSON, L. P. EKSTRÖM, AND J. LYTTKENS, *Nuclear data sheets for $A = 59$*, Nuclear Data Sheets **39** (1983) 641.

[AS 83]   F. AJZENBERG-SELOVE, *Energy levels of light nuclei $A = 18 - 20$*, Nucl. Phys. **A392** (1983) 1–216.

[AS 88]   ———, *Energy levels of light nuclei $A = 5 - 10$*, Nucl. Phys. **A490** (1988) 1–225.

[AS 90]   ———, *Energy levels of light nuclei $A = 11 - 12$*, Nucl. Phys. **A506** (1990) 1–158.

[AS 91]   ———, *Energy levels of light nuclei $A = 13 - 15$*, Nucl. Phys. **A523** (1991) 1–196.

[Aub 79]   R. L. AUBLE, *Nuclear data sheets for $A = 63$*, Nuclear Data Sheets **28** (1979) 559.

[Awa 79]   T. AWAYA, *A new method for curve fitting to the data with low statistics not using the χ^2-method*, Nucl. Instr. Meth. **165** (1979) 317–323.

[Bag 93]   C. M. BAGLIN, *Nuclear data sheets update for $A = 59$*, Nuclear Data Sheets **69** (1993) 733.

[Bag 96]   ———, *Nuclear data sheets for $A = 81$*, Nuclear Data Sheets **79** (1996) 447.

[BakCou 84] S. BAKER AND R. D. COUSINS, *Clarification of the use of chi-square and like-lihood functions in fits to histograms*, Nucl. Instr. Meth. **221** (1984) 437–442.

[BasMel 79] M. I. BASKES AND C. F. MELIUS, *Pair potentials for fcc metals*, Phys. Rev. B **20** (1979) 3197–3204.

[BevRob 92] P. R. BEVINGTON AND D. K. ROBINSON, *Data Reduction and Error Analysis for the Physical Sciences*, McGraw-Hill, New York, 2nd ed. (1992).

[Bha 88]   M. R. BHAT, *Nuclear data sheets for $A = 68$*, Nuclear Data Sheets **55** (1988) 1.

[Bha 89]   ——, *Nuclear data sheets for A = 69*, Nuclear Data Sheets **58** (1989) 1.

[Bha 91]   ——, *Nuclear data sheets update for A = 67*, Nuclear Data Sheets **64** (1991) 875.

[Bha 92]   ——, *Nuclear data sheets update for A = 57*, Nuclear Data Sheets **67** (1992) 195.

[Bha 93a]   ——, *Nuclear data sheets update for A = 65*, Nuclear Data Sheets **69** (1993) 209.

[Bha 93b]   ——, *Nuclear data sheets update for A = 71*, Nuclear Data Sheets **68** (1993) 579.

[Bha 95]   ——, *Nuclear data sheets update for A = 68*, Nuclear Data Sheets **76** (1995) 343.

[Bha 98]   ——, *Nuclear data sheets for A = 57*, Nuclear Data Sheets **85** (1998) 415.

[Bha 99]   ——, *Nuclear data sheets for A = 61*, Nuclear Data Sheets **88** (1999) 417.

[Bhu 96]   G. M. BHUIYAN, M. SILBERT, AND M. J. STOTT, *Structure and thermodynamic properties of liquid transition metals: An embedded-atom-method approach*, Phys. Rev. B **53** (1996) 636–645.

[BloLoh 98]   V. BLOBEL AND E. LOHRMANN, *Statistische und numerische Methoden der Datenanalyse*, Teubner, Stuttgart (1998).

[Bör 88]   H. G. BÖRNER, J. JOLIE, F. HOYLER, S. ROBINSON, M. S. DEWEY, G. GREENE, E. KESSLER, AND R. D. DESLATTES, *Determination of short lifetimes with ultra high resolution (n,γ) spectroscopy*, Phys. Lett. B **215** (1988) 45–49.

[BörJol 93]   H. G. BÖRNER AND J. JOLIE, *Sub-picosecond lifetime measurements by gamma ray induced Doppler broadening*, J. Phys. G: Nucl. Part. Phys. **19** (1993) 217–248.

[Bra 99]   S. BRANDT, *Datenanalyse*, Spektrum, Akad. Verl., Heidelberg, 4th ed. (1999).

[Bri 94]   E. BRINGUIER, *Tentative anatomy of ZnS-type electroluminescence*, J. Appl. Phys. **75** (1994) 4291–4312.

[Bur 95]   T. W. BURROWS, *Nuclear Data Sheets Update for A = 49*, Nuclear Data Sheets **76** (1995) 191– 284.

[Cas 79]   W. CASH, *Parameter estimation in astronomy through application of the likelihood ratio*, The Astrophysical Journal **228** (1979) 939–947.

[Chu 97]   Z. CHUNMEI, *Nuclear data sheets for A = 51*, Nuclear Data Sheets **81** (1997) 183.

[DawBas 83]   M. S. DAW AND M. I. BASKES, *Semiempirical, quantum mechanical calculation of hydrogen embrittlement in metals*, Phys. Rev. Letters **50** (1983) 1285–1288.

[DawBas 84]   ——, *Embedded-atom method: Derivation and application to impurities, surfaces, and other defects in metals*, Phys. Rev. B **29** (1984) 6443–6453.

[Dol 00]   C. DOLL, H. G. BÖRNER, T. VON EGIDY, H. FUJIMOTO, M. JENTSCHEL, AND H. LEHMANN, *GAMS 5*, J. Res. Natl. Inst. Stand. Technol. **105** (2000) 167–171.

[Ead 71]   W. T. EADIE, D. DRIJARD, F. E. JAMES, M. ROOS, AND B. SADOULET, *Statistical Methods in Experimental Physics*, North-Holland Publishing, Amsterdam, 1st ed. (1971).

[Eck 91]   W. ECKSTEIN, *Computer Simulation of Ion-Solid Interactions*, Springer Series in Materials Science 10, Springer, Berlin (1991).

[Enc 85]   Z. ENCHEN, H. JUNDE, Z. CHUNMEI, L. XIANE, AND W. LIZHENG, *Nuclear data sheets for $A = 55$*, Nuclear Data Sheets **44** (1985) 463.

[End 90]   P. M. ENDT ET AL., *Energy levels of $A = 21 - 44$ nuclei (VII)*, Nucl. Phys. **A521** (1990).

[EndvdLeu 78]   P. M. ENDT AND C. VAN DER LEUN, *Energy levels of $A = 21 - 44$ nuclei (VI)*, Nucl. Phys. **A310** (1978) 1–752.

[Far 95]   A. R. FARHAN, *Nuclear data sheets update for $A = 74$*, Nuclear Data Sheets **74** (1995) 529.

[FarSin 97]   A. R. FARHAN AND B. SINGH, *Nuclear data sheets for $A = 77$*, Nuclear Data Sheets **81** (1997) 417.

[FarSin 99]   A. R. FARHAN AND B. SINGH, *Nuclear data sheets for $A = 75$*, Nuclear Data Sheets **86** (1999) 785.

[Fir 96]   R. B. FIRESTONE, *Table of Isotopes*, Wiley-Interscience, New York, 8th ed. (1996).

[Foi 85]   S. M. FOILES, *Calculation of the surface segregation of Ni-Cu alloys with the use of the embedded-atom method*, Phys. Rev. B **32** (1985) 7685–7693.

[Foi 86]   S. M. FOILES, M. I. BASKES, AND M. S. DAW, *Embedded-atom-method functions for the fcc metals Cu, Ag, Au, Ni, Pd, Pt, and their alloys*, Phys. Rev. B **33** (1986) 7983–7991.

[Fra 55]   H. FRAUENFELDER, *Angular distribution of nuclear radiation*, in K. Siegbahn [Sie 55], 531–599.

[FraSte 65]   H. FRAUENFELDER AND R. M. STEFFEN, *Angular distribution of nuclear radiation*, in K. Siegbahn [Sie 65], 997–1198.

[Gär 95]   K. GÄRTNER ET AL., *Round robin computer simulation of ion transmission through crystalline layers*, Nucl. Instr. Meth. B **102** (1995) 183–197.

[Gär 98]   K. GÄRTNER, *Gärtner-Hehl potential for Zn–S, S–S, and Zn–Zn*. private communication (1998).

[Gär 00]   ——, *Gärtner-Hehl potential for Ti–O, Ti–Ti, and O–O*. private communication (2000).

[GärHeh 79]   K. GÄRTNER AND K. HEHL, *Theoretical description of elastic atom–atom scattering*, phys. stat. sol. (b) **94** (1979) 231–238.

[GirWei 59]   L. A. GIRIFALCO AND V. G. WEIZER, *Application of the Morse potential function to cubic metals*, Phys. Rev. **114** (1959) 687–690.

[GolJeu 63]   P. GOLDFINGER AND M. JEUNEHOMME, *Mass spectrometric and Knudsen-cell vaporization studies of group 2B-6B compounds*, Trans. Faraday Soc. **59** (1963) 2851–2867.

[Gre 91]   K. E. GREGORICH, *Maximum likelihood decay curve fits by the simplex method*, Nucl. Instr. Meth. A **302** (1991) 135–142.

[GruSpi 67]   H. GRUPPELAAR AND P. SPILLING, *Thermal-neutron capture gamma rays from natural calcium*, Nucl. Phys. **A102** (1967) 226–236.

[GueAda 92]   A. M. GUELLIL AND J. B. ADAMS, *The application of the analytic embedded atom method to bcc metals and alloys*, J. Mater. Res. **7** (1992) 639–652.

[Gum 43]   E. J. GUMBEL, *On the reliability of the classical chi-square test*, Annals of Mathematical Statistics **14** (1943) 253–263.

[Hab 95]   R. HABERLANDT, S. FRITZSCHE, G. PEINEL, AND K. HEINZINGER, *Molekular-dynamik, Grundlagen und Anwendungen*, Vieweg, Braunschweig (1995).

[Hai 92]   J. M. HAILE, *Molecular Dynamics Simulation, Elementary Methods*, John Wiley & Sons, New York (1992).

[HanTho 99]   M. D. HANNAM AND W. J. THOMPSON, *Estimating small signals by using maximum likelihood and Poisson statistics*, Nucl. Instr. Meth. A **431** (1999) 239–251.

[HauJen 01]   T. HAUSCHILD AND M. JENTSCHEL, *Comparison of maximum likelihood estimation and chi-square statistics applied to counting experiments*, Nucl. Instr. Meth. A **457** (2001) 384–401.

[Hee 90]   D. W. HEERMANN, *Computer Simulation Methods in Theoretical Physics*, Springer-Verlag, Berlin, 2nd ed. (1990).

[HeiJan 92]   K. H. HEINIG AND D. JANSSEN, *The fine structure of Doppler profiles in molecular dynamics channeling calculation*, ILL Internal Report 92HGB16T (1992).

[Hoe 54]   P. G. HOEL, *Introduction to Mathematical Statistics*, John Wiley & Sons, New York, 2nd ed. (1954).

[Ich 96]   M. ICHIMURA, *Stillinger-Weber potentials for III-V compound semiconductors and their application to the critical thickness claculation for InAs/GaAs*, phys. stat. sol. (a) **153** (1996) 431–437.

[JadRii 96]   Y. JADING AND K. RIISAGER, *Systematic errors in χ^2-fitting of Poisson distributions*, Nucl. Instr. Meth. A **372** (1996) 289–292.

[Jen 96a]   M. JENTSCHEL, H. G. BÖRNER, AND C. DOLL, *New applications of the GRID-technique in nuclear and solid state physics*, in Proceedings of the 9th International Symposium on Capture Gamma-Ray Spectroscopy and related topics (CGS 9, Budapest, Hungary, 8–12 October 1996), G. L. Molnár, T. Belgya, and Z. Révay, eds., Springer (1996), 755–768.

[Jen 96b]   M. JENTSCHEL, K. H. HEINIG, H. G. BÖRNER, J. JOLIE, AND E. G. KESSLER, *Atomic collision cascades studied with the Crystal-GRID method*, Nucl. Ins. Meth. **B115** (1996) 446–451.

[Jen 97a]   M. JENTSCHEL, *Crystal-GRID: Eine neue nukleare Sonde zur Untersuchung atomarer Bewegung im Festkörper*, PhD thesis, TU Dresden (1997).

[Jen 97b]   M. JENTSCHEL, K.-H. HEINIG, H. G. BÖRNER, AND C. DOLL, *Crystal-GRID investigation of atomic collision cascades in ionic compounds*, Materials Science Forum **248-249** (1997) 49–52.

[Jen 00]   M. JENTSCHEL, H. G. BÖRNER, H. LEHMANN, AND C. DOLL, *The GRID technique: Current status and new trends*, J. Res. Natl. Inst. Stand. Technol. **105** (2000) 25–32.

[Joh 64]   R. A. JOHNSON, *Interstitials and vacancies in α iron*, Phys. Rev. **134** (1964) A1329–A1336.

[Jol 89]   J. JOLIE, S. ULBIG, H. G. BÖRNER, K. P. LIEB, S. J. ROBINSON, P. SCHILLE-BEECKX, E. G. KESSLER, M. S. DEWEY, AND G. L. GREENE, *Study of low energetic atomic collisions in solids using high-resolution (n,γ) spectroscopy*, Europhys. Lett. **10** (1989) 231–236.

[Jol 92]   J. JOLIE, *Nuclear structure at high level densities: theoretical studies and a new method to measure short lifetimes.* Professorial Dissertation, Universiteit Gent (1991/1992).

[JolStr 00]   J. JOLIE AND N. STRITT, *Neutrino induced Doppler broadening*, J. Res. Natl. Inst. Stand. Technol. **105** (2000) 89–96.

[Jun 93]   H. JUNDE, S. HUIBIN, Z. WEIZHONG, AND Z. QING, *Nuclear data sheets update for A = 54*, Nuclear Data Sheets **68** (1993) 887.

[Jun 99]   H. JUNDE, *Nuclear data sheets for A = 53*, Nuclear Data Sheets **87** (1999) 507.

[Jur 97]   E. T. JURNEY, J. W. STARNER, J. E. LYNN, AND S. RAMAN, *Thermal-neutron capture by ^{14}N*, Phys. Rev. C **56** (1997) 118–134.

[Kah 97]   T. KAHN, T. VON EGIDY, F. HARTMANN, J. OTT, AND M. JENTSCHEL, *Gamma-ray induced Doppler shift attenuation after (n,γ) reactions in Si and Ti*, Nucl. Instr. Meth. A **385** (1997) 100–107.

[Kar 99]   A. KARMANN, *Resolution and sensitivity of GAMS spectrometer crystals.* private communication (1999).

[Kar 00]   A. KARMANN, W. WESCH, B. WEBER, H. G. BÖRNER, AND M. JENTSCHEL, *Application of GRID to foreign atom localization in single crystals*, J. Res. Natl. Inst. Stand. Technol. **105** (2000) 177–182.

[Kea 66]   P. N. KEATING, *Effect of invariance requirements on the elastic strain energy of crystals with application to the diamond structure*, Phys. Rev. **145** (1966) 637–645.

[Kei 91]   J. KEINONEN, A. KURONEN, P. TIKKANEN, H. G. BÖRNER, J. JOLIE, S. ULBIG, E. G. KESSLER, R. M. NIEMINEN, M. J. PUSKA, AND A. P. SEITSONEN, *First-principles simulation of intrinsic collision cascades in KCl and NaCl to test interatomic potentials at energies between 5 and 350 eV*, Phys. Rev. Lett. **67** (1991) 3692–3695.

[KenStu 67]   M. G. KENDALL AND A. STUART, *The Advanced Theory of Statistics*, vol. 2, Charles Griffin & Company, London, 2nd ed. (1967).

[Kes 88]   E. G. KESSLER, G. L. GREENE, M. S. DEWEY, R. D. DESLATTES, H. BÖRNER, AND F. HOYLER, *High accuracy, absolute wavelength determination of capture gamma-ray energies for $E \leq 5$ MeV and the direct determination of binding energies in light nuclei*, J. Phys. G: Nucl. Phys. Suppl. **14** (1988) S167–S174.

[Kes 01]   E. G. KESSLER, JR., M. S. DEWEY, R. D. DESLATTES, A. HENINS, H. G. BÖRNER, M. JENTSCHEL, AND H. LEHMANN, *The GAMS4 flat crystal facility*, Nucl. Instr. Meth. A **457** (2001) 187–202.

[Kim 96]   D.-W. KIM, N. ENOMOTO, AND Z. NAKAGAWA, *Molecular dynamic simulation in titanium dioxide polymorphs: Rutile, brookite, and anatase*, J. Am. Ceram. Soc. **79** (1996) 1095–1099.

[KinCho 93] M. M. KING AND W.-T. CHOU, *Nuclear data sheets update for $A = 73$*, Nuclear Data Sheets **69** (1993) 857.

[Kis 94]   KISSINGER, *Kerne mit effektiven (n,γ) Querschnitten $s_{eff} = s \cdot$ Häufigkeit als Kandidaten für GRID-Experimente am ILL* (1994).

[Kov 91]   S. A. KOVALENKO, Y. E. KOSHUTSKY, V. T. KUPRYASHKIN, N. S. KRAVETS, V. A. STEPANENKO, N. V. STRILCHUK, A. I. FEOKTISTOV, AND I. P. SHAPOVALOVA, *Ismerenie vremen schisni urovnei ^{54}Cr v (n,γ)-reakzii*, Proc. 41st Ann. Conf. Nucl. Spectros. Struct. At. Nuclei, Minsk (1991) 48–48.

[Kru 82]   B. KRUSCHE, K. P. LIEB, H. DANIEL, T. VON EGIDY, G. BARREAU, H. G. BÖRNER, R. BRISSOT, C. HOFMEYR, AND R. RASCHER, *Gamma ray energies and ^{36}Cl level scheme from the reaction ^{35}Cl(n,γ)*, Nucl. Phys. **A386** (1982) 245–268.

[Kur 91]   A. KURONEN, *Molecular dynamics simulation of atom-atom collisional scattering*, J. Phys.: Condens. Matter **3** (1991) 1363–1370.

[Kur 92]   A. KURONEN, J. KEINONEN, H. G. BÖRNER, J. JOLIE, AND S. ULBIG, *Molecular dynamics simulations applied to the determination of nuclear lifetimes from Doppler-broadened γ-ray line shapes produced in thermal neutron capture reactions*, Nucl. Phys. **A549** (1992) 59–83.

[Law 56a]   D. N. LAWLEY, *A general method for approximating to the distribution of likelihood ratio criteria*, Biometrika **43** (1956) 295–303.

[Law 56b]   ———, *Tests of significance for the latent roots of covariance and correlation matrices*, Biometrika **43** (1956) 128–136.

[Leh 99]   H. LEHMANN, *Angular correlation in Ti.* private communication (1999).

[Lie 88]   K. P. LIEB, H. G. BÖRNER, M. S. DEWEY, J. JOLIE, S. J. ROBINSON, S. ULBIG, AND C. WINTER, *Doppler shift attenuation lifetime measurements in ^{54}Cr following thermal neutron capture*, Phys. Lett. B **215** (1988) 50–54.

[Mad 82]   O. MADELUNG, ed., *Physik der II-VI und I-VII-Verbindungen, semimagnetische Halbleiter*, vol. III, 17b of Landolt-Börnstein, Springer, Berlin (1982).

[Mar 70]   R. M. MARTIN, *Elastic properties of ZnS structure semiconductors*, Phys. Rev. B 1 (1970) 4005–4011.

[Mic 89]   S. MICHAELSEN, C. WINTER, K. P. LIEB, B. KRUSCHE, S. ROBINSON, AND
               T. VON EGIDY, *High-resolution spectroscopy of ^{32}P*, Nuclear Physics **A501**
               (1989) 437–461.

[Mig 99]   K. J. MIGHELL, *Parameter estimation in astronomy with Poisson-distributed
               data, I. The χ^2 statistic*, The Astrophysical Journal **518** (1999) 380–393.

[MK 94]   T. MAYER-KUCKUK, *Kernphysik*, Teubner Studienbücher, Stuttgart, 6th ed.
               (1994).

[MoSen 83]   J. N. MO AND S. SEN, *Nuclear data sheets for $A = 67$*, Nuclear Data Sheets **39**
               (1983) 741.

[Mur 98]   V. A. MURAVSKY, S. A. TOLSTOV, AND A. L. KHOLMETSKII, *Comparison of
               the least squares and the maximum likelihood estimators for gamma-spectrometry*,
               Nucl. Instr. Meth. B **145** (1998) 573–577.

[NeyPea 28]   J. NEYMAN AND E. S. PEARSON, *On the use and interpretation of certain test
               criteria for purposes of statistical inference. Part II*, Biometrika **20A** (1928) 263–
               294.

[OgoPok 91]   V. V. OGORODNIKOV AND V. V. POKROPIVNY, *Empirical N-body interatomic
               potential for b.c.c. transition metals*, phys. stat. sol. (b) **166** (1991) 69–78.

[OhJoh 88]   D. J. OH AND R. A. JOHNSON, *Simple embedded atom method model for fcc
               and hcp metals*, J. Mater. Res. **3** (1988) 471–478.

[Ose 95]   Y. N. OSETSKY, A. G. MIKHIN, AND A. SERRA, *Study of copper precipitates
               in α-iron by computer simulation, I. Interatomic potentials and properties of Fe
               and Cu*, Phil. Mag. A **72** (1995) 361–381.

[Pas 91]   R. PASIANOT, D. FARKAS, AND E. J. SAVINO, *Empirical many-body interatomic
               potential for bcc transition metals*, Phys. Rev. B **43** (1991) 6952–6961.

[Pic 74]   M. PICHEVAR, J. DELAUNAY, AND B. DELAUNAY, *Lifetime measurements in
               ^{59}Ni and ^{57}Ni*, Nuclear Physics **A224** (1974) 34–44.

[PosHei 95]   M. POSSELT AND K.-H. HEINIG, *Comparison of BC and MD simulations of
               low-energy ion implantation*, Nucl. Instr. Meth. B **102** (1995) 236–241.

[Pre 89]   W. H. PRESS, B. P. FLANNERY, S. A. TEUKOLSKY, AND W. T. VETTER-
               LING, *Numerical Recipes. The Art of Scientific Computing*, Cambridge University
               Press, Cambridge (1989).

[Rab 91]   S. RAB, *Nuclear data sheets update for $A = 78$*, Nuclear Data Sheets **63** (1991)
               1.

[Ram 85]   S. RAMAN, R. F. CARLTON, J. C. WELLS, E. T. JURNEY, AND J. E. LYNN,
               *Thermal neutron capture gamma rays from sulfur isotopes: Experiment and the-
               ory*, Phys. Rev. C **32** (1985) 18–69.

[Ram 92]   S. RAMAN, E. T. JURNEY, J. W. STARNER, AND J. E. LYNN, *Thermal-neutron
               capture by silicon isotopes*, Phys. Rev. C **46** (1992) 972–983.

[Ram 96]   S. RAMAN, E. K. WARBURTON, J. W. STARNER, E. T. JURNEY, J. E. LYNN, P. TIKKANEN, AND J. KEINONEN, *Spectroscopy of* ^{20}F *levels*, Phys. Rev. C **53** (1996) 616–646.

[RobJol 90] S. J. ROBINSON AND J. JOLIE, *The computer code GRIDDLE*, ILL Internal Report **90RO14T, 92RO15T** (1990).

[Rud 96]   M. RUDA, D. FARKAS, AND J. ABRIATA, *Embedded-atom interatomic potentials for hydrogen in metals and intermetallic alloys*, Phys. Rev. B **54** (1996) 9765–9774.

[Sch 82]   H. H. SCHMIDT ET AL., *Levels and gamma energies of* ^{28}Al *studied by thermal neutron capture*, Phys. Rev. C **25** (1982) 2888–2901.

[SE 81]   W. SEELMANN-EGGEBERT, G. PFENNIG, H. MÜNZEL, AND H. KLEWE-NEBENIUS, *Karlsruher Nuklidkarte*. Kernforschungszentrum Karlsruhe, 5. Auflage (1981).

[Sie 55]   K. SIEGBAHN, ed., *Beta- and Gamma-Ray Spectroscopy*, North-Holland Publishing, Amsterdam (1955).

[Sie 65]   ——, ed., *Alpha-, Beta- and Gamma-Ray Spectroscopy*, vol. 2, North-Holland Publishing, Amsterdam (1965).

[StiWeb 85] F. H. STILLINGER AND T. A. WEBER, *Computer simulation of local order in condensed phases of silicon*, Phys. Rev. B **31** (1985) 5262–5271.

[StoDen 97] M. R. STONEKING AND D. J. DEN HARTOG, *Maximum-likelihood fitting of data dominated by Poisson statistical uncertainties*, Rev. Sci. Instrum. **68** (1997) 914–917.

[Str 97]   N. STRITT, J. JOLIE, M. JENTSCHEL, AND H. G. BÖRNER, *Study of atomic motion in oriented EuO single crystals using neutrino induced Doppler broadening*, Phys. Rev. Lett **78** (1997) 2592–2595.

[Str 98]   N. STRITT, J. JOLIE, M. JENTSCHEL, H. G. BÖRNER, AND C. DOLL, *Neutrino-induced Doppler-broadening study on oriented EuO single crystals*, Phys. Rev. B **58** (1998) 2603–2613.

[Str 99a]   N. STRITT, *Etude des potentiels interatomiques dans des cristaux en utilisant l'élargissement Doppler*, PhD thesis, Université de Fribourg (Suisse) (1999).

[Str 99b]   N. STRITT, J. JOLIE, M. JENTSCHEL, H. G. BÖRNER, AND C. DOLL, *Investigation of the interatomic potential using the crystal gamma-ray-induced Doppler-broadening method on oriented Ni single crystals*, Phys. Rev. B **59** (1999) 6762–6773.

[Str 99c]   N. STRITT, J. JOLIE, M. JENTSCHEL, H. G. BÖRNER, AND H. LEHMANN, *Slowing down of atoms in metals studied by the Doppler-broadened γ-ray line shapes produced after thermal-neutron capture in Fe and Cr crystals*, Phys. Rev. B **60** (1999) 6476–6483.

[Str 00]   N. STRITT, J. JOLIE, M. JENTSCHEL, H. G. BÖRNER, AND C. DOLL, *Study of interatomic potentials using the Crystal-GRID method on oriented single crystals of Ni, Fe, and Cr*, J. Res. Natl. Inst. Stand. Technol. **105** (2000) 71–80.

[Stu 80]   A. E. STUCHBERY, I. MORRISON, D. L. KENNEDY, AND H. H. BOLOTIN, *Level structure and lifetimes of low excitation states in ^{54}Cr*, Nucl. Phys. **A337** (1980) 1–12.

[Swo 82]   W. C. SWOPE, H. C. ANDERSEN, P. H. BERENS, AND K. R. WILSON, *A computer simulation method for the calculation of equilibrium constants for the formation of physical clusters of molecules: Application to small water clusters*, J. Chem. Phys. **76** (1982) 637–649.

[Til 93]   D. R. TILLEY, H. R. WELLER, AND C. M. CHEVES, *Energy levels of light nuclei $A = 16 - 17$*, Nucl. Phys. **A565** (1993) 1–184.

[Ulb 89]   S. ULBIG, K. P. LIEB, C. WINTER, H. G. BÖRNER, J. JOLIE, S. ROBINSON, P. A. MANDO, P. SONA, N. TACCETTI, M. S. DEWEY, J. G. L. BOOTEN, AND F. BRANDOLINI, *Lifetime measurements in ^{57}Fe following the $^{56}Fe(n,\gamma)$ and $^{56}Fe(d,p)$ reactions*, Nucl. Phys. **A505** (1989) 193–214.

[Ulb 91a]   S. ULBIG, *Untersuchung Dopplerverbreiterter γ-Übergänge nach thermischem Neutroneneinfang mittels der GRID-Methode*, PhD thesis, Universität Göttingen (1991).

[Ulb 91b]   S. ULBIG, K. P. LIEB, H. G. BOERNER, B. KRUSCHE, S. J. ROBINSON, AND J. G. L. BOOTEN, *GRID lifetime measurements in $^{59,61,63}Ni$ following thermal neutron capture*, Z. Phys. A **338** (1991) 397–404.

[vEgi 84]   T. VON EGIDY ET AL., *Levels and gamma transitions of ^{40}K studied by neutron capture*, J. Phys. G: Nucl. Phys. **10** (1984) 221–239.

[Vei 71]   W. J. VEIGELE, E. BRIGGS, L. BATES, E. M. HENRY, AND B. BRACEWELL, *X-ray cross section compilation from 0.1 keV to 1 MeV*, vol. 1, revision 1, Defense Nuclear Agency, Washington DC (1971).

[Ver 67]   L. VERLET, *Computer "experiments" on classical fluids. I. Thermodynamical properties of Lennard-Jones molecules*, Phys. Rev. **159** (1967) 98–103.

[VotChe 87] A. F. VOTER AND S. P. CHEN, *Accurate interatomic potentials for Ni, Al and Ni_3Al*, in Characterization of Defects in Materials, MRS Symposia Proceedings No. 82, R. W. Siegel et al., eds., Pittsburgh (1987), Materials Research Society, 175–180.

[WanBoe 95] Y. R. WANG AND D. B. BOERCKER, *Effective interatomic potential for body-centered-cubic metals*, J. Appl. Phys. **78** (1995) 122–126.

[Wes 98]   W. WESCH, A. KARMANN, H. G. BÖRNER, M. JENTSCHEL, AND K.-H. HEINIG, *GRID spectroscopy — a new nuclear method for lattice site localization of foreign atoms*, Nucl. Inst. Meth. B **136-138** (1998) 494–498.

[WesKar 98] W. WESCH AND A. KARMANN, *Entwicklung und Einsatz einer kernphysikalischen Methode für die Materialanalyse auf der Grundlage der höchstauflösenden Spektroskopie Doppler-verbreiterter γ-Linien.* Zwischenbericht zum Förderprojekt 06 OJ 859 1 (1998).

[Whe 95]   W. A. WHEATON, A. L. DUNKLEE, A. S. JACOBSON, J. C. LING, W. A. MAHONEY, AND R. G. RADOCINSKI, *Multiparameter linear least-squares fitting*

to Poisson data one count at a time, The Astrophysical Journal **438** (1995) 322–340.

[Wil 63]   S. S. WILKS, *Mathematical Statistics*, John Wiley, New York, 2nd printing ed. (1963).

[Wil 77]   W. D. WILSON, L. G. HAGGMARK, AND J. P. BIERSACK, *Calculations of nuclear stopping, ranges, and straggling in the low-energy region*, Phys. Rev. B **15** (1977) 2458–2468.

[Won 91]   B. WONG, P. E. JESSOP, AND A. H. KITAI, *Pockels' effect in polycrystalline ZnS planar waveguides*, J. Appl. Phys. **70** (1991) 1180–1184.

[Zie 85]   J. F. ZIEGLER, J. P. BIERSACK, AND U. LITTMARK, *The Stopping and Range of Ions in Solids*, vol. 1 of The Stopping and Ranges of Ions in Matter, Pergamon Press, New York (1985).

[Zie 92]   J. ZIEGLER, ed., *Handbook of Ion Implantation Technology*, North-Holland, Amsterdam (1992).

Versicherung

Hiermit versichere ich, dass ich die vorliegende Arbeit ohne unzulässige Hilfe Dritter und ohne Benutzung anderer als der angegebenen Hilfsmittel angefertigt habe; die aus fremden Quellen direkt oder indirekt übernommenen Gedanken sind als solche kenntlich gemacht. Die Arbeit wurde bisher weder im Inland noch im Ausland in gleicher oder ähnlicher Form einer anderen Prüfungsbehörde vorgelegt.

Die Dissertation wurde unter wissenschaftlicher Betreuung von Dr. Karl-Heinz Heinig und Prof. Wolfhard Möller am Forschungszentrum Rossendorf sowie von Dr. Michael Jentschel am Institut Laue-Langevin in Grenoble, Frankreich, angefertigt.